

EVOLUTION AND VARIABILITY OF CIRCUMSTELLAR MATERIAL  
AROUND YOUNG STELLAR OBJECTS

by  
Kevin Flaherty

---

A Dissertation Submitted to the Faculty of the  
DEPARTMENT OF ASTRONOMY  
In Partial Fulfillment of the Requirements  
For the Degree of  
DOCTOR OF PHILOSOPHY  
In the Graduate College  
THE UNIVERSITY OF ARIZONA

2011

THE UNIVERSITY OF ARIZONA  
GRADUATE COLLEGE

As members of the Dissertation Committee, we certify that we have read the dissertation prepared by Kevin Flaherty entitled "Evolution and Variability of Circumstellar Material Around Young Stellar Objects" and recommend that it be accepted as fulfilling the dissertation requirement for the Degree of Doctor of Philosophy.

\_\_\_\_\_  
George Rieke

Date: 2 August 2011

\_\_\_\_\_  
James Muzerolle

Date: 2 August 2011

\_\_\_\_\_  
John Biegging

Date: 2 August 2011

\_\_\_\_\_  
Phil Hinz

Date: 2 August 2011

\_\_\_\_\_  
Desika Narayanan

Date: 2 August 2011

Final approval and acceptance of this dissertation is contingent upon the candidate's submission of the final copies of the dissertation to the Graduate College.

I hereby certify that I have read this dissertation prepared under my direction and recommend that it be accepted as fulfilling the dissertation requirement.

\_\_\_\_\_  
Dissertation Director: George Rieke

Date: 2 August 2011

## STATEMENT BY AUTHOR

This dissertation has been submitted in partial fulfillment of requirements for an advanced degree at The University of Arizona and is deposited in the University Library to be made available to borrowers under rules of the Library.

Brief quotations from this dissertation are allowable without special permission, provided that accurate acknowledgment of source is made. Requests for permission for extended quotation from or reproduction of this manuscript in whole or in part may be granted by the head of the major department or the Dean of the Graduate College when in his or her judgment the proposed use of the material is in the interests of scholarship. In all other instances, however, permission must be obtained from the author.

SIGNED: Kevin Flaherty

## ACKNOWLEDGMENTS

There are a tremendous number of people that deserve as much credit for this thesis as I do. They have all taught me a great deal and helped me through the long and slow process that is putting together a thesis.

Thanks to all of the people that have taught me about astronomy and have helped me learn what it takes to be an effective researcher. I owe a debt of gratitude to those at the University of Rochester who helped me get started, including Judy Pipher and Rob Gutermuth. Thanks to Tom Megeath for supporting me for a summer and getting me started on my first real research paper. Thanks to my current advisors, James Muzerolle, who was always available to talk whenever I randomly stopped in his office, and George Rieke, who has kept me moving forward and made sure I always kept an eye on the big picture. To the numerous other people who I have been able to talk to about research: Catherine Espaillet, Jared Leisenring, William Herbst, Serena Kim, Josh Eisner, Joan Najita, Dawn Peterson, Tom Allen and many others.

To all of my friends over the years, thanks for making my time at Arizona some of the best years of my life. Thanks to my classmates, Stéphane Herbert-Fort, Stephanie Cortes, Stephanie Juneau and Jared Gabor. I can't imagine a better group of people to spend long hours with while working on homeworks, studying for the prelim, and dealing with the general bullshit of grad school. Thanks to all of the other astronomers who I have known at Arizona: Brandon Kelly, Jon Trump, Desika Narayanan, Shane Bussman, Iva Momcheva, Dennis Just, Greg Walth, Amanda Ford, Brandon Swift (owner of the greatest house for random summer pool parties) and Ben Weiner. Thanks especially to Amy Stutz for her sense of humor and Andy Skemer for giving me someone to talk to about much of my research. Thanks to everyone else I have met in Tucson who has made my time here enjoyable: Monica Stephens, Lauren Zentz, Lindsay Butler, Suz and Coley Ward, Linda Imonode, Marrie Kessler, Jelena Vukomanovic (who probably knows more general astronomy than I do at this point), Catfish, Molly Keck, Kate Mahady, Scott Olmstead, Jon Horst, Tiffany Bartz, James Davies. Thanks to Maggie Diamond-Stanic for joining me in building houses and for feeding us on more occasions than I can count, and Aleks Diamond-Stanic for his sense of humor and his calming influence on the frisbee field. An extra shout-out to Will 'Pacman Diamond Ice' Diamond-Stanic for being his awesome self.

Last but not least, thanks to my family. Thanks to Pat and Meg for everything. Thanks especially to my parents for more than I could every recount.

## DEDICATION

I dedicate this thesis to my family, for everything they have done to help me during all of my years here in arizona.

## TABLE OF CONTENTS

LIST OF FIGURES . . . . .	9
LIST OF TABLES . . . . .	12
ABSTRACT . . . . .	14
CHAPTER 1 INTRODUCTION . . . . .	16
CHAPTER 2 EVIDENCE FOR EARLY CIRCUMSTELLAR DISK EVOLUTION IN NGC 2068/71 . . . . .	22
2.1 Introduction . . . . .	22
2.2 Data . . . . .	24
2.3 Results . . . . .	27
2.3.1 Membership Selection . . . . .	27
2.3.2 HR Diagram . . . . .	30
2.3.3 Radial and Rotational Velocity . . . . .	35
2.3.4 Accretion Activity . . . . .	37
2.3.5 Disk Emission . . . . .	42
2.4 Discussion . . . . .	51
2.4.1 Evolved Disks . . . . .	53
2.5 Conclusion . . . . .	62
CHAPTER 3 MODELING MID-INFRARED VARIABILITY OF CIRCUMSTELLAR DISKS WITH NON-AXISYMMETRIC STRUCTURE . . . . .	82
3.1 Introduction . . . . .	82
3.2 Models . . . . .	84
3.2.1 Motivation . . . . .	84
3.2.2 Deriving the SED . . . . .	86
3.2.3 Middle Warp . . . . .	90
3.2.4 Inner Warp . . . . .	95
3.2.5 Spiral Wave . . . . .	100
3.3 Comparison to Observations . . . . .	106
3.3.1 LRLL 31 . . . . .	106
3.3.2 Application to Other Variables . . . . .	112
3.4 Conclusions . . . . .	115
4 THE HIGHLY DYNAMIC BEHAVIOR OF THE INNERMOST DUST AND GAS IN THE TRANSITION DISK VARIABLE LRLL 31 . . . . .	117
4.1 Introduction . . . . .	118
4.2 Data . . . . .	119
4.3 Evidence for Fluctuating Gas and Dust Properties . . . . .	124

TABLE OF CONTENTS — <i>Continued</i>	
4.3.1	Stellar Properties . . . . . 124
4.3.2	Dust Properties . . . . . 129
4.3.3	Gas Properties . . . . . 141
4.4	Theoretical Implications . . . . . 146
4.4.1	Variable Accretion . . . . . 147
4.4.2	Winds . . . . . 149
4.4.3	Perturbation by a Companion . . . . . 151
4.4.4	Magnetic Fields . . . . . 154
4.5	Conclusion . . . . . 157
CHAPTER 5 TRANSITION DISK VARIABLES . . . . . 174	
5.1	Introduction . . . . . 174
5.2	Variability Observations . . . . . 176
5.2.1	Data . . . . . 176
5.2.2	Stellar Properties . . . . . 178
5.2.3	Infrared Variability . . . . . 183
5.2.4	Gas Properties . . . . . 196
5.3	Perturbation of the Disk . . . . . 204
5.3.1	Is the infrared variability in all of these stars caused by a similar perturbation to the disk? . . . . . 204
5.3.2	LRLL 67 . . . . . 207
5.3.3	Comparing Transition Disk Variables to Other Variables . . 208
5.4	What could be causing these variations? . . . . . 215
5.4.1	No Apparent Connection between the Infrared Variability and the Stellar/Accretion flux . . . . . 215
5.4.2	Winds . . . . . 218
5.4.3	Companion . . . . . 220
5.4.4	Magnetic Fields . . . . . 221
5.5	Conclusion . . . . . 224
CHAPTER 6 CONCLUSION . . . . . 246	
6.1	Disk Evolution in NGC 2068/71 . . . . . 246
6.2	Modeling Infrared Variability . . . . . 247
6.3	Multi-wavelength, Multi-epoch observations of Transition Disks . . 248
6.4	Future Directions . . . . . 250
APPENDIX A DETAILED CALCULATION OF THE SED . . . . . 253	
A.1	Outer Warp + Flat Extension . . . . . 253
A.1.1	Adding $\alpha$ Dependence to Outer Warp . . . . . 253
A.1.2	Flat Extension of Outer Warp . . . . . 255
A.2	Inner Warp . . . . . 256

TABLE OF CONTENTS — <i>Continued</i>	
A.2.1	Temperature Profile of Inner Warp . . . . . 256
A.2.2	Calculating the SED for an Inner Warp . . . . . 258
A.3	Spiral Wave . . . . . 264
A.3.1	Temperature Profile of Spiral Wave . . . . . 264
A.3.2	Calculating SED of Spiral Wave . . . . . 265
A.4	Stellar Flux . . . . . 267
REFERENCES	. . . . . 271



## LIST OF FIGURES

2.1	POSS blue plate of NGC 2068/71 . . . . .	26
2.2	SDSS color-magnitude diagram of sources toward NGC 2068/71 . .	28
2.3	NIR color-magnitude diagram for sources toward NGC 2068/71 . .	29
2.4	NIR color-color diagram of NGC 2068/71 cluster members . . . . .	29
2.5	HR diagram of likely members of NGC 2068/71 . . . . .	33
2.6	Radial velocity histogram of the likely NGC 2068/71 members . . .	36
2.7	Rotational velocity as a fraction of break-up velocity versus mass for NGC 2068/71 members . . . . .	37
2.8	Hectochelle spectra focusing on the $H\alpha$ profiles for select NGC 2068/71 members . . . . .	39
2.9	Equivalent width versus full width at 10% maximum height for the $H\alpha$ line of NGC 2068/71 members . . . . .	40
2.10	Veiling, accretion luminosity and accretion rate as a function of mass for NGC 2068/71 members . . . . .	42
2.11	Slope of IRAC SED versus $T_{eff}$ for NGC 2068/71 members . . . . .	44
2.12	IRAC color-color diagram of NGC 2068/71 members . . . . .	45
2.13	IRAC+MIPS color-color diagram of NGC 2068/71 members . . . . .	45
2.14	SED slope from the IRAC bands versus the SED slope from 8-24 $\mu$ m	46
2.15	Sample SEDs of different shapes based on NGC 2068/17 members	47
2.16	Extinction map of NGC 2068/71 . . . . .	54
3.1	Schematic drawing of our three simple geometric models. . . . .	88
3.2	Temperature structure and SED of middle warp . . . . .	91
3.3	SED of a precessing disk with a middle warp. . . . .	92
3.4	SED for a growing middle warp. . . . .	94
3.5	Temperature structure and SED of inner warp . . . . .	96
3.6	SED of a precessing disk with an inner warp . . . . .	97
3.7	SED for a growing inner warp . . . . .	100
3.8	Temperature structure and SED of disk with a spiral wave . . . . .	102
3.9	SED of a precessing disk with a spiral wave . . . . .	103
3.10	SED for a growing spiral wave . . . . .	105
3.11	SED for a thermal instability wave . . . . .	106
3.12	Observations of LRL 31 . . . . .	108
3.13	SEDs for a growing middle warp compared to LRL 31 . . . . .	110
3.14	SEDs of a growing inner warp compared to LRL 31 . . . . .	111
3.15	SEDs of a growing spiral wave compared to LRL 31 . . . . .	112
3.16	SEDs of an inner warp around stars of different mass . . . . .	114
4.1	Observed 0.8-5 $\mu$ m spectra of LRL 31 . . . . .	121
4.2	More Observed 0.8-5 $\mu$ m spectra of LRL 31 . . . . .	122

4.3	Optical spectra of LRL 31 . . . . .	126
4.4	Veiling of LRL 31 . . . . .	131
4.5	Infrared excess of LRL 31 . . . . .	133
4.6	LRL 31 0.8-5 $\mu$ m spectra with fit to the excess . . . . .	134
4.7	3.6 and 4.5 $\mu$ m light curves for LRL 31 . . . . .	139
4.8	Observed SED of LRL 31 . . . . .	140
4.9	Line measurements of LRL 31 . . . . .	143
4.10	High resolution H $\alpha$ profiles of LRL 31 . . . . .	145
4.11	HeI and Pa $\beta$ lines in LRL 31 . . . . .	146
4.12	Schematic diagrams of various models for the infrared variability of LRL 31 . . . . .	148
4.13	Limits on the presence of a companion to LRL 31 . . . . .	153
5.1	Spitzer data for LRL 2 . . . . .	181
5.2	Spex spectra for LRL 2 . . . . .	185
5.3	Spitzer data for LRL 21 . . . . .	186
5.4	Spex data for LRL 21 . . . . .	188
5.5	The 2-5 $\mu$ m infrared excess of LRL 21 . . . . .	189
5.6	Dereddened 0.8-2.5 $\mu$ m spectra of LRL 21 . . . . .	190
5.7	Spitzer data for LRL 58 . . . . .	192
5.8	Spex spectra of LRL 58 . . . . .	192
5.9	Dereddened 0.8-5 $\mu$ m spectra of LRL 58 . . . . .	193
5.10	Spitzer data for LRL 67 . . . . .	194
5.11	Spitzer data for LRL 1679 . . . . .	195
5.12	Spex spectra of LRL 1679 . . . . .	195
5.13	Pa $\beta$ and Br $\gamma$ spectra of LRL 2 . . . . .	198
5.14	Pa $\beta$ and Br $\gamma$ spectra for LRL 21 . . . . .	199
5.15	H $\alpha$ spectra for LRL 21 . . . . .	200
5.16	Pa $\beta$ and Br $\gamma$ spectra for LRL 58 . . . . .	201
5.17	H $\alpha$ spectra for LRL 58 . . . . .	201
5.18	H $\alpha$ spectra of LRL 67 . . . . .	202
5.19	Pa $\beta$ and Br $\gamma$ spectra of LRL 1679 . . . . .	203
5.20	H $\alpha$ spectra of LRL 1679 . . . . .	203
5.21	Strength versus shape of the 10 $\mu$ m silicate feature for the variable transition disks . . . . .	209
5.22	Infrared RMS fluctuations comparison of transition disks to the rest of the cluster . . . . .	211
5.23	Structure function of the transition disk variables and the rest of the cluster . . . . .	213
5.24	HeI and Pa $\gamma$ spectra for the variable transition disks . . . . .	219
5.25	Areas near the transition disk variables excluded from having a companion . . . . .	222

A.1	Schematic diagram of the limits on $\delta$ for the convex side of the disk	257
A.2	Schematic diagram of the limits on $\delta$ when the star is blocked by some of the disk . . . . .	257
A.3	Schematic diagram of the limits on $\delta$ for the concave side of the disk.	258
A.4	Schematic diagram demonstrating when the star blocks some of the disk . . . . .	261
A.5	Schematic diagram demonstrating the part of the overheated disk that gets blocked by the star. . . . .	262
A.6	Schematic diagram demonstrating the part of the shadowed disk blocked by the star . . . . .	263
A.7	Schematic diagram demonstrating when the disk is steep enough to block itself. . . . .	263
A.8	Schematic diagram demonstrating the position of M and P in the disk when the wave can block part of the disk. . . . .	266
A.9	Schematic diagram demonstrating how the spiral wave can block part of the disk. . . . .	267
A.10	Schematic diagram defining angles for integrating the stellar flux .	268
A.11	Schematic diagram showing the case where $i < 90^\circ$ and the disk can block the star. . . . .	269
A.12	Schematic diagram showing the case where $i > 90$ and the disk can block the star. . . . .	270

## LIST OF TABLES

2.1	Photometry of likely members . . . . .	64
2.2	Cluster members identified from Low-Resolution Spectra . . . . .	69
2.3	Stellar Parameters for Likely Members . . . . .	75
2.4	High-Resolution Spectra of Likely Members . . . . .	79
2.5	Fraction of Evolved Disks . . . . .	81
4.1	Observing Log . . . . .	159
4.2	Photometry . . . . .	162
4.3	IRAC photometry . . . . .	163
4.4	Extinction . . . . .	164
4.5	Stellar Luminosity . . . . .	165
4.6	Infrared Excess . . . . .	166
4.7	Polarimetry . . . . .	167
4.8	Emission Line Tracers of Accretion Rate . . . . .	168
4.9	Accretion Rates . . . . .	169
4.10	H $\alpha$ EW . . . . .	171
4.11	IRAC Warm Mission Photometry . . . . .	172
5.1	Observing Log . . . . .	226
5.2	MIPS photometry . . . . .	229
5.3	IRAC Photometry . . . . .	230
5.4	IRAC Warm Mission Photometry . . . . .	232
5.5	Extinction . . . . .	234
5.6	LRL 21 NIR Photometry . . . . .	235
5.7	LRL 21 Stellar Luminosity . . . . .	235
5.8	Radial and Rotational Velocity . . . . .	236
5.9	Infrared Excess . . . . .	237
5.10	Emission Lines . . . . .	239
5.11	Accretion Rates . . . . .	240
5.12	Strength and shape of silicate feature . . . . .	242

5.13 Inner radii of disk . . . . .	245
A.1 Limiting inclination for occultation of disk by star . . . . .	261

## ABSTRACT

Using multi-wavelength and multi-epoch observations we examine the evolution of circumstellar disks around pre-main sequence stars from massive, optically thick flared disks to wispy debris disks.

We examine a young cluster of nearby stars, identifying likely members and studying dust properties using 3-24 $\mu$ m photometry and accretion rates using optical spectroscopy. We find that 79% of the stars have disks and that almost all of the stars with disks are actively accreting. The stars that show evidence for evolution in their dust properties also exhibit a decrease in the accretion activity suggesting that the evolution of the dust and gas is closely connected.

Focusing on a sub-sample of transition disks we study the source of recently discovered infrared variability and whether it can be used to further our understanding of disk structure. We are particularly interested in sources that show a ‘seesaw’ behavior in their SED in which the short wavelength infrared flux increases while the long wavelength flux decreases causing the SED to pivot about one wavelength. We develop simple geometric models of disks with non-axisymmetric structure and find that the precession of this structure is not able to reproduce the strength or the wavelength dependence of observed infrared variability while a model with an inner warp whose scale height rapidly varies is much more successful. We follow this up with detailed observations covering a wide range of wavelengths from optical to mid-infrared of six transition disks in order to better understand the physical source of the variability. We find that the variability is consistent with a variable scale height of the inner disk, finding direct evidence for this effect in two transition disks. Contemporaneous measures of the infrared flux and the accretion rate find in some cases a correlation between

these two properties, although in none of our stars is it likely that the accretion rate variability is the source of the infrared variability. The most likely cause is either a companion embedded in the disk or a dynamic interface between the stellar magnetic field and the disk.

## CHAPTER 1

## INTRODUCTION

The general picture of the formation and evolution of low mass stars involves the complex interplay of the newly created star and the reservoir of dust and gas surrounding it, feeding it and often shielding it from our view. The first step toward star formation involves the collapse of a gravitationally unstable clump of gas and dust. After the initial hydrostatic protostellar core develops, it is surrounded by a massive envelope and disk that continues to feed it. During this stage the material from the envelope falls onto the disk, from where it accretes onto the protostar building up a majority of the stellar mass. After thousands of years the envelope dissipates, the protostar has accreted most of its mass, and the system is left with a disk of gas and dust. During the subsequent phases of stellar evolution, the star is revealed and planet formation occurs within the disk. Over the years many studies have illuminated the properties of these primordial disks. They are typically 200 AU in size (Andrews & Williams, 2007), with masses ranging from  $10^{-4} - 10^{-1} M_{\odot}$  (Andrews & Williams, 2005). Material flows through the disk at an average rate of  $10^{-8} M_{\odot} yr^{-1}$  (Gullbring et al., 1998) driven most likely by magneto-rotational instabilities (Balbus & Hawley, 1991). They are geometrically thin and are filled with dust grains of a few microns in size (D'Alessio et al., 2006). Their scale height increases with radius, creating a flared structure (Chiang & Goldreich, 1997), and the inner edge is set by the radius at which dust is hot enough to sublimate, where the disk becomes puffed up due to the direct illumination by the central star (Dullemond, 2001). It is also known that they typically last for a few million years (Haisch, Lada & Lada, 2001; Hernandez et al., 2007). What is not well known is how they transition from this state to a situation where



the star is surrounded by an optically thin debris disk whose dust mass can be measured in lunar masses (e.g. Roccatagliata et al., 2009) and whose gas mass is almost non-existent (Pascucci et al., 2006).

The nature of this transition has been difficult to study because for many years it has been challenging to find stars that were between states. Studies that focused on ground-based near and mid-infrared photometry of pre-main sequence stars found many stars with primordial disks, many stars without disks and almost nothing in between (e.g. Haisch, Lada & Lada, 2001). From this, the timescale for the evolution of circumstellar disks was believed to last only a few tenths of a million years, much more rapid than the lifetime of a typical disk.

The ability to study these evolved disks was greatly advanced by the launching of the Spitzer Space Telescope, which provided unprecedented sensitivity to mid-infrared wavelengths that were more accurate probes of the circumstellar disk. While a handful of systems had been previously found to have spectral energy distributions (SEDs) between that of a flared optically thick primordial disk, and an optically thin debris disk (Strom et al., 1989), but Spitzer greatly expanded the number of sources available for study. One class of disks that was found to lie in between these states is the so-called ‘transition’ disks. They are characterized by a deficit of emission at short-wavelengths, typically  $\lambda < 10\mu\text{m}$ , but with a long-wavelength flux that is similar to an optically thick disk (Muzerolle et al., 2010; Merín et al., 2010; Kim et al., 2009). Radiative transfer models have had success explaining these SED shapes with a decrease in the mass of small dust grains in the inner disk (Calvet et al., 2002; D’Alessio et al., 2005; Calvet et al., 2005). This lack of inner disk material has been confirmed with interferometric observations at sub-mm and mm wavelengths that are able to spatially resolve the disk structure (e.g. Andrews et al., 2011). The inner depleted disk stretches

out to a few to tens of AU from the central star. The inner region may be filled with a tenuous disk of optically thin dust, or there may be optically thick dust at the dust destruction radius (Espaillat et al., 2007). They typically make up about  $\sim 10\%$  of a cluster (Muzerolle et al., 2010; Merín et al., 2010).

Multiple theories have been developed to explain this disk evolution. It is possible that the inner disk has been depleted of small grains due to their coagulation into very large grains, reducing the amount of infrared emission. Particles larger than  $\sim 10\mu\text{m}$  within the inner disk will not produce strong emission at  $\lambda < 8\mu\text{m}$  (Tanaka et al., 2005) and models of grain coagulation find that it is a very rapid process (Dullemond & Dominik, 2005). Another possible scenario involves the photoevaporation of the disk by high-energy photons from the star (Clarke et al., 2001; Alexander et al., 2006). Disks around low-mass stars have been observed to be truncated by the radiation from nearby massive O stars (Johnstone et al., 1998), and it is possible that the ionizing radiation of the central star initiates a similar process. High-energy photons, most often in the extreme ultraviolet and far-ultraviolet range, heat the surface layers of gas to a high temperature, creating a thermal wind that slowly removes material from the disk. This wind peaks at a critical radius, typically on the order of 1 AU, where the gravity from the star has weakened enough to allow the hot gas to escape while the high-energy flux is still strong enough to sufficiently heat the gas. For much of the disk's lifetime this wind is counteracted by the inflow of material from the outer disk, but when the accretion rate drops below a critical value the photoevaporative flow takes over. A gap is opened within the disk at the critical radius as the inner disk is starved of material. The inner disk then quickly accretes onto the star on a viscous timescale, leaving a hole and a directly exposed outer disk. Once the outer disk is subject to the full force of the high-energy radiation from the star it is heated to a very high

temperature and the photoevaporative wind quickly drives material outward.

Possibly the most exciting theory involves the creation of one or more planets within the disk. Planets larger than  $\sim$  a Jupiter mass can have a large gravitational effect on the surrounding disk material (Pardekooper & Mellema, 2004). They exert torques on the disk that remove angular momentum from material within its orbit, and impart angular momentum on material outside of its orbit, leading to the opening of a large gap (Artymowicz & Lubow, 1994). Gas and dust may still stream through this gap (Rice et al., 2006), either accreting onto the planet or eventually falling onto the star, but the surface density is severely reduced within the gap (Bryden et al., 1999). Despite the many planets that have been discovered around main sequence stars (e.g. Borucki et al., 2011) their formation process is still not well understood. If the transition disks represent systems in which a planet has recently formed, then studying them in detail could offer clues to how planets form and evolve early in their lifetimes.

Observations of these systems have relied heavily on single-epoch measurements of the spectral energy distribution, which have been successful in determining the geometry of the optically thick dust, but have difficulty distinguishing between the theories of disk evolution. Missing from these observations is the behavior of the gas, which makes up a majority of the mass within the disk. Gas is still being accreted onto the star at levels comparable to full disks (Najita et al., 2007) implying a substantial amount of gas must be flowing through the inner disk. Direct observations of the gas in the inner few AU of transition disks, where the dust is depleted, find that gas still exists in significant quantities (Pontoppidan et al., 2008; Salyk et al., 2009), consistent with the ongoing accretion. This occurs in spite of the orders of magnitude depletion of small dust grains, implying either all of the dust has grown to very large sizes or the gas to dust

mass ratio is much higher than is assumed for full disks. Rice et al. (2006) find, using numerical simulations, that a high gas to dust ratio may be a natural consequence of the pressure gradient created by the barrier between the optically thick outer disk and the inner depleted disk. The presence of gas, and active accretion through the disk, has been a challenge for photoevaporative wind models of transition disks. These models require that the inner disk is not being actively replenished by the outer disk, although recent work has found that the critical accretion rate below which a wind can dominate is  $\sim 10^{-8} M_{\odot} \text{yr}^{-1}$ , more comparable to observed accretion rates than previously thought (Owen et al., 2010). There has also been direct evidence of a photoevaporation based on gas emission line observations around the transition disk TW Hya (Pascucci & Sterzik, 2009). Studying the dynamics of the gas in a large sample of evolved disks would offer more clues to the origin of the depleted inner regions.

There have also been signs of infrared variability within samples of transition disks (Muzerolle et al., 2009; Espaillat et al., 2011). Little is known about the source of these variations, and whether they can be used to understand more about how disks evolve. These early observations found that the inner disk, the exact region that is depleted of small dust grains, is the most likely source of the variability, hinting that it may be related to the evolution of the disk.

Transition disks are not the only form of evolved disk. Another class, sometimes referred to as anemic (Lada et al., 2006) or ‘homologously depleted’ disks (Currie et al., 2009), consists of sources whose flux at all infrared wavelengths has decreased. The SEDs are reminiscent of models that employ completely flat, rather than flared, disks suggesting that the dust grains have experienced a great deal of settling toward the midplane. This class has received less attention than transition disks, although they are likely one form of disk evolution in progress.

This thesis attempts to study evolved disks in detail by taking advantage of multi-wavelength and multi-epoch observations, focusing on both the infrared SED and diagnostics of the gas within the system. In chapter 2 we survey a young cluster, identify a sample of cluster members, use the infrared photometry to study the SEDs of these members, and compare the SEDs with diagnostics of the flow of gas in the disk. From there we move on to discuss the implications of infrared variability of these young systems and what can be learned from synoptic observations. In chapter 3 we develop a simple radiative transfer model that is designed to explain infrared variability with structural perturbations of the circumstellar disk. These models are motivated by observations of the transition disk LRL 31. Chapter 4 discusses multi-wavelength observations of this system, designed to further characterize the strength and timescale of the variability as well as its connection to the flow of gas in the system. Multi-wavelength multi-epoch observations of five additional transition disks are presented in chapter 5. These data are used to determine if their variability can be explained with one model and if it can be used to understand the transition disk phase.

## CHAPTER 2

### EVIDENCE FOR EARLY CIRCUMSTELLAR DISK EVOLUTION IN NGC 2068/71

We study the disk and accretion properties of young stars in the NGC 2068 and NGC 2071 clusters. Using low-resolution optical spectra, we define a membership sample and determine an age for the region of  $\sim 2$  Myr. Using high-resolution spectra of the  $H\alpha$  line we study the accretion activity of these likely members and also examine the disk properties of the likely members using IRAC and MIPS mid-infrared photometry. A substantial fraction (79%) of the 67 members have an infrared excess while all of the stars with significant infrared excess show evidence for active accretion. We find three populations of evolved disks (IRAC-weak, MIPS-weak and transition disks) all of which show decreased accretion activity in addition to the evidence for evolution in the dust disk.

#### 2.1 Introduction

Circumstellar disks are a common, if not universal, part of the star formation process. The dust and gas within them provide the building blocks for planetary systems, hence their study is of critical importance for understanding planet formation processes and timescales. A considerable amount of work has been done in the past 20 years to inventory circumstellar disks in star forming regions and young stellar clusters, constraining their properties and lifetimes as a function of stellar age, mass, and environment. The advent of the Spitzer Space Telescope, with its unprecedented mid-infrared sensitivity, has opened up the field in this regard and is now providing the most complete census of disks to date.

In young clusters the disk fraction is a strong function of age, decreasing from  $\sim 80\%$  for clusters at 1 Myr down to almost no stars with disks for clusters older

than 10 Myr (Haisch, Lada & Lada, 2001; Hernandez et al., 2007). However, large variations in the disk properties exist at any age. Observations of the infrared spectral energy distribution (SED), which traces dust emission from the disk within a few AU of the star, show a wide range of excess for single clusters (Megeath et al., 2005; Sicilia-Aguilar et al., 2006; Dahm & Hillenbrand, 2007; Currie et al., 2007; Gorlova et al., 2007; Winston et al., 2007; Balog et al., 2007) as well as a decrease in the median excess with age (Sicilia-Aguilar et al., 2006; Hernandez et al., 2007; Lada et al., 2006). Submillimeter observations (Beckwith & Sargent, 1991; Miyake & Nakagawa, 1993; Andrews & Williams, 2007) and spectra of the  $10\mu\text{m}$  silicate feature (Bouwman et al., 2001; Kessler-Silacci et al., 2006; Sargent et al., 2006) also show a large variation in the dusts properties between circumstellar disks. The exact nature of this evolution, and why some stars lose their disks before others, has not been completely solved. Strong dependences on the stellar mass have been found, particularly at ages  $>2\text{-}3$  Myr, where less massive stars tend to hold onto their disks longer (e.g. Lada et al., 2006; Carpenter et al., 2006). The role of environment is less clear; while some disks are clearly destroyed more quickly in strong photoionizing environment, there is some evidence that the overall disk frequency changes little (Balog et al., 2007).

Much of the recent Spitzer studies concerning disk evolution have focused on somewhat older regions with ages  $>2$  Myr (Lada et al., 2006; Megeath et al., 2005; Sicilia-Aguilar et al., 2006; Dahm & Hillenbrand, 2007). In order to investigate earlier disk evolution, we present here an analysis of the stellar population of a young embedded cluster associated with the NGC 2068 and 2071 reflection nebulae (hereafter treated as one region NGC 2068/71). As a site of ongoing star-formation with hundreds of young stellar objects, this region provide a unique environment to study early disk evolution. As part of the much larger Orion B

molecular cloud, they are located at a distance of approximately 400 pc (Anthony-Twarog, 1982). The large number of sources with an infrared excess indicate it is still a very young cluster. Studies of dense gas (Lada et al., 1991) and dust continuum (Johnstone et al., 2001) reveal a large number of dense molecular clumps and cores, consistent with the youthful nature of this region.

We have analyzed optical spectra along with optical, near and mid-infrared photometry to identify members of the NGC 2068/71 cluster and study the stellar and circumstellar properties of these members. Section 2.2 describes the data we have obtained, section 2.3 describes our results derived from these data, and section 2.4 includes a discussion of the implications of these results.

## 2.2 Data

Low-resolution optical spectra were taken with the Hectospec instrument on the MMT. Hectospec is a fiber-fed multi-object spectrograph that uses 300 fibers to cover a  $1^\circ$  field of view (Fabricant et al., 2005). These spectra have a resolution of  $R=1200$  and cover the wavelength range 3700-9150Å. They were obtained on Nov 5, 2004 and Oct 23, 2005 with an exposure time of 3x900 sec. Our sample selection methodology will be discussed below.

High-resolution optical spectra were taken with the Hectochelle instrument on the MMT. Hectochelle uses 240 of Hectospec's 300 fibers to cover a similar field of view at much higher resolution (Szentgyorgyi et al., 1998). Spectra were centered on the  $H\alpha$  line at 6563Å covering a wavelength range of 6460-6648Å with a resolution of  $R=32,000$ . Two fields, each with an exposure time of 3x1200 sec, were observed on Dec 3, 2004 and Nov 14, 2005. Five stars (#177, 326, 458, 618 and 1116) were included in both high-resolution observing runs in order to examine the variability in the  $H\alpha$  profile of these objects.



Near-infrared  $JHK_s$  photometry was taken from the Two-Micron All Sky Survey (2MASS). Mid-infrared photometry was obtained using the IRAC and MIPS cameras aboard the *Spitzer* Space telescope. The IRAC observations were taken as part of GTO program 29, IRAC Survey of the Orion Molecular Clouds. IRAC images were taken in High-Dynamic Range (HDR) mode with exposures of 10.4 and 0.4 seconds (Fazio et al., 2004). Individual BCD frames (pipeline version S9.5.0) were mosaicked using a custom IDL program creating separate mosaics from the short exposures and the long exposures. Source selection on these mosaics was completed using PhotVis v1.08 (Gutermuth et al., 2004). Photometry was derived from individual BCD frames using the highest signal to noise data that did not have any saturated pixels (Megeath et al. in prep). The photometry used an aperture of  $2.4''$ , and a sky annulus with inner and outer radii of  $2.4''$  and  $7.2''$ . Magnitude zero points of 21.93, 21.26, 19.08, 19.44, including the aperture correction, were used for these data.

The MIPS observations were taken in scan mode using medium scan rate and half-array offsets, with a total areal coverage of about  $40' \times 45'$  common to the three arrays. The total effective exposure times are 80, 40, and 8 seconds at 24, 70, and 160 microns. Since only a few Class II sources were detected at 70 microns and none at 160, we have omitted those data in this study. The images were reduced using the MIPS instrument team Data Analysis Tool, which includes basic calibration as well as mosaicking of individual exposures (Gordon et al., 2005). The final mosaic was created with half-pixel subsampling. We then performed photometry on individual point sources in the  $24\mu\text{m}$  mosaic using PSF fitting with an empirical PSF constructed from bright isolated point sources in the field. A PSF fit radius of  $5.6''$  and sky annulus of  $15\text{--}22.5''$  were used. An aperture correction of 1.73, as estimated from the STiny Tim PSF model (e.g. Engelbracht et

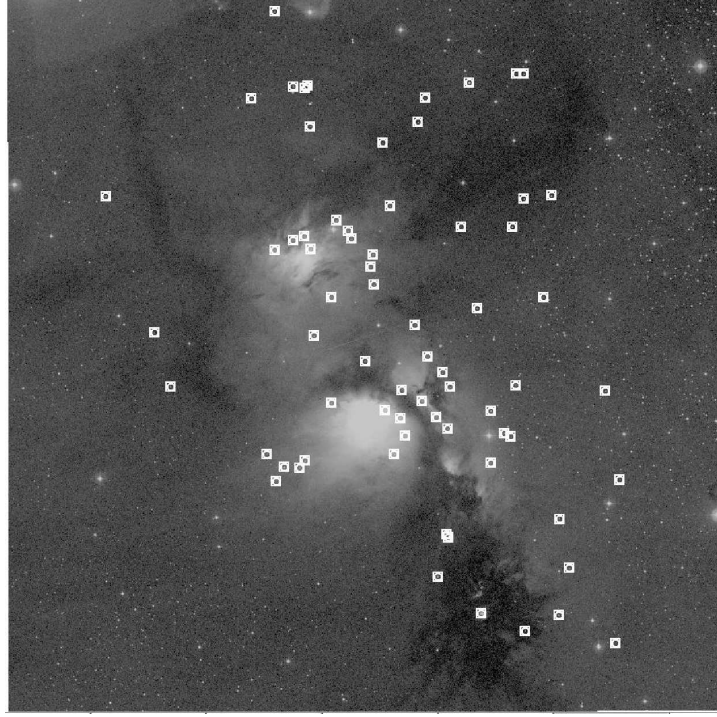


Figure 2.1 POSS blue plate centered at  $\alpha_{2000} = 05^h 46^m 47^s$   $\delta_{2000} = +00^\circ 09' 50''$  spanning one degree on each side overlaid with the positions of cluster members.

al., 2007), was applied to the raw photometry. Fluxes were converted to absolute units using a conversion factor of 150 DN/s/mJy.

Optical photometry was taken from the Sloan Digital Sky Survey (SDSS) (York et al., 2000). The Orion field was observed as part of an early calibration run through the Galactic plane in the fall of 1998 and the fall of 1999 (Finkbeiner et al., 2004). SDSS photometry includes measurements at *ugriz*, whose effective wavelengths are 3540, 4760, 6290, 7690, 9250Å. In total we have photometry extending from 0.35-24 $\mu$ m over a field roughly  $0.8^\circ \times 1.2^\circ$  centered on the NGC 2068 and 2071 nebulae. The MIPS field is slightly smaller, which only affects a few of our selected cluster members. Table 2.1 lists the photometry for the cluster members and Figure 2.1 shows our cluster members overlaid on an optical image of the cluster.

## 2.3 Results

### 2.3.1 Membership Selection

Targets for the spectroscopic survey were chosen based on their position on the  $r$  vs.  $r-i$  color magnitude plot above the expected position of the main sequence at the distance of NGC 2068/71, as seen in Figure 2.2. We restricted ourselves to stars with  $r$  magnitude between 13 and 18.5 to exclude stars that would saturate and those that are too faint to be easily observed. The faint limit corresponds to an unextincted 2 Myr old M6 star at 400pc. Of these stars many are foreground/background stars unrelated to the cluster. The cluster members were identified from the presence of Lithium (6707 Å) absorption and  $H\alpha$  emission in the low-resolution spectra. Since  $H\alpha$  emission can be seen in older stars, such as dMe stars, we use strong Li absorption as the primary indicator of youth, while  $H\alpha$  and other emission lines are used as a secondary indicator. Lithium absorption is an accurate indicator of youth in low-mass stars, but is more ambiguous for G type stars and earlier; with smaller convective envelopes these stars do not burn the Li in their atmospheres as quickly and Li absorption can be observed in older stars. Along with our flux limit, this focuses our survey to low mass stars of spectral type K to mid M. We do not attempt to characterize the high mass or brown dwarf population of young stars within NGC 2068/71.

Our survey is also limited by extinction. Since we define our members based on optical spectra, we cannot survey the deeply embedded population. Figure 2.3 shows a  $J$  vs.  $J-H$  color-magnitude diagram, similar to Figure 2.2, with a reddening vector extending from a 3 Myr old M0 star at 400 pc. Our sample is limited to  $A_V < 5$  although many sources further along the reddening vector have excess emission at 3.6-24 $\mu$ m consistent with circumstellar disks and hence are probably embedded cluster members. A  $J-H$  vs.  $H-K$  color-color diagram for the cluster

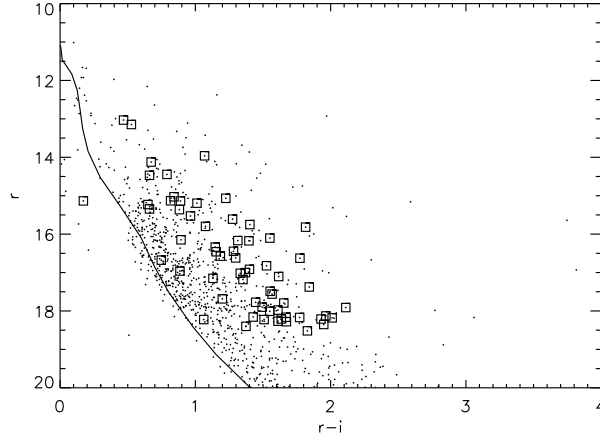


Figure 2.2 SDSS color-magnitude diagram for those stars with optical photometry (dots) and those stars we classify as likely members (squares). Most of the likely members lie above the main sequence locus (Siess et al., 2000), as expected for these young stars.

members is shown in Figure 2.4. The cluster members without a near-infrared excess fall within  $A_V = 5$  of the main sequence locus due to extinction limit imposed by the use of optical spectra.

Table 2.2 lists the stars identified as likely cluster members along with their spectral types and Li and  $H\alpha$  equivalent widths. Of the 453 stars observed spectroscopically, 69 are likely members. They are a mix of classical and weak T-Tauri stars (CTTS, WTTS respectively) and range in spectral type from G6-M6. Two are continuum stars that do not show any significant features that could be used to derive a spectral type. They are added as members, but are not included in the rest of our analysis. CTTS and WTTS are separated based on their  $H\alpha$  equivalent width, using the  $H\alpha$  EW versus spectral type boundary from White & Basri (2003). Resolved  $H\alpha$  profiles are needed to better discriminate between accretors and non-accretors, as will be discussed later.

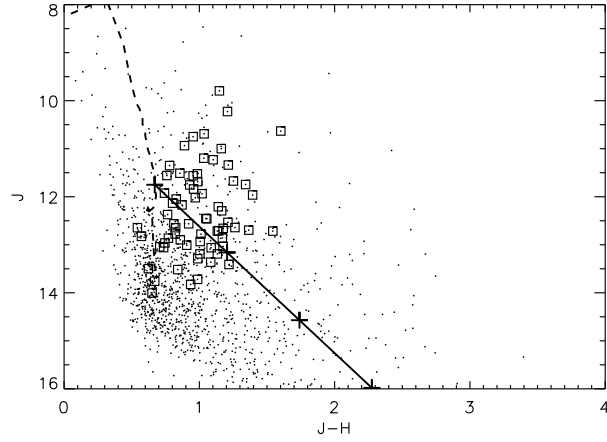


Figure 2.3 NIR color-magnitude diagram for all sources observed toward NGC 2068/71 (dots) and all members (squares). The dashed line is the 2 Myr isochrone from Siess et al. (2000) at the distance of NGC 2068/71. The solid line is a reddening vector extending from a 2 Myr M0 star at the distance of NGC 2068/71, with every  $5 A_V$  marked with an plus sign.

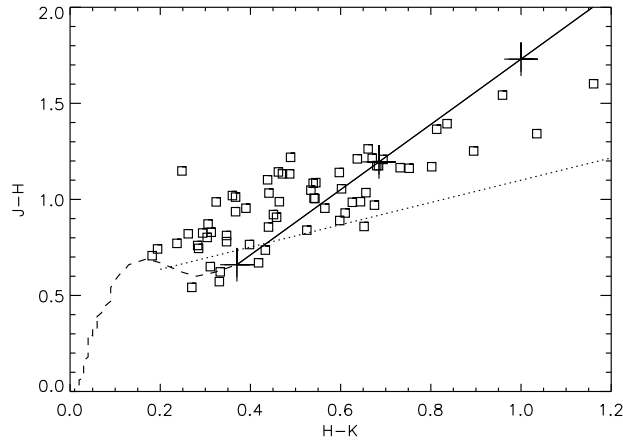


Figure 2.4 NIR color-color diagram of the clusters members. Dashed line shows the main sequence locus from Kenyon & Hartmann (1995) and the dotted line is the CTTS locus from Meyer et al. (1997). The solid line is the reddening vector extending from an M6 star with every  $A_V = 5$  marked with a plus sign. The one star with anomalously blue colors is object 458 which may be contaminated by scattered light in the near-infrared.

### 2.3.2 HR Diagram

To construct an HR diagram and estimate an age for NGC 2068/71, the luminosity and effective temperature are derived for each star. The effective temperature is derived from the strength of multiple absorption bands and lines within the low-resolution spectra, based on the prescription of Sicilia-Aguilar et al. (2004) with a few modifications. In the prescription of Sicilia-Aguilar et al. (2004) the spectra are split into broad categories of early ( $<K1$ ), medium ( $K1-M0$ ) and late ( $M0-M6$ ) spectral types, and separate bands/lines are used within each broad category to derive an effective temperature. Indices were formed for these bands based on the ratio of flux in the feature to flux in the continuum. We did not use the TiO2 (4975Å) band for the medium spectral types or the TiO1 (4775Å) band for late spectral types because they produced  $T_{eff}$  that were inconsistent with the other bands. The spurious temperature from the TiO1 band could be caused by low signal to noise in the later spectral types or veiling from accretion shocks, while the spurious temperature from the TiO2 band could be caused by  $H\beta$  emission in the continuum interval next to the feature. The TiO3 (6185Å) and TiO4 (7140Å) bands are best used for stars with TiO1 index  $> 1.2$  and TiO2 index  $> 1.26$  indicative of later spectral types, but we used them whenever possible because of their tight correlation between band strength and  $T_{eff}$ . When multiple bands were used to determine the  $T_{eff}$  of the star the spread in  $T_{eff}$  was used to estimate the uncertainty in spectral type. Spectral types of the members were visually confirmed by comparing to the standard spectra of Allen & Strom (1995). The spectral types of M stars were also double-checked with the CaII and CaH spectral bands of Allen & Strom (1995), as well as the VO bands of Wilking et al. (2005). Effective temperatures were transformed to spectral types using the conversion of Kenyon & Hartmann (1995).

Veiling can systematically affect our spectral typing since it will reduce the band strengths, resulting in an earlier spectral type. We can estimate the effect of veiling for those star where measurements of the veiling exist (see section 2.3.4). Since veiling is roughly constant redward of  $5000\text{\AA}$  (Basri & Batalha, 1990) our measurements of the veiling at  $6500\text{\AA}$  should be equal to the veiling at the bands that are used to measure spectral type. For these stars the effect of veiling is on the order of the spectral type uncertainty. Overall we do not account for veiling when deriving spectral type, but we do not expect it to substantially change our results.

The luminosity of each star was calculated from its optical photometry, transformed from SDSS ugriz magnitudes to Johnsons-Cousins UBVRI magnitudes (Jordi et al., 2006). The extinction was derived using the observed R-I color along with the intrinsic R-I color from Kenyon & Hartmann (1995) and the extinction law of Rieke & Lebofsky (1985). We chose the extinction law of Rieke & Lebofsky (1985) because it forms the basis for more detailed extinction law studies (Cardelli et al., 1989). It also is comparable to recent determinations of the extinction law in the 2MASS passbands (Indebetouw et al., 2005) allowing us to use it when deriving reddening from R-I colors and from JHK colors (discussed below). The luminosity was then determined from the dereddened I band using bolometric corrections from Kenyon & Hartmann (1995) and a distance of 400 pc. Two objects, #984 and 458, have no optical photometry and no optical luminosity is calculated. Table 2.3 lists the luminosities, effective temperatures and radii, derived assuming  $L=4\pi R^2\sigma T_{eff}^4$ . The typical uncertainty in effective temperature is 5%, while the typical uncertainty in luminosity, which includes uncertainty in  $T_{eff}$  and photometric uncertainty, is 10%.

The luminosity can also be derived from the 2MASS J band magnitude. To

determine the amount of extinction for each star, the observed J-H color was dereddened to the intrinsic J-H color, taken from Kenyon & Hartmann (1995), for the WTTS while the CTTS were dereddened to the CTTS locus from Meyer et al. (1997). Bolometric corrections from Kenyon & Hartmann (1995) were used and a distance of 400 pc was assumed. There is no systematic difference between the extinction or luminosity derived from the optical colors or the near-infrared colors. For three stars where dereddening based on R-I colors resulted in negative extinction, i.e. the observed colors are bluer than the intrinsic colors, the extinction was instead derived from the near-infrared. Two of these stars have late spectral types (M5-M6) for which a different choice of intrinsic colors (e.g. Luhman et al. (2003)) would result in positive extinction. For these stars the extinction is close to zero and a change in the intrinsic colors will have a significant effect on the reddening derived. Object 1171 is much brighter in the optical than in the near-infrared, possibly due to variability, and the extinction and luminosity are both derived from the near-infrared. For objects #984 and 458 the extinction and luminosity were derived from the near-infrared photometry because of the lack of optical photometry. Object 458 appears extended in the 2MASS images giving it anomalous colors as seen in figure 2.4, and its extinction is assumed to be zero even though it is likely to be much higher. Since the extinction is most likely non-zero the luminosity we derive is a lower limit. For the rest of the stars we use the optically derived luminosities for our analysis.

Figure 2.5 shows the HR diagram for NGC 2068/71 along with theoretical isochrones from Siess et al. (2000). The members are spread from above the 1 Myr isochrone to below the 10 Myr isochrone, a spread beyond our errors in luminosity and temperature and typically seen in HR diagrams of similar regions (Hillenbrand, 1997). There appears to be no significant age difference between the



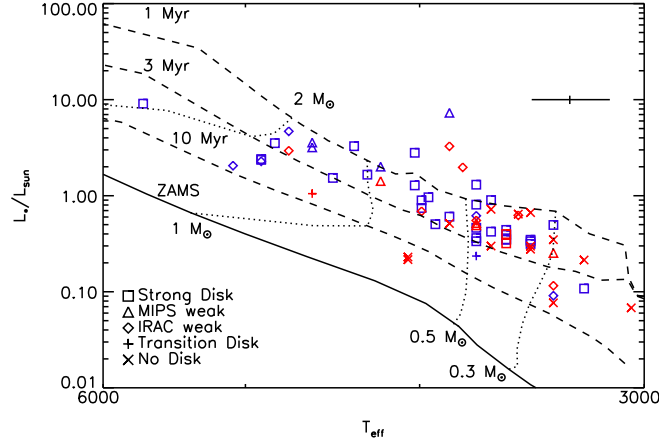


Figure 2.5 HR diagram for the likely members of NGC 2068/71. Different symbols represent different types of disks. Blue symbols are CTTS and red symbols are WTTS. See text for definition of strong/IRAC-weak/MIPS-weak/no disk as well as description of derivation of luminosity and effective temperature. Dotted lines show mass tracks for a 0.3, 0.5, 1, 2  $M_{\odot}$  star. A typical error bar is shown in the upper right corner.

CTTS or WTTS. The median age for the cluster is 2 Myr, with the majority of the stars lying between the 1 and 3 Myr isochrones. Using optical spectroscopy limits our study to the stars that are not heavily embedded within the molecular cloud. Our measured age of 2 Myr may be an overestimate of the true mean age if the substantial population of embedded stars is systematically younger. Without any information about their luminosities or  $T_{eff}$  we use an age of 2 Myr for the rest of our analysis.

When studying the age and masses of the stars in NGC 2068/71 we have chosen to use the theoretical isochrones of Siess et al. (2000). Other isochrones, such as those by Baraffe et al. (1998) and D’Antona & Mazzitelli (1997) would result in a different estimate for the age of the cluster and the masses of individual stars. The D’Antona & Mazzitelli tracks tend to produce younger ages, with most of the NGC 2068/71 members lying above the 1 Myr isochrone. The Baraffe et al.

models agree more accurately with dynamical mass estimates of binaries, with large scatter (Hillenbrand & White, 2004), although the models do not extend to our most massive members. The Siess et al. tracks measure systematically low masses, similar to the D’Antona & Mazzitelli tracks, although the tracks do follow the locus of cluster members in the HR diagram. We do not account for these systematic effects but only note that the age of the cluster and the masses of individual stars is model dependent.

Contamination from the nearby older, 4-6 Myr, OB1b association might affect our estimate of the age of NGC 2068/71. Without proper motion it is difficult to distinguish members of NGC 2068/71 from members of OB1b that have strayed into our field of view. We can estimate the contamination by considering the radial distribution of Orion OB1b members from Briceño et al. (2005). Based on the size of our NGC 2068/71 field and distance from the center of the OB1b association we expect roughly one star from the OB1b association to fall within our field. This will not substantially affect our estimate of the age of the cluster, or our study of the disk population.

The mass of each star was derived based on its position in the HR diagram by interpolating along a theoretical isochrone between the nearest model masses using effective temperature. This was done for the isochrone above and below each member, and the two mass estimates were averaged. Isochrones at 1, 2, 3, 5, 10, and 20 Myr were used while stars above the 1 Myr isochrone were assumed to lie on the 1 Myr isochrone and stars below the 20 Myr isochrone were assumed to lie on the 20 Myr isochrone. There is little difference in the mass estimate when using the two isochrones because many of these stars are young enough to still lie on vertical convective tracks. For those higher mass stars that lie on older isochrones there is more uncertainty in the mass estimate because this po-

sition in the HR diagram corresponds to an evolution along constant luminosity rather than constant  $T_{eff}$ . For these stars, typically with  $M > 1M_{\odot}$ , we interpolated along each isochrone using luminosity instead of  $T_{eff}$ . Since most of our stars are K to mid-M this only applied to the handful of stars with the earliest spectral types. The typical uncertainty in the mass estimates is 10%, based on the uncertainty in effective temperature, ignoring systematic uncertainties in the theoretical models. Masses are listed in Table 2.3.

### 2.3.3 Radial and Rotational Velocity

Radial velocities were derived for those stars with high-resolution spectra using the cross-correlation program *fxcor* in IRAF, along with 3 late G, early K type standard stars. Hartmann et al. (1986) describe in detail the methodology used to derive radial and rotational velocities. Our results are given in Table 2.4. Two objects (#584,373) do not have any spectral lines above the noise that can be used to measured an accurate radial velocity, and no radial velocity is recorded. The distribution of radial velocities for all members is shown in Figure 2.6, along with just the CTTS, which show a similar distribution. A gaussian fit to the radial velocities of the members has a center at 27.1 km/sec and a standard deviation of 1.3 km/sec, which is similar to the uncertainties in the radial velocities. A similar spread is measured in the radial velocities of Taurus and ONC members (Hartmann et al., 1986; Sicilia-Aguilar et al., 2005). The radial motion of the members is consistent with the motion of the surrounding molecular cloud (Lada et al., 1991; Wilson et al., 2005). Given the youth of the members, they have not had much time to travel outside of the cloud in which they were born. If we assume the velocity spread represents the difference between stellar and cloud velocities, it would take 5 Myr to travel 5 pc, roughly the size of the molecular cloud (Wilson et al., 2005).

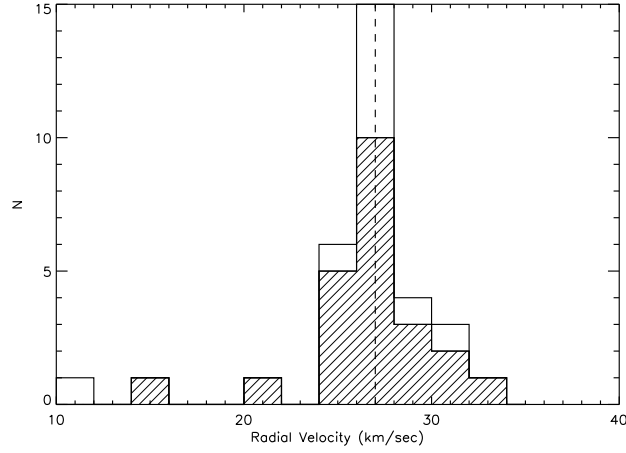


Figure 2.6 Radial velocity histogram for the likely members. Dashed line shows the median velocity of likely members at 27.1 km/sec. Hatched histogram shows the CTTS in the cluster, which make up most of the likely cluster members around this median velocity.

Rotational velocities were derived from the width of the cross-correlation function determined by the program *fxcor*. The relationship between the width of the cross-correlation function and the rotational velocity is determined by artificially broadening spectral standards, which all have a rotational velocity below the resolution limit of 8 km/sec. A quadratic function was fit to the width versus  $v_{\text{ sini}}$ , and the average of these fits for the three spectral standards was used to convert the width of the correlation function for the object spectra to  $v_{\text{ sini}}$  values. The  $H\alpha$  line was excluded when measuring the rotational velocity since it is not broadened by rotation alone. Rotational velocities, listed in Table 2.4, are plotted as a function of break-up velocity ( $v_{\text{ breakup}} = (GM/R)^{1/2}$ ) in Figure 2.7. Most of the members have  $v_{\text{ sini}}$  below the resolution limit of 8 km/sec and almost all have a rotational velocity which is a small fraction of the break-up velocity. The two stars with the highest fractional rotational velocity have noisy continua, which could lead to a spuriously high rotational velocity. The rotation rates are consis-

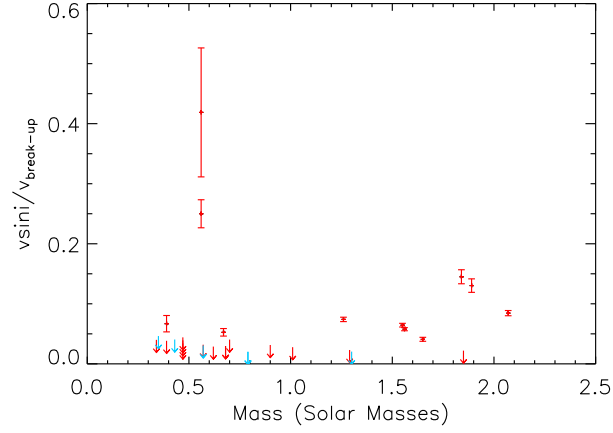


Figure 2.7 Rotational velocity as a fraction of the break-up velocity ( $v_{breakup} = (GM/R)^{1/2}$ ) versus mass. Upper limits are marked with arrows. Red symbols indicate stars with disks based on the presence of infrared excess and blue symbols represent stars without disks.

tent with the small  $v \sin i$  seen in other regions of similar ages (Sicilia-Aguilar et al., 2005, 2006; Clarke & Bouvier, 2000).

#### 2.3.4 Accretion Activity

The  $H\alpha$  line is a sensitive measure of accretion activity. For our sample the equivalent width (EW) of the  $H\alpha$  line, measured from the low-resolution spectra and listed in Table 2.2, was used to differentiate between actively accreting stars (CTTS) and stars that are not actively accreting (WTTS). We have used the EW boundary as a function of spectral type between CTTS and WTTS defined by White & Basri (2003). Self-absorption generally does not affect the EW. When the absorption is the strongest, the emission is also very strong because the accretion and mass loss that the two components trace are related to each other. With this in mind resolved  $H\alpha$  profiles are still the preferred accretion diagnostic.

High-resolution hectochelle spectra, examples of which are shown in Figure 2.8, were available for 34/67 of our likely members, as well as our two con-

continuum stars. For these stars the  $H\alpha$  profile was used to delineate active accretors from non-accretors instead of the  $H\alpha$  EW. A full width at 10% maximum flux of 250 km/sec was used to separate accretors and non-accretors. Measuring the width at 10% maximum flux rather than half maximum helps to avoid any self-absorption features in the profile while still measuring the profile above the noise of the continuum. White & Basri (2003) use a boundary of 270 km/sec, while we choose 250 km/sec to consistently include veiled stars as actively accreting, see below and Figure 2.9. Four exceptions (#1262, 326, 994, 998) out of the 35 members with high-resolution spectra show signs of accretion although their high-resolution  $H\alpha$  EW lies below the CTTS boundary. Object 1262 ( $H\alpha$  EW=8Å FW 10%=340 km/sec) has a very large absorption dip in the center of the  $H\alpha$  profile, reducing the flux in the line, and the measured EW, while object 326 ( $H\alpha$  EW=5.9Å, FW 10%=170 km/sec) has an inverse P Cygni profile. The presence of a strong absorption feature, such as the inverse P Cygni profiles in objects 326 and 515 in figure 2.8, can lower the velocity width below our threshold of 250 km/sec. In these cases the presence of strong absorption features due to accretion flows, as well as an asymmetric profile, indicate that accretion is still ongoing. Object 984 has a very noisy high-resolution spectra, possibly due to its high reddening,  $A_V = 4.5$ , making it difficult to evaluate its accretion status. Object 998 also has a noisy profile and the high-resolution spectra of these two stars was binned to increase the signal to noise. The width of the  $H\alpha$  profile is above our threshold for active accretion; however the accretion status of these stars is still questionable without a higher signal to noise  $H\alpha$  profile, or another sign of active accretion such as a U band excess. Unfortunately the red leak in the SDSS u-band prevents us from accurately measuring the U-band excess in this filter. The  $H\alpha$  EWs measured from the high-resolution spectra, listed in Table 2.4, are

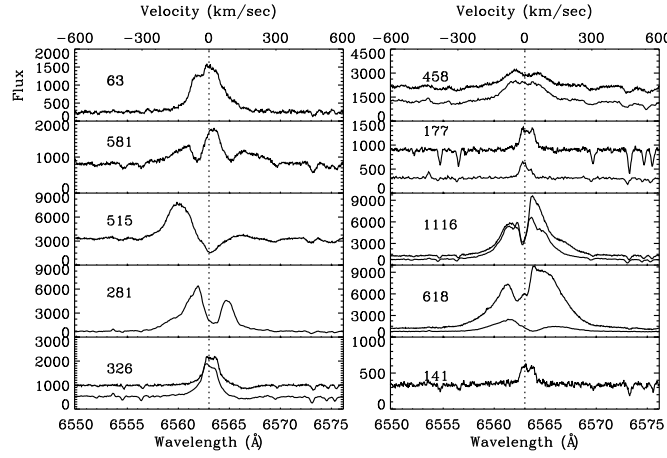


Figure 2.8 Sample hectochelle spectra focusing on the  $H\alpha$  profiles. The stars include a strong disk (63), a MIPS-weak disk (581), an IRAC-weak disk (515), a transition disk (281), the five stars with repeat hectochelle spectra taken 11 months apart (326, 458, 177, 1116 and 618) and one star without a disk (141). Stars #177, 141 demonstrate the narrow, symmetric profiles due to chromospheric emission while the rest show broad, asymmetric features due to accretion. Object ID numbers are included in each plot, along with a vertical line marking the line center, and the spectra of stars with multiple observations have been shifted vertically for easier comparison.

consistent with the  $H\alpha$  EW measured from the low-resolution spectra.

Continuum veiling of the photospheric absorption features provides an additional measure of accretion activity, albeit one that is less sensitive than the  $H\alpha$  profile. Accretion shocks produce a featureless continuum that adds to the photosphere, reducing the strength of photospheric lines relative to the observed continuum. The change in these photospheric features can be measured by comparing a veiled spectra with an unveiled spectra of the same spectral type. The method of Hartigan et al. (1989) was used to calculate the veiling ( $r = F_{excess}/F_{cont}$ ) over the wavelength range 6490-6501 Å. This wavelength range was chosen because it contains a number of strong stellar lines while other wavelength ranges in our high-resolution spectra did not consistently have strong lines useful for

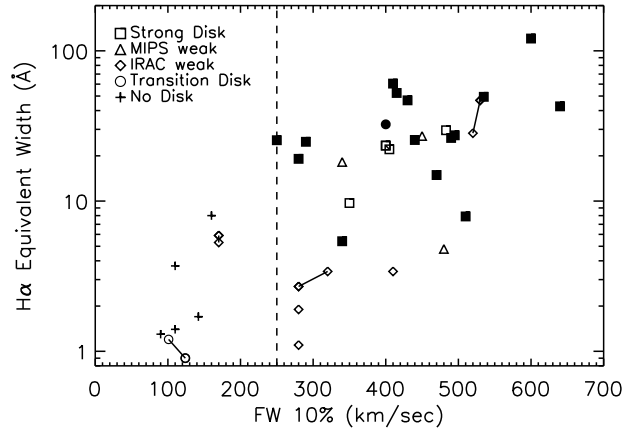


Figure 2.9 Equivalent width of the  $H\alpha$  line versus the full width at 10% maximum height for the  $H\alpha$  line for those likely members with high-resolution spectra. Vertical dashed line is located at 250 km/sec, our boundary for actively accreting stars. Different symbols represent different types of disks while filled symbols are stars with a measurable amount of veiling. Stars with multiple spectra have the two observations connected by a line

veiling and were ignored. We added a constant flux to the unveiled spectra until the strength of the photospheric features relative to the continuum matches that of the veiled spectra. This constant flux level relative to the continuum is designated  $r$ . The uncertainty in the veiling is approximately 0.15, and was estimated by comparing standards of similar spectral types to each other. Standards of spectral type K1.5, K2.5, K7, M0, M1 were used and veiled spectra were compared to standards within one spectral type. For the veiled stars that have a measurable rotational velocity, the standard was artificially broadened to match the rotational velocity of the veiled star. We found veiling measures ranging from 0.31 to 3.2, similar to those found near 6500Å by Hartigan et al. (1991).

Accretion rates were estimated from the veiling measures using the procedure of White & Hillenbrand (2004). The conversion starts by using the R band magnitude as a measure of the continuum emission in this wavelength range, then



from the definition of  $r$  we determine the excess flux, converting to an accretion luminosity by assuming the total accretion flux was 11 times larger than the flux observed over the R band and then assuming the accretion infall comes from  $3R_*$  to convert accretion luminosity to accretion rate. Correcting the observed accretion flux for the total accretion flux depends on the model of the accretion shock chosen. We use a correction factor of 11, a logarithmic average of various models, which is consistent with the analysis of White & Hillenbrand (2004). The radius  $3R_*$  is typical for the truncation of the disk by the magnetosphere, where material from the disk flows onto the magnetic field lines (Kenyon et al., 1996; White & Hillenbrand, 2004). Instead of using theoretical R band magnitudes, we used observed R band magnitudes, correcting for the contribution from the veiling and extinction. This avoids the assumption that all of the stars have exactly the same age, and is not subject to the systematic uncertainties associated with theoretical isochrones. For those stars with no measurable veiling but signs of accretion, such as a wide and/or asymmetric  $H\alpha$  profile, an upper limit on the accretion rate was calculated assuming a veiling of  $r=0.15$ . Accretion rates are listed in Table 2.4 and veiling, excess flux from accretion in the R band, accretion luminosity and accretion rate are plotted in Figure 2.10 as a function of mass. The  $\dot{M}$  values are typical of the range in young regions such as Taurus (Gullbring et al., 1998). We do not cover a large enough range in mass to look for any statistically significant trends.

Five of our likely members, objects 326, 177, 458, 618 and 1116 have two high-resolution spectra taken a year apart. Object 618 has the largest variation with both a change in the shape and strength of the profile, even though the width of the profile does not significantly change, as seen in Figure 2.8. The other stars do not vary significantly in the shape or strength of the  $H\alpha$  profile. The 10% FW vary

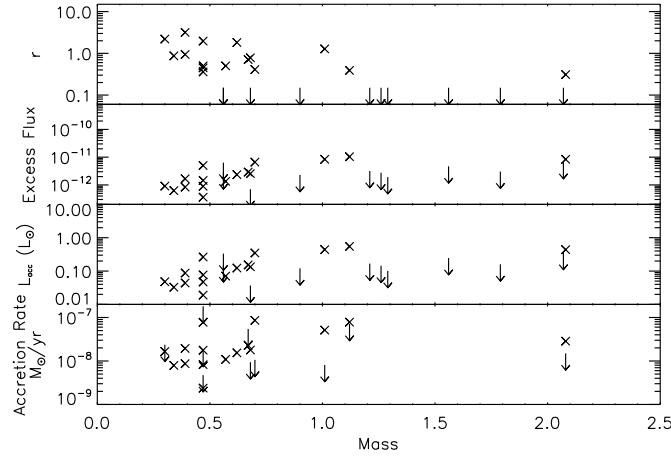


Figure 2.10 Veiling, accretion luminosity and accretion rate as a function of mass. Upper limits are marked with arrows. See text for description of conversion from veiling to accretion rate.

by less than 40 km/sec for all of these stars, similar to other stars with similar  $H\alpha$  profiles (Johns & Basri, 1995; Jayawardhana et al., 2006).

Accretion is often associated with outflows and jets driving material away from the star (Konigl & Pudritz, 2000). The NGC 2068/71 cluster has a number of strong molecular outflows (White & Phillips, 1981; Snell & Edwards, 1982; Bally, 1982; Fukui et al., 1986) as well as Herbig-Haro objects (Zhao et al., 1999; Reipurth, 1999) throughout the cloud. None of these outflows appear to be associated with the pre-main sequence stars studied here, and may instead be related to the younger, less evolved stellar population of NGC 2068/71. In the optical spectra, a number of stars exhibit [OI] 6300Å emission associated with outflows. These stars, marked in table 2.2, all have an infrared excess and are actively accreting supporting the view that accretion and outflows are physically connected.

### 2.3.5 Disk Emission

The shape of the infrared SED contains information about warm dust surrounding the young star and can be used to distinguish between stars with disks and

stars without disks. Lada et al. (2006) and Hernandez et al. (2007) used the slope of the SED in the IRAC bands,  $\alpha_{IRAC}$ , to distinguish between stars with strong infrared excess coming from optically thick accretion disks, stars with a weaker excess indicative of evolved, or “anemic”, disks, and stars with no measurable excess associated with a lack of disk material within 1 AU. We refer to the evolved objects as IRAC-weak because they may have strong excess at longer wavelengths indicative of optically thick outer disks. Figure 2.11 shows  $\alpha_{IRAC}$  versus effective temperature for NGC 2068/71. As in Lada et al. (2006) we find two distinct populations, one around  $\alpha_{IRAC} = -1.0$  and a second around  $\alpha_{IRAC} = -2.8$ . We have not dereddened the SEDs since the low extinction ( $A_v < 5$ ) and relatively flat extinction law across the IRAC bands (Flaherty et al., 2007) means that dereddening will have a small effect on the SED slopes. Previously a boundary of  $\alpha_{IRAC} = -1.8$  has been used to distinguish evolved disks from strong disks (Lada et al., 2006; Hernandez et al., 2007). We use a boundary of  $\alpha_{IRAC} = -1.6$  because of the stars near  $\alpha_{IRAC} = -1.8$  that likely have some evolution in the structure of their disks. For our analysis stars with  $\alpha_{IRAC} > -1.6$  were treated as having strong disks, stars with  $-2.5 < \alpha_{IRAC} < -1.6$  have IRAC-weak disks and stars without disks have  $\alpha_{IRAC} < -2.5$ .

An IRAC color-color diagram, Figure 2.12, shows a similar progression in disk properties. There is a population of sources with no infrared excess, a population with strong infrared excess, and population in between with weak but significant infrared excess. Including the  $24\mu\text{m}$  band of MIPS adds additional information on the dust properties of the disk. Figure 2.13 shows the [8.0]-[24] vs. [4.5]-[5.8] color-color diagram. All of the detections at  $24\mu\text{m}$ , 33/34 strong disks and 8/12 IRAC-weak disks, have some sort of disk emission as expected given the  $24\mu\text{m}$  sensitivity. Of the stars with an infrared excess not detected at  $24\mu\text{m}$  one

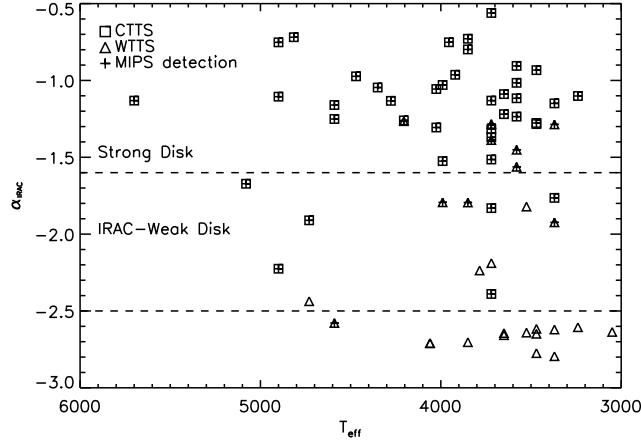


Figure 2.11 Slope of IRAC SED versus effective temperature for the likely members. CTTS are marked with a square, WTTS are marked with a triangle. Dashed lines mark boundaries between stars with strong or MIPS-weak disks, stars with IRAC-weak disks and stars without disks.

is outside the MIPS field of view and the other three are in regions of strong nebulous emission where the sensitivity is decreased.

There is a population of sources with  $[8.0]-[24] < 2.4$ , which we refer to as MIPS-weak. These sources are singled out because this  $[8.0]-[24]$  color indicates spectral slopes  $< -1$ , similar to  $\lambda F_\lambda \propto \lambda^{-4/3}$ , and because of the evidence for lower accretion activity, discussed below. A perfectly flat disk has an SED with the form  $\lambda F_\lambda \propto \lambda^{-4/3}$ , which represents the limit of a disk with a substantial amount of grain settling. Figure 2.14 shows  $\alpha_{IRAC}$  vs.  $\alpha_{MIPS}$ , the SED slopes from  $3 - 8\mu\text{m}$  and  $8 - 24\mu\text{m}$  respectively. The MIPS-weak sources all have a strong excess at the IRAC bands, even though they have a weak excess at  $24\mu\text{m}$ . The lack of MIPS weak sources with small  $\alpha_{IRAC}$  may be caused by the limited sensitivity at  $24\mu\text{m}$ . The majority of sources show strong excesses at both the IRAC bands and at  $24\mu\text{m}$ , while the IRAC-weak sources have a range of excesses at  $24\mu\text{m}$ . Figure 2.15 shows sample SEDs for each of the types of circumstellar disks. The biggest change in the SED between the MIPS weak star and the strong

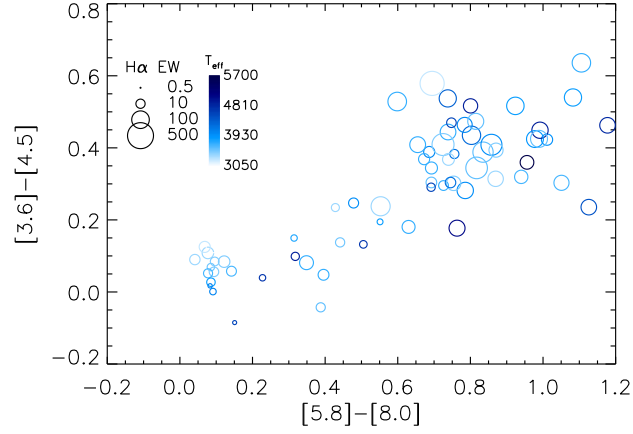


Figure 2.12 IRAC color-color diagram for those stars in our spectroscopic sample. Size of the symbol indicates strength of  $H\alpha$ , as measured by its equivalent width, while the color of the symbol scales with its  $T_{eff}$ . The stars with the smallest infrared excess tend to have the smallest  $H\alpha$  EW, while the stars with the largest infrared excess in both colors have the largest  $H\alpha$  EW.

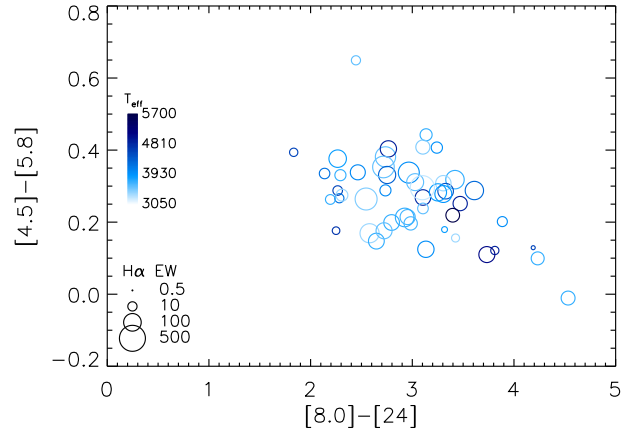


Figure 2.13 IRAC+MIPS color-color diagram for those stars in our spectroscopic sample. Size of the symbol indicates strength of  $H\alpha$ , while color indicates  $T_{eff}$ , as in figure 2.12.

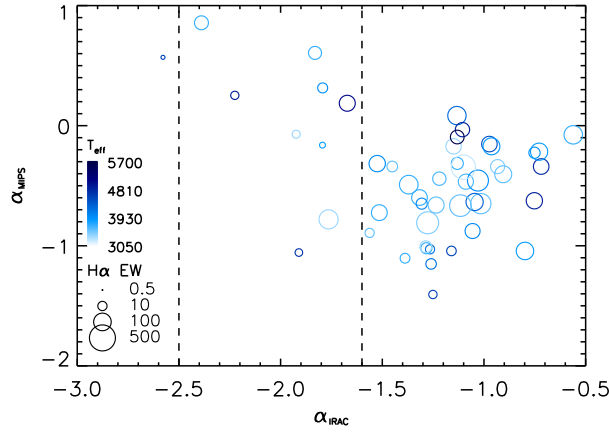


Figure 2.14 SED slope for the IRAC bands versus the SED slope from 8-24 $\mu$ m. The size of the points has been scaled to the size of the H $\alpha$  equivalent width, while color scales with  $T_{eff}$  as in figure 2.12. The dashed lines delineates between strong disks, IRAC weak disks and stars with no disk. The MIPS weak sources are also evident around  $\alpha_{MIPS} \approx -1$ , and the transition disks have large  $\alpha_{MIPS}$  and small  $\alpha_{IRAC}$ . The SEDs have not been dereddened.

disk star is between 8 and 24 $\mu$ m with the MIPS-weak disk having a much steeper SED beyond 6 $\mu$ m. The SED of the IRAC-weak sources looks similar to the SED of the strong disk but with a steeper 2-8 $\mu$ m slope.

Stars contaminated by background PAH emission may appear to have an excess at [8.0], even though they have no circumstellar material within a few AU. Three stars, #802, 984, 1078, are in regions of high nebular emission and have an excess primarily at [8.0]. Excess emission at 24 $\mu$ m would help to better characterize the presence of a disk, but none of these stars are detected at [24] possibly due to the high background emission surrounding the stars. We leave them as IRAC-weak disks but note that their disk status is still uncertain

Including all stars with  $\alpha_{IRAC} > -2.5$  as having a disk as well as the stars with  $\alpha_{IRAC} < -2.5$  but a 24 $\mu$ m excess indicative of an optically thick outer disk, 79% (53/67) of the spectroscopically confirmed members have disks. This disk frac-

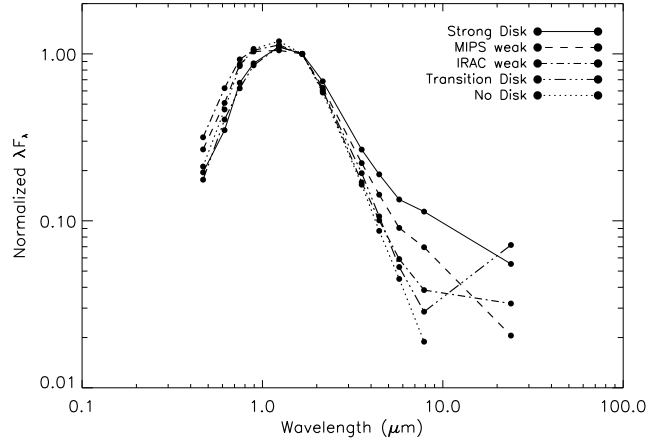


Figure 2.15 SEDs of stars exhibiting different levels of infrared excess emission. SEDs have been dereddened using Mathis (1990) for  $\lambda < 3\mu\text{m}$  and Flaherty et al. (2007) for  $\lambda > 3\mu\text{m}$  and normalized to the H band flux. All of these stars have spectral type M1-M2.

tion may not accurately reflect the disk fraction in the entire cluster, since sources with interesting mid-infrared colors were added to our spectroscopic sample. To constrain the true disk fraction we consider the photometry of those confirmed members, as well as stars with similar colors. In the  $r$  vs.  $r-i$  color-magnitude diagram (shown in Figure 2.2), there are 397 stars that sit above the main sequence locus and have  $r < 18.6$ , 230 of which have been observed spectroscopically. Of these 230, 44 are members with disks ( $\alpha_{IRAC} > -2.5$ ) and 14 are members without disks. Our sample of members without disks is unbiased since we have no prior information on whether or not they are members. Scaling up from the spectroscopic sample to the photometric sample, we expect 24 stars without disks in the entire sample of 397 stars. If we assume that we have found all the members with disks, then out of the entire sample there would be 24 stars without a disk, and 44 stars with a disk for a disk fraction of  $44/68$  (65%). We have likely not found all the members with disks, and the true disk fraction is likely higher than 65%.

Out of the 397 stars, 58 have infrared colors consistent with disk emission. If we instead assume that we have found all of the members without disks and that all of the objects with an infrared excess are members, then the disk fraction would be 58/72 (81%). Some of the objects with an infrared excess may be background AGN or AGB stars and it is also unlikely that we have found all of the members without disks so we expect the true disk fraction to be less than 81%. This does not count stars that could be missing material within 1 AU but the small number of these objects (see § 2.3.5.1) will not have a significant effect. The spectroscopic sample has a disk fraction of 79%, while we expect the true fraction for the entire cluster to be in the range 65-81%.

Another estimate of the disk fraction can be made from the X-ray emitting stars observed by Skinner et al. (2007). X-ray emission as a tracer of young stars is not biased towards stars with disks. We detect 23 of the 33 X-ray emitting stars with IRAC, mainly at [3.6], [4.5]. We use these two colors, with a boundary of  $[3.6]-[4.5]=0.2$  to differentiate stars with or without disks. One star is not detected by 2MASS, which combined with its faint IRAC flux suggests it is an extragalactic source and we exclude it. Where possible we use detections in other bands to better characterize the presence of a disk around these stars. Two stars with  $[3.6]-[4.5]> 0.2$  have colors consistent with highly reddened photospheres while two stars with  $[3.6]-[4.5]< 0.2$ , which are both part of our spectroscopic sample (#984,1078), have a slight excess at [8.0]. In total there are 14/22 ( $64 \pm 17\%$ ) stars with an infrared excess in this field. This is consistent with our previous estimate of the true disk fraction. Ten of these stars, six of which have an infrared excess, are deeply embedded and are not detected in the optical. The X-ray fields are in areas of high background emission at  $24\mu\text{m}$  reducing the sensitivity at this band and making it difficult to estimate the fraction of evolved disks in this field.



If the deeply embedded population has a higher disk fraction than our spectroscopic sample then this will introduce an additional bias in our measure of the cluster disk fraction. Ices are expected to form on dust grains within the molecular cloud above  $A_v=3$  (Whittet et al., 2001). We might expect that the stars with  $A_v > 3$  differ from the less embedded population because of the change in the surrounding molecular cloud. Of the stars with  $A_v > 3$ , 93% (28/30) have disks while 71% (20/28) of the stars with  $A_v < 3$  have disks. This only includes stars earlier than M4; embedded stars later than M4 are too faint in the optical to be observed here. There does not appear to be a significant age difference between these two groups although the change in the disk fraction is suggestive of a difference between the embedded population and the revealed population. Observations of more heavily extincted cluster members are needed to characterize this difference fully.

#### 2.3.5.1 Disk Hole Sources

A number of stars have been observed towards other young clusters that appear to be missing dust within a few AU of the central star (Quillen et al., 2004; Calvet et al., 2002; Rice et al., 2003). These objects, often referred to as transition disks, lack infrared emission shortward of  $10\mu\text{m}$  but exhibit strong emission longwards of  $10\mu\text{m}$ . NGC 2068/71 has two such objects, objects 177 and 281. They have  $[8.0]-[24] > 4$  and  $[3.6]-[4.5] < 0.1$ . Our high-resolution spectra allows a search for any weak accretion. Object 177 (FW 10%=124 km/sec,  $\text{H}\alpha$  EW=1.2Å) does not appear to be actively accreting, while object 281 has a broad, asymmetric  $\text{H}\alpha$  profile indicating active accretion (FW 10%=400 km/sec,  $\text{H}\alpha$  EW=18.1Å). A veiling of  $r=0.36$  was measured for object 281 corresponding to an accretion rate of  $\dot{M} = 2.4 \times 10^{-9} M_{\odot} \text{yr}^{-1}$ . This accretion rate is the smallest rate measured among the stars in this cluster, although our measured accretion rates are biased toward

those stars whose accretion rate is high enough to have a measurable veiling.

### 2.3.5.2 Infrared Excess and Accretion

The stars with strong disks (32/67, 48%), with spectral types ranging from G6-M5, all have signs of active accretion. They have strong  $H\alpha$  EW (5-300Å) and broad asymmetric  $H\alpha$  profiles. The full width at 10% maximum flux for the stars with strong disks ranges from 260 to 640 km/sec. For those stars with measurable veiling the accretion rates are in the range  $7.9 \times 10^{-9} - 8.6 \times 10^{-8} M_{\odot} yr^{-1}$ . The stars with no disks (14/67, 21%) show no sign of active accretion, either in  $H\alpha$  EW (1.3-9.5Å) or the  $H\alpha$  profile (FW at 10%=90-200 km/sec). Figure 2.9 shows the  $H\alpha$  EW versus FW at 10% where the strong disks and stars with no disks form two distinct groups.

The MIPS-weak sources (8/67, 12%), with spectral types ranging from K4-M4, show signs of lowered accretion activity in addition to lower infrared excess. In the color-color diagrams, Figures 2.13, 2.14, the size of the symbols scales with the  $H\alpha$  EW and the MIPS-weak sources have smaller  $H\alpha$  EW than the strong disks. These eight stars have  $H\alpha$  EW between 3 and 48Å. Three have high-resolution spectra with 10% full-widths of 480, 340 and 450 km/sec, and accretion upper limits of  $2.4 \times 10^{-8} M_{\odot} yr^{-1}$ ,  $1.79 \times 10^{-8} M_{\odot} yr^{-1}$  and  $1.8 \times 10^{-7} M_{\odot} yr^{-1}$ . In Figure 2.9 some of the MIPS-weak sources with high-resolution spectra are distinct from the strong disks and the stars with no disk. The  $H\alpha$  EW is lower than the strong disks with comparable FW at 10%.

The IRAC-weak sources (12/67, 18%, not including #281), with spectral types ranging from K1-M4, have  $-2.5 < \alpha_{IRAC} < -1.6$  and also tend to have  $[8.0]-[24] > 2$ . Lada et al. (2006) find a similar spread in  $[8.0]-[24]$  color for their optically thin/"anemic" disks. Of these twelve stars, six have high-resolution spectra that show 10% full widths for  $H\alpha$  of 280, 410, 280, 260, 170 and 520 km/sec, close

to the boundary between accretors and non-accretors. For these six objects only upper limits of 7.11, 0.94, 1.78, 5.4, 0.47,  $1.06 \times 10^{-8} M_{\odot} yr^{-1}$  can be placed on the accretion rate since no veiling is measured. Figure 2.9 indicates they have the same accretion activity as the three MIPS-weak stars, separate from the strong disks and the stars with no disk. These stars have  $H\alpha$  EW between 2 and 32 Å, with one star having an  $H\alpha$  EW of 75 Å. With the exception of the one active accretor, these stars show less accretion activity than the strong disks.

## 2.4 Discussion

Many studies now show that the disk fraction decreases rapidly with age, with nearly all stars losing their primordial disks after roughly 10 Myr (Haisch, Lada & Lada, 2001; Hernandez et al., 2007). For NGC 2068/71 we measure an age of  $2 \pm 1.5$  Myr and a disk fraction of 79%. Our disk fraction is consistent with ground-based estimates from JHK<sub>L</sub> for regions such as the Trapezium and NGC 2024 with ages of 1-2 Myr (Haisch, Lada & Lada, 2001).

In NGC 2068/71 the members with disks do not show a systematically different rotational velocity than those stars without disks. Rotational velocities,  $v \sin i$ , relative to the break-up speed are shown in Figure 2.7, with the stars with and without disks marked as red and blue respectively. There appears to be no significant separation, although the substantial number of upper limits makes it difficult to evaluate any difference fully. It has been suggested that the slow rotation rates for pre-main sequence stars are due to disk-locking, where the star is connected to the disk by its magnetic field lines and angular momentum is transferred from the star to the disk. Rebull et al. (2004) suggest that even if the slow rotation speed was due to disk locking, a significant difference between the rotation velocity of stars with disks and stars without disks would be difficult to

measure. More data are needed to test these hypotheses in detail with the members of this region.

The high-resolution spectra not only allow us to measure rotational velocities, but also obtain a more sensitive measure of the accretion activity with the  $H\alpha$  profile. All of the WTTS, classified based on  $H\alpha$  EW, that have a disk and high resolution spectra exhibit  $H\alpha$  profiles consistent with active accretion, except the transition disk #177. Objects #849, 458, 581 and 998 all have low-resolution  $H\alpha$  EW which would make them appear as WTTS, while their high-resolution  $H\alpha$  profiles indicate that they are still accreting material. This is especially important when examining the accretion activity of the evolved disks which tend to have low  $H\alpha$  EW although they are still accreting (see Figure 2.9).

The location of our selected members does not strictly overlap with either the dense gas emission (Lada et al., 1991) or the dense dust emission (Johnstone et al., 2001). Star formation is ongoing in these regions of dense gas and dust, based on observable outflows and class I sources. To compare the distribution of members to the dust cloud we created an extinction map (Figure 2.16) by selecting background stars, assuming they have the same intrinsic  $H-K_s$  color, and calculating  $E(H - K_s) = H - K_s - (H - K_s)_0$ . A  $30''$  gaussian kernel was used to smooth the map and the extinction law of Rieke & Lebofsky (1985) was used to convert from  $E(H-K_s)$  to  $A_V$ . A more detailed description of this method is given in Goetz et al. (2003). The extinction map closely matches the CS emission measured by Lada et al. (1991). It also agrees with the lower resolution extinction map of Dobashi et al. (2005), although their map does show a more extended peak at  $\alpha_{2000} = 05^h 47^m 36^s$ ,  $\delta_{2000} = +00^\circ 18' 00''$  which could be due to our small number of background stars in this area. As seen in Figure 2.16, our selected members follow the general shape of the diffuse dust traced by the extinction map, but are not confined to the

peaks of the dust, where the SCUBA clumps (Johnstone et al., 2001) and class I sources (Muzerolle et al. in prep) are located. Our sample may be biased toward those areas of lower extinction away from the dense gas and dust because the use of optical spectra for spectral type classification limits our survey to those young stars that are not deeply embedded within the cloud. Another possibility is that the star formation in this region has progressed from west to east. Stellar winds and photoionizing flux from the OB associations to the west of NGC 2068/71 may have been interacting with the cloud, causing stars to form on the western side of the cloud first and on the eastern side of the cloud later. A third possibility is that the selected members may have had time to disperse from their original birthplace and have spread throughout the cloud. For a typical velocity of 1-2 km/sec relative to the cloud, these members could have traveled 2-4 pc in their lifetime of 2 Myr, roughly the east-west extent of the members.

Binarity may have a significant impact on disk properties, however, our data lack the spatial resolution to address this. One star (object #739) was observed to be a binary by Padgett, Strom & Ghez (1997). This binary has a separation of  $0.97''$ , which corresponds to 390 AU at a distance of 400pc. Interestingly this star has a MIPS-weak disk, which might be explained by tidal truncation of the outer disk. Padgett, Strom & Ghez (1997) estimate a binary fraction of 15%, which would imply that 10 of our sources are binaries. None of our stars with high-resolution spectra appear to be spectroscopic binaries but more epochs are needed to rule out single-line spectroscopic binaries.

#### 2.4.1 Evolved Disks

There are a number of possible explanations for the SEDs of strong disks vs. MIPS-weak/IRAC-weak disks. Grain growth and settling is one process that may have a measurable effect on the SED of an accretion disk. Models suggest

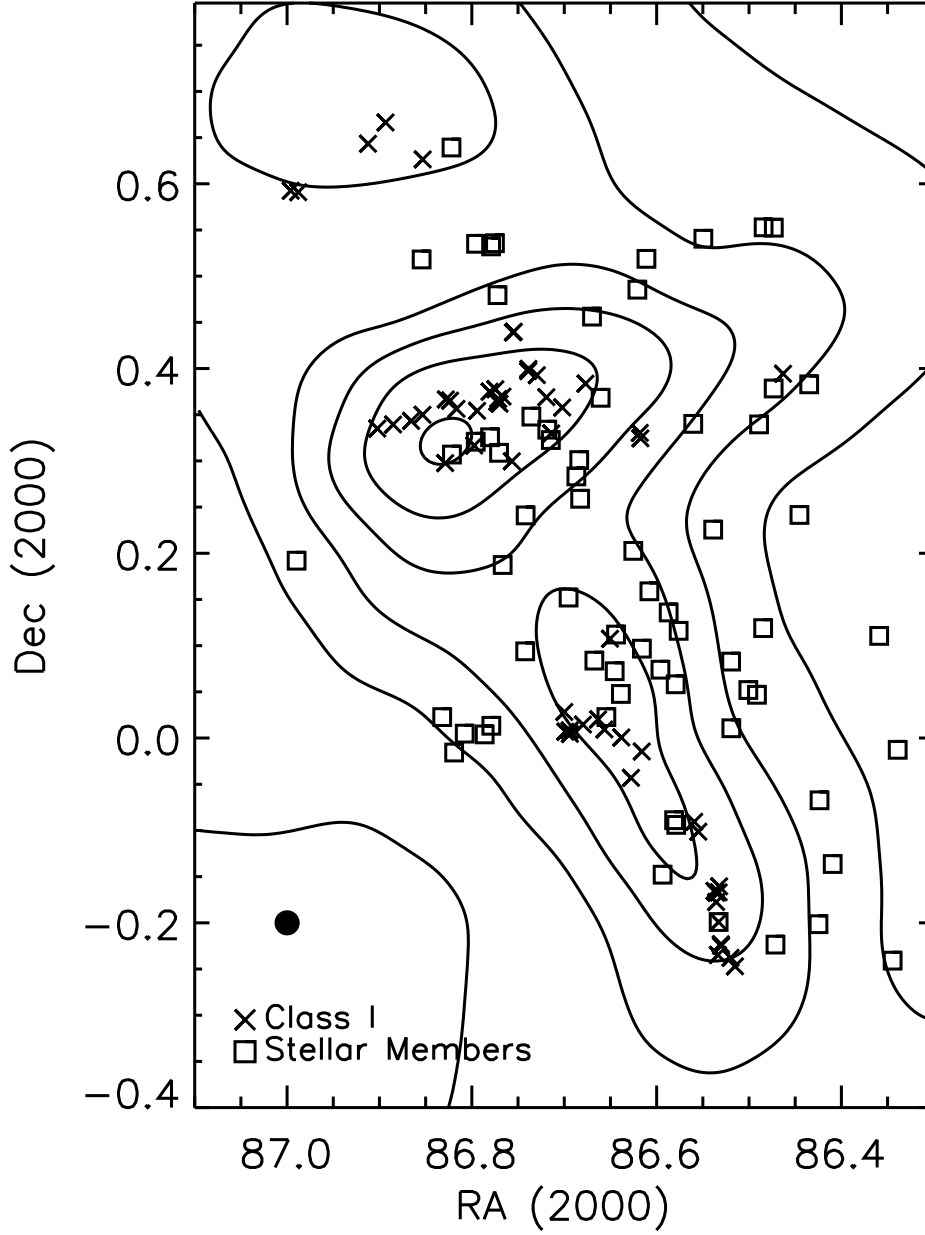


Figure 2.16 Extinction map (axes in degrees) with class I sources from Muzerolle et al. (in prep) and the stellar members identified in this paper. The circle in the lower left shows the size of the gaussian kernel used to smooth the extinction map. The class I sources are located near the peaks in the extinction while the members follow the broader distribution of dust. Contours correspond to  $A_V = 1, 2, 3, 4, 5$  using the extinction law of Rieke & Lebofsky (1985)

that this can be a very fast process producing noticeable differences in the SED in less than a million years (Dullemond & Dominik, 2005). The overall effect is to quickly deplete grains out of the upper layers of the disk, while grains in the inner disk will grow and settle more quickly than in the outer disk.

As the degree of settling increases, the most direct effect is a decrease in the irradiation surface of the disk, which leads to less emerging flux. The SED approaches that of a perfectly flat disk,  $\lambda F_\lambda \propto \lambda^{-4/3}$  at wavelengths corresponding to the disk radii that are affected by settling (D'Alessio et al., 2006). Assuming the amount of grain growth and settling is constant throughout the disk, the change in flux is most noticeable for  $\lambda > 10\mu\text{m}$  because these wavelengths trace regions in the disk where flaring becomes prominent and the surface height is most sensitive to grain growth and settling. The emission at  $\lambda < 10\mu\text{m}$  is dominated by the wall at the dust destruction radius, which is less affected by the degree of flaring of the disk. For a substantial amount of grain growth and settling the height of the wall will decrease by a factor of 2, while the height of the outer disk can decrease by more than an order of magnitude (D'Alessio et al., 2006). Theory predicts grain growth and settling should occur more rapidly in the inner disk than the outer disk since the orbital period is shorter (Dullemond & Dominik, 2004, 2005). The IRAC-weak stars may have a substantial amount of grain growth and settling in the inner disk, whereas the MIPS-weak sources may have advanced settling over a wider range of radii.

The predicted SEDs for grain growth and settling are not unlike those corresponding to a decrease in the accretion rate. A lowered accretion rate will affect the disk in three ways: (1) decrease the surface density, (2) decrease the viscous heating and (3) decrease the accretion luminosity emitted by the stellar accretion shock. A decrease in surface density will lower the flux at all wavelengths, while

the smaller viscous heating will lead to a cooler midplane temperature and a change in the scale height of the disk similar to that of grain growth and settling. The decrease in the accretion luminosity will have an effect on the inner disk edge which dominates the flux at  $\lambda < 10\mu\text{m}$ . Accretion luminosity, along with stellar irradiation, illuminates the inner dust edge of the disk. A decrease in accretion luminosity will cause the dust destruction radius to move closer to the star. While the inner edge will still be at 1500K, its solid angle will decrease and the emission from the inner edge will decrease. For  $\dot{M} > 10^{-8} M_{\odot} \text{yr}^{-1}$  the accretion luminosity is comparable to the stellar luminosity and a change in accretion rate leads to a change in the radius of the wall, and a change in the flux in the IRAC bands. Since the accretion luminosity ( $L = GM\dot{M}/R$ ) and the stellar luminosity roughly scale with stellar mass, the dependence on accretion rate dominates the ratio of accretion to stellar luminosity. For  $\dot{M} < 10^{-8} M_{\odot} \text{yr}^{-1}$  the change in the radius of the wall with accretion rate is smaller because the stellar luminosity dominates.

A change in the SED slope could be due to grain growth and settling or a decreased accretion rate separately or it could be caused by a combination of the two. As the amount of settling increases the effect of a change in the accretion rate becomes more significant (D'Alessio et al., 2006). For high accretion rates, viscous heating dominates over other forms of heating in the surface layers. Since viscous heating has little dependence on the grains in these layers, there is little change in the SED when grains start to grow. For lower accretion rates, stellar irradiation dominates the heating of the surface layers, and this form of heating is very sensitive to the grain distribution. The MIPS-weak and IRAC-weak sources may be separating themselves from the strong disks because their low accretion rates lead to a more significant difference in the SED. However, we need more estimates of  $\dot{M}$  to directly compare to disk models.



This picture is confused by the  $10\mu\text{m}$  silicate feature which overlaps with the  $8\mu\text{m}$  band of IRAC. A strong silicate emission feature will artificially increase  $\alpha_{IRAC}$  despite a steeper continuum slope. As the accretion rate decreases the intensity of this feature increases due to the contrast in temperature between the surface (heated by stellar irradiation) and the midplane (heated by viscous dissipation and emission from the upper layers) (D'Alessio et al., 2006). The silicate feature is most sensitive to grain growth in the upper layers of the disk and does not trace grain growth in the midplane. Spectroscopy of the  $10\mu\text{m}$  silicate feature would help to break the degeneracy between grain growth and settling and a change in accretion rate (D'Alessio et al., 2006; Furlan et al., 2006), as well as separate out its contribution to  $\alpha_{IRAC}$ .

Another possibility for the observed SEDs of the MIPS-weak stars is the truncation of the disk by a close binary. A close binary will truncate the disk around the primary at  $1/2$  to  $1/3$  the semimajor axis of the binary system (Artymowicz & Lubow, 1994). The majority of the  $24\mu\text{m}$  emission comes from within  $0.5\text{--}5\text{ AU}$ , depending on the spectral type and degree of settling in the disk (D'Alessio et al., 2006). A binary companion separated by  $\sim 1\text{--}15\text{ AU}$  would truncate the disk and reduce the  $24\mu\text{m}$  emission without affecting the shorter wavelength excess. The frequency of MIPS-weak stars in NGC 2068/71 is roughly consistent with the frequency of binaries at separations  $\sim 1\text{--}15\text{ AU}$  (Mathieu, 1994). The smaller reservoir of material available to accrete onto the central star may lead the accretion rate to decrease earlier than it would for stars with disks that have not been truncated. The smaller disks imply a smaller viscous timescale for the evolution of the disk, which may lead it to be quickly dissipated unless it is resupplied by a circumbinary disk. The binary fraction within a cluster seems to be a function of environment, rather than of age, with low-density clusters such as Taurus

and Ophiuchus showing a higher binary fraction than dense clusters such as the Trapezium (Mathieu et al., 2000). Millimeter observations find that disk masses are much lower for binaries separated by 1-100 AU than single stars or wide binaries, suggesting truncation of the disk (Mathieu et al., 2000). If MIPS-weak disks are due to the presence of a binary then we may expect the MIPS-weak fraction to be a strong function of environment rather than age. Interestingly one of our MIPS-weak stars (#739) is a known binary (Padgett, Strom & Ghez, 1997), although its separation (390AU) is likely to be too large for any truncation of the disk to affect the  $24\mu\text{m}$  flux.

The third group of evolved disks are the transition disks, with AU-scale optically thin or evacuated holes in the center of the disks. We have two such objects, #177, and 281, making up 3% of our spectroscopic sample. One appears to be actively accreting (#281) while the other is not. Sicilia-Aguilar et al. (2006), who define transition disks as having no excess shortward of  $6\mu\text{m}$ , find that half of the transition disks in Tr 37 are still actively accreting, based on high-resolution  $\text{H}\alpha$  profiles. The transition disks around TW Hya, GM Aur and DM Tau are all seen to be accreting (Calvet et al., 2002, 2005) while CoKu Tau/4 is not actively accreting (D'Alessio et al., 2005). Accretion rates of  $10^{-8} - 10^{-10} M_{\odot} \text{yr}^{-1}$  have been measured for GM Aur, DM Tau, and TW Hya (Gullbring et al., 1998; Calvet et al., 2005; Muzerolle et al., 2000), similar to that measured for object #281.

A hole could be swept out by a planet, be caused by substantial grain growth in the inner disk or be due to photoevaporation of the disk. The formation of a planet would cause material outside the planet's orbit to gain orbital angular momentum and be pushed outwards, while material within the planets orbit would lose angular momentum and quickly accrete onto the star (Rice et al., 2003). The mass of the planet and the disk will affect whether a gap can be created, and

how the planet reacts to the material in the outer disk (Papaloizou et al., 2007). A planet has been invoked to explain the observed inner holes in GM Aur (Rice et al., 2003), CoKu Tau/4 (Quillen et al., 2004) and TW Hya (Calvet et al., 2002). For object # 281, the material within the planet's radius may not have completely accreted onto the star, or the planet may be small enough that some gas may be able to stream past it (Lubow & D'Angelo, 2006). This gas would transport small grains into the gap, creating an optically thin disk, which would not be detectable from photometry alone (Rice et al., 2006). It is also possible that grains within 10 AU have grown to millimeter sizes or larger, while the grains at larger radii have not grown as much. The growth of grains should proceed on an orbital timescale, which would result in more grain growth in the inner disk than the outer disk (Dullemond & Dominik, 2004, 2005), although this process should not produce a sharp boundary in the dust disk. Any accretion onto the central star may also transport small grains back into this gap. A third possibility arises from a photo-evaporative wind from the disk driven by stellar UV and X-ray photons (Clarke et al., 2001; Alexander et al., 2006). When the accretion rate is low the wind will counteract the inward flow of material outside of the gravitational radius and will prevent additional gas from being transported into the inner disk. With the inner disk starved for material any gas will quickly accrete onto the star and disappear producing an inner hole for a short time before the entire disk dissipates. This process requires very low ( $< 10^{-10} M_{\odot} \text{yr}^{-1}$ ) accretion rates in order for the wind to counteract the inward flow of material due to accretion. This would rule out the photoevaporative model for object #281, but it is still possible for object #177.

None of these three groups of evolved disks appear to be systematically older than the rest of the cluster, according to the HR diagram shown in Figure 2.5. Al-

though the two transition disks are below the 3 Myr isochrone their small number make any statistically significant conclusion impossible. While the number of sources in each group is small enough that we cannot do a detailed study of the ages, we can say that it is unlikely that either the IRAC-weak, MIPS-weak or transition disks are systematically older or younger than the other stars in the cluster. This indicates that the disks around different stars evolve at different rates. Dullemond & Dominik (2005) find that grain growth proceeds much more quickly than the typical age of a T-Tauri star and small grains must be replenished in the disk in order to retain a significant IR excess. If replenishment occurs then the typical grain size in a disk does not reflect the age of the system. We would then not expect these stars to appear systematically older if the change in SED for the IRAC-weak and MIPS-weak disks is due in part to grain growth.

IRAC-weak disks are observed in cluster regions from Taurus at 1 Myr (Lada et al., 2006) to NGC 2362 at 5 Myr (Dahm & Hillenbrand, 2007). The fraction of IRAC-weak disks depends on the spectral type range under consideration. Lada et al. (2006) find the fraction of stars with IRAC-weak disks ranges from 8-25% depending on the spectral type. Later spectral types have a larger fraction of IRAC-weak disks although this trend may be affected by larger photometric uncertainties at later spectral types blurring the boundary between IRAC-weak and diskless stars (Hernandez et al., 2007). We examine the fraction of disked stars that have an IRAC-weak SED for broad spectral type ranges to look for trends with age. Here we use  $\alpha_{IRAC} = -1.8$  as the boundary for IRAC-weak stars to be consistent with previous studies. We consider K0-M1 stars in Taurus at 1 Myr (Hartmann et al., 2005), NGC 2068/71 at 2 Myr, IC 348 at 2-3 Myr (Lada et al., 2006),  $\sigma$  Ori at 3 Myr (Hernandez et al., 2007), Tr 37 at 4 Myr (Sicilia-Aguilar et al., 2006) and NGC 2362 at 5 Myr (Dahm & Hillenbrand, 2007). The fractions

of disked stars with IRAC-weak SEDs are listed in Table 2.5. The fractions of cluster members with disks in these clusters decrease from 80% to  $\sim 20\%$  with age, but the fractions of disks with IRAC-weak SEDs do not show an obvious decrease with age, although the small number statistics for some of these clusters make this trend uncertain. Typical  $H\alpha$  EW for the IRAC-weak disks in Tr 37 and IC 348 are  $< 15\text{\AA}$  (Sicilia-Aguilar et al., 2006; Lada et al., 2006), consistent with the IRAC-weak stars in NGC 2068/71, and available high-resolution  $H\alpha$  profiles indicate they are actively accreting. However Hernandez et al. (2007) find that the median SED slope for all disks in a given region decreases with age from 1-3 Myr, which may contribute to the fraction of disks with IRAC-weak SEDs if the entire distribution of infrared excess is shifting to a smaller excess.

Of the 54 stars with disks detected by MIPS in Tr 37, 7 have MIPS-weak disks (Sicilia-Aguilar et al., 2006), while out of the 38 K0-M4 stars with disks in IC 348, 3 have MIPS-weak disks, none of which are earlier than M1 (Lada et al., 2006). In  $\sigma$  Ori, three out of 16 K0-M1 stars with disks detected by MIPS have MIPS-weak disks (Hernandez et al., 2007). The sensitivity limit at  $24\mu\text{m}$  makes any trends with age harder to evaluate although we note that the fraction of disks with MIPS-weak SEDS does not significantly decrease with age. The  $H\alpha$  EW of the MIPS-weak stars in Tr 37 are between 4 and  $47\text{\AA}$ , with most below  $15\text{\AA}$  (Sicilia-Aguilar et al., 2006). Of the stars with measured accretion rates, most are below  $10^{-8}M_{\odot}\text{yr}^{-1}$  (Sicilia-Aguilar et al., 2006). This is consistent with the properties of MIPS-weak disks in NGC 2068/71, although overall accretion rates are lower in Tr 37 and the low accretion rates for the MIPS-weak stars may simply reflect viscous evolution of the disks.

If disk evolution is not solely dependent on age then it may depend on environment or the initial conditions of the protostar. Material falling onto the disk

from the surrounding cloud could replenish the small grains in the disk as well as maintain the presence of a disk. The longevity of a disk would then depend on the reservoir of material surrounding the star. During the early stages of star formation material accretes from an envelope onto the disk, and this infall rate depends on the properties of the envelope. More material accreting onto the disk will create a more massive disk, which can affect its subsequent evolution (Dullemond & Dominik, 2005). Unfortunately sub-mm observations are not sensitive to circumstellar disks in NGC 2068/71 and cannot be used to estimate disk masses for these stars (Johnstone et al., 2001). The initial angular momentum of the system may influence the initial size of the disk and how quickly it evolves (Dullemond et al., 2006) as well as affect the possibility of forming a binary, which could enhance the subsequent evolution of the disk. A nearby O/B star would increase the ionizing flux impinging on the surface of the disk, and possibly increase the speed with which the disk dissipates, although the evolved disks we observe do not appear preferentially close to the B stars in this cluster and with the earliest member being a B2 star the UV flux is not especially strong.

## 2.5 Conclusion

We have studied the young stellar population of NGC 2068/71 and identified 69 members, for 67 of which we have derived spectral type and luminosity. Our cluster members range from G6-M6 with a median age of 2 Myr. A large fraction (79%) of these stars have an infrared excess, although this is likely an overestimate of the true disk fraction. Of the stars with an infrared excess and a high-resolution  $H\alpha$  profile, sensitive to low-accretion rates, all but one are actively accreting. The stellar members are not confined to regions of dense gas and dust, although there is some evidence that the disk fraction is higher in dense ( $A_V > 3$ )

regions.

Combining accretion information from the  $H\alpha$  line with the 3-24 $\mu$ m infrared SED we find three populations of evolved disks: IRAC-weak, MIPS-weak and transition disks. All of the populations show a change in the shape of the infrared SED as well as a decrease in the accretion activity. For the IRAC-weak disks this could solely be due to a decrease in the accretion rate (which affects the structure of the disk), substantial grain growth and settling, or a combination of the two. These two processes could also explain the MIPS-weak SEDs, although truncation of the outer disk by a close binary companion is also a viable possibility. The transition disks could be explained by a giant planet opening a gap in the disk, or a photoevaporative wind evacuating the inner disk. The latter mechanism requires a very low accretion rate and can be ruled out for the transition disk in our sample that is still accreting.

None of the groups of evolved disks appear systematically older than the rest of the cluster, although the small numbers make any difference harder to evaluate. Initial conditions in the disk and surrounding envelope could influence how quickly disks evolve. The initial angular momentum or mass of the disk could also have an influence.

Table 2.1. Photometry of likely members

Object ID	g	r	i	z	J	H	$K_s$	[3.6]	[4.5]	[5.8]	[8.0]	[24]
17	18.723	17.104	15.488	14.567	12.962	12.217	11.932	$11.697 \pm 0.009$	$11.612 \pm 0.011$	$11.611 \pm 0.027$	$11.515 \pm 0.033$	...
29	19.946	18.352	16.403	15.281	13.497	12.874	12.541	$12.279 \pm 0.011$	$12.153 \pm 0.014$	$12.167 \pm 0.040$	$12.077 \pm 0.047$	...
63	17.635	16.174	14.778	13.952	12.371	11.606	11.208	$10.619 \pm 0.005$	$10.318 \pm 0.005$	$10.006 \pm 0.014$	$9.252 \pm 0.007$	...
141	18.160	16.337	15.190	14.415	12.645	11.820	11.526	$11.356 \pm 0.005$	$11.329 \pm 0.008$	$11.319 \pm 0.021$	$11.233 \pm 0.022$	...
174	18.373	16.823	15.297	14.436	12.863	12.092	11.855	$11.584 \pm 0.008$	$11.528 \pm 0.009$	$11.597 \pm 0.030$	$11.503 \pm 0.030$	...
177	15.897	14.469	13.808	13.378	11.925	11.183	10.989	$10.862 \pm 0.006$	$10.947 \pm 0.007$	$10.818 \pm 0.024$	$10.667 \pm 0.017$	$6.478 \pm 0.036$
204	17.221	15.528	14.564	13.862	12.021	11.051	10.376	$9.387 \pm 0.003$	$8.943 \pm 0.003$	$8.744 \pm 0.007$	$8.006 \pm 0.004$	$5.209 \pm 0.033$
229	19.843	18.279	16.606	15.638	14.005	13.355	13.044	$12.806 \pm 0.014$	$12.716 \pm 0.016$	$12.781 \pm 0.056$	$12.740 \pm 0.066$	...
281	17.718	16.147	15.253	14.508	12.777	11.956	11.694	$11.362 \pm 0.006$	$11.280 \pm 0.009$	$11.291 \pm 0.021$	$10.942 \pm 0.022$	$6.410 \pm 0.032$
285	18.420	16.458	15.304	14.423	12.452	11.404	10.870	$10.201 \pm 0.004$	$9.857 \pm 0.006$	$9.504 \pm 0.009$	$8.686 \pm 0.007$	$5.970 \pm 0.032$
288	16.758	15.346	14.685	14.275	13.042	12.335	12.153	$12.067 \pm 0.008$	$12.066 \pm 0.012$	$12.047 \pm 0.029$	$11.956 \pm 0.038$	...
322	19.394	17.911	15.799	14.694	12.824	12.252	11.921	$11.601 \pm 0.008$	$11.476 \pm 0.010$	$11.450 \pm 0.028$	$11.382 \pm 0.029$	...
326	16.791	15.137	14.247	13.641	12.133	11.331	11.027	$10.167 \pm 0.004$	$9.921 \pm 0.004$	$9.719 \pm 0.012$	$9.241 \pm 0.008$	$5.355 \pm 0.031$
344	16.564	15.029	14.187	13.517	11.754	10.825	10.215	$9.291 \pm 0.003$	$9.009 \pm 0.004$	$8.885 \pm 0.008$	$8.099 \pm 0.005$	$4.965 \pm 0.032$
351	19.240	17.774	16.328	15.258	13.517	12.677	12.152	$11.372 \pm 0.007$	$11.134 \pm 0.008$	$10.965 \pm 0.022$	$10.412 \pm 0.018$	$7.832 \pm 0.034$
373	18.355	16.627	14.854	13.850	12.047	11.218	10.905	$10.424 \pm 0.005$	$10.110 \pm 0.004$	$9.802 \pm 0.013$	$8.933 \pm 0.006$	$5.627 \pm 0.031$



Table 2.1—Continued

Object ID	g	r	i	z	J	H	$K_s$	[3.6]	[4.5]	[5.8]	[8.0]	[24]
416	20.237	18.009	16.459	15.365	13.362	12.278	11.739	$11.055 \pm 0.005$	$10.752 \pm 0.007$	$10.514 \pm 0.013$	$9.821 \pm 0.015$	$6.716 \pm 0.032$
418	17.062	15.362	14.480	13.642	11.339	10.125	9.455	$8.296 \pm 0.002$	$7.887 \pm 0.003$	$7.550 \pm 0.003$	$6.692 \pm 0.003$	$3.726 \pm 0.033$
458	...	...	...	...	9.795	8.647	8.399	$8.106 \pm 0.003$	$7.974 \pm 0.003$	$7.798 \pm 0.004$	$7.292 \pm 0.003$	$5.042 \pm 0.033$
480	16.846	15.135	14.963	13.377	11.686	10.698	10.054	$8.947 \pm 0.003$	$8.603 \pm 0.003$	$8.161 \pm 0.004$	$7.468 \pm 0.004$	$4.332 \pm 0.033$
515	14.447	13.147	12.620	12.295	10.936	10.046	9.448	$8.680 \pm 0.003$	$8.581 \pm 0.003$	$8.460 \pm 0.005$	$8.142 \pm 0.005$	$4.330 \pm 0.033$
543	20.419	18.517	16.689	15.636	13.825	12.889	12.522	$12.199 \pm 0.010$	$11.965 \pm 0.011$	$11.809 \pm 0.029$	$11.380 \pm 0.032$	$7.955 \pm 0.032$
571	18.808	16.447	15.165	14.279	12.208	11.068	10.471	$9.534 \pm 0.004$	$9.085 \pm 0.003$	$8.682 \pm 0.008$	$7.690 \pm 0.009$	$4.925 \pm 0.033$
581	16.797	15.016	16.570	13.143	11.198	10.165	9.724	$8.945 \pm 0.004$	$8.654 \pm 0.002$	$8.261 \pm 0.006$	$7.569 \pm 0.003$	$5.735 \pm 0.031$
584	18.588	16.103	14.552	13.762	10.632	9.030	7.869	$6.542 \pm 0.001$	$6.005 \pm 0.001$	$5.674 \pm 0.002$	$4.936 \pm 0.002$	$2.184 \pm 0.033$
590	15.605	13.962	12.894	12.572	10.690	9.655	8.999	$7.960 \pm 0.002$	$7.497 \pm 0.002$	$7.229 \pm 0.004$	$6.051 \pm 0.002$	$2.946 \pm 0.031$
601	19.965	17.488	15.935	14.912	12.533	11.322	10.685	$9.923 \pm 0.003$	$9.500 \pm 0.004$	$9.094 \pm 0.008$	$8.082 \pm 0.006$	$4.841 \pm 0.034$
618	15.905	14.446	13.656	13.137	11.510	10.654	10.214	$9.542 \pm 0.003$	$9.365 \pm 0.003$	$9.255 \pm 0.008$	$8.491 \pm 0.005$	$4.758 \pm 0.031$
628	20.090	17.977	16.367	15.222	13.061	11.974	11.429	$10.786 \pm 0.005$	$10.398 \pm 0.005$	$10.017 \pm 0.013$	$9.182 \pm 0.019$	$6.446 \pm 0.037$
656	19.721	17.793	16.139	15.135	13.190	12.186	11.643	$10.847 \pm 0.005$	$10.373 \pm 0.006$	$10.197 \pm 0.013$	$9.382 \pm 0.021$	$6.660 \pm 0.036$
663	19.260	16.916	15.516	14.501	12.695	11.330	10.517	$9.546 \pm 0.003$	$9.163 \pm 0.004$	$8.897 \pm 0.007$	$8.141 \pm 0.005$	$5.858 \pm 0.031$
677	20.403	18.209	16.280	15.014	12.714	11.581	11.110	$10.794 \pm 0.004$	$10.725 \pm 0.007$	$10.699 \pm 0.021$	$10.613 \pm 0.045$	...

Table 2.1—Continued

Object ID	g	r	i	z	J	H	$K_s$	[3.6]	[4.5]	[5.8]	[8.0]	[24]
689	18.100	16.168	14.854	13.969	12.170	11.298	10.992	$10.755 \pm 0.005$	$10.703 \pm 0.006$	$10.671 \pm 0.015$	$10.593 \pm 0.017$	...
699	20.568	18.163	16.493	15.044	12.642	11.379	10.718	$9.840 \pm 0.004$	$9.521 \pm 0.004$	$9.324 \pm 0.010$	$8.384 \pm 0.005$	$5.400 \pm 0.032$
712	17.662	15.846	14.773	13.721	11.632	10.441	9.627	$8.445 \pm 0.003$	$7.887 \pm 0.002$	$7.466 \pm 0.004$	$6.440 \pm 0.002$	$3.367 \pm 0.031$
730	18.805	16.620	15.322	14.266	12.715	11.172	10.213	$8.838 \pm 0.003$	$8.374 \pm 0.002$	$8.036 \pm 0.005$	$7.251 \pm 0.005$	$4.787 \pm 0.032$
739	20.094	17.561	15.994	14.744	11.963	10.569	9.733	$8.735 \pm 0.003$	$8.266 \pm 0.003$	$7.978 \pm 0.006$	$7.230 \pm 0.009$	$4.964 \pm 0.034$
741	20.192	18.130	16.165	14.957	12.706	11.563	11.101	$10.752 \pm 0.006$	$10.614 \pm 0.007$	$10.325 \pm 0.026$	$9.884 \pm 0.052$	...
760	17.699	15.797	14.722	13.766	11.672	10.420	9.525	$8.226 \pm 0.002$	$7.791 \pm 0.003$	$7.504 \pm 0.004$	$6.701 \pm 0.008$	$3.090 \pm 0.032$
782	20.679	18.266	16.655	15.474	13.411	12.192	11.703	$11.137 \pm 0.006$	$10.842 \pm 0.007$	$10.579 \pm 0.018$	$9.853 \pm 0.011$	$7.659 \pm 0.032$
802	19.386	17.020	15.688	14.729	12.779	11.767	11.400	$11.085 \pm 0.007$	$11.038 \pm 0.008$	$10.916 \pm 0.036$	$10.520 \pm 0.090$	...
813	19.992	18.169	16.398	15.131	12.897	12.038	11.386	$10.275 \pm 0.003$	$9.866 \pm 0.004$	$9.602 \pm 0.008$	$8.877 \pm 0.006$	$6.331 \pm 0.031$
843	19.311	17.150	16.020	14.773	12.932	11.926	11.385	$10.351 \pm 0.004$	$10.394 \pm 0.005$	$9.745 \pm 0.010$	$9.357 \pm 0.008$	$6.911 \pm 0.031$
849	17.078	15.131	14.314	13.275	11.562	10.608	10.218	$9.433 \pm 0.004$	$9.130 \pm 0.004$	$8.795 \pm 0.006$	$8.049 \pm 0.005$	$5.912 \pm 0.032$
856	20.608	18.157	16.730	15.309	13.190	12.057	11.570	$11.001 \pm 0.006$	$10.820 \pm 0.007$	$10.721 \pm 0.021$	$10.091 \pm 0.024$	$5.858 \pm 0.033$
878	18.967	16.961	16.075	14.712	12.292	11.127	10.395	$9.613 \pm 0.004$	$9.073 \pm 0.003$	$8.791 \pm 0.013$	$7.708 \pm 0.025$	$4.456 \pm 0.036$
934	19.906	17.685	16.486	15.120	13.290	12.302	11.838	$11.232 \pm 0.007$	$10.929 \pm 0.007$	$10.715 \pm 0.024$	$9.664 \pm 0.022$	$6.710 \pm 0.043$
941	18.562	16.677	15.929	14.651	12.658	11.482	10.802	$9.739 \pm 0.003$	$9.314 \pm 0.004$	$9.036 \pm 0.008$	$8.058 \pm 0.015$	$4.753 \pm 0.034$

Table 2.1—Continued

Object ID	g	r	i	z	J	H	$K_s$	[3.6]	[4.5]	[5.8]	[8.0]	[24]
984	...	...	...	...	11.937	10.917	10.557	$10.341 \pm 0.004$	$10.302 \pm 0.005$	$10.220 \pm 0.016$	$9.992 \pm 0.050$	...
997	20.356	18.400	17.026	15.316	13.009	12.102	11.644	$10.658 \pm 0.005$	$10.264 \pm 0.005$	$9.856 \pm 0.013$	$8.985 \pm 0.017$	$5.881 \pm 0.033$
998	18.092	15.752	14.349	13.290	11.230	10.128	9.690	$9.395 \pm 0.004$	$9.200 \pm 0.003$	$9.021 \pm 0.010$	$8.469 \pm 0.021$	$5.152 \pm 0.032$
1062	18.392	16.573	15.388	14.337	12.460	11.405	10.803	$10.074 \pm 0.004$	$9.649 \pm 0.004$	$9.338 \pm 0.010$	$8.349 \pm 0.005$	$5.321 \pm 0.031$
1078	19.855	17.001	15.631	14.260	11.839 <sup>a</sup>	10.882	10.449	$10.040 \pm 0.005$	$9.890 \pm 0.006$	$9.811 \pm 0.029$	$9.496 \pm 0.072$	...
1089	20.339	18.208	16.573	15.556	13.720	12.733	12.409	$12.084 \pm 0.009$	$12.026 \pm 0.012$	$12.040 \pm 0.030$	$11.898 \pm 0.038$	...
1099	19.666	17.182	15.830	14.714	11.745	10.403	9.368	$8.095 \pm 0.003$	$7.578 \pm 0.002$	$7.327 \pm 0.004$	$6.526 \pm 0.002$	$3.055 \pm 0.032$
1116	15.603	14.124	13.451	12.932	11.350	10.570	10.223	$9.817 \pm 0.003$	$9.582 \pm 0.004$	$9.296 \pm 0.008$	$8.170 \pm 0.005$	$4.842 \pm 0.032$
1117	20.262	18.223	16.715	15.522	12.858	11.688	10.886	$10.138 \pm 0.004$	$9.502 \pm 0.004$	$9.184 \pm 0.008$	$8.078 \pm 0.005$	$4.658 \pm 0.031$
1119	17.576	15.067	13.842	12.556	10.226	9.018	8.324	$7.399 \pm 0.001$	$6.882 \pm 0.002$	$6.506 \pm 0.002$	$5.582 \pm 0.004$	$3.316 \pm 0.033$
1134	17.306	15.610	14.335	13.373	11.558	10.798	10.515	$10.281 \pm 0.004$	$10.196 \pm 0.005$	$10.192 \pm 0.015$	$10.070 \pm 0.015$	...
1171	14.938	13.031	12.562	12.373	12.563	11.642	11.191	$10.404 \pm 0.004$	$10.035 \pm 0.005$	$9.705 \pm 0.009$	$9.032 \pm 0.008$	$6.739 \pm 0.031$
1173	17.355	15.194	14.182	13.028	10.998	9.836	9.084	$8.314 \pm 0.002$	$7.954 \pm 0.003$	$7.735 \pm 0.005$	$6.779 \pm 0.013$	$3.381 \pm 0.033$
1211	16.678	14.878	15.280	13.019	10.749	9.795	9.230	$8.233 \pm 0.002$	$7.824 \pm 0.003$	$7.677 \pm 0.004$	$7.022 \pm 0.002$	$4.375 \pm 0.046$
1212	14.380	13.489	12.558	11.974	10.765	9.844	8.963	$6.685 \pm 0.001$	$5.703 \pm 0.001$	$5.152 \pm 0.001$	$3.974 \pm 0.001$	$0.95 \pm 0.034$
1247	19.881	18.179	16.168	15.021	13.060	12.324	11.891	$11.209 \pm 0.005$	$10.841 \pm 0.008$	$10.567 \pm 0.014$	$9.827 \pm 0.013$	$7.519 \pm 0.032$

Table 2.1—Continued

Object ID	g	r	i	z	J	H	$K_s$	[3.6]	[4.5]	[5.8]	[8.0]	[24]
1259	19.901	17.900	16.406	15.376	13.035	11.860	11.176	$10.065 \pm 0.004$	$9.537 \pm 0.004$	$9.324 \pm 0.018$	$8.725 \pm 0.066$	$5.800 \pm 0.045$
1262	16.508	15.819	14.004	13.217	11.522	10.537	9.911	$8.811 \pm 0.003$	$8.423 \pm 0.004$	$8.135 \pm 0.004$	$7.448 \pm 0.003$	$4.712 \pm 0.037$
1284	20.059	18.223	17.161	15.850	13.759	13.089	12.671	$11.737 \pm 0.008$	$11.158 \pm 0.007$	$10.863 \pm 0.019$	$10.168 \pm 0.012$	$7.069 \pm 0.031$
1333	16.519	15.230	14.581	14.226	12.644	12.102	11.832	$11.620 \pm 0.007$	$11.603 \pm 0.010$	$11.588 \pm 0.024$	$11.504 \pm 0.030$	...
1643	19.202	17.376	15.534	14.453	12.565	11.753	11.406	$11.162 \pm 0.007$	$11.054 \pm 0.008$	$11.034 \pm 0.022$	$10.957 \pm 0.022$	...

<sup>a</sup>The source is not resolved from a nearby star in the J band and only an upper limit is reported.

Note. — SDSS u band data is not reported here because of the red leak in the filter.

Table 2.2. Cluster members identified from Low-Resolution Spectra

Object ID	RA (J2000)	Dec (J2000)	Spectral Type Range	Adopted Spectral Type	H $\alpha$ EW ( $\text{\AA}$ )	Li EW ( $\text{\AA}$ )	CTTS/WTTS
17	05 45 21.36	-00 00 45.72	M3	M3	4.4	0.2	WTTS
29	05 45 22.68	-00 14 27.13	M6	M6	12.2	0.55	WTTS
63	05 45 26.16	00 06 37.91	M3	M3	20.8	0.35	CTTS
141	05 45 38.26	-00 08 10.97	K7-M0	M0	4.1	0.43	WTTS
174	05 45 41.68	-00 04 02.42	M2-M4	M3	5.4	0.4	WTTS
177	05 45 41.94	-00 12 05.33	K3-K4	K4	1.2	0.48	WTTS
204 <sup>†</sup>	05 45 44.37	00 22 58.22	M0-M2	M1	29.4	0.6	CTTS
229	05 45 46.91	00 14 29.36	M3-M5	M4	6.8	0.7	WTTS
281	05 45 53.11	-00 13 24.89	M1	M1	18.1	0.59	CTTS
285 <sup>†</sup>	05 45 53.54	00 33 08.82	M1-M2	M2	150	0.15	CTTS
288	05 45 53.60	00 22 42.10	K7	K7	2.4	0.28	WTTS
322	05 45 56.20	00 33 10.33	M5-M6	M5.5	8.3	0.4	WTTS
326	05 45 56.31	00 07 08.58	K7-M0	K9	6.2	0.68	CTTS

Table 2.2—Continued

Object ID	RA (J2000)	Dec (J2000)	Spectral Type Range	Adopted Spectral Type	H $\alpha$ EW (Å)	Li EW (Å)	CTTS/WTTS
344	05 45 57.38	00 20 22.20	K6-M0	K7	35.3	0.5	CTTS
351 <sup>†</sup>	05 45 57.93	00 02 48.55	M3-M5	M4	75	0.4	CTTS
373	05 46 00.18	00 03 07.06	M4	M4	27.2	0.36	CTTS
416	05 46 04.58	00 00 38.16	M2	M2	7.4	0.2	WTTS
418 <sup>‡</sup>	05 46 04.64	00 04 58.15	K7-M1	K9	126	0.26	CTTS
458	05 46 07.89	-00 11 56.87	K2-K3	K3	3.2	0.58	CTTS
480	05 46 09.27	00 13 32.63	M0-M1	M1	10.8	0.48	CTTS
515	05 46 11.86	00 32 25.91	K1-K2	K2	3.8	0.7	CTTS?
543	05 46 14.48	00 20 24.36	M3-M4	M4	3.6	<0.35	WTTS
571	05 46 18.30	00 06 57.85	K1-K3	K1	34.7	0.4	CTTS
581	05 46 18.89	-00 05 38.11	K3-K4	K4	3.9	0.73	CTTS
584 <sup>†</sup>	05 46 19.06	00 03 29.59	K4-K6	K5	44.5	0.44	CTTS
590	05 46 19.47	-00 05 20.00	K2-K3	K2.5	28.5	0.5	CTTS

Table 2.2—Continued

Object ID	RA (J2000)	Dec (J2000)	Spectral Type Range	Adopted Spectral Type	H $\alpha$ EW ( $\text{\AA}$ )	Li EW ( $\text{\AA}$ )	CTTS/WTTS
601	05 46 20.88	00 08 09.42	K6-M1	K8	8.7	0.7	CTTS
618	05 46 22.44	-00 08 52.62	K1-K2	K1	32	0.55	CTTS
628	05 46 22.99	00 04 26.44	M1-M3	M2	104	0.5	CTTS
656	05 46 25.89	00 09 31.97	M1-M2	M2	32.4	<0.4	CTTS
663	05 46 26.65	00 31 07.50	K4-K8	K6	4.9	0.6	WTTS
677	05 46 27.83	00 05 48.37	M2-M3	M2.5	3	0.3	WTTS
689	05 46 29.00	00 29 07.19	M1-M2	M1.5	4.8	0.5	WTTS
699	05 46 30.06	00 12 09.68	M1-M2	M1.5	15.4	0.5	CTTS
712 <sup>†</sup>	05 46 31.05	00 25 33.37	continuum	-	92.3	0.25	CTTS
730	05 46 33.28	00 02 51.90	K5-M0	K7	24.4	0.6	CTTS
739 <sup>b</sup>	05 46 34.54	00 06 43.45	K3-K5	K4	5.5	0.5	CTTS
741	05 46 34.90	00 04 20.68	M2-M3	M2.5	5	0.2	WTTS
760	05 46 37.06	00 01 21.79	K4-K7	K5.5	61	0.4	CTTS

Table 2.2—Continued

Object ID	RA (J2000)	Dec (J2000)	Spectral Type Range	Adopted Spectral Type	H $\alpha$ EW ( $\text{\AA}$ )	Li EW ( $\text{\AA}$ )	CTTS/WTTS
782	05 46 38.57	00 22 05.99	M0-M1	M1	5.8	0.2	WTTS
802	05 46 40.18	00 05 01.86	M0-M1	M1	7.8	0.8	WTTS
813 <sup>†</sup>	05 46 40.77	00 27 22.50	M2-M4	M3	166	0.1	CTTS
843	05 46 43.85	00 15 32.36	M2	M2	4.9	0.6	WTTS
849 <sup>c</sup>	05 46 44.09	00 18 03.17	K5-K7	K6	7.1	0.7	CTTS
856	05 46 44.84	00 16 59.77	M1-M2	M1	14	0.4	CTTS
878 <sup>†</sup>	05 46 46.87	00 09 07.63	M0	M0	45	0.4	CTTS
934 <sup>c</sup>	05 46 51.48	00 19 21.32	M1-M2	M1.5	25.1	0.3	CTTS
941	05 46 52.41	00 20 01.68	K7-M1	K9	41	0.5	CTTS
984 <sup>c</sup>	05 46 56.54	00 20 52.91	K2-K4	K3	2.3	0.7	WTTS
997 <sup>†</sup>	05 46 58.03	00 14 27.82	M3-M4	M3	19	0.45	CTTS
998	05 46 58.13	00 05 38.15	K7-M0	M0	2	0.73	WTTS
1062	05 47 03.97	00 11 14.35	M1-M2	M2	42	0.45	CTTS



Table 2.2—Continued

Object ID	RA (J2000)	Dec (J2000)	Spectral Type Range	Adopted Spectral Type	H $\alpha$ EW ( $\text{\AA}$ )	Li EW ( $\text{\AA}$ )	CTTS/WTTS
1078 <sup>c</sup>	05 47 04.94	00 18 31.64	M0-M1	M0.5	2.3	0.4	WTTS
1089	05 47 05.34	00 28 46.13	M1-M2	M1.5	6	0.3	WTTS
1099 <sup>†</sup>	05 47 06.00	00 32 08.48	K0-K3	K0	20	0.7	CTTS
1116	05 47 06.96	00 00 47.74	K3-K6	K4.5	28.4	0.5	CTTS
1117	05 47 06.99	00 31 55.96	M0-M2	M1	63	0.3	CTTS
1119 <sup>c</sup>	05 47 07.26	00 19 32.23	K7-M0	M0	48	0.3	CTTS
1134	05 47 08.69	00 00 14.04	M2-M4	M3	9.4	0.42	WTTS
1171	05 47 10.89	00 32 05.96	M1-M2	M1.5	8.4	0.57	WTTS
1173 <sup>c</sup>	05 47 10.98	00 19 14.81	G4-G8	G6	17	0.6	CTTS
1211 <sup>†</sup>	05 47 13.85	00 00 17.06	M0-M2	M1	30.4	0.7	CTTS
1212 <sup>†</sup>	05 47 14.11	00 09 07.34	continuum	-	78	0.06	CTTS
1247	05 47 16.58	-00 00 56.38	M4-M5	M4	10.3	0.36	WTTS
1259 <sup>†</sup>	05 47 17.16	00 18 24.59	M0-M2	M1	65.5	0.3	CTTS

Table 2.2—Continued

Object ID	RA (J2000)	Dec (J2000)	Spectral Type Range	Adopted Spectral Type	H $\alpha$ EW (Å)	Li EW (Å)	CTTS/WTTS
1262	05 47 17.28	00 38 21.37	K5-M0	K7	8.3	0.6	CTTS
1284 <sup>†</sup>	05 47 19.72	00 01 21.83	M5-M6	M5	300	0.47	CTTS
1333	05 47 25.05	00 31 04.94	K6-K7	K7	1.3	0.24	WTTS
1643	05 47 57.53	00 11 31.24	M3-M5	M4	9.5	0.4	WTTS

<sup>†</sup>[O I] 6300 Å emission detected in optical spectra

<sup>a</sup>Variable in the optical as observed by Briceño et al. (2005). They measured a spectral type of K6, and H $\alpha$  and Li EWs of 98 and 0.4Å respectively.

<sup>b</sup>Binary from Padgett, Strom & Ghez (1997).

<sup>c</sup>X-ray emission detected by Skinner et al. (2007)

Table 2.3. Stellar Parameters for Likely Members

Object ID	Luminosity $L_{\odot}$	$T_{eff}$ K	Mass $M_{\odot}$	Radius $R_{\odot}$	$A_V$	Accretion Rate $10^{-8} M_{\odot} yr^{-1}$	$\alpha_{IRAC}$	Disk?
17	0.298	3470	0.35	1.54	1.9	-	-2.65	no
29	0.068	3050	0.15	0.95	0.0	-	-2.64	no
63	0.348	3470	0.34	1.66	1.1	0.79	-1.28	strong
141	0.514	3850	0.57	1.64	2.3	0	-2.70	no
174	0.277	3470	0.34	1.48	1.6	-	-2.77	no
177	1.051	4590	1.30	1.65	1.8	0	-2.58	Transition
204	0.463	3720	0.47	1.67	1.1	0.83	-1.32	strong
229	0.077	3370	0.26	0.83	1.2	-	-2.79	no
281	0.235	3720	0.47	1.19	1.1	0.24	-2.39	Transition
285	0.348	3580	0.39	1.56	1.5	0.87	-1.12	strong
288	0.230	4060	0.79	0.99	0.7	0	-2.71	no
322	0.214	3240	0.25	1.49	1.5	-	-2.61	no
326	0.687	3990	0.68	1.77	1.6	<0.47	-1.79	IRAC-weak
344	0.745	3990	0.69	1.84	1.6	1.79	-1.52	strong
351	0.091	3370	0.28	0.90	0.8	-	-1.76	IRAC-weak
373	0.496	3370	0.30	2.10	1.5	1.65	-1.15	strong
416	0.319	3580	0.39	1.49	3.1	-	-1.45	strong
418	0.895	3990	0.67	2.01	2.2	2.27	-1.03	strong
458 <sup>a</sup>	4.679	4730	2.07	3.33	0.0 <sup>b</sup>	<7.11 <sup>c</sup>	-1.91	IRAC-weak
480	0.807	3720	0.47	2.20	1.4	1.77	-1.13	strong
515	2.280	4900	1.55	2.13	1.3	<1.09	-2.23	IRAC-weak

Table 2.3—Continued

Object ID	Luminosity $L_{\odot}$	$T_{eff}$ K	Mass $M_{\odot}$	Radius $R_{\odot}$	$A_V$	Accretion Rate $10^{-8} M_{\odot} yr^{-1}$	$\alpha_{IRAC}$	Disk?
543	0.116	3370	0.30	1.01	1.8	-	-1.92	IRAC-weak
571	2.407	4900	1.65	2.19	4.7	<1.10	-0.75	strong
581	3.576	4590	1.56	3.04	3.8	<2.37	-1.25	MIPS-weak
584	3.280	4350	1.12	3.244	4.5	7.83	-1.06	strong
590	3.525	4815	1.85	2.74	2.6	3.22	-0.72	strong
601	0.963	3955	0.64	2.13	4.3	-	-0.75	strong
618	2.053	5080	1.26	1.88	2.6	<1.06	-1.67	IRAC-weak
628	0.391	3580	0.39	1.65	3.4	-	-1.02	strong
656	0.352	3580	0.39	1.57	3.1	-	-1.24	strong
663	1.419	4205	0.89	2.28	4.4	-	-1.27	MIPS-weak
677	0.643	3525	0.37	2.19	4.1	-	-2.64	no
689	0.721	3650	0.43	2.16	2.2	0	-2.66	no
699	0.899	3650	0.43	2.41	4.6	-	-1.21	strong
730	1.280	4025	0.72	2.37	3.9	-	-1.06	strong
739	3.182	4590	1.63	2.87	6.2	-	-1.16	MIPS-weak
741	0.625	3525	0.37	2.16	4.0	-	-1.82	IRAC-weak
760	1.655	4277	1.01	2.38	3.5	5.13	-1.13	strong
782	0.491	3720	0.47	1.72	4.0	-	-1.39	MIPS-weak
802	0.552	3720	0.47	1.82	2.7	-	-2.19	IRAC-weak?
813	0.335	3470	0.34	1.63	3.2	-	-1.28	strong
843	0.399	3580	0.39	1.67	2.4	-	-1.56	strong

Table 2.3—Continued

Object ID	Luminosity $L_{\odot}$	$T_{eff}$ K	Mass $M_{\odot}$	Radius $R_{\odot}$	$A_V$	Accretion Rate $10^{-8} M_{\odot} yr^{-1}$	$\alpha_{IRAC}$	Disk?
849	2.006	4205	0.90	2.71	2.9	<1.79	-1.26	MIPS-weak
856	0.618	3720	0.47	1.93	4.2	-	-1.83	IRAC-weak
878	0.605	3850	0.57	1.78	3.2	1.09	-0.73	strong
934	0.422	3650	0.42	1.65	3.2	-	-1.09	strong
941	0.505	3920	0.62	1.57	2.8	1.54	-0.96	strong
984	2.094	4730	1.89	2.19	4.5	<1.78	-2.44	IRAC-weak?
997	0.315	3470	0.34	1.58	3.4	-	-0.93	strong
998	3.269	3850	0.56	4.13	3.7	<5.44	-1.79	IRAC-weak
1062	0.441	3580	0.39	1.76	2.0	1.94	-0.91	strong
1078	1.973	3785	0.51	3.32	4.2	-	-2.24	IRAC-weak?
1089	0.299	3650	0.42	1.39	3.4	-	-2.64	no
1099	2.361	4900	1.64	2.17	5.5	-	-1.11	strong
1116	1.532	4470	1.29	2.10	1.8	<0.81	-0.97	strong
1117	0.362	3720	0.47	1.47	3.8	-	-0.56	strong
1119	7.294	3850	0.56	6.18	3.8	<18.2	-0.80	MIPS-weak
1134	0.667	3470	0.35	2.30	1.2	0	-2.62	no
1171	0.519	3720	0.47	1.74	2.4	-	-1.28	MIPS-weak
1173	9.082	5700	1.84	3.14	5.1	no stand	-1.13	strong
1211	1.302	3720	0.47	2.80	1.6	7.75	-1.51	strong
1247	0.253	3370	0.30	1.50	2.5	-	-1.29	MIPS-weak
1259	0.336	3720	0.47	1.42	3.3	-	-1.37	strong

Table 2.3—Continued

Object ID	Luminosity $L_{\odot}$	$T_{eff}$ K	Mass $M_{\odot}$	Radius $R_{\odot}$	$A_V$	Accretion Rate $10^{-8} M_{\odot} yr^{-1}$	$\alpha_{IRAC}$	Disk?
1262	2.798	4025	0.70	3.50	4.5	8.60	-1.31	strong
1284	0.108	3240	0.22	1.06	1.4	-	-1.10	strong
1333	0.216	4060	0.79	0.96	0.5	0	-2.71	no
1643	0.348	3370	0.30	1.76	1.9	-	-2.62	no

<sup>a</sup>Photometry may be contaminated by background source with very cool SED, possible a Class 0/I source.

<sup>b</sup>With no available optical photometry, and extended emission contaminating the 2MASS photometry, an accurate extinction could not be derived and we assume a lower limit of 0

<sup>c</sup>R band magnitude from Siess et al. (2000) 2 Myr isochrone used instead of observed R band magnitude to derive accretion rate from veiling.

Note. — A dash in the accretion rate column indicates no high-resolution spectra was available, a 0 is used for those stars with high-resolution spectra, but the H $\alpha$  profile indicated there was no active accretion. Disk descriptors: strong ( $\alpha_{IRAC} > -1.6$ , [8.0]-[24] > 2.4), MIPS-weak ( $\alpha_{IRAC} < -1.6$ , [8.0]-[24] < 2.4), IRAC-weak ( $-1.6 > \alpha_{IRAC} > -2.5$ ), gap (small short wavelength excess, large [24] excess), no disk ( $\alpha_{IRAC} < -2.5$ ).

Table 2.4. High-Resolution Spectra of Likely Members

Object ID	Radial Velocity (km/sec)	Vsini (km/sec)	T&D R <sup>a</sup>	H $\alpha$ FW 10% (km/sec)	H $\alpha$ EW $\text{\AA}$	Veiling
63	31.7 $\pm$ 3.0	<8	3.7	280	19.1	0.88
141	27.0 $\pm$ 1.3	<8	12.0	142	1.7	-
177	27.7 $\pm$ 0.8	<8	23.6	124(101)	0.9(1.2)	-
204	25.5 $\pm$ 1.2	<8	11.5	250	25.4	0.51
281	27.3 $\pm$ 1.3	<8	16.7	400	32.4	0.36
285	26.2 $\pm$ 3.6	14.8	3.9	600	120.7	0.94
288	30.2 $\pm$ 1.3	<8	13.4	110	1.4	-
326 <sup>b</sup>	27.0 $\pm$ 1.1	<8	15.5	170(170)	5.9(5.3)	-
344	21.6 $\pm$ 1.3	<8	12.1	495	27.4	0.76
373	-	-	-	290	24.8	2.2
418	27.0 $\pm$ 2.1	13.4	7.4	410	60.5	0.76
458	24.5 $\pm$ 1.1	29.7	18.4	280(320)	2.7(3.4)	<0.15
480	26.8 $\pm$ 1.3	<8	12.5	510	7.9	0.45
515 <sup>b</sup>	14.1 $\pm$ 1.0	24.3	20.1	410	3.4	<0.15
571	28.8 $\pm$ 1.5	15.7	11.3	483	29.6	<0.15
581	25.9 $\pm$ 0.9	18.3	21.2	480	4.8	<0.15
584	-	-	-	640	42.7	0.39
590	28.2 $\pm$ 0.7	<8	23.1	470	14.9	0.31
618	27.0 $\pm$ 0.7	26.8	19.2	530(520)	46.8(28.3)	<0.15

Table 2.4—Continued

Object ID	Radial Velocity (km/sec)	Vsini (km/sec)	T&D R <sup>a</sup>	H $\alpha$ FW 10% (km/sec)	H $\alpha$ EW $\text{\AA}$	Veiling
689	27.2 $\pm$ 1.2	<8	10.9	110	3.7	-
760	28.5 $\pm$ 1.8	<8	8.2	535	49.4	1.28
849	27.3 $\pm$ 1.6	<8	9.8	340	18.2	<0.15
878	27.1 $\pm$ 1.3	<8	12.6	440	25.5	0.49
941	26.8 $\pm$ 2.3	<8	6.5	415	52.4	1.82
984	25.4 $\pm$ 2.4	49.2	10.6	280	1.1	<0.15
998	11.6 $\pm$ 2.3	40.7	9.7	280	1.9	<0.15
1062	26.9 $\pm$ 2.9	<8	4.3	430	46.8	3.18
1116	25.8 $\pm$ 0.8	<8	21.9	400(405)	23.4(22.1)	<0.15
1119	31.3 $\pm$ 3.8	55.8	2.9	450	27.1	<0.15
1134	27.1 $\pm$ 1.5	<8	8.7	160	8.0	-
1173	32.7 $\pm$ 2.3	49.1	11.4	350	9.7	-
1211	25.9 $\pm$ 2.5	<8	5.2	490	26.3	1.97
1262	26.2 $\pm$ 1.2	<8	14.1	340	5.4	0.41
1333	28.3 $\pm$ 1.1	<8	15.6	90	1.3	-

Note. — FW at 10% values in parenthesis are from the second set of high-resolution spectra. Only objects 326,177,458,618 and 1116 have two sets of high-resolution spectra.

<sup>a</sup>Tonry & Davis R value (Tonry & Davis, 1979). The 90% confidence interval for  $v \sin i$  is approximately  $v \sin i / (1+R)$ .

<sup>b</sup>H $\alpha$  profile shows an inverse P Cygni shape indicating active accretion, despite the small FW 10%.



Table 2.5. Fraction of Evolved Disks

Cluster	Age	Strong disks	MIPS-weak	IRAC-weak
K0-M1				
Taurus	1	$94 \pm 24\%$ (16/17)	-	$6 \pm 6\%$ (1/17)
NGC2068/71	2	$66 \pm 14\%$ (23/35)	$16 \pm 7\%$ (5/32)	$20 \pm 8\%$ (7/35)
IC 348	2-3	$80 \pm 20\%$ (16/20)	0% (0/17)	$20 \pm 10\%$ (4/20)
$\sigma$ Ori	3	$75 \pm 19\%$ (15/20)	$19 \pm 11\%$ (3/16)	$10 \pm 7\%$ (2/20)
Tr 37	4	$68 \pm 9\%$ (59/87)	$13 \pm 5\%$ (7/54)	$24 \pm 5\%$ (21/87)
NGC 2362	5	$30 \pm 17\%$ (3/10)	-	$70 \pm 26\%$ (7/10)

Note. — Statistics for MIPS-weak disks only include those stars detected at  $24\mu\text{m}$ . IRAC-weak disks defined as  $-2.56 < \alpha_{IRAC} < -1.8$ .

## CHAPTER 3

### MODELING MID-INFRARED VARIABILITY OF CIRCUMSTELLAR DISKS WITH NON-AXISYMMETRIC STRUCTURE

Recent mid-infrared observations of young stellar objects have found significant variations possibly indicative of changes in the structure of the circumstellar disk. Previous models of this variability have been restricted to axisymmetric perturbations in the disk. We consider simple models of a non-axisymmetric variation in the inner disk, such as a warp or a spiral wave. We find that the precession of these non-axisymmetric structures produce negligible flux variations but a change in the height of these structures can lead to significant changes in the mid-infrared flux. Applying these models to observations of the young stellar object LRL 31 suggests that the observed variability could be explained by a warped inner disk with variable scale height. This suggests that some of the variability observed in young stellar objects could be explained by non-axisymmetric disturbances in the inner disk and this variability would be easily observable in future studies.

#### 3.1 Introduction

Variability has been one of the prominent features of T Tauri stars since they were first observed (Joy, 1945). In the optical flux changes up to 0.5 magnitudes over a few days are common with most of the variability explained by hot and cold spots rotating across the surface of the star (Herbst et al., 1994). In a few cases, circumstellar disk variability has been inferred from stochastic or quasi-periodic optical occultation events. In the case of AA Tau a warped inner disk occults the star leading to periodic optical variations (Bouvier et al., 2003). For HH 30,

putative structural changes in the disk may lead to the observed changes in the scattered light emission in as little as a few days (Watson & Stapelfeldt, 2007). Variations in the scattered light images of HD 163296 are also attributed to a change in the structure of the disk (Wisniewski et al., 2008). FU Ori outbursts, which show an orders of magnitude increase in the optical flux followed by a slow decrease over decades, are associated with changes in the accretion rate of the disk brought about by thermal or gravitational instabilities (Hartmann & Kenyon, 1996). EXor stars also show variability on month to yearly timescales probably related to changes in the accretion rate through the disk (Herbig, 2007).

Infrared observations provide a more direct way of looking for variability of the circumstellar disk. Emission at these wavelengths comes from dust near the surface of the central  $\lesssim 10$  AU of the disk and is sensitive to changes in the disk temperature and structure. The dust temperature is set by a combination of viscous energy release as disk gas accretes toward the central star and irradiation of the disk surface by light from the stellar photosphere and accretion shock. Variations in the near-infrared cannot always be explained simply by a change in the stellar flux, but a change in the structure of the circumstellar disk must also be included (Carpenter et al., 2001; Eiroa et al., 2002; Skrutskie et al., 1996; Alves de Oliveira & Casali, 2008). Plavchan et al. (2008) find variable disk emission at 3-8  $\mu\text{m}$  around the star WL 4, which also exhibits periodic near-infrared changes suggestive of influence by a binary companion. Variability as far out as 100  $\mu\text{m}$  has been observed (Liu et al., 1996; Juhász et al., 2007; Barsony, Ressler, & Marsh, 2005) although the limited wavelength coverage and time sampling do not provide strong constraints on the physical cause. Some of this variation can be explained by changes in the structure of the inner disk. Variability of the 10  $\mu\text{m}$  silicate feature, which is sensitive to grain properties at the surface of the inner

few AU of the disk, has also been observed suggesting that the grain properties of disks are rapidly varying (Ábrahám et al., 2009; Bary, Leisenring, & Skrutskie, 2009; Skemer et al., 2010).

Most disk models assume axisymmetry, and thus explore axisymmetric structure variations or asymmetric irradiation fields to explain the observed variability. Muzerolle et al. (2009) suggest that a non-axisymmetric inner disk may explain the strange wavelength dependence of the variations seen in LRL 31, a transition disk in the young cluster IC 348. In this paper we further explore the possibility that these mid-infrared variations could be caused by a non-axisymmetric structure in the inner disk. First we consider three simple models for a non-axisymmetric structure: a warp in the middle of the disk, a warp at the inner edge of the disk and a spiral wave in the disk. We examine how the SED of these disks varies as the structures precesses/corotates around the star and as the height of the structure changes with time. We then apply these models to the variations in LRL 31 as well as to other mid-infrared variable stars.

## 3.2 Models

### 3.2.1 Motivation

A number of authors have recently found strong wavelength dependent mid-infrared variability in both Herbig AeBe stars and T Tauri stars. Juhász et al. (2007) observe 3-100 $\mu$ m variability of SV Cep over a two year period. These variations can be up to a factor of two at 100 $\mu$ m, and there appears to be a correlation between the 100 $\mu$ m flux and the optical flux and a weak anti-correlation between the 3.6 $\mu$ m flux and the optical flux. Sitko et al. (2008) find significant variations in the 3-13 $\mu$ m flux of the Herbig AeBe star HD 31648 over almost a quarter-century. Hutchinson et al. (1994) find two stars, UX Ori and AK Sco, whose optical flux

decreases as the  $10\mu\text{m}$  flux increases. Morales-Calderón et al. (2009) find that  $3\text{--}8\mu\text{m}$  variability of 0.05-0.2 mag is common in pre-main sequence stars in the young cluster IC 1396A. Muzerolle et al. (2009) find mid-infrared variations of up to 60% in as little as one week in the young star LRL 31. The IRS spectra show a clear wavelength dependence of the flux variations, where the  $5\text{--}8\mu\text{m}$  flux decreases and the  $8\text{--}40\mu\text{m}$  flux increases. This variation is especially interesting since LRL 31 exhibits an SED typical of a transition disk, indicative of a deficit of small grains in the inner disk.

Typical sources of optical variability in pre-main sequence stars have difficulty explaining the observed mid-infrared variations in these stars. Cold spots on the star cannot produce a large enough variation in the mid-infrared, where the flux is dominated by the circumstellar disk. They would not be able to produce variability out as far as  $100\mu\text{m}$ , as has been seen in a number of stars. Hot spots, due to the accretion flow striking the surface of the star, produce large optical variations that may affect the infrared flux. As the star rotates, the hot spot acts as a flashlight heating a localized portion of the disk. If the disk is viewed close to edge-on then the asymmetric heating can produce noticeable variations in the infrared (Morales-Calderón et al., 2009). However, it is difficult for this model to explain some of the larger variations and different wavelength dependences seen in many young stellar objects.

Juhász et al. (2007) and Sitko et al. (2008) use detailed radiative transfer models of a varying height at the inner edge of the disk to reproduce their observations. Increasing the scale height raises the near-infrared flux while shadowing the outer disk, and occulting the star if the system is close to edge on. The long-wavelength variation is difficult to explain with in-situ changes in the structure of the disk because the dynamical timescale is years to decades longer than the

observations, thus models with variations in the inner disk that shadow the outer disk are used. Due to the restrictions of the radiative transfer code, the perturbations were assumed to be axisymmetric within the disk. Muzerolle et al. (2009) suggest that the variation in LRL 31 may be a warp, spiral wave or some other non-axisymmetric structure in the inner disk. Some of the observations of LRL 31 are difficult to explain with a puffed inner rim and other configurations were considered. Here we follow up on that possibility and develop a simple model of such structures. When examining these non-axisymmetric models we consider two time-dependent effects: azimuthal motion such as precession and corotation, and variations in the scale height of the perturbation. Precession is a natural consequence of the torques that originally warped the disk while a variable scale height may be related to the dynamical process that causes a warp in the first place. Both of these are possible sources of variability for a non-axisymmetric structure.

### 3.2.2 Deriving the SED

Disks are generally modeled as axisymmetric flared disks that are heated by stellar irradiation (Chiang & Goldreich, 1997) or a combination of stellar irradiation and viscous dissipation from accretion (D'Alessio et al., 2006). But the disks can become disturbed from this initial state by the gravitational influence of a binary companion or passing star (Artymowicz & Lubow, 1994; Larwood & Papaloizou, 1997) or an instability within the disk (Watanabe & Lin, 2008). This can lead to the disk becoming warped, which will change the temperature structure and emission of the disk. To study how structural changes will effect the SED we consider three simple models (1) a disk with a middle warp, (2) a disk with an inner warp and (3) a disk with a spiral wave, shown in figure 3.1. All of these disks are taken to be geometrically thin blackbody emitters. Flaring and an optically thin atmo-

sphere will have a substantial effect on the SED but these simple models present a useful starting point. If our models were completely confined to the midplane the SED would have the simple form  $\lambda F_\lambda \propto \lambda^{-4/3}$ . How our models depart from the power law will depend on the location of the structural disturbance within the disk. To calculate the SED for our simple models we follow the derivation presented in Terquem & Bertout (1996, hereafter TB96). TB96 lay out a procedure for estimating the temperature structure of a blackbody disk whose height,  $h$ , is an arbitrary function of  $r$  and  $\theta$  within the disk. The coordinate system is defined as centered on the star with  $\theta = 0$  along the line with the highest warp above the midplane. The flux intercepting a point  $P(r, \theta)$  in the disk is given by:

$$F_\lambda = 2B_\lambda(T_*) \int_{\delta_{min}}^{\delta_{max}} \gamma \sin(\delta) \left( \int_{\varepsilon_{min}}^{\varepsilon_{max}} |A \cos \delta + B \sin \delta \sin \varepsilon + C \sin \delta \cos \varepsilon| d\varepsilon \right) d\delta \quad (3.1)$$

where

$$\gamma = \frac{1}{\sqrt{1 + (\partial h / \partial r)^2 + (\partial h / \partial \theta)^2 / r^2}} \quad (3.2)$$

and

$$A = \left( \frac{\partial h}{\partial r} \right) \cos \beta - \sin \beta \quad (3.3)$$

$$B = \frac{1}{r} \left( \frac{\partial h}{\partial \theta} \right) \quad (3.4)$$

$$C = \left( \frac{\partial h}{\partial r} \right) \sin \beta + \cos \beta \quad (3.5)$$

with  $\tan(\beta) = h(r, \theta)/r$ . The variables  $\delta$  and  $\varepsilon$  are the polar and azimuthal coordinates of a point on the surface of the star with respect to the axis joining the

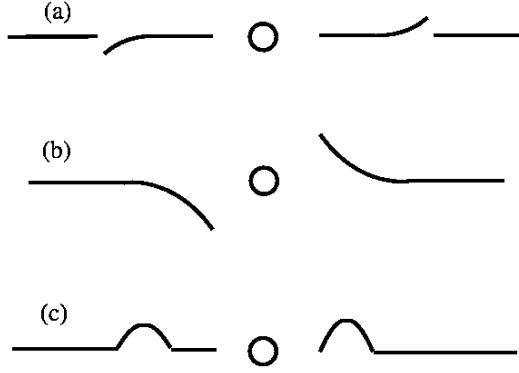


Figure 3.1 Schematic drawing of our three simple geometric models. The three models are (a) the middle warp, (b) the inner warp and (c) the spiral wave all viewed edge on along  $i = 90^\circ$ ,  $\alpha = -90^\circ$ .

polar axis to the center of the star. Converting to temperatures, and performing the integration over  $\varepsilon$ , the equation then becomes:

$$T^4(r, \theta) = \frac{2}{\pi} T_*^4 \int_{\delta_{min}}^{\delta_{max}} \gamma \sin \delta \{ A[\varepsilon_{max} - \varepsilon_{min}] \cos \delta + B[-\cos \varepsilon_{max} + \cos \varepsilon_{min}] \sin \delta + C[\sin \varepsilon_{max} - \sin \varepsilon_{min}] \sin \delta \} d\delta + \frac{3G\dot{M}M_*}{8\pi\sigma r^3} \left( 1 - \sqrt{\frac{R_*}{r}} \right) \quad (3.6)$$

The last term in this equation is the energy from viscous dissipation, which for typical T Tauri accretion rates is much less than the heating from irradiation. We assume that the accretion rate onto the star is small enough that the accretion luminosity is negligible compared to the stellar luminosity and thus does not contribute to the heating of the disk. The process of evaluating the temperature of the disk reduces to a determination of  $\delta_{max}$ ,  $\delta_{min}$ ,  $\varepsilon_{min}$ ,  $\varepsilon_{max}$ . The three models will vary in their evaluation of  $\delta_{max}$ ,  $\delta_{min}$ ,  $\varepsilon_{min}$ ,  $\varepsilon_{max}$  for each point  $P(r, \theta)$  on the disk surface, which is discussed in more detail in the appendix.

From TB96, the flux emitted by the disk is:



$$F_{\nu, \mathbf{u}} = \int \int_{\text{disk surface}} B_{\nu}(T(r, \theta)) dS \mathbf{n}_d \cdot \mathbf{u} \quad (3.7)$$

In this case  $\mathbf{u}$  is the vector along the line of sight to the observer from the center of the star and  $\mathbf{n}_d$  is the normal to the disk at the point  $P(r, \theta)$ . The vector  $\mathbf{u}$  can be defined in terms of the azimuthal and polar angles to the line of sight,  $\alpha$  and  $i$  respectively. The disk surface extends from  $r_{min}$ , which we take to be  $8R_*$ , out to  $R_{disk}$ , typically 100 AU. The inner radius  $8R_*$  is roughly equal to the dust destruction radius for a frontally illuminated disk with well-mixed small dust grains around a  $0.5M_{\odot}$  T Tauri star (Muzerolle et al., 2003).

The area of the disk along the line of sight is given by

$$dS \mathbf{n}_d \cdot \mathbf{u} = r \left[ \left( \frac{1}{r} \frac{\partial h}{\partial \theta} \sin \theta - \frac{\partial h}{\partial r} \cos \theta \right) \cos \alpha \sin i - \left( \frac{1}{r} \frac{\partial h}{\partial \theta} \cos \theta + \frac{\partial h}{\partial r} \sin \theta \right) \sin \alpha \sin i + \cos i \right] dr d\theta \quad (3.8)$$

We also include the possibility of the star being occulted by the disk. These prescriptions are described in detail in the appendix. This is highly dependent on the viewing angle, which for the non-axisymmetric disks considered here depends on both inclination,  $i$ , and the azimuthal viewing angle,  $\alpha$ . The line of sight  $\alpha = 0$  corresponds to looking at the disk along the line  $\theta = 0$ , while an observer along  $i = 0^\circ$  is viewing the disk face-on. TB96 do not examine the dependence on azimuthal angle, although their generic equations repeated above do include  $\alpha$ . In the appendix we demonstrate how this dependence has been included in the models.

For our fiducial models we take the central source to be a G6 star with a radius of  $2.9 R_{\odot}$ , a mass of  $1.8 M_{\odot}$  and an accretion rate of  $\dot{M} = 10^{-8} M_{\odot} \text{yr}^{-1}$ . These specific parameters are chosen in anticipation of modeling the disk around LRL 31. As we will show later, the shape and strength of the variability does not

depend strongly on the central star and the results presented in the next sections are applicable to a broad range of pre-main sequence stars.

### 3.2.3 Middle Warp

We first consider a warp similar to that originally discussed by TB96 whose functional form is:

$$h(r, \theta) = g R_{warp} \left( \frac{r}{R_{warp}} \right)^n \cos(\theta) \quad (3.9)$$

for  $r \leq R_{warp}$ . The parameter  $R_{warp}$  specifies the outer radius of the warp. TB96 take  $R_{warp}$  to be equal to the radius of the disk, while here we consider situations where the disk extends beyond the warp, shown in figure 3.1a, in order to examine shadowing effects. Past  $R_{warp}$  the disk is confined to the midplane and this flat passive extension can be shadowed by the warp, changing its temperature structure. Since the warp occurs in the middle of the disk we refer to it as a middle warp. We consider disks with  $R_{warp}$  of a few AU or less in order to probe any effects on the 2 to  $24\mu\text{m}$  flux. The parameter  $g$  sets the height of the warp, and is equivalent to the maximum value of  $h/r$  within the disk. According to Terquem & Bertout (1993) a warp created by an equal mass binary will have  $n = 4$ ,  $g = 0.01$ . Figure 3.2 shows the temperature structure of disks with  $g = 0.01, 0.05$  and  $R_{warp} = 0.5$  AU. These warps demonstrate the shadowing of the outer disk and how it can change with radius. Immediately behind the warp (dark line beyond 0.5 AU) the disk is completely shadowed and is only heated by viscous dissipation. Further out the warp only blocks part of the star and the temperature approaches that of a flat passive disk. The height of the warp will change the temperature at the warp as well as the shadowing of the outer disk. Figure 3.2 compares the SED of this warped disk with a flat passive disk and a flat accretion disk. The short wavelength flux rises above a flat passive disk because

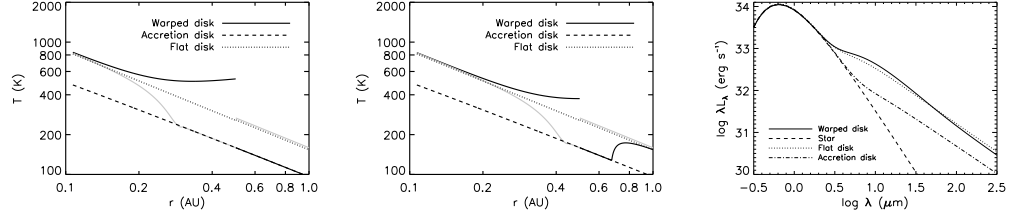


Figure 3.2 Middle Warp disk. In the left and middle panels are the temperature structures of a disk with a warp that reaches its maximum  $h/r$  of  $g = 0.05, 0.01$ , respectively, at  $r = 0.5$  AU with a flat disk extending beyond the warp to 100 AU. The dark solid line is the side of the disk facing the star, while the grey solid line is the side of the warp facing away from the star. On the right is the SED for a disk with an middle warp that grows to  $g = 0.05$  at  $R_{warp} = 0.5$  AU and a flat extension to the disk that extends to 100 AU. The disk is viewed along  $i = 60^\circ, \alpha = 0^\circ$ . Also shown are a flat accretion disk, a flat passive disk and a blackbody at  $T_{eff} = 5700$  K for comparison.

of the high temperature on the side of the warp facing the star. The shadowing of the outer disk reduces the flux at long wavelengths so that it is less than a flat passive disk.

A warped disk will be driven to precess by the torques on the system which originally warped the disk. To mimic a precessing warped disk, we vary the azimuthal viewing angle,  $\alpha$ , of the observer. The method of TB96 needs to be modified to account for a changing azimuthal angle, and these changes are described in the appendix. In figure 3.3 we show the precession of a warp with  $g = 0.05$  which extends to  $R_{warp} = 0.5$  AU with a flat disk extending to 100 AU. As the disk precesses the infrared excess only changes by  $\sim 0.05$  dex. The flux change at short and long wavelengths is correlated. The observed wavelength dependence can be understood by considering the schematic middle warp drawn in figure 3.1. The observer is rotating from the upper right to the upper left in this drawing and as the observer rotates the hot side of the warp comes directly into view. This increases the short wavelength flux, and since the orientation rel-

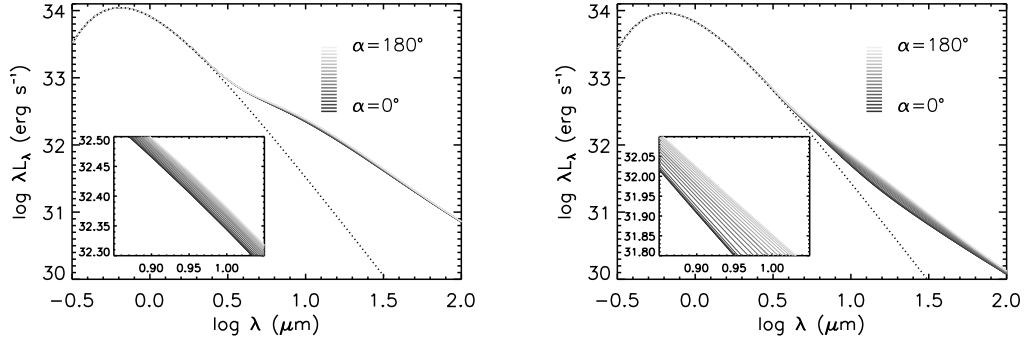


Figure 3.3 SED of a precessing disk with an middle warp extending to  $R_{\text{warp}} = 0.5$  AU with  $g = 0.05$  and a flat extension seen at an inclination of  $60^\circ$  (left panel) and  $85^\circ$  (right panel). From dark to light lines the disk rotates through  $180^\circ$ . The inset shows a closeup of the models near  $10\mu\text{m}$ . The dotted line is the photosphere. The change in the infrared flux is small, but it increases as the disk is viewed closer to edge on.

ative to the cold outer disk does not change with  $\alpha$  the long wavelength flux does not change significantly. The distance between the warp and the star keeps the warp cold and causes the change in the SED to be at longer wavelengths. Figure 3.3 also shows the precession of a warp seen at  $i = 85^\circ$ . The infrared excess is smaller, because of the more highly inclined observing angle, while the change in flux is larger although the wavelength dependence is the same. As the disk becomes more inclined the warp is seen closer to face-on, creating more significant variations as it rotates in and out of view.

Creating a warp in the middle of the disk is possible with a (sub)stellar companion embedded in the disk. If the companion is not coplanar with the disk then the gravitational perturbation from the companion can drive material out of the midplane. The disk around  $\beta$  Pic displays a warp in the middle of the disk due to an unseen companion (Augereau et al., 2001). The variable star WL 4 displays periodic variability in the near-infrared, indicative of a multiple system, as well as mid-infrared variability, indicative of a change in the dust structure

near the star (Plavchan et al., 2008). Roughly 10% of stellar systems have a binary companion within 1 AU (Mathieu, 1994). If the companion is within one AU of the central star then the precession period of such a configuration is years to decades, depending on the exact configuration of the system (Caprari et al., 2006). The combination of the small flux change and long timescale would make precession difficult to observe.

We next consider the effect of changing the height of the warp. As the warp height increases the disk will get heated to a higher temperature since it is more directly illuminated by the radiation field. This is the same reason that a flared disk gets heated to a higher temperature and has a higher flux than a flat passive disk. The larger warp will also cast a larger shadow on the outer disk which will decrease its temperature and lower its flux. If the warp changes substantially enough then the change in the temperature structure would be evident in the SED. The hot surface layers of the disk that are seen in the mid-infrared respond almost instantaneously to a change in the stellar radiation field (Chiang & Goldreich, 1997). This means that the timescale for the SED to change will depend on how quickly the disk can change its structure, which is the dynamical timescale. For the central star considered here the dynamical timescale can be as low as one week within 0.1 AU.

In order to examine this effect we take the disk we used to study precession ( $R_{warp} = 0.5\text{AU}$ ) and vary its scale height, parameterized by the factor  $g$ , from 0.01-0.1. This corresponds to a physical height of 0.005-0.05 AU. The results are shown in figure 3.4. We find that as the height of the warp increases the flux at  $\lambda < 15\mu\text{m}$  increases while the flux longward of  $15\mu\text{m}$  decreases. The flux variations are small but the unique wavelength dependence would make infrared variability due to a changing scale height at the inner edge of the disk easy to

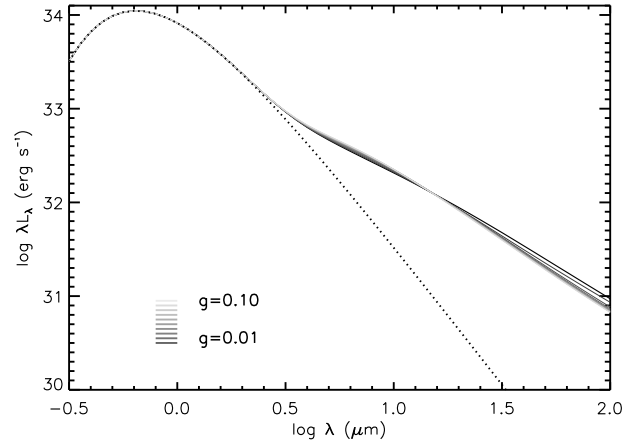


Figure 3.4 SED for a growing warp ( $g = 0.01 - 0.1$  from dark to light lines) viewed at  $i = 60^\circ$ ,  $\alpha = 0^\circ$ .

diagnose.

The same mechanism that drove the disk to become warped may also cause it to change the height of the warp. If the warp is caused by a companion, then this object could drag material as its orbit takes it out of the midplane (Fragner & Nelson, 2010). For a binary companion whose orbit is misaligned with the disk, the plane of the disk will equilibrate with the plane of orbit over thousands of years, but on the timescale of a single orbit dust will be shifted by the passing of the companion. As the companion's orbit takes it out of the plane of the disk it will drag material with it, but when the companion's orbit takes it back into the midplane of the disk this dust will quickly settle down. This would lead to periodic variations in the scale height of the warp on top of the long term variations. It may also be possible that a long-lived asymmetric structure within the disk, such as a warp caused by a companion, is experiencing variable illumination from the central source. This is possible if the accretion flow is localized into hot spots that rotate around the star. As the hot spot illuminates the warp, it will heat the side facing the star, causing its scale height to increase. The scale height of the warp

will decrease as the hot spot rotates around to the far side of the star.

### 3.2.4 Inner Warp

As the warp moves closer to the star, the deviation in the SED from a flat passive disk moves to shorter wavelengths. To affect the flux at  $5 - 8\mu\text{m}$  we need to move the warp almost to the inner edge of the disk. We could also consider a warp that reaches its maximum height above the midplane at the inner, rather than the outer, edge of the disk. An inner warp has been invoked to explain the variability observed in AA Tau (Bouvier et al., 2003) in which the stellar magnetic field is misaligned with the disk causing it to warp as material flows onto the field lines. A inner warp can be described by the function:

$$h(r, \theta) = gr_{min} \left( \frac{r}{r_{min}} \right)^{-4} \cos(\theta) \quad (3.10)$$

The temperature distribution for disks with  $g = 0.05, 0.01$ ,  $r_{min} = 8R_*$  are shown in figure 3.5. The exponent for the power law was chosen to match the middle warp and depends on the exact physical cause of the warp. The inner warp can be split into two pieces, a convex piece which directly faces the star and a concave piece which is turned away from the star. In the schematic drawing of the inner warp in figure 3.1b on the right side the convex piece is on the bottom while the concave piece is on the top. The inner edge of the convex side reaches a very high temperature and departs significantly from a flat passive disk. The concave side just behind the warp has a low temperature because the warp completely blocks the star and the disk is only heated by viscous dissipation. Moving outwards, a point on the disk will be able to see some of the star, although it is still partially blocked. The temperature on the concave side far from the warp will be between that of a flat passive disk which experiences no shadowing and a fully shadowed disk which is only heated by viscous dissipation. As the warp grows

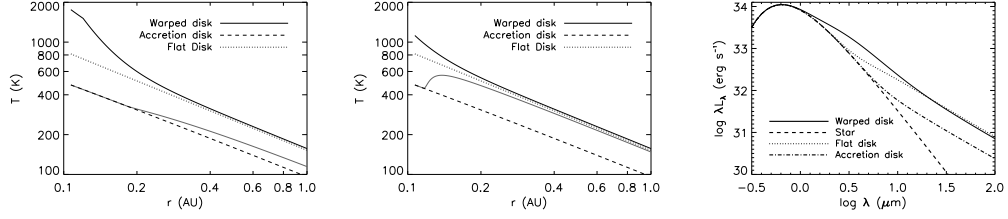


Figure 3.5 Inner warp disk. The left and middle panels show the temperature distribution for a disk with an inner warp of  $g = 0.05$  and  $g = 0.01$  respectively. The dashed line is the temperature of a disk heated solely by viscous dissipation ( $\dot{M} = 10^{-8} M_\odot \text{yr}^{-1}$ ), the dotted line is a perfectly flat passive disk, while the solid (dark and light) lines are the warped disk (convex and concave sides respectively). The maximum temperature of the warp, and the shadowing of the outer disk changes with the size of the warp. On the right is the SED for a warped inner disk with  $g = 0.05$  seen at  $i = 60^\circ$ ,  $\alpha = 0^\circ$ . For comparison a flat passive disk, a disk heated by viscous accretion ( $\dot{M} = 10^{-8} M_\odot \text{yr}^{-1}$ ) and the photosphere are also included.

the temperature on the convex side increases and on the concave side it decreases. In limit of a very large warp the concave side will be completely shadowed while the convex side will be much warmer than a flat passive disk.

Figure 3.5 compares the SED of the inner warp disk to that of a flat passive disk and a disk heated by viscous dissipation. The warped disk significantly departs from the flat passive disk at short wavelengths because of the high temperature on the convex side while its SED is lower at long wavelengths because of the shadowing on the concave side. The warp drops below the midplane for  $90^\circ < \theta < 270^\circ$  (the left side of the top half of the disk shown in figure 3.1b) and only half of the disk is shadowed. Since at most half of the disk can be shadowed, the flux always lies above a flat accretion disk even for very large warps.

Figure 3.6 shows the variation in the SED as the warp moves around the star. The short wavelength flux changes as the convex side rotates more directly into the line of sight while the long-wavelength flux does not change because this part of the disk is essentially flat and the SED of a flat disk does not depend



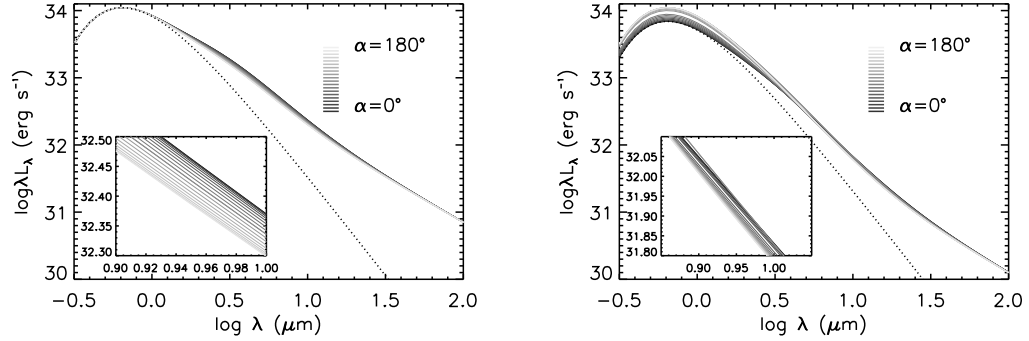


Figure 3.6 SEDs for a warped inner disk with  $g = 0.05$  showing the change in flux as the disk precesses. From dark to light the disk changes orientation from  $\alpha = 0^\circ$  to  $\alpha = 180^\circ$  with an inclination of  $i = 60, 85^\circ$  (left and right panels respectively).

on azimuthal viewing angle. If the warp does not occult the star (left panel of figure 3.6) there is a small change in the flux. Viewing the disk at a high enough inclination (right panel of figure 3.6) changes the form of the SED variations. The infrared variations are smaller when the disk is viewed edge on than when it is seen closer to face on. This is because when the warp on the near side of the disk blocks the star, the hot side of the warp on the far side of the star is directly visible. These two effects work in opposite direction; blocking stellar flux reduces infrared flux, while seeing the convex side of the warp increases the flux. This can cause the change in optical flux and infrared flux to be in opposite directions, while for the more face-on case the flux variations are in the same direction at all wavelengths.

The type of warp described here can be created by a number of different physical mechanisms. One possibility is a (sub)stellar companion embedded in the disk. As with the middle warp, if the companion is not coplanar with the disk then the gravitational perturbation from the companion can drive material out of the midplane. If the companion is located close to the star then this disturbance will be at the inner edge of the disk. In the models of Larwood & Papaloizou

(1997), for small mass ratios ( $q=0.01-0.1$ ), the warp changes the scale height of the disk by  $\Delta h/r \approx 0.1$ , similar to the scale height considered here.

For the T Tauri star AA Tau, a warped disk caused by a tilted stellar magnetic field is believed to explain the observed variations (Bouvier et al., 2003). The stellar magnetic field is misaligned with the disk and the flow of material onto the magnetic field warps the disk. This warp would occur near the corotation radius where the magnetic field from the star truncates the disk, where the dynamical timescale of the disk will only be a few days. Interferometric observations generally find that the hottest circumstellar dust is at distances consistent with the dust sublimation radius, much larger than the corotation radius for higher mass stars (Milan-Gabet et al., 2007). The exact location of the dust sublimation radius depends on the size of the dust grains and the geometry of the inner disk. If the disk is close to flat, as is assumed in our models, or consists of large grains, then it may be possible for the dust to extend close enough to the star to trace a warp caused by a tilted magnetic field.

The timescale for the inner warp to rotate around the star depends on the process originally responsible for creating the warp. If the motion is precession driven by a companion on a misaligned orbit then the period will be 1.5 years for a warp at 0.1 AU (Caprari et al., 2006). A warp created by a tilted magnetic field will rotate at the same rate as the star. Typical rotation periods for pre-main sequence stars are a few days to a week (e.g. Cohen et al., 2004), which would produce rapid flux variations.

A variable stellar accretion rate could also change the structure of the inner disk. The height of the inner rim is set by the incident luminosity, which is a combination of stellar and accretion luminosity (Muzerolle et al., 2003). Increasing the accretion luminosity will raise the temperature of the inner rim causing

its scale height to increase. If the accretion luminosity is comparable to the stellar luminosity then a rapidly varying accretion luminosity could lead to a rapid change in the inner rim height. The accretion rate onto young stars varies rapidly on short timescales (Hartigan et al., 1991; Gullbring et al., 1996). If the accretion luminosity was not evenly distributed around the star, but instead confined to a hot spot then this may lead to preferential heating and growth of part of the inner disk. Growing part of the inner disk creates a non-axisymmetric structure that may be comparable to the inner warp structure, producing similar changes in the SED.

The growth of an inner warp can create an anti-correlation in the disk flux as it did with the middle warp. In figure 3.7 we show a model for  $g = 0.005 - 0.1$  ( $h = 0.005 - 0.01 AU$ ) at  $i = 60^\circ$ . As the warp grows the short wavelength flux increases while the long wavelength flux decreases due to the shadowing effect discussed above for the middle warp. The large temperature change in the inner disk leads to the significant variation in the near and mid-infrared flux. This flux variation would be easily observable in the near and mid-infrared.

The timescale to change the structure of the disk is the dynamical timescale, equal to the keplerian period, which is roughly one week at 0.1 AU. After the dust moves within the disk, its temperature will readjust to its new orientation relative to the radiation field on a thermal timescale. For the surface layers of the disk responsible for the mid-infrared emission this timescale is a few seconds, effectively instantaneous compared to the dynamical timescale (Chiang & Goldreich, 1997). We compute warps of different sizes independently of each other, which is the same as assuming that as the warp grows its temperature responds instantaneously to the changing intercepted radiation field. These rapid variations in the scale height could be caused by the motion of a companion misaligned with the

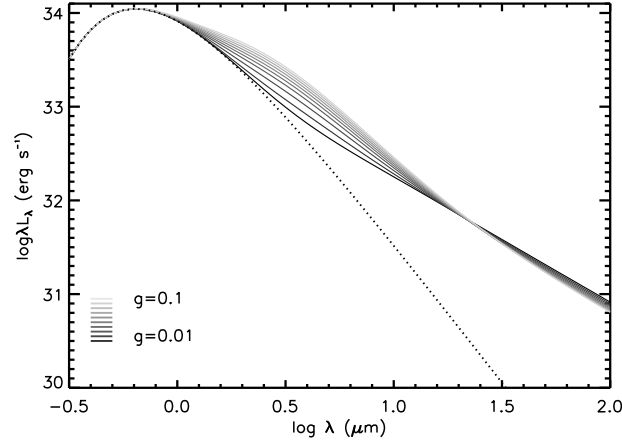


Figure 3.7 SEDs showing a growing inner warp. The models vary  $g$  from 0.01 to 0.1 (from dark to light lines) seen at an inclination of  $i = 60^\circ$ . There is a substantial change in the mid-infrared flux as the warp grows

disk, as in the middle warp (Fragner & Nelson, 2010).

### 3.2.5 Spiral Wave

We can also use the framework of TB96 to derive the SED of a simple spiral wave. Spiral waves are a common feature in the disks surrounding stars with planets or a stellar companion (Goldreich & Tremaine, 1979; Kley, 1999). The shocks created by the passing density waves can change the scale height of the disk (Edgar & Quillen, 2008; Boley & Durisen, 2006) causing heating and shadowing effects similar to a warp. We use a simple parameterization of a spiral wave as a modification of a flat disk to study its effects on the SED. The position of the spiral wave is given by:

$$r_{sw} = r_{min-sw}(1 + n\theta) \quad (3.11)$$

The value of  $n$  sets the maximum radius of the wave and we keep  $n$  fixed at  $0.8/(2\pi)$  to match more detailed descriptions of a spiral wave (Ogilvie & Lubow,

2002). The parameter  $r_{min-sw}$  sets the minimum radius for the center of the wave, which is taken to be slightly larger than the innermost radius of the disk. Our wave only runs from  $0 < \theta < 360^\circ$ , although it could continue to wrap around the star until it reaches the outer edge of the disk. The height above the midplane is given by:

$$h(r, \theta) = g \left( 1 - \frac{m\theta}{2\pi} \right) r_{min-sw} \exp \left( - \left( \frac{r - r_{sw}}{\sigma_r} \right)^2 \right) \quad (3.12)$$

The shape of the wave is a gaussian with width  $\sigma_r$  centered at  $r_{sw}$ . The function  $\left( 1 - \frac{m\theta}{2\pi} \right)$  modifies the height of the wave so that it decreases as it extends around the disk. Spiral waves grow weaker as they get further from their point of origin and the parameter  $m$  can be used to modify how quickly the wave height decreases. In our fiducial model the wave disappears at  $2\pi$  ( $m=1$ ). The factor  $g$  serves a similar purpose as before; it sets  $h/r$  for the wave. Although this parameterization allows us to modify many details of the spiral wave we generally keep  $m = 1$ ,  $\sigma_r = 0.1r_{min}$ ,  $r_{min-sw} = r_{min} + 2 * \sigma_r$ ,  $n = 0.8/2\pi$  and modify  $g$ .

The temperature structure of spiral disks with  $g = 0.05, 0.1$  is shown in Figure 3.8. On the side of the wave facing the star the disk reaches a very high temperature, while directly behind the wave the temperature drops. Further out from the wave the disk is only partially shadowed and the temperature lies between that of a flat passive disk and the base flat accretion disk. In the models shown in figure 3.8 the radius of the wave increases with  $\theta$  while the height decreases, hence at  $\theta = 180^\circ$ , shown as the grey line, the temperature is lower on the front side of the wave and higher behind the wave than for  $\theta = 0^\circ$ . Comparing the two models, we find that as the size of the wave increases the temperature of the side of the disk facing the star increases while the outer disk becomes more shadowed.

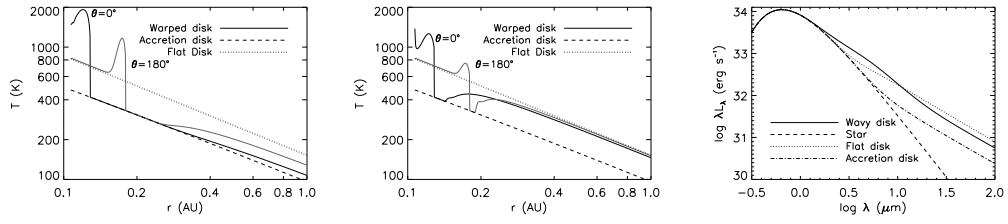


Figure 3.8 Spiral wave disk. The left and middle panels show the temperature distribution for a spiral wave with  $g = 0.05$  (left panel) and with  $g = 0.01$  (middle panel). The dark and light solid lines are cuts at  $\theta = 0, 180^\circ$  respectively. The dotted and dashed lines are temperature structures for a flat passive and flat accretion disk respectively. On the right is the SED of a typical disk with a spiral wave ( $g = 0.05, i = 60^\circ, \alpha = 0^\circ$ ).

The resulting SED for  $g = 0.05$  is shown in Figure 3.8. It rises above the flat passive disk shortward of  $\log \lambda = 1.0$  while longward it drops significantly below the flat passive disk. The short wavelength increase over a flat passive disk is smaller for the spiral disk than for the inner warp because less of the disk is heated up to a high temperature (compare Figure 3.5 and 3.8). The decrease at long wavelengths is much larger because in the outer disk every  $\theta$  is exposed to a wave inside its radius. For the warp only half of the disk is shadowed at one time, while the spiral wave can shadow all of the disk (figure 3.1). Comparing the temperature of the outer convex side of the inner warp disk with the  $\theta = 180^\circ$  spiral wave we can see that the temperature is lower for the spiral wave, which will result in a lower flux at longer wavelengths.

An embedded massive planet within the disk will create a spiral wave (Papaloizou et al., 2007). These waves drive shocks which can substantially increase the scale height of the disk (Boley & Durisen, 2006; Edgar & Quillen, 2008), up to  $\Delta h/r \approx 0.6$  (Boley & Durisen, 2006). The shadow cast by the planet on the outer disk could be imaged in scattered light, but would be difficult to observe in the infrared (Jang-Condell, 2009). The presence of massive planets have often been

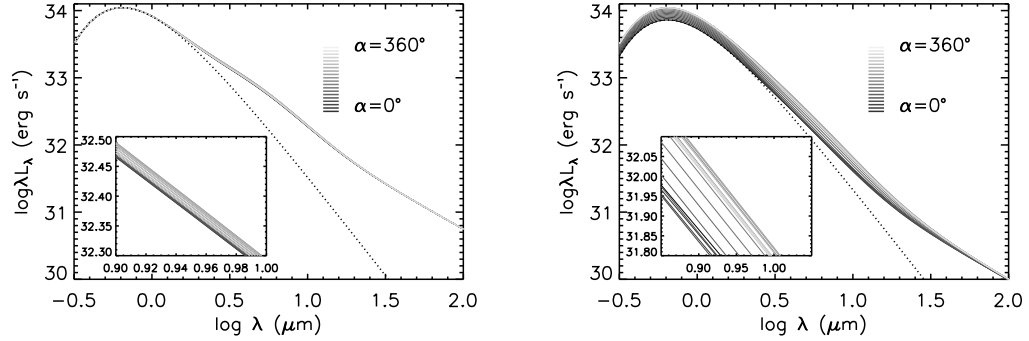


Figure 3.9 SEDs of a precessing spiral wave with  $g = 0.05$  seen at  $i = 60, 85^\circ$  (left and right panels respectively). From dark to light solid lines the disk rotates from  $\alpha = 0^\circ$  to  $\alpha = 360^\circ$ . Viewing the spiral wave from different orientations has a small change on the infrared flux, unless the wave occults the star.

invoked to explain the lack of short-wavelength excess within young circumstellar disks, and spiral waves are a natural extension of this situation. A spiral wave created by a planet embedded in the disk will stay fixed relative to the planet and will travel around the star at the orbital frequency of the planet. For a planet within 0.1 AU of a star this can approach one week, which is much shorter than the precession of the warped disks. We can demonstrate the change in SED as the planet orbits around the star by observing the spiral wave at different azimuthal angles, shown in figure 3.9. The flux changes by  $< 0.05$  dex and the change in the short and long wavelength flux is correlated, when the disk is viewed close to edge on. The small change in flux is due to the spiral wave being closer to an axisymmetric structure than either the middle warp or the inner warp. If the disk is highly inclined then the spiral wave will occult the star and this occultation will dominate the variations in the infrared (right panel of figure 3.9). Here the infrared variations are substantial and strongly dependent on viewing angle, but are mainly due to changing the underlying flux from the star rather than changing the flux from the disk.

Varying the wave height will change the shadowing of the disk and can produce an anti-correlation in flux (Figure 3.10), as in the previous models. In these models ( $g = 0.005 - 0.1$ ,  $h = 0.0006 - 0.013$  AU) we view the disk along  $\alpha = 180^\circ$  in order to directly observe the warmest part of the wave and produce the largest mid-infrared variations. As the wave grows the short-wavelength ( $\lambda < 10\mu\text{m}$ ) flux does not change as much as the inner warp because only a small part of the disk will be heated as it grows. The extra heated part of the spiral disk is confined to the inner edge of the wave, whose position does not change. When the inner warp grows, more of the disk is directly exposed to the star. This means that not only does the temperature at one point rise, but the area of the disk that departs from a flat disk is larger. The spiral disk only has the effect of increasing the temperature at a point, without increasing the area over which the disk is warmer than a flat disk. Beyond  $10\mu\text{m}$  the disk flux drops dramatically with an increase in the height of the wave. This is because all angles  $\theta$  are subject to being shadowed; for the inner warp only  $-90^\circ < \theta < 90^\circ$  will be shadowed. These changes can reach up to  $\sim 0.2\text{dex}$  at  $30\mu\text{m}$ . Changes in the height of the wave may be caused by the nonlinear shock as it passes through the disk (Boley & Durisen, 2006) or it may be caused by localized accretion hot spots heating different portions of the wave, as discussed for the warped disk models.

Our spiral wave model can also be used to simulate other disturbances in a disk that appear as a wave. One such situation is a thermal instability in which a vertical disturbance grows into a wave that slowly travels inward toward the star (Watanabe & Lin, 2008). In accretion disks the temperature and structure of the disk are closely connected since the scale height depends on the disk temperature at a given radius. If the disk is flared, it is more directly illuminated by the stellar radiation field and hence is warmer at a given radius than if it were flat. If a



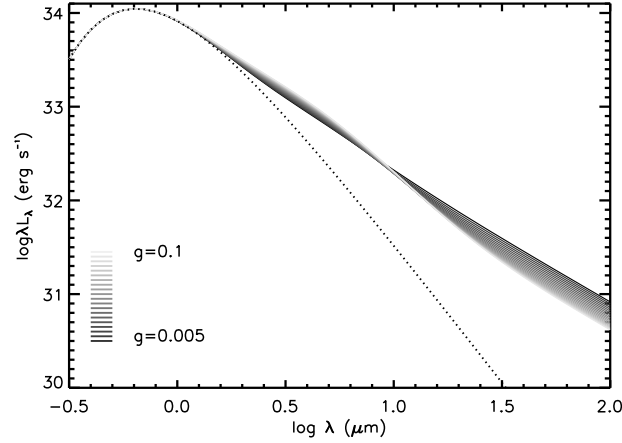


Figure 3.10 SEDs for a growing spiral wave. The disk is viewed at  $i = 60^\circ$ ,  $\alpha = 180^\circ$  and the models vary  $g$  from 0.005 to 0.1. The change in the far-infrared flux is much larger than the change in the mid-infrared flux.

small disturbance raised a piece of the disk above the midplane it would heat up as it became more directly illuminated. The frontside of this disturbance will grow because it is warmer, while behind the disturbance the disk is shadowed and it will shrink. As a result, the disturbance will propagate towards the star as a wave. Watanabe & Lin (2008) find that this type of instability can develop in the outer disk and is long lived enough to travel within a few AU of the star.

We treat the instability as a spiral wave whose radial position and height do not change as a function of  $\theta$  within the disk ( $n = 0$ ,  $m = 0$ ), and compare three locations and heights of the instability ( $r=0.5, 0.4, 0.3$  AU with  $g=0.05, 0.02, 0.01$  respectively) that are typical of thermal instability models (D'Alessio et al., 1999). The results, shown in figure 3.11 have a pivot point in the SED at much longer wavelengths than the other models. At  $>3\mu\text{m}$  the flux change is  $\sim 0.1$  dex until the far-infrared where the flux change can be much larger. In the models with  $g = 0.05, 0.02$  the entire outer disk is shadowed and there is very little change in the far-infrared flux between these models. The flux from the outer disk only

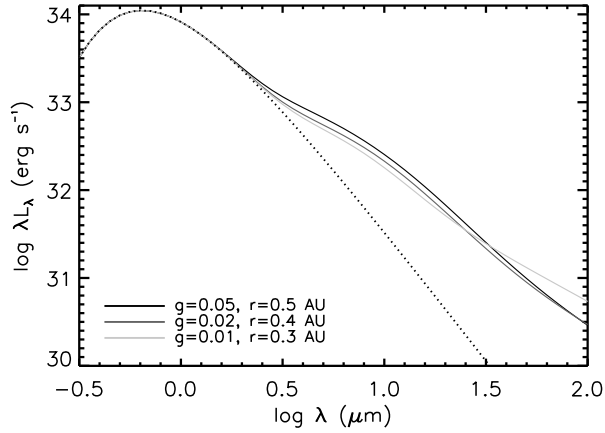


Figure 3.11 SEDs for the thermal instability wave. The three models represent  $g=0.05$  at  $r=0.5$  AU,  $g=0.02$  at  $r=0.4$  AU and  $g=0.01$  at  $r=0.1$  AU from dark to light lines. The photosphere is shown for comparison.

changes for the  $g=0.01$  model where less of the disk is in shadow, which increases its flux. These waves travel inward on a thermal timescale, which is on the order of years.

### 3.3 Comparison to Observations

#### 3.3.1 LRLL 31

Muzerolle et al. (2009) suggested that the mid-infrared variability of LRLL 31 may be due to a non-axisymmetric structure in the inner disk, and with our simple models we can more directly test this hypothesis. The observations of LRLL 31, described in detail by Muzerolle et al. (2009) and summarized here, include multiple epochs with the *Spitzer* IRAC (Fazio et al., 2004), MIPS (Rieke et al., 2004) and IRS (Houck et al., 2004) instruments. Originally identified as variable based on two earlier IRAC and MIPS surveys of the field, it was followed up with further imaging and spectroscopic observations in the fall of 2007 and the spring of 2008. The entire set of data are shown in SED form in Figure 3.12. IRS spectra

taken a week apart (October 9, 16 2007) show that the  $5\text{-}8\mu\text{m}$  flux decreases by 0.2 dex, while the  $12\text{-}40\mu\text{m}$  flux increases by a similar amount. After four months (February 24, 2008) the  $5\text{-}8\mu\text{m}$  flux has risen, with a corresponding decrease in  $12\text{-}40\mu\text{m}$  flux, close to its original state. Another IRS spectra taken a week later (March 2, 2008) show the disk still in its high  $5\text{-}8\mu\text{m}$  state with the same anticorrelated change in the short and long-wavelength flux. IRAC observations taken from the GTO (Lada et al., 2006) and C2D (Jørgensen, et al., 2006) surveys (February 11, 2004 and September 8, 2004 respectively) also show substantial changes consistent with the IRS spectra. The MIPS  $24\mu\text{m}$  measurements include observations from the original GTO and C2D (Rebull et al., 2007) maps (February 21, 2004 and September 19, 2004 respectively), as well as more intensive observations from our GO program (PID 40372). The MIPS followup includes five consecutive days (September, 23-27, 2007) and two further maps the following spring (March 12, 19, 2008). The  $24\mu\text{m}$  fluxes change by a few tenths of a magnitude on weekly to monthly timescales. The uncertainty in the infrared observations is  $< 5\%$  while the changes range from 20-60% suggesting that the variations being observed are real. In Figure 3.12 the October 9, 2007 spectra is shown with error bars to demonstrate the typical uncertainty in the spectra, which is smaller than the observed flux changes. A more detailed description of the data reduction, as well as the uncertainties in the data, is presented in Muzerolle et al. (2009). All of our observations show variations at all timescales over the entire observed wavelength range.

The low  $5\text{-}8\mu\text{m}$  flux seen in the October 16, 2007 observation is difficult to explain with the standard axisymmetric puffed inner rim model. In that case, the amount of dust emission is set by the scale height, which in turn depends on the stellar plus accretion luminosity. In the limit of low  $L_{acc}$  and/or high  $L_*$ , as is

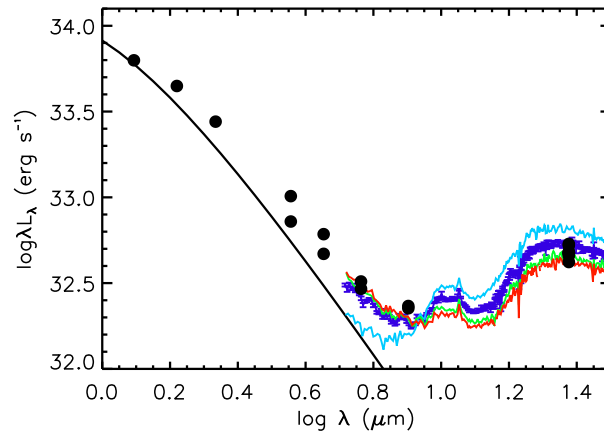


Figure 3.12 Observations of LRL 31. Black circles are the photometry from 2MASS, two epochs of IRAC photometry and 10 epochs of MIPS  $24\mu\text{m}$  photometry. Colored lines are the four IRS spectra of LRL 31. The dark blue and light blue were taken in October 2007 and were separated by one week. The green and red spectra were taken in February/March 2008 and were separated by one week. Substantial variability is seen throughout the mid-infrared. Error bars on the dark blue spectra show the uncertainty in the spectra, which are similar to the uncertainties in the other spectra, and are smaller than the variability in the flux. The dark solid line is a 5700 K blackbody representing the stellar photosphere for comparison, and the observations have been scaled to match the photospheric luminosity at J band, assuming the J band flux is completely photospheric.

the case for LRL 31, the irradiation of the inner rim cannot change significantly, and its emission should always be considerably in excess of the photospheric level. Disk models with large scale asymmetries such as warps or spiral waves, coupled with highly inclined viewing angles, offer a way around the problem.

We take LRL 31 to be a G6 star, based on NIR spectra (Muzerolle et al., 2009), with a radius of  $2.9R_{\odot}$  and a mass of  $1.8M_{\odot}$  derived using the Siess et al. (2000) isochrones. It has high polarization and its extinction is roughly  $A_V = 10$ . When presenting the observations below, all of the data have been dereddened by  $A_V = 10$ . Dahm (2008) find the accretion rate in the range  $10^{-8} - 10^{-7} M_{\odot} \text{yr}^{-1}$  based on optical veiling and various emission line diagnostics. The inclination of the disk has not been directly measured, but given the high extinction and high polarization, which are signs that some of the light passes through the disk, we focus on inclinations close to edge on.

Given the modeling results presented earlier, we focus on changing the height of the warp/wave. The middle warp, inner warp and spiral wave all produced a wavelength dependence similar to LRL 31, where the short-wavelength flux would increase while the long-wavelength flux would decrease due to the shadowing of the outer disk. Figures 3.13, 3.14 and 3.15 show the middle warp, inner warp and spiral wave close to edge on with varying heights along with the observations of LRL 31. An inclination of  $i=85^{\circ}$  was chosen for these three models, while different values of  $\alpha$  were chosen to maximize the flux change. The middle warp displays a similar wavelength dependence as the observations, but is unable to match the size of the variations at  $3.6, 4.5 \mu\text{m}$ . Also the location of the pivot in the SEDs is at a longer wavelength than observed. The inner warp does a better job of fitting the size of the variation as well as the slope of the IRAC and short-wavelength IRS data. For the inner warp we consider two inclinations that

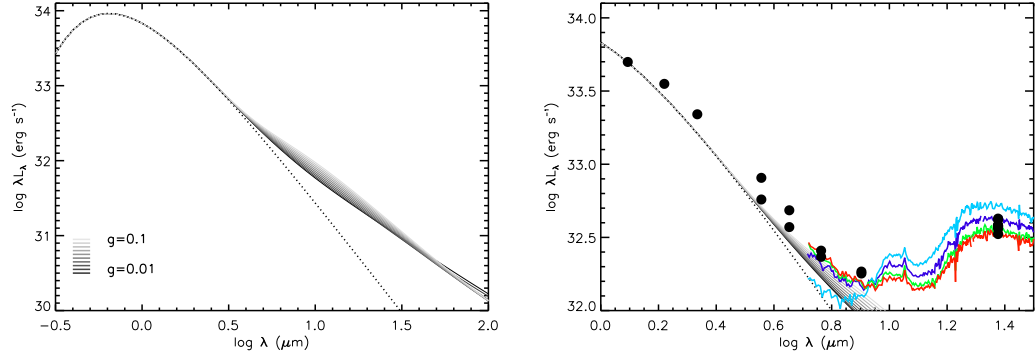


Figure 3.13 SEDs for a growing middle warp ( $g = 0.01 - 0.1$  from dark to light lines) viewed at  $i = 85^\circ, \alpha = 180^\circ$ . On the left is the entire model, while on the right is a close-up of the model with the observations. The observations have been scaled to match the J band flux of the model, assuming the J band observation is completely photospheric.

are both close to edge-on but produce different SEDs. The difference in the two edge-on inclinations comes in the optical where the  $i=85^\circ$  disk occults the star while the  $i=95^\circ$  disk does not. This model also shows a pivot point in the SED, but it is also at a longer wavelength than observed. For the spiral wave model the pivot point moves to a wavelength that is close to  $8\mu\text{m}$  but the short wavelength flux variation is too small to match the observations, in particular the  $3.6, 4.5\mu\text{m}$  photometry and the spectra with the lowest  $5-8\mu\text{m}$  flux. The timescale for the warp to change height, which is the dynamical timescale, approaches one week at 0.1 AU around LRL 31. This is short enough to match the rapid variations seen in the mid-infrared. We do not consider the thermal instability because the timescale is much longer than one week.

Based on our simple models, we find that a disk with an inner warp whose height rapidly varies is able to best explain the observations of LRL 31. It can fit the flux change at  $\lambda < 8\mu\text{m}$ , it includes a pivot point in the SED, and the timescale is consistent with the observations, but the simplicity of the model pre-

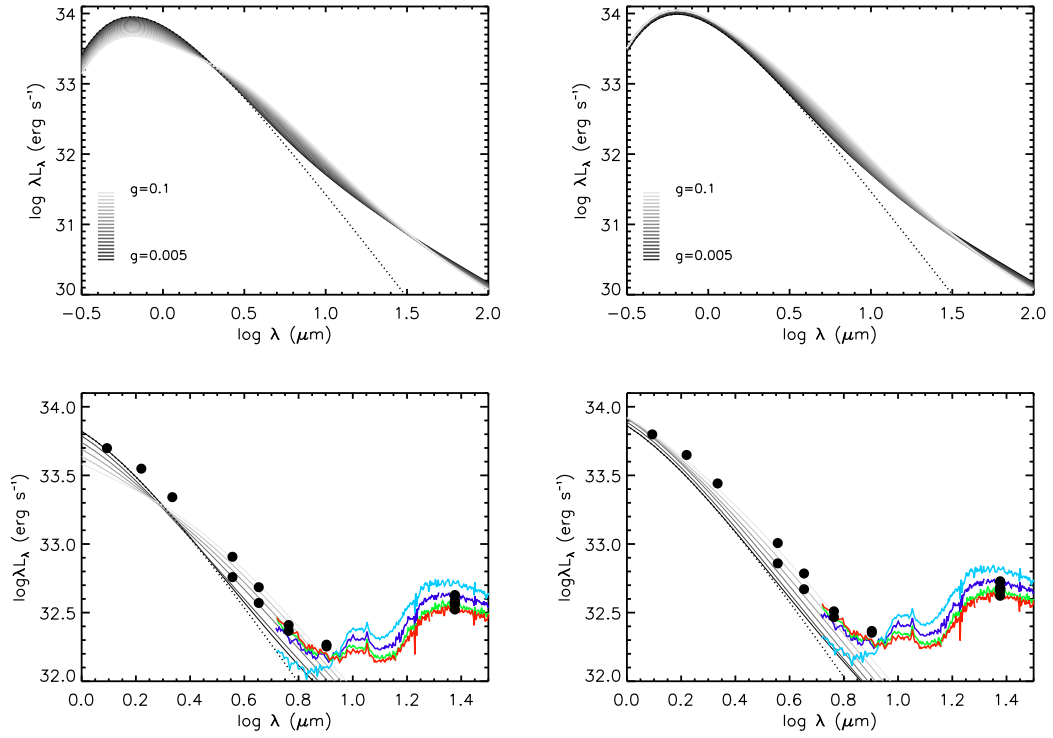


Figure 3.14 SEDs of LRL 31 with a growing inner warp. The models vary  $g$  from 0.005 to 0.1 (from dark to light lines). The models on the left are seen at an inclination of  $i = 85^\circ$ , while on the right are the models seen at  $i = 95^\circ$ . The top panels show the entire models while the bottom panels zoom in and include the observations. Only models for  $g = 0.005, 0.02, 0.04, 0.06, 0.08, 0.1$  are shown for clarity. The observations have been scaled to match the J band flux of the model, assuming the J band observation is completely photospheric.

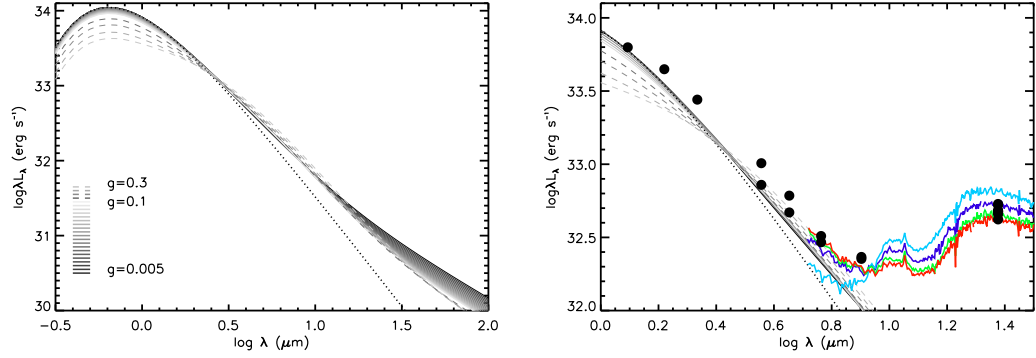


Figure 3.15 SEDs for a growing spiral wave around LRL 31. The disk is viewed at  $i = 85^\circ$ ,  $\alpha = 180^\circ$ . The models vary  $g$  from 0.005 to 0.1. The dashed lines are models with  $g = 0.15, 0.2, 0.25, 0.3$ , larger than previously used for the inner warp. On the right is a close up of the observations along with the models for  $g = 0.005, 0.02, 0.04, 0.06, 0.08, 0.1, 0.15, 0.2, 0.25, 0.3$ . The observations have been scaled so that the J band flux matches the models, assuming the J band observation is completely photospheric.

vents it from fitting in detail. More detailed radiative transfer models would help to further constrain the shape of the perturbation. Future work should also tie these parametric models to specific physical mechanisms in order to provide predictions for the detailed time-dependent behavior of the flux changes.

### 3.3.2 Application to Other Variables

In the previous models we considered a star whose mass was on the high end for a typical T Tauri star and a lower mass star with a lower effective temperature will not heat the disk to as high of a temperature at the same distance from the star, which will result in a weaker excess for a given value of  $h/r$ . As the disk precesses, only the orientation of the disk relative to the observer changes, which does not depend on the central star or the temperature at a particular location within the disk. The change in infrared excess with precession will then be similar over a wide range of masses. The same is true if we vary the scale height of the disk. In figure 3.16 we show an inner warp seen at  $i = 60^\circ$  around LRL 31, a typ-



ical T Tauri star ( $T_{eff}=4000$  K,  $M_*=1M_\odot$ ,  $R_*=2R_\odot$ ,  $\dot{M}=5*10^{-9}M_\odot yr^{-1}$ ,  $R_{min}=8R_*$ ) and a brown dwarf ( $T_{eff}=3000$  K,  $M_*=0.08M_\odot$ ,  $R_*=0.7R_\odot$ ,  $\dot{M}=10^{-9}M_\odot yr^{-1}$ ,  $R_{min}=8R_*$ ) with a height varying from  $g=0.01-0.1$ . The accretion rates were chosen to decrease with mass, but they only contribute significantly to the heating of the outer disk where our assumption of a flat disk severely underestimates the flux from typical disks. The change in the mid-infrared flux around all three stars is almost identical. While the exact structure and temperature of these three disks differs, as the mass decreases the temperature of the disk decreases and the physical distance between the disk and the star is smaller, the change in the warp is the same resulting in similar variations in the infrared flux. Changing from an inner warp to a middle warp or a spiral wave will also show a similar lack of dependence on the central source as the height of the warp/wave varies. If the structural change in the inner disk does not depend on the mass of the central star then such a change in the disk structure would be easily detectable in the near and mid infrared flux from many young stellar objects.

Since changing the spectral type of the central star does not have a significant effect on the infrared variability presented here, these models can provide insight into other variable objects. Morales-Calderón et al. (2009) use IRAC to survey 3-8 $\mu$ m variability among young stellar objects within IC 1396A. They find that variability occurs in more than half of the young stellar objects, typically showing colorless variations with amplitudes of 0.05-0.2 magnitudes on timescales of a few days to a week. This is consistent with our models of a growing inner warp, which when the warp does not occult the star, can produce large variations in flux without a large change in the color in this wavelength range. Hutchinson et al. (1994) find two stars whose BVRI fluxes and 4.5,10 $\mu$ m fluxes vary in opposite directions while the near-infrared fluxes stay constant. Juhász et al. (2007) find

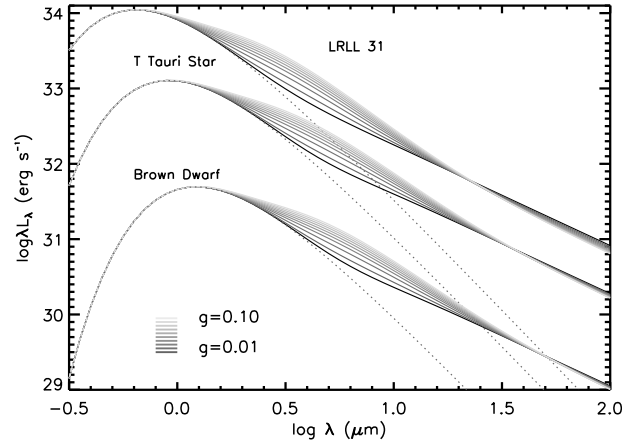


Figure 3.16 SEDs for an inner warp surrounding LRL 31, a typical T Tauri star and a brown dwarf seen at  $i = 60^\circ$ . For each star the models vary  $g$  from 0.01 to 0.1 (dark to light grey solid lines) and the stellar photosphere is shown with the dotted line. The change in mid-infrared flux does not depend strongly on the central star.

similar results for SV Cep where the V band and  $3.6\mu\text{m}$  flux are anti-correlated. They also find that the V band and  $100\mu\text{m}$  flux are correlated with each other, while there is very little change in the flux at  $25\mu\text{m}$ . This is qualitatively similar to our model of a growing inner warp seen at  $i = 85^\circ$  (Figure 3.14). As the warp grows the star becomes blocked, dropping the optical flux, and more of the outer disk is shadowed, dropping the long wavelength flux, producing a correlation between the optical and  $100\mu\text{m}$  flux. Also the larger warp emits more flux in the mid-infrared, producing an anti-correlation between the optical and  $3\text{--}10\mu\text{m}$  flux, while the near-infrared bands stay roughly constant.

UX Ori stars are a type of optical variable that exhibit occasional dimming and reddening of their optical colors due to occultations of the star by clumps of gas and dust. These clumps are thought to arise from the inner edge of the circumstellar disk, which can occult the star since the system is seen very close to edge on (Dullemond et al., 2003). In some models of the infrared excess from

these stars it has been assumed that the disturbance at the inner edge does not cover enough area to substantially shadow the disk (Pontoppidan et al., 2007). Our models show that there can be significant mid-infrared variations even if the perturbations at the inner edge of the disk do not shadow the entire disk.

Ongoing studies of mid-infrared variability will help to determine how common this type of variability is among young stellar objects. Multiple programs in progress gathering multi-epoch Spitzer data at 3.6 and  $4.5\mu\text{m}$  will constrain the frequency of mid-infrared variability among T Tauri stars. Given the wavelength coverage of these variability studies, and the expected mid-infrared variability due to non-axisymmetric variations in the inner disk, any changes in the structure of the inner disk will be readily observable. Using these observations to look for periodicity, which is a sign of a perturbing companion, or a correlation with accretion rate will help to constrain the physical processes that influence the inner structure of circumstellar disks.

### 3.4 Conclusions

We have used simple geometric models to investigate the effects of non-axisymmetric structure in a circumstellar disk on the system's SED. By simplifying the models we have been able to investigate a wide range of geometries including a warp in the middle of the disk, a warp at the inner edge of the disk and a spiral wave. These models show an anticorrelation between the flux at short and long wavelengths because of variable shadowing of the outer disk, in qualitative agreement with many observations. However, precession or corotation of these structures produces a negligible change in the infrared excess amplitude. Only by changing the scale height of the perturbations, as may be produced by the dynamical interactions or variable illumination of disk structures, do we find significant flux

variations as observed. Further observations spanning a range of timescales and covering multiple objects will help to discriminate between models as well as indicate the frequency of such structural variations. The similarity in the size of the infrared variations across a wide range of masses also indicates that the type of non-axisymmetric variability explored here would be detectable around many young stellar objects. Numerous observations of mid-infrared variability around young stellar objects are consistent with our models.

## CHAPTER 4

THE HIGHLY DYNAMIC BEHAVIOR OF THE INNERMOST DUST AND GAS IN THE  
TRANSITION DISK VARIABLE LRL 31

We describe extensive synoptic multi-wavelength observations of the transition disk LRL 31 in the young cluster IC 348. We combined four epochs of IRS spectra, nine epochs of MIPS photometry, seven epochs of cold-mission IRAC photometry and 36 epochs of warm-mission IRAC photometry along with multi-epoch near-infrared spectra, optical spectra and polarimetry to explore the nature of the rapid variability of this object. We find that the inner disk, as traced by the  $2\text{--}5\mu\text{m}$  excess stays at the dust sublimation radius while the strength of the excess changes by a factor of 8 on weekly timescales, and the  $3.6$  and  $4.5\mu\text{m}$  photometry show a drop of 0.35 magnitudes in one week followed by a slow 0.5 magnitude increase over the next three weeks. The accretion rate, as measured by  $\text{Pa}\beta$  and  $\text{Br}\gamma$  emission lines, varies by a factor of five with evidence for a correlation between the accretion rate and the infrared excess. While the gas and dust in the inner disk are fluctuating the central star stays relatively static. Our observations allow us to put constraints on the physical mechanism responsible for the variability. The variable accretion, and wind, are unlikely to be causes of the variability, but are both effects of the same physical process that disturbs the disk. The lack of periodicity in our infrared monitoring indicates that it is unlikely that there is a companion within  $\sim 0.4$  AU that is perturbing the disk. The most likely explanation is either a companion beyond  $\sim 0.4$  AU or a dynamic interface between the stellar magnetic field and the disk leading to a variable scale height and/or warping of the inner disk.

## 4.1 Introduction

The widely accepted view is that a pre-main sequence star slowly evolves from a deeply embedded core to a fully revealed star. After initial collapse of a dense core, the star enters the class 0/I phase in which it is rapidly accreting mass from its massive envelope and disk. As the envelope dissipates and the accretion rate decreases, the star enters the class II phase where it becomes optically revealed and is being fed slowly by a viscously-evolving irradiated accretion disk. The dust in the disk eventually coalesces into large grains and the gas dissipates from the system leaving a class III star.

Confounding this picture of slow evolution, there is growing evidence that these systems are in fact highly dynamic. It has been known since the discovery of T Tauri stars, which are at the heart of class II systems, that the star is usually variable (Joy, 1945). Hot and cold spots rotating across the surface of the star, as well as variable accretion onto the star can create changes of a magnitude or more in only a few days in the optical (e.g. Herbst et al., 1994). Recent observations have shown that the circumstellar disk, as traced by the infrared emission, can also change dramatically in only a few days. The shape of the disk continuum appears to change (Morales-Calderón et al., 2009; Juhász et al., 2007; Muzerolle et al., 2009) and the silicate feature, which traces the properties of the dust in the upper layers of the disk close to the star, also varies rapidly (Bary, Leisenring, & Skrutskie, 2009; Sitko et al., 2008; Skemer et al., 2010). The behavior may be related to large structural changes in the inner disk (Sitko et al., 2008), large accretion events, such as in FU Ori outbursts (Hartmann & Kenyon, 1996) or to turbulence within the disk (Turner et al., 2010). The previous studies provide some insight into the source of the variability, but are limited by the lack of ancillary data and limited temporal or wavelength coverage.

To understand better what could be causing these changes, we have studied one object, the highly variable star LRL 31, in detail. This object shows dramatic mid-infrared variability (Muzerolle et al., 2009) that may be due to a non-axisymmetric structure in the inner disk with a changing scale height (Flaherty & Muzerolle, 2010). We report continued monitoring in the mid-infrared, as well as multiple epochs of near-infrared spectra, optical spectra and polarimetry measurements to understand the dynamics of the system better. Using these observations, we study the changes in the dust, the gas and the central star, and any connections among them. The near simultaneity of these data sets allow us to rule out specific mechanisms that might be responsible for the observed variability.

## 4.2 Data

Our monitoring of LRL 31 consists of multiple epochs of ground and space based observations covering the optical as well as the near and mid-infrared. We obtained 0.8-5 $\mu$ m spectra with the SpeX instrument (Rayner et al., 2003) on the NASA Infrared Telescope Facility (IRTF) in fall 2008 and 2009. Table 4.1 lists the observing log for all of our observations, and the spectra are shown in Figures 4.1 and 4.2. On all but two nights we used both the SXD (0.8-2.2 $\mu$ m) and LXD2.1 (2-4.8 $\mu$ m) gratings, while on October 8,9 2009 we only obtained SXD spectra. On Oct 10,18,19 2008 we used the 0.5"x15" slit ( $R \sim 1500$ ) while on the other nights we used the 0.8"x15" ( $R \sim 800$ ) slit due to poorer seeing conditions. We also supplement our observations with SXD spectra taken in 2005 (Muzerolle et al., 2009) and 2006 (Dahm, 2008). The data were reduced using Spextool (Cushing et al., 2004) and corrected for telluric absorption using *xtellcor* (Vacca et al., 2003). Our telluric standards were the nearby A0V stars HD 19600 and HD 23441. The total

exposure times were 30 minutes for the SXD and one hour for the LXD spectra. A set of calibration exposures, including flat field and argon arc spectra, were obtained for each target-standard star pair.

We also observed the bright weak line T Tauri star (WTTS) HD 283572, which shows no sign of accretion or an infrared excess, with an exposure time of 10 minutes. It has the same spectral type (G6) as LRLL 31 and is used as a comparison star when measuring the veiling and strength of the emission lines. We took SXD spectra of this star with a slit of  $0.8'' \times 15''$  on 5 Jan 2010. The spectra were reduced in the same manner as the LRLL 31 spectra using the telluric standard HD 25152.

In addition to the spectra taken by Spex, we also obtained JHK photometry (Table 4.2) from the slit-viewing near-infrared guide camera. LRLL 31 was observed with three dithers, standard reduction techniques were used and aperture photometry was performed on the two stars in the field of view. We did not observe any photometric standards, but instead derived the photometry of LRLL 31 relative to the other star in the field (LRLL 169, 2MASS03441776+3204476). This allows us to derive accurate relative photometry, but there could be large uncertainties in the absolute photometry. LRLL 169 is a diskless cluster member and is not marked as variable ( $\sigma=0.06$  mag) in the optical monitoring of Cohen et al. (2004). Our Spitzer warm mission photometry (described below) of LRLL 169 shows variations of 1-2% at 3.6 and  $4.5\mu\text{m}$  which is consistent with the uncertainty in the photometry. This suggests that the photometric variability is no more than a few percent, which is smaller than the absolute uncertainty (0.1 mag) associated with using only one standard and we ignore it.

We also include high-resolution  $\text{H}\alpha$  spectra from Keck (kindly provided by Scott Dahm) and from the MMT. The MMT spectrum was taken with Hectochelle (Szentgyorgyi et al., 1998) in 29 Feb 2008 with a resolving power of  $R \sim 30,000$ .



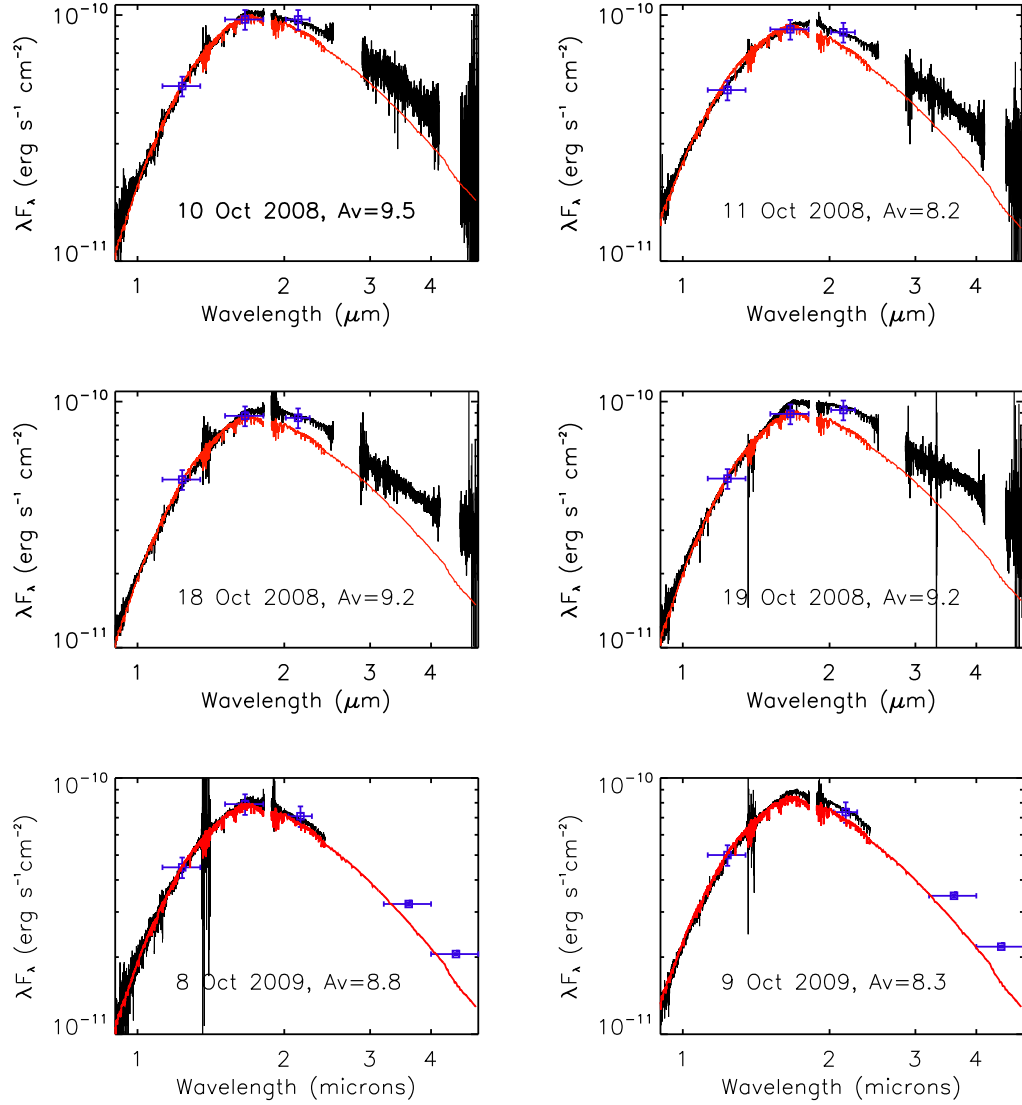


Figure 4.1 Observed 0.8-5 $\mu$ m spectra of LRL 31 (black). Also included are simultaneous JHK and 3.6,4.5 $\mu$ m photometry (blue), when available. The spectra are compared to the standard with our best fit reddening (red spectra). All spectra have been scaled to match the near-infrared photometry, except the 2005 and 2006 spectra for which we do not have contemporaneous photometry and have not been flux calibrated. For the photometric points the 'error bars' in the x-axis show the size of the passband.

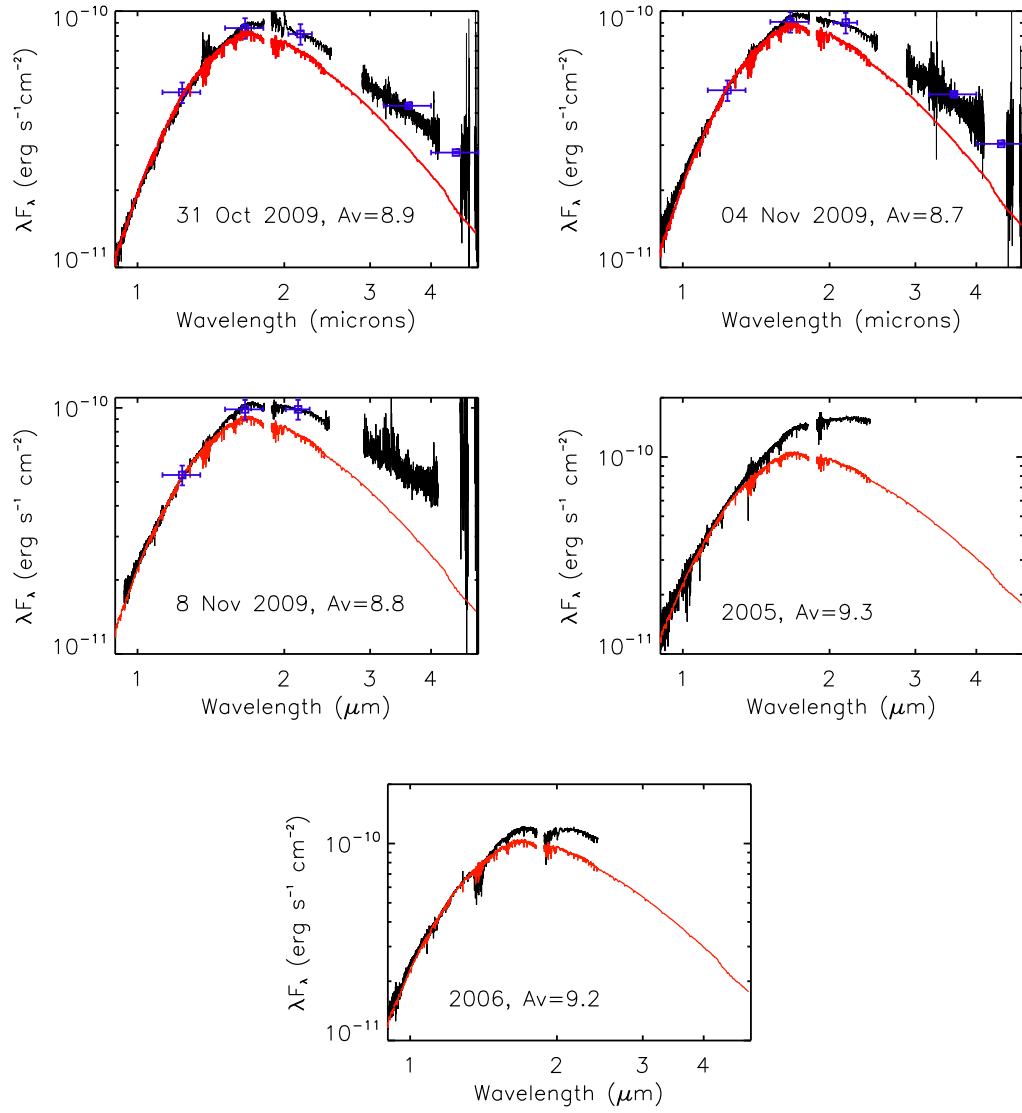


Figure 4.2 Fig 4.1 continued. Curved shape of the H and K band near 1.8  $\mu$ m in 2006, which is not seen in the other spectra, is a sign of imperfect telluric correction.

The Keck spectra were taken with HIRES (Vogt et al., 1994) on 28 Nov 2006 and 03 Dec 2008 with a resolving power of  $R \sim 33,000$ . Observing details for the MMT spectra are reported in Flaherty & Muzerolle (2008) while the reduction process for the Keck spectra is reported in Dahm (2008).

We include spectro-polarimetric observations taken on several nights using the SPOL imaging/spectropolarimeter (Schmidt et al., 1992) on the Steward Observatory 2.3 m telescope. These low-resolution optical spectra, shown in Figure 4.3, extend from 4000-7500 Å, and from them we can extract the strength of the H $\alpha$  line as well as the shape of the continuum, which is useful for measuring the reddening toward the source. Details on the observational mode and the data reduction can be found in Smith et al. (2003). An intermediate resolution optical spectrum of LRL 31 was obtained on 2009 October 11 using the CAFOS instrument on the 2.2-m telescope of the Calar Alto Observatory. The exposure time was 1880s. The R-100 grism covered the wavelength range 5800-9000 Å. The resolving power, using a 1.5-arcsec slit, was  $R \sim 3500$  at 6600 Å. We observed the spectrum of a He-Ne-Rb lamp for wavelength calibration. The spectrum was reduced using standard IRAF routines.

We have observed LRL 31 on multiple epochs with all three instruments on-board the Spitzer Space Telescope. IRS (Houck et al., 2004) data were originally obtained on 09 Oct 2007, 16 Oct 2007, 24 Feb 2008 and 02 Mar 2008 and these spectra were presented in Muzerolle et al. (2009). The IRS data reduction pipeline has been improved and the updated spectra are presented here. The spectra were extracted using the Spectroscopic Modeling, Analysis and Reduction Tool (SMART; Higdon et al. (2004)) version 8.1.2, starting with the basic calibrated data products from the Spitzer Science Center reduction pipeline version S18.7. Rogue pixels were first removed using the "IRS\_CLEAN" program, constructing a pixel mask

for each of the SL and LL modes using off-order images as a reference. SMART was then used with optimal manual point source extraction using local sky subtraction. The local sky background was calculated by fitting a polynomial to all sky pixels on either side of the source at each row in the spatial direction. The final calibrated spectra for each nod and order were then combined using the sigma-clipped averaging function in SMART; typical measurement uncertainties were about 2% at most wavelengths.

IRAC (Fazio et al., 2004) observations were taken during the cryo-mission, when all four channels were available, on 19-23 March 2009 (PID 50596) (Table 4.3) along with the original GTO (Lada et al., 2006) and C2D (Jørgensen, et al., 2006) data taken on 11 Feb 2004 and 08 Sep 2004. A warm-mission observing program (PID 60160) obtained repeated  $3.6, 4.5\mu\text{m}$  photometry at a varying cadence with observations ranging from every four hours to every other day over most of the 40 day visibility window of IC 348 (Table 4.11). The IRAC data reduction pipeline is described in Gutermuth et al. (2009) with updates appropriate for the warm Spitzer mission described in Gutermuth et al. (in prep). MIPS (Rieke et al., 2004) observations were taken on 21 Feb 2004 (Lada et al., 2006), 19 Sep 2004 (Rebull et al., 2007) and 24-27 Sep 2007, 12 Mar 2008, 19 Mar 2008 (Muzerolle et al., 2009). Details on the reduction of the MIPS data are in Muzerolle et al. (2009). Information on all of these observations is included in Table 4.1.

### 4.3 Evidence for Fluctuating Gas and Dust Properties

#### 4.3.1 Stellar Properties

The stellar luminosity can be derived from the J band assuming it is dominated by stellar flux, as demonstrated in Figure 4.1, once it has been dereddened. We use the shapes of both the near-infrared and spectro-polarimetry spectra to mea-

sure the reddening of LRL 31. The spectra can be dereddened until their shapes match that of a standard of the same spectral type. We ignore the K band spectrum since it could be modified by emission from dust, rather than just extinction. We use the  $R_V=5.5$  extinction law from Weingartner & Draine (2001) in both the optical and near-infrared, which is more appropriate for a star embedded in a molecular cloud than  $R_V=3.1$ , and provides a good fit in comparing LRL 31 and the standard. For our standard we use the SpeX spectrum of HD 283572 in the near-infrared, and in the optical we used a Kurucz model ( $T_{\text{eff}}=5750$ ,  $\log g=2.5$ ) (Castelli & Kurucz, 2004). The results are listed in Table 4.4. Since the shapes of the standard and the spectral do not match perfectly due to effects such as imperfect telluric correction and scattered light within the instrument, there is a 0.5 mag uncertainty in the best fit extinction. We find that on average the extinction is  $A_V \sim 8.8$ . This is lower than previous estimates (Muzerolle et al., 2009) because of our use of a different extinction law, which will convert the same amount of reddening to a smaller value of  $A_V$ . Occasionally the extinction appears to drop down to  $A_V \sim 8.2$ , but these values are consistent with the average given the large error bars. Figures 4.1 and 4.2 show the observed near-infrared spectra compared with a reddened standard along with the observed JHK photometry and simultaneous 3.6, 4.5  $\mu\text{m}$  photometry where available. The agreement between the shape of the spectra and the photometry suggests that we are accurately measuring the shape of the SED. Figure 4.3 shows the optical spectra along with a reddened standard. Using the optical spectra we derive extinctions that are consistent with the near-infrared, including occasional apparent drops in  $A_V$ .

The reddening is combined with the J band photometry, a bolometric correction from Kenyon & Hartmann (1995) and a distance of 320 pc (Luhman et al., 2003) to produce the stellar luminosity, which is listed in Table 4.5. The uncer-

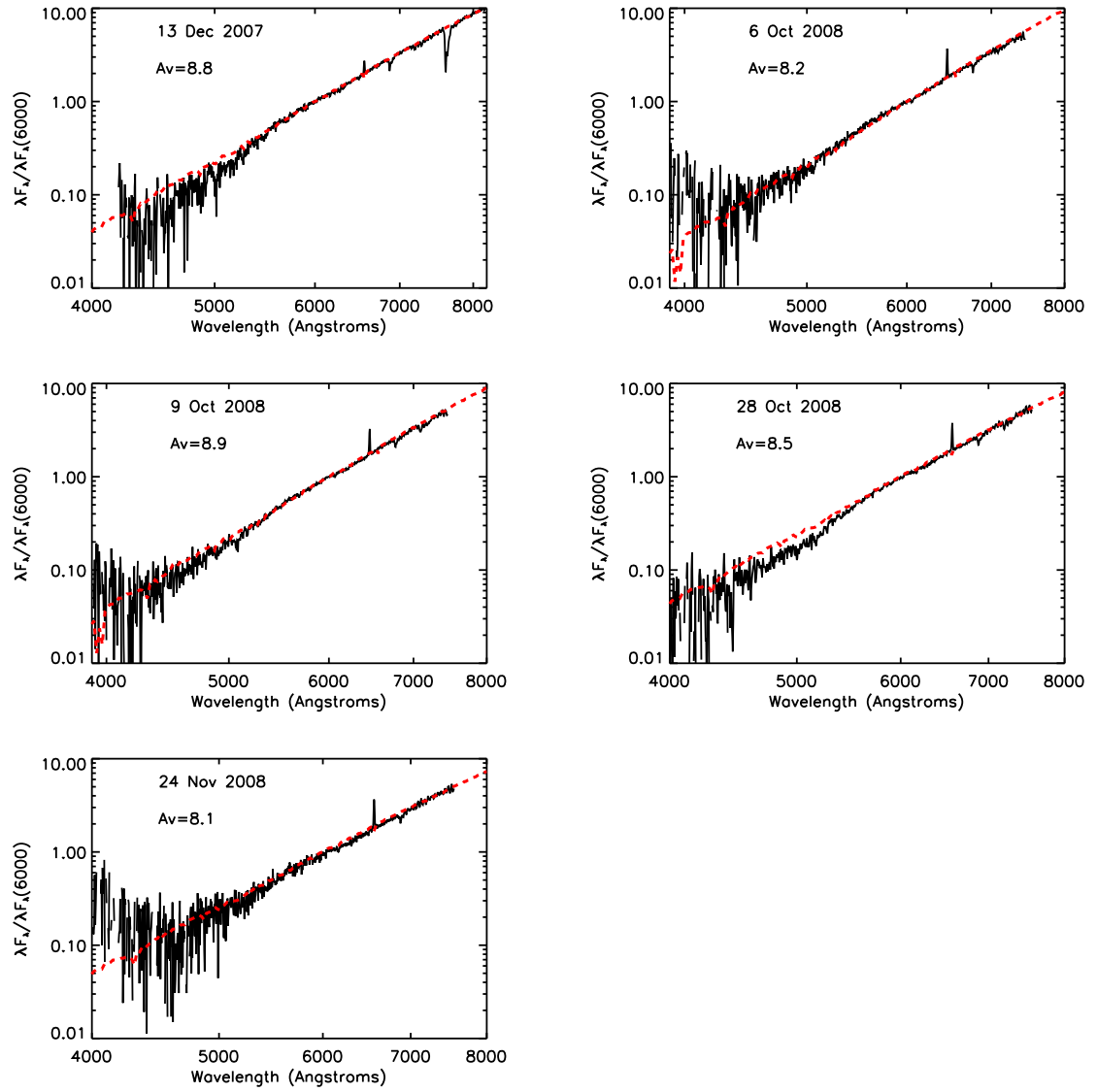


Figure 4.3 Optical spectra of LRL 31 normalized at 6000 Å. Red dashed line shows a reddened kurucz model that best matches the shape of the spectra.

tainties are due to the errors in the photometry and the extinction and are typically  $0.6L_{\odot}$ . There is a range of luminosities, but given the error bars they are consistent with a constant luminosity of  $4.3L_{\odot}$ . This luminosity corresponds to a radius of  $2.1R_{\odot}$  given a G6 ( $T_{eff}=5700$ ) spectral type. If the low values of luminosity represent a real deviation from the mean, they may illustrate moments where the star is partially obscured by dust that is not taken into account in our estimate of the extinction. Overall the star appears to be underluminous relative to a G6 star at the age of IC 348 (2-3 Myr), based on the Siess et al. (2000) isochrones, although it is roughly consistent with the 3 Myr isochrone of Palla & Stahler (1999) which Luhman et al. (2003) finds is more appropriate for the high mass members of IC 348. Based on the Siess et al. (2000) isochrones and the observed luminosity, LRL 31 is roughly  $1.5 M_{\odot}$ .

Recent monitoring in I-band (Baliber et al. in prep) shows small variations of  $\sim 3\%$  with a period of 3.4 days, which are consistent with the rotation of cool spots across the stellar surface suggesting that 3.4 days is the rotation period of the star. Despite the frequent monitoring of IC 348, this periodicity has not been observed (Cohen et al., 2004; Littlefair et al., 2005; Cieza & Baliber, 2006; Nordhagen et al., 2006). These previous observations were taken in 1998-2004 and found  $I=15.24$  (Cohen et al., 2004) and  $I=15.36$  with occasional dips down to  $I=15.5$  (see star 0130 in Figure 4 of Littlefair et al., 2005), while the most recent observations measured  $I=15.82$  for LRL 31. The near-infrared photometry shows a long term decrease from the 2MASS data (operated from 1997-2001) to our measurements in 2008 and 2009. This suggests that there may be a long term decrease in the stellar flux. Continued optical monitoring of this star will be useful in confirming the periodicity and dimming of LRL 31.

Our J-band photometry does not show a large change in the stellar flux, and

some of the optical monitoring by Baliber et al. overlaps the first week of our Spitzer warm-mission monitoring and does not show a substantial decrease in the optical flux, which leads us to assume that the stellar flux is constant during our infrared monitoring. With the period information and the  $v \sin i$  measurement from Dahm (2008) we can estimate the inclination of this star to be  $i = 38 \pm 7^\circ$ , which includes both the uncertainty in the  $v \sin i$  measurement and the radius as derived from the luminosity. This is the inclination to the stellar rotation axis, and it is possible for the stellar magnetosphere and the disk to be misaligned with this axis.

We find a change in the radial velocity based on three epochs of high resolution optical spectra. On 28 Nov 2006 the radial velocity was  $12.82 \pm 0.42$  km/sec, on 29 Feb 2008 it was  $8.36 \pm 0.27$  km/sec and on 03 Dec 2008 it was  $15.7 \pm 1.0$  km/sec. These changes could be due to the influence of a companion, or partial obscuration of the surface by cool spots or circumstellar material. If part of the stellar surface, such as the side rotating toward us, is partially blocked then the radial velocity will appear to become red-shifted. As the obscuring material rotates around the star the apparent radial velocity will change. The rotation of a spot across the surface of the star has been suggested to explain the radial velocity variations in AA Tau (Bouvier et al., 2007a) and the transitional disk T Cha (Schisano et al., 2009). The rotational velocity of LRL 31 has been measured to be 19.8 km/sec (Dahm, 2008), which is consistent with the observed radial velocity variation, although the size of the spot required to produce such large radial velocity variations is bigger than typically seen around G-type stars. A change in the shape of the bisector of the cross correlation function used to derive the radial velocity would indicate the presence of an obscuring source rotating in front of the star, but we do not have the signal to noise to test this theory. A clump of



obscuring material, either in the disk or in the molecular cloud, would need to block almost half of the star in order to create the observed radial velocity variation. This would produce a drop in the optical flux of 0.75 mag, along with a substantial increase in the extinction, neither of which are observed. If these radial velocity measurements are confirmed then the most likely explanation is the presence of a companion somewhere in the system, although this does not prove that the companion is responsible for the observed infrared variability. In section 4.4.3 we place constraints on the mass and location of such a companion using the available data, although more radial velocity measurements are needed to confirm and fully characterize this companion.

#### 4.3.2 Dust Properties

LRL 31 was originally singled out based on its mid-infrared variability (Muzerolle et al., 2009). In IRS spectra separated by one week the 5-8 $\mu$ m flux dropped almost to the photosphere while the 8-40 $\mu$ m flux increased. This behavior was unique and difficult to explain given typical sources of variability, such as the rotation of hot/cold spots across the surface of the star or extinction events. Modeling finds that the wavelength dependence, and timescale, of the variability is consistent with fluctuations in the scale height of the inner disk on a dynamical timescales, which is on the order of one week (Flaherty & Muzerolle, 2010). As the inner disk grows it increases the short wavelength flux, while at the same time shadowing the outer disk, decreasing the long wavelength flux. The previous observations of the continuum emission were limited to probing material far from the star, at 1-10 AU, which may not be the source of the variability. The silicate emission may arise from closer to the star (e.g. Kessler-Silacci et al., 2007), but this location is difficult to constrain without detailed radiative transfer models, especially given the transition disk nature of LRL 31

Our  $3\text{-}5\mu\text{m}$  spectra give us information on the dust close to the star. By subtracting the stellar photosphere from the spectra we are left with only the emission from the dust. When the dust at the inner edge of the disk is optically thick, the emission should appear as a single temperature blackbody at the dust destruction temperature (Muzerolle et al., 2003; Espaillat et al., 2010). The shape of the excess spectra will tell us the temperature of the hot dust which translates to the location of the inner edge of the dusty disk. To subtract the photosphere we must first normalize the standard to the LRL 31 stellar component. We use the veiling at  $2.15\mu\text{m}$  to separate the stellar and excess emission of LRL 31.

We can derive the veiling based on the strength of photospheric lines in the K band relative to the G6 standard. Veiling is defined as  $r = F/F_{phot}$  where  $F$  is an excess continuum flux that comes from the accretion disk; as  $r$  increases the strength of the lines relative to the continuum decreases. The value of  $r$  can be used to measure the amount of excess emission. We calibrate the veiling by adding a constant flux to our G6 standard in 16 small bands  $0.05\mu\text{m}$  wide from  $0.8\text{-}2.5\mu\text{m}$  and comparing the veiled standard to the observed spectra. The best-fit is determined independently in each band using the minimum chi-squared. These multiple measurements provide  $r$  as a function of wavelength and we use this linear fit to derive the veiling at  $2.15\mu\text{m}$ . There is substantial scatter between individual measurements, but we are able to use the line fit to estimate  $r$  with an uncertainty of  $\pm 0.1$ . Figure 4.4 shows the measurements in our 16 bands for one day, demonstrating that we can obtain good fits across much of the spectrum, showing a trend of increasing veiling with increasing wavelength. The results are listed in Table 4.6.

Once we have used the veiling to determine the excess emission at  $2.15\mu\text{m}$  we normalize the standard and LRL 31 spectra at this wavelength. Since our

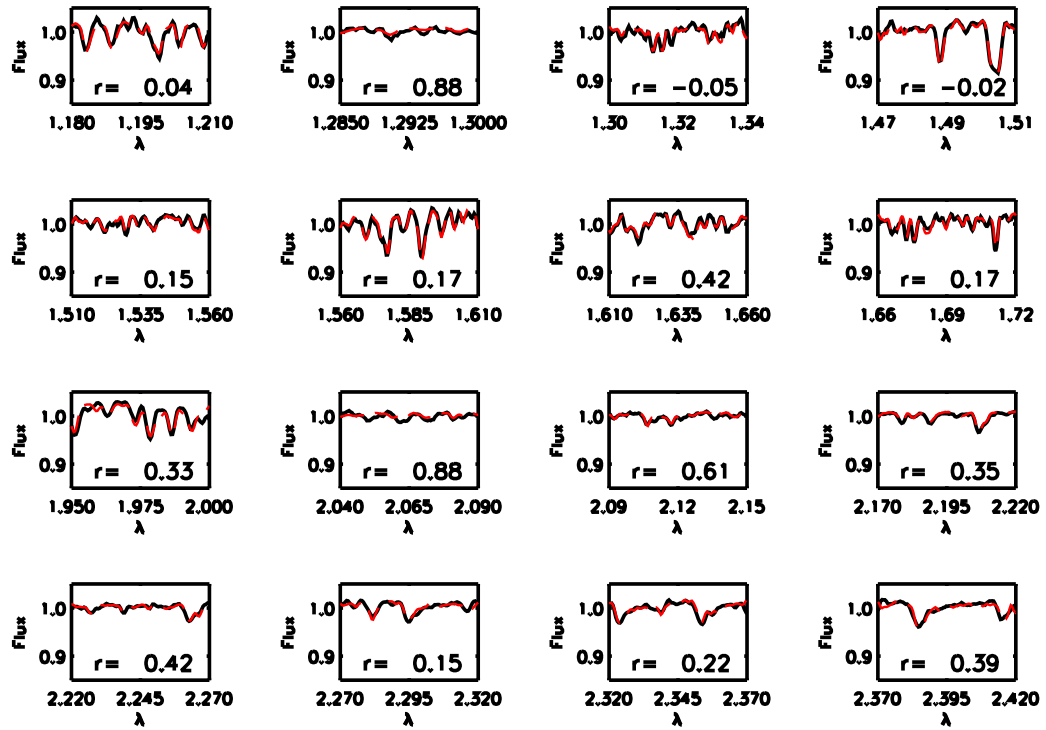


Figure 4.4 Continuum normalized flux as a function of wavelength for the 16 bands used to measure the veiling for 08 Nov 2009. In each panel both the observed spectra (black line), along with the best fit veiled standard (red dashed line) are shown. The veiling increases from 0 in J band to a few tenths in K band. There can be a large spread in the veiling from band to band depending on the strength of the lines in the band and the continuum fit.

G6 WTTS standard spectrum only extends to  $2.3\mu\text{m}$  we use a Kurucz model ( $T_{\text{eff}}=5750$ ,  $\log g = 2.5$ ) (Castelli & Kurucz, 2004) to extend it out to  $5\mu\text{m}$ . The standard and LRL 31 are subtracted yielding an excess spectrum whose flux is relative to the photospheric flux at  $2.15\mu\text{m}$ . These excess spectra are shown in Figure 4.5.

To find the temperature of the hot dust we fit a single temperature blackbody to the excess spectrum. We artificially increased the uncertainties in the wavelength ranges  $2.4 < \lambda < 3.5\mu\text{m}$  and  $\lambda > 4.3\mu\text{m}$  in order to account for systematic effects from an incomplete telluric correction, which affect some regions of the spectrum more than others. This is especially important for 08 Nov 2009 when the large airmass difference between the telluric standard and LRL 31 (0.48) resulted in a poor correction of the telluric features. Typical uncertainties on the derived temperature are 250K, which is mostly due to the uncertainties in the veiling and in the extinction.<sup>1</sup> As seen in Figure 4.5 a blackbody is a good fit to the excess spectra. The full spectra, along with the veiling measurements as a function of wavelength are shown in Figure 4.6.

We can double check the shape of the excess spectra by normalizing both the standard and LRL 31 at  $1.15\mu\text{m}$ , where we expect and measure zero veiling. This avoids using the veiling to normalize the spectra, since the large uncertainties in the veiling lead to large changes in the derived temperature. Veiling presents an extinction independent measure of the shape of the LRL 31 spectra relative to the standard, which can be used in this case to confirm the shape of the spectra, rather than relying on them to define the shape. We find that the temperatures derived in this instance are consistent with our previous derivation within the uncertainties. The largest discrepancies are for the 31 Oct 2009, where the new

---

<sup>1</sup>We derive the extinction assuming that there is very little excess in the J and H bands, which could potentially change the shape of the spectra.

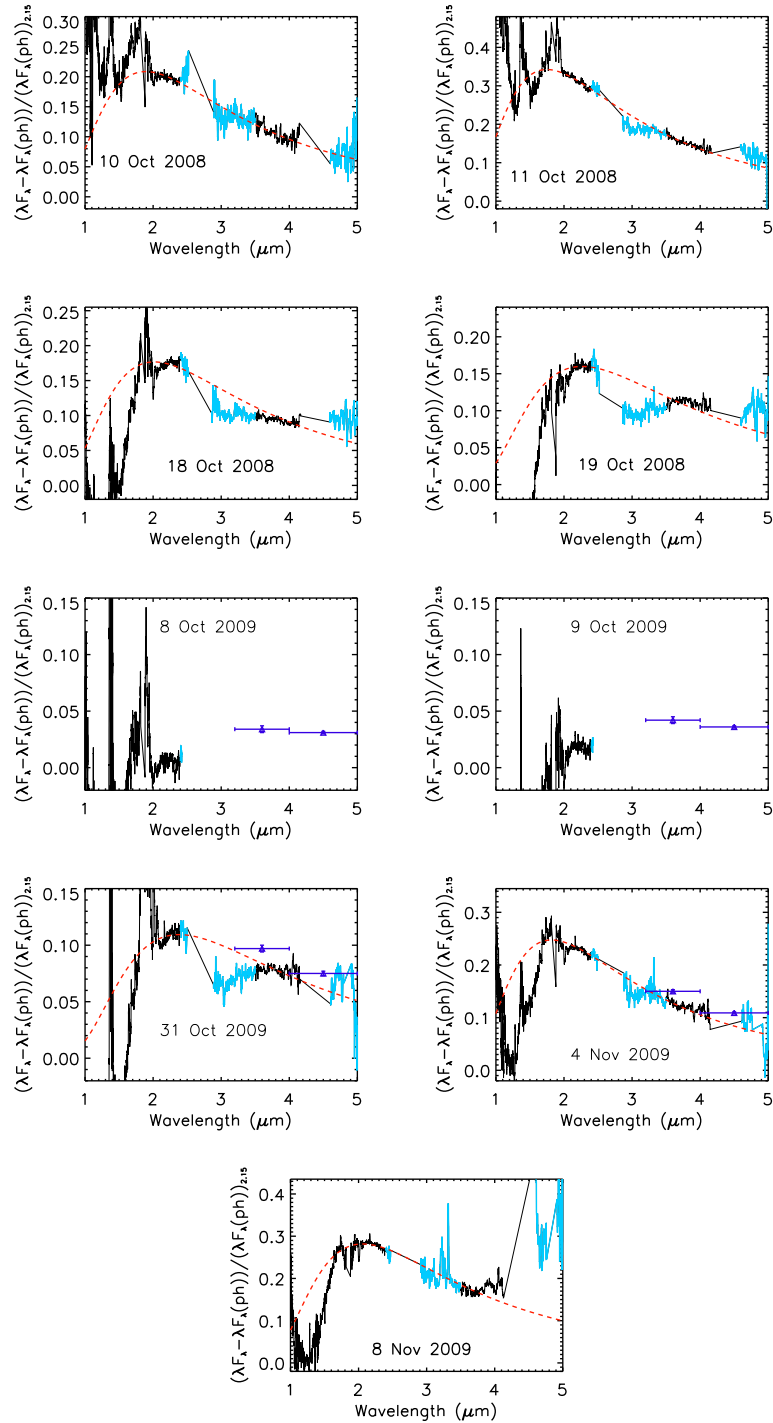


Figure 4.5 The infrared excess. Each plot show the difference between LRL 31 and the standard, normalized to the photospheric flux at  $2.15\mu\text{m}$ . On each plot the best fit is shown with a red dashed line and  $3.6, 4.5\mu\text{m}$  photometry is included when available. Each spectra has been smoothed by a median filter  $0.01\mu\text{m}$  wide in order to reduce the noise in the continuum. The parts of the spectra marked in blue are strongly affected by the telluric correction. Note that the scale changes for each plot. The strength of the excess shows large variations from night to night, although the temperature stays roughly constant.

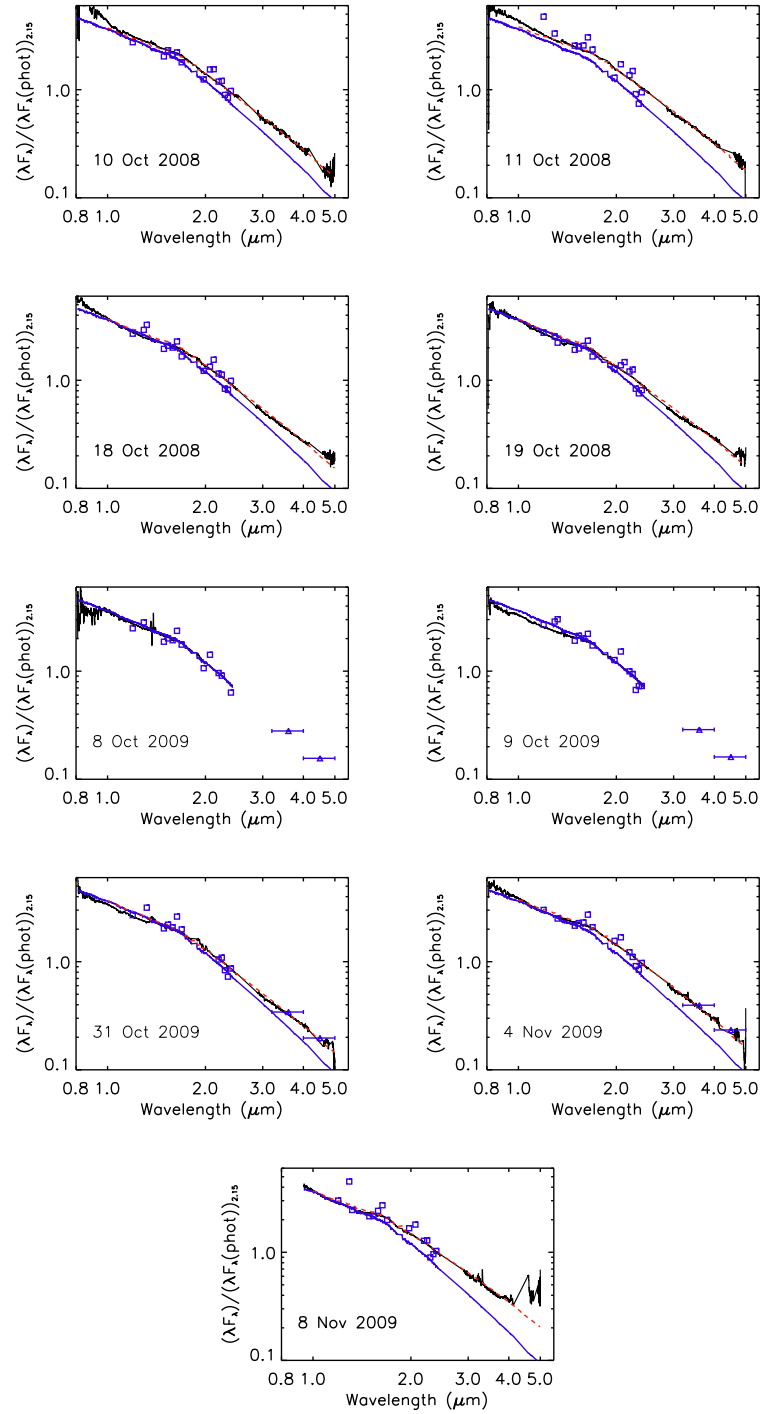


Figure 4.6 The spectra for each night, along with a standard and the blackbody fit the the excess. Dark blue line is the standard, red dashed line is the standard plus the best fit blackbody. Blue squares are the veiling measurements, and blue triangles are the 3.5,4.5  $\mu\text{m}$  photometry, where available. Spectra have been normalized by the photosphere at 2.15  $\mu\text{m}$  and smoothed by a median filter 0.01  $\mu\text{m}$  wide.

temperature is 1900 K, and 11 Oct 2008, where the new temperature is 1620 K. Normalizing the spectra at  $1.15\mu\text{m}$  brings these two measurements into better agreement with the derived temperatures from the other five nights.

The temperatures, listed in Table 4.6, are consistent with each other, within the uncertainties, and the average temperature of 1830 K is consistent with the dust sublimation temperature (e.g. Dullemond & Monnier, 2010). This implies that the sublimation of dust sets the inner edge of the disk rather than some other process, such as the sculpting of the disk by a companion. Converting the dust temperature to a location in the disk depends on the properties of the dust, the luminosity of the star, and also on the covering fraction of the inner rim (Isella & Natta, 2005). If one of these dependencies was rapidly varying then the location of the inner rim could fluctuate while the temperature stays constant. Our measurements indicate that the accretion luminosity is much less than the stellar luminosity, the stellar luminosity does not vary significantly, and we do not expect the dust properties, such as grain size and crystallinity, to change on the observed timescales, suggesting that a constant dust temperature corresponds to a constant sublimation radius ( $\sim 0.15\text{AU}$ ).

While the average temperature of the hottest dust is roughly consistent with the dust sublimation temperature, it is still higher than is typically measured (Muzerolle et al., 2003; Espaillat et al., 2010). This discrepancy may either be due to unique gas and dust properties that allow for higher than normal temperatures or systemic effects in our measurements that cause us to overestimate the dust temperature. Dust composed of irons and olivines at high gas densities has a higher sublimation temperature than dust particles more commonly seen around young stars (Pollack et al., 1994). An inner disk composed mostly of this material would have an abnormally high temperature. While we cannot directly measure

the dust and gas properties of the inner disk we can use the silicate feature and the accretion rate as proxies. The silicate feature is sensitive to dust properties at radii of a few tenths of an AU to a few AU (Kessler-Silacci et al., 2007) and the dust properties responsible for this feature generally do not change by orders of magnitude throughout the disk (van Boekel et al., 2004). The shape of the silicate feature in LRL 31 is consistent with typical ISM-like silicate dust with sub-micron sized grains, not a heavy mix of iron and olivines. Also the accretion rate, which is proportional to the gas density in a viscously evolving disk, is inconsistent with an extremely high gas density. The fact that this star is a transition disk would suggest that there is a decrease in the gas density rather than an increase.

This suggests that there is a systematic effect in our measurements that lead to an overestimation of the dust temperature. Overestimating the veiling or the extinction, possibly due to an imperfect match between the standard star and the intrinsic photospheric emission of LRL 31 will lead to a higher measured dust temperature. Given the difficulty in measuring the veiling at such low levels, this is the most likely source of the discrepancy. Our conclusions about the change in veiling should be unaffected by this systematic uncertainty since we use the same standard, accounting for changes in resolution, and derive the veiling using the same method on each night.

While the temperature of the dust is constant, the strength of the excess fluctuates throughout our observations. The variations in the strength of the excess occur on weekly to monthly timescales, but do not show daily fluctuations (Figure 4.6). We integrate a blackbody at the derived temperature and strength for each night to determine the luminosity of the excess relative to the stellar luminosity, which is an estimate the covering fraction of the inner disk, since the flux



from the disk is reradiated stellar flux. Our results are listed in Table 4.6. For the nights of 8,9 Oct 2009 we assume the dust is at 1830 K, the average of the other seven nights, and fit the blackbody to the IRAC data to determine the strength of the excess. We find that the covering fraction varies by a factor of 8, from 1-8%.

In a typical T Tauri star, with a puffed inner rim, the covering fraction is 12% (Dullemond, 2001), while typical debris disks have covering fractions of  $<0.1\%$  (e.g. Plavchan et al., 2009). On average the covering fraction of the dust in LRL 31 is below that expected for an optically thick puffed inner disk. In section 4 we discuss physical models that can produce changes in the infrared excess on short timescales, but here we consider what the small average covering fraction implies about the inner disk structure. The covering fraction for an optically thick disk is proportional to the ratio of disk height to radius,  $H/R$  (Dullemond & Monnier, 2010), and if we assume that  $R$  stays constant, then we are observing a reduction in the scale height relative to a normal disk. This deviation in the average scale height from a typical disk could be due to (1) a dramatic decrease in the local surface density or (2) a decrease in the dust opacity, possibly due to the growth of the dust grains. Both of these effects would reduce the  $\tau = 1$  surface of the disk where stellar photons are absorbed, reducing the covering fraction. The accretion rate, which in a viscous disk is proportional to the surface density, is not unusually low for a T Tauri star, suggesting that enhanced grain growth and settling may be causing the decrease in the covering fraction, rather than a decrease in the surface density.

This long term evolution of the grain size and settling toward the midplane may or may not be related to the rapid fluctuations seen in our data. The change in covering fraction implies a change in the scale height of a factor of 8 if the perturbation is axisymmetric. A model of the infrared fluctuations does not need to

produce axisymmetric perturbations of the disk but does need to create features that are large enough to match the observations. If the change in covering fraction is due to a localized blob being launched from the disk and the disk always has a covering fraction of 1% then the other 7% can be due to a blob with a circular diameter of  $\sim 50^\circ$  as seen from the star.

The 3.6 and 4.5  $\mu\text{m}$  flux (Figure 4.7), where we have more complete monitoring, shows a slow variation over the course of weeks, consistent with the change in the infrared excess measured from the spectra. The infrared flux is a mix of stellar and disk emission and our excess spectra taken during the warm mission monitoring suggest that most of the change in the infrared flux comes about from a change in the disk emission, not from variability in the stellar emission. Some of the optical monitoring of Baliber et al. overlaps with our infrared monitoring, and the stellar flux does not follow the same trend as the infrared data, supporting our interpretation that the dust is varying while the star is constant.

In our mid-infrared observations the flux varies continuously (Figure 4.8). This suggests that the physical cause is not a single event, but a continuously occurring phenomenon. Unlike a FU Ori or EXor outburst, the variability in LRL 31 does not occur once and slowly decay. Our IRS spectra separated by six months show that the wavelength dependence of the variability does not change. This suggests that the same mechanism dominates the variability over many years. It also supports our assumption that the variability we study in any one year has the same characteristics as in any other year.

The extinction and polarization (Tables 4.4 and 4.7) can provide clues to the structure of the disk, assuming that they come from the disk. If the grains in the molecular cloud are aligned, they can create polarized flux from the star. Starlight that is parallel to the long axis of the grains will be more highly extinguished than

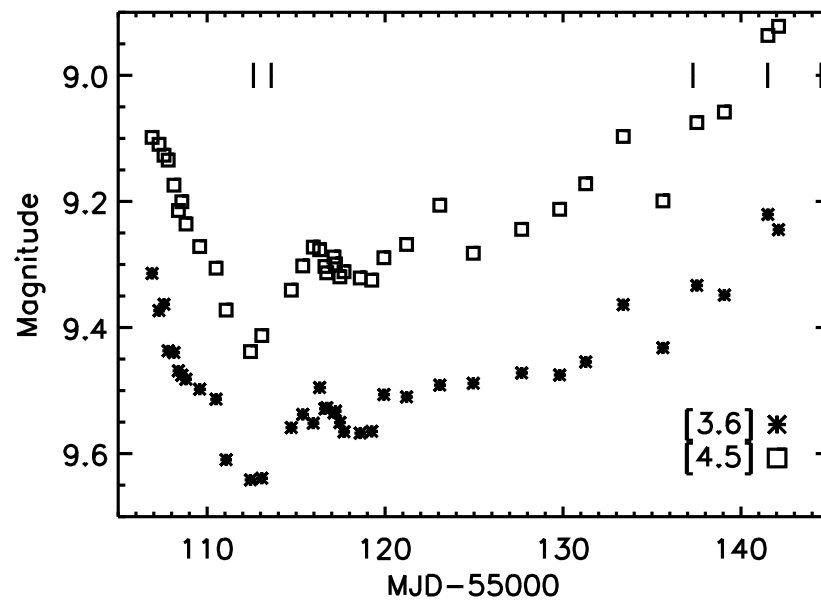


Figure 4.7 3.6 and 4.5  $\mu\text{m}$  light curves for LRL 31. The data show a rapid drop in flux followed by a slow increase over the course of a few weeks. Uncertainties in the photometry are similar to the size of the points. Vertical lines mark the times when we obtained spectra.

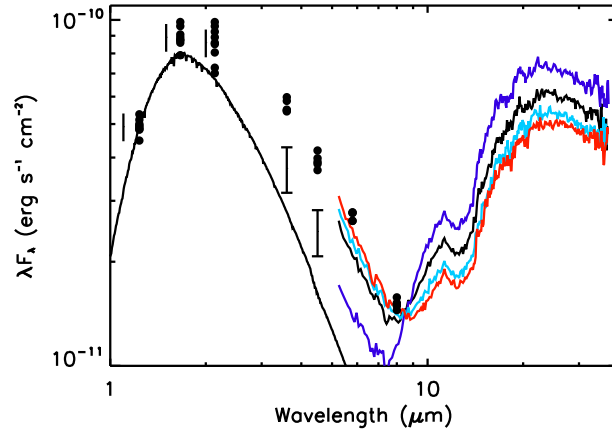


Figure 4.8 Spectral energy distribution of LRL 31 showing our early IRS data (rereduced), the IRAC-cryo data, the JHK photometry and the range of magnitudes seen in the IRAC warm mission data (error bars at 3.6, 4.5  $\mu\text{m}$ ). A Kurucz model photosphere, reddened by  $A_V=8.8$  and scaled to the average J band magnitude has been included for comparison. Vertical lines near the near-infrared photometry demonstrate the uncertainties in this data. Uncertainties in the mid-infrared photometry are similar to the size of the data points

starlight that is parallel to the short axis of the grains. This differential extinction will lead to polarized light leaving the cloud, with the polarization being proportion to the extinction. Two other nearby cluster members were observed by SPOL and have previous polarimetry measurements. LRL 169 (11'' from LRL 31) has a  $P=4.2\%$  and  $q=6.9^\circ$  while LRL 4 (3.5' from LRL 31) has  $P=2.8\%$  and  $q=166.5^\circ$ , and the extinction is  $A_V=2.8$  and 1.8 respectively (Luhman et al., 2003). If the polarization is from the molecular cloud then the ratio of polarization to extinction should slightly decrease with extinction (Gerakines et al., 1995). For LRL 169, 4 and 31 the ratio is 1.5, 1.6 and 0.9 %/mag respectively, which is consistent with the expected decrease. The molecular cloud density needs to be highly variable in order to explain the observations since LRL 169 is only 3500 AU away from LRL 31 and shows a much smaller extinction and a different polarization angle.

The high polarization/extinction could also be coming from the outer disk, if the disk is close to edge on and the system is moderately flared. Differential extinction can work with material in the outer disk in much the same way as it would operate in the molecular cloud. An edge-on disk is consistent with the inclination used by Flaherty & Muzerolle (2010) to fit the LRLL 31 SED with models of a warped disk. We can exclude the inner disk as the source of the extinction and polarization because of the lack of strong variability in these quantities, whereas we have observed continuous and large fluctuations of the inner disk.

#### 4.3.3 Gas Properties

Next we consider the activity of the gas, which we trace through a combination of emission lines from the infrared and optical. Our observations of the  $\text{Pa}\beta$  and  $\text{Br}\gamma$  lines in the infrared let us measure the accretion rate onto the star directly (Muzerolle et al., 1998). To derive the line fluxes, we first subtract the photospheric absorption as measured by the G6 WTTS standard. In this case we find that using a WTTS, rather than a dwarf or giant spectrum, does better at subtracting the photospheric absorption especially in the wings of the line. We normalize the absorption-subtracted spectrum to the continuum around the line. These spectra for each day are shown in Figure 4.9. The equivalent widths of the lines, as measured from the continuum normalized spectra (Figure 4.9), are listed in Table 4.8. Veiling will change the strength of a line, especially for  $\text{Br}\gamma$  where the veiling is significant, and in Table 4.8 we include the veiling corrected equivalent width (EW), which is derived by artificially veiling HD 283572 and subtracting this new standard from the observed spectrum. Using our nearly simultaneous measurements of J and K band photometry to estimate the continuum level, we derive the line flux. Since we use the observed K band photometry, which is a mix of stellar emission and veiling flux, we had to account for the veiling when measur-

ing the EW, resulting in the corrected EW being lower than the uncorrected EW. The smaller EW, combined with the stellar plus veiling flux of the K band continuum produces an accurate estimate of the line flux. While others have found significant veiling near  $1\mu\text{m}$  in some stars (Fischer et al., 2008), we measure little veiling in the J band, and assume it is negligible when deriving the flux of the  $\text{Pa}\beta$  line. Assuming a distance of 320pc to the star, we can then derive line luminosities. These line luminosities are directly correlated with the accretion luminosity (Muzerolle et al., 1998) and we can derive the accretion rate using the formula:

$$L_{acc} = \frac{3GM\dot{M}_*}{5R_*} \quad (4.1)$$

The measured line luminosities and accretion rates are listed in Table 4.9. We cannot derive accurate accretion rates from the 2005 and 2006 spectra because we do not have simultaneous photometry, but the strong emission lines suggest that they were on the high end of the range of measured accretion rates. There is a large discrepancy between the accretion rate derived by  $\text{Pa}\beta$  and  $\text{Br}\gamma$  that is unexpected given that both measure the accretion rate onto the star. The uncertainties listed in Table 4.9 only include the uncertainty in the photometry and the equivalent width measurements and do not include the uncertainty in the conversion between line flux and accretion luminosity, or the uncertainties in the mass and radius of LRL 31. The conversion uncertainty is closer to a factor of 2, much larger than the typical 10% uncertainty, and can account for the discrepancy between the accretion rate derived by  $\text{Pa}\beta$  versus  $\text{Br}\gamma$ . Unresolved absorption in the line may also explain some of the observed differences. Further conclusions drawn about the accretion rate are based on the  $\text{Pa}\beta$  because it is the stronger and is less susceptible to veiling, which makes it a more reliable tracer of the accretion rate.

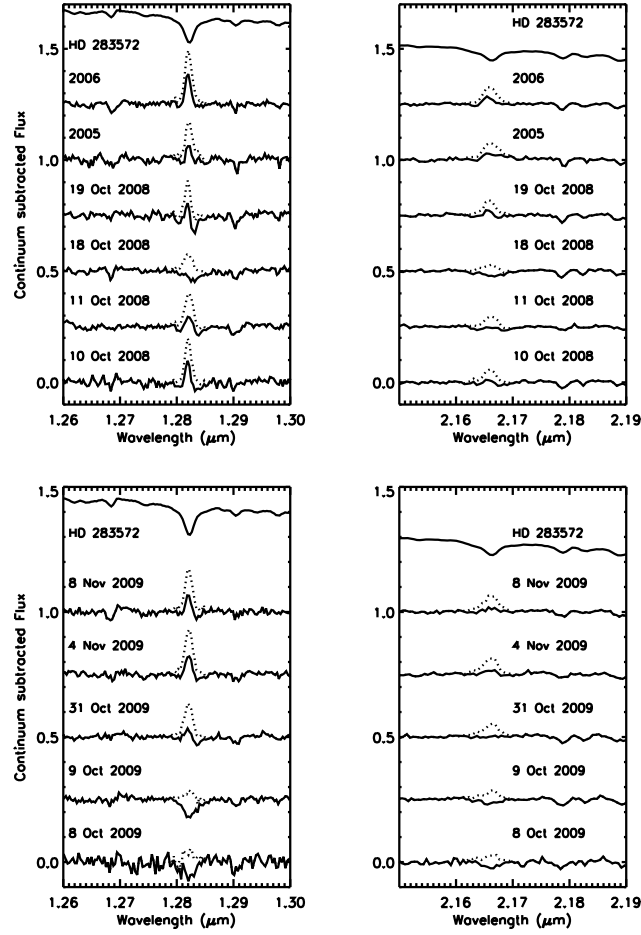


Figure 4.9 Line measurements from 2005, 2006, 2008 (left two panels) and 2009 (right two panels). Both the Pa $\beta$  line ( $\lambda = 1.282 \mu\text{m}$ ) and Br $\gamma$  ( $\lambda = 2.16 \mu\text{m}$ ) are shown for each day. The solid line is the observed spectrum, while the dashed line has had the photospheric absorption subtracted from the line. At the top of each panel is the G6 WTTs standard. There are large variations in the emission lines, mainly on timescales of weeks.

There are large variations in the  $\text{Pa}\beta$  and  $\text{Br}\gamma$  emission throughout our observations. The EW ranges from almost zero up to  $4.5\text{\AA}$ . The accretion rates vary by a factor of 5. The infrared emission lines demonstrate that the accretion is changing constantly with the largest changes occurring on weekly, rather than daily, timescales. Accretion variability is common among T Tauri stars, and the daily level of variability seen in LRL 31 is similar to that seen in many other stars (Hartigan et al., 1991; Gullbring et al., 1996). The change seen in 2009, when the  $\text{Pa}\beta$  line goes from absorption to emission is less common.

Our measurements of the  $\text{H}\alpha$  equivalent width (Table 4.10) from the optical spectra show emission at every epoch, implying that accretion is continuous in LRL 31. The equivalent width is continuously changing with a range of a factor of 3.4, suggesting that the accretion rate is always varying as was found with the infrared hydrogen recombination lines. Similar to the dust emission, the variations in the accretion rate onto the star are not a single isolated event, and are always occurring with varying amplitude. Our high-resolution  $\text{H}\alpha$  spectra are shown in Figure 4.10. They show broad profiles, consistent with the presence of accretion. It appears as though the red side of the feature experiences the largest variations, while the blue side stays relatively constant. This may be due to partial obscuration of the accretion flow by the disk, or a change in the magnetospheric geometry.

The outflow of material, as traced by the blue-shifted emission/absorption in the  $\text{HeI}$  line (Figure 4.11), changes on daily to weekly timescales. In 2008 it shows large variations from night to night, while in 2009 the line slowly goes from showing very strong blue-shifted absorption to no blue-shifted features. Blue-shifted absorption in the  $\text{HeI}$  line is believed to come from a combination of stellar wind and disk winds (Fischer et al., 2008) and variability in the lines is sometimes



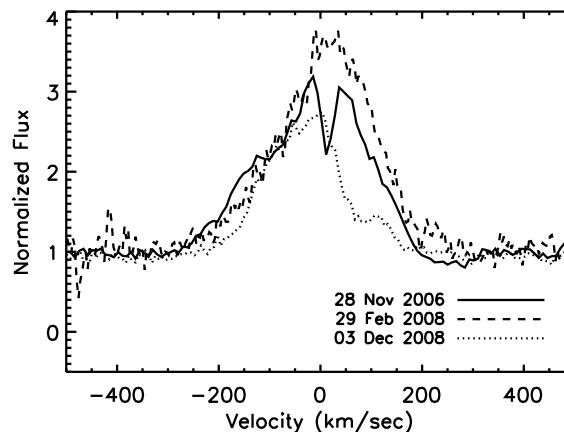


Figure 4.10 High resolution  $H\alpha$  measurements, normalized to the continuum. The line shows continuous variations in its shape and strength.

seen (Edwards et al., 2006). The red side of the  $HeI$  line is connected with the accretion flow, and the strength of the red-shifted absorption is broadly correlated with the strength of the  $Pa\beta$  and  $Br\gamma$  emission lines. When the  $Pa\beta$  line is the strongest in 2005 and 2006, the red-shifted absorption is the deepest, and in 2009 the absorption increases with the accretion rate. This red-shifted absorption may result if we are looking down the accretion column, so the gas that is flowing onto the star absorbs the emission from the hot column of shocked gas striking the surface of the star. The variations in the relative strengths of the two sides of the line suggest that the two do not change contemporaneously. There are days with just red-shifted absorption, days with just blue-shifted absorption and days with both.

There is also evidence for correlated changes in the accretion rate and the infrared excess. In 2009 we were able to obtain near-infrared spectra during our Spitzer warm mission monitoring (vertical tick marks in Figure 4.7). We observed two spectra during the minimum in the light curve and three spectra after the infrared excess had substantially increased. We find that while the infrared ex-

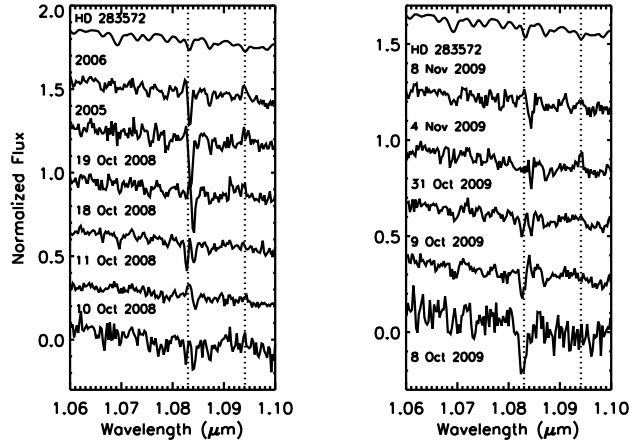


Figure 4.11 HeI ( $\lambda = 1.083\mu\text{m}$ ) and Pa $\gamma$  ( $\lambda = 1.0941\mu\text{m}$ ) lines in LRL 31. The HeI line shows large variations in both the blue and the red side in as little as one day.

cess is at its minimum, the Pa $\beta$  line (8,9 Oct) is weaker than in any other epoch. As the infrared excess increases over the next few weeks the Pa $\beta$  line emission also increases. We have one observation of the H $\alpha$  line taken on 12 Oct 2009, close to the infrared minimum, and the equivalent width is lower than seen in other epochs. This suggests that the dust at the inner edge of the disk and the gas flowing onto the star are closely connected by the physical mechanism that causes this variability, which has been previously considered as a source of infrared variability (Carpenter et al., 2001). Also, the blue-shifted absorption in the HeI line is strongest at the infrared minimum and slowly disappears as the excess gets stronger, suggesting that the dust and outflowing gas are also connected.

#### 4.4 Theoretical Implications

Our observations of LRL 31 target the inner disk, as shown by the variability timescales of a few days to a week and the temperature of the dust close to the sublimation temperature. Studies of circumstellar disks have gained a reasonably

complete and consistent picture of the behavior of the accretion/protoplanetary disks at radii greater than 1 AU, but the zone within this radius presents many puzzles. Not only is it beyond our ability to resolve well observationally, but it is the venue for complex processes involving intense magnetic fields, gas flow, accretion luminosity, and extreme heating and sublimation of dust. The variability observed here can help to provide constraints on some of the physics occurring in this part of the disk. In this section, we consider possible physical causes for this behavior such as variable accretion, perturbations by a companion, winds, and the influence of magnetic fields. Schematic diagrams of the various models considered are shown in Figure 4.12.

#### 4.4.1 Variable Accretion

In a disk in hydrostatic equilibrium, the scale height of the dust is set partly by the luminosity illuminating its surface (Dullemond, 2001), which is a combination of stellar luminosity and accretion luminosity. A substantial change in either would lead to a variation in the scale height of the disk (Figure 4.12a). Our observations rule out any large changes in the star, but do indicate large variations in the accretion. Since the accretion luminosity is much smaller than the stellar luminosity, a much larger change in the accretion luminosity than the observed variation would be needed to produce the observed fluctuations in scale height. We can then rule out a variable illumination of the inner disk as the source of the variability.

The viscous nature of the disk also means that the accretion rate through the disk is directly tied to its surface density (D'Alessio et al., 1998). If the surface density of the disk were to suddenly increase, possibly due to a large inflow of material from the outer disk, then the height of the  $\tau = 1$  surface would increase (Figure 4.12b). Outgoing stellar photons will be absorbed by the disk below

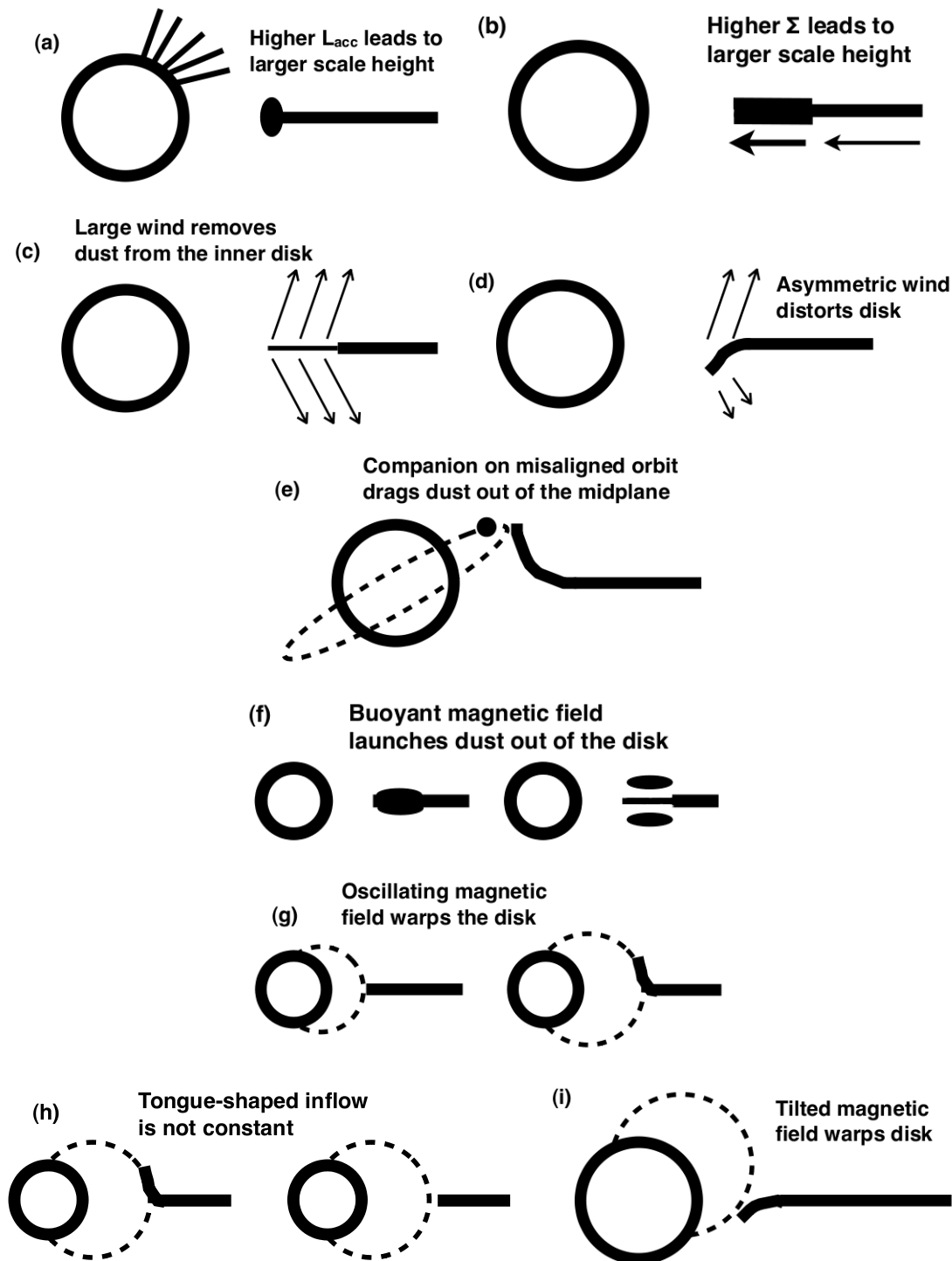


Figure 4.12 Schematic diagrams of the various models considered for the variability of LRL 31.

the height of the  $\tau = 1$  surface of the disk. A change in the height of this surface would change the amount of stellar light that is absorbed by the disk. This would lead to a change in the covering fraction of the inner disk and the shadowing of the outer disk, consistent with the behavior of this system. The timescale for a large mass of dust to travel through the inner disk is the viscous timescale, which is roughly 2000 years at 0.2 AU. This is much longer than the dust continuum variability timescales we observe. Also, if the magnetosphere radius where the stellar accretion flow is launched is significantly less than the dust sublimation radius (see below), then the long viscous timescale is also inconsistent with the observed correlation between dust and stellar accretion rate variations.

These arguments suggest that the variations are not caused directly by changes in the accretion rate. It is possible that the relationship between the infrared excess and accretion is not a causal one. The change in accretion rate may not directly lead to a variation in the covering fraction of the inner disk, but instead they may both be effects of another physical process.

#### 4.4.2 Winds

A highly variable wind could lead to a loss of material in the inner disk. This wind could carry both gas and dust out from the inner disk (Vinković & Jurkić, 2007; Konigl & Pudritz, 2000) and this rapid removal of material would lead to a drop in both the infrared excess and the accretion rate, if gas were removed just before it began its free fall along the magnetic field lines (Figure 4.12c). Disk wind models usually start the wind with a velocity on the order of the sound speed, and then it rapidly accelerates to larger than the Keplerian velocity (Blandford & Payne, 1982), which would imply a slower decrease in the disk emission than is observed. The strong blue-shifted absorption on the HeI line during the minimum of the infrared excess, and the rapid fluctuations in this component are

consistent with a strong wind. If we assume that the inner disk is just barely optically thick before the wind starts to remove material with a gas to dust mass ratio of 100, and the wind removes the entire inner disk in only 5 days (the length of the drop in the infrared light curve) then the outflow rate is  $2 \times 10^{-5} M_{\odot}/yr$ . The accretion rate required to refill the disk over the next 30 days is  $3 \times 10^{-6} M_{\odot}/yr$ . This accretion rate is a lower limit since the disk is not just barely optically thick but it is still much larger than is observed for LRL 31. Also, filling the inner disk by accretion from the outer disk should occur on a viscous timescale, which is much longer than the timescale for the increase in the infrared flux.

The wind could be asymmetric about the plane of the disk, leading to a variation in the disk structure (Figure 4.12d). This can arise when a stellar magnetic field that is not symmetric about the equatorial plane launches the wind (Lovelace et al., 2010). If the mass flow in the wind is larger on one side of the disk than the other, then the asymmetric loss of angular momentum would lead to warping of the disk, which would then shadow the outer disk, leading to infrared variability (Flaherty & Muzerolle, 2010). If the fluctuations in the wind were rapid enough, as is suggested by the fast changes in the blue-shifted side of the HeI line, then they could cause the observed variability. This model suggests that a large wind would be associated with more warping in the disk, and a larger infrared flux, which is inconsistent with our observations. As with the accretion flow, it is difficult to get a wind to explain the infrared variations directly, and the fluctuations seen in the blue-shifted side of the HeI line may be a result of the same physical process that changes the infrared excess and the accretion rate rather than the source of this behavior.

#### 4.4.3 Perturbation by a Companion

A companion on an orbit that is misaligned with the disk (Figure 4.12e) can lead to a warped disk (Larwood & Papaloizou, 1997). The height of the warp will periodically vary as the companion passes out of the midplane of the disk and drags dust with it (Fragner & Nelson, 2010). If a companion were sitting inside the inner disk then it could create large perturbations while also periodically disturbing the accretion rate, assuming it did not get close enough to the inner disk to completely remove all of the dust (Artymowicz & Lubow, 1996). It is also possible for a companion to be sitting outside of the inner disk, again assuming it isn't close enough to remove the inner disk. The deficit of flux around  $10\mu\text{m}$  relative to a typical T Tauri star indicates that the disk is missing material within a few AU of the star, i.e. it is a transition disk. Our near-infrared observations indicate that there is still an optically thick disk at the dust destruction radius, but beyond this point there may be a gap in the disk. If so, gas and dust would still flow through this gap as evidenced by the continuous accretion of gas onto the star. If the gap were caused by a companion clearing out material near its orbit, then the accretion rate through the gap would be expected to be periodic, and material would cross the gap at a speed much higher than the typical velocity through a full disk (Artymowicz & Lubow, 1996). If the inner disk is narrow enough, then the shock heating as this material strikes the inner disk at its outer edge could lead to heating of the inner edge of the disk, which would change its scale height.

Our data allow us to provide some constraints on the position and mass of a companion. A companion larger than  $1M_{\odot}$  would be noticeable in our near-infrared spectra as anomalously strong photospheric lines in the K band. An equal mass binary would not produce anomalous line strengths, but would make

the star appear over-luminous, which is not seen, although there is a large uncertainty in the luminosity. A smaller companion near the dust destruction radius can still lead to a large change in the structure of the dust, and would be consistent with the observed changes in the radial velocity. Figure 4.13 shows our constraints on the mass and location of a companion in the disk. The upper and lower limits on the mass come from the near-infrared spectra and the RV data. The limits on the location of a companion come from the requirement that the companion cannot remove material from the dust destruction radius (taken to be 0.15 AU) or from the outer disk ( $\sim 7$  AU) (Artymowicz & Lubow, 1996). The exact location of the inner disk, along with the limits on the location of a companion near this dust, depends on the dust composition, the luminosity of the central source and the assumption that the central source is a single star rather than a binary (Nagel et al., 2010). Moving the inner disk in or out will change the absolute position of the boundary, but not the relative positions, which are at  $r/a \sim 0.3, 1.7$  for the outer and inner limits respectively, where  $a$  is the binary separation and  $r$  is the location of the dust. The radial velocity data suggests that this system is a binary, and the presence of dust at certain locations within the disk limits the location of this companion.

Even if this system is a binary, the companion may not be responsible for the infrared variability. A companion in a circular orbit in the plane of the disk will not cause substantial mid-infrared variability (Nagel et al., 2010). Making the companion misaligned with the disk could lead to periodic perturbations (Fragner & Nelson, 2010). Figure 4.13 shows the periodogram based on the monitoring at  $3.6$  and  $4.5\mu\text{m}$ . We are most sensitive to periods in the range 2-25 days and no significant peak is seen indicating that there is no periodicity over these timescales. If a companion were located 0.04-0.2 AU from the central star and



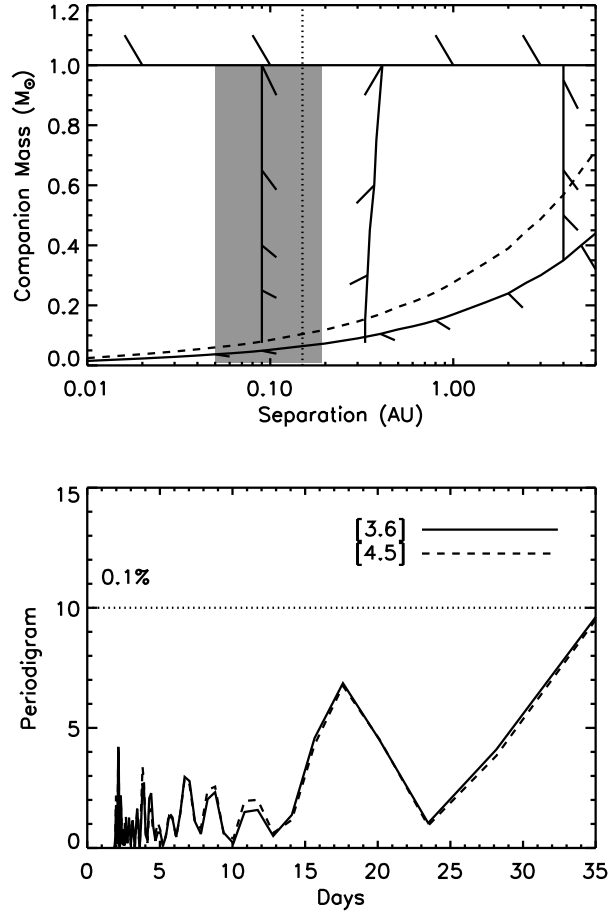


Figure 4.13 (Left) Limits on the mass of a companion. Hashed areas show regions of mass and position of a companion that can be ruled out based on our data. The upper limit is from the near-infrared spectra and the lower limit is from our RV data (dashed line assumes  $i=38^\circ$ ). The limits on position come from the dynamical clearing of the disk by a companion. Disk material exists at the dust sublimation radius ( $\sim 0.15$  AU, dotted line) and in the outer disk ( $\sim 7$  AU), and we can rule out a companion close to these locations. The lack of periodicity in the  $3.6, 4.5\mu\text{m}$  photometry rules out a companion within the grey area perturbing material on every orbit. (Right) Lomb-Scargle Normalized Periodogram based on the  $3.6$  and  $4.5\mu\text{m}$  photometry. The dashed lined indicates a false alarm probability of 0.1%. There are no peaks above this line, indicating that there is no significant periodic signal in the data.

perturbed the disk on every orbit then we would see evidence of this in the IRAC data. This excluded region is marked in left-hand side of Figure 4.13. This data suggests that it is unlikely that there is a companion on an inclined orbit within the inner disk, but does allow an object further out in the disk. Based on the limits discussed above, if the inner disk is at 0.15 AU then the companion is restricted to outside of 0.4 AU where the orbital period is  $\sim 100$  days. The rapid decline in the flux at the beginning of our infrared monitoring is difficult to explain in the context of the slow variations expected from a companion this far from the star. It is possible that the inner disk is closer than 0.15 AU, pushing in the outer limit on the position of a companion inward resulting in a timescale more comparable to what is observed. The companion could also be on an eccentric orbit, which would allow it to rapidly disturb the disk during its high velocity periastron motion, while still having a long period.

#### 4.4.4 Magnetic Fields

A magnetic field threading a turbulent disk could lead to variable structure. Using magneto-hydrodynamic simulations Turner et al. (2010) find rapid variations in the disk due to the turbulence caused by the magneto-rotational instability (Figure 4.12f). They see sharp drops in the scale height of the disk by 30% in an orbital timescale as dust is lifted out of the disk by a buoyant magnetic field. There is evidence for a small change in the silicate feature (Muzerolle et al., 2009), which could be explained by the limiting of dust out of the midplane (Turner et al., 2010). The speed of the changes in this model is consistent with our observations, but the small amount of excess in the minimum of the  $3.6, 4.5\mu\text{m}$  light curve would require that the entire inner disk have a scale height close to zero. Such global behavior is not seen in these models and the changes in the scale height

are smaller than have been observed.<sup>2</sup>

The interaction between the disk and stellar magnetosphere can be highly dynamic (Bouvier et al., 2007b). According to some models, where the magnetic field truncates the disk oscillates (Figure 4.12g) on timescales of  $\sim 25$  days (Goodson & Winglee, 1999), which is similar to the timescale seen in the warm-mission photometry. The oscillations can be very large (a factor of 3 change in the size) due to the expansion, opening and reconnection of the magnetosphere, although we do not see a large change in the location of the dusty disk. Romanova et al. (2009) find large variations in both the accretion rate and the outflow rate associated with these magnetic field oscillations. The timescale between bursts is  $\sim 60$  days for rapidly rotating stars, which is consistent with our infrared light curve. Kulkarni & Romanova (2008) present a set of three-dimensional simulations of magnetospheric accretion and they show that strong instabilities develop in the inward flow of material, breaking it up into a small number of tongue-shaped features extending from the disk, along the magnetic field lines, to the stellar surface, where they create hot spots (Figure 4.12h). Variations in the number and geometry of the tongues occur on the dynamical timescale of the inner disk. If the tongues originate at or just beyond the sublimation radius and dust is carried along with the gas flow, they might provide a framework for explaining our observations. They would carry the dust out of the disk plane, potentially shadow the outer disk from the star when this occurs (as needed to explain the longer wavelength variations reported in Flaherty & Muzerolle (2010)), and would appear as a large increase in disk scale height, all occurring on a timescale compatible with that of the observed variations.

---

<sup>2</sup>If the dips in the extinction that are sometimes seen in LRL 31 are proven to be real, the large error bars on  $A_V$  mean they are still marginally consistent with each other, and the extinction arises from a nearly edge-on disk then the model of Turner et al. (2010) would be a promising explanation for them.

Another possibility related to the interface of the stellar magnetic field and the disk is if the magnetic field is misaligned with respect to the plane of the disk (Figure 4.12i). As material flows onto the field lines it is pulled out of the midplane, preferentially on one hemisphere, creating a warp in the inner disk. Lai & Zhang (2008) develop a model in which the magnetic field coupling between the star and disk can excite waves in the disk when the stellar rotation axis, stellar magnetic axis and disk axis are misaligned. This mechanism could set in place a disk geometry similar to the warps proposed by Flaherty & Muzerolle (2010) to explain the variability, assuming either the density of the inflowing material or the structure of the magnetic field rapidly varies in order to change the height of the warp.

These types of interaction require that the dust extend close to where the disk is truncated by the stellar magnetosphere. We can estimate where material stops flowing in through the disk and is loaded onto the magnetic field lines using the corotation radius, 0.05 AU based on the optical photometric period. Material needs to be within the corotation radius before it is loaded onto the magnetic field lines or else it will be flung out in a wind rather than accreted onto the star (Bouvier et al., 2007b), although the exact location where the magnetic field truncates the disk depends on the strength of the magnetic field and the accretion rate. Our observations of the infrared excess find that the dust extends to the sublimation point, but translating this information into a position requires detailed knowledge of the density and composition of the dust (Isella & Natta, 2005; Kama et al., 2009). Based on different assumptions about the dust properties and the maximum temperature of the dust results in a range of dust sublimation radii from 0.05 - 0.3 AU given the measured luminosity of LRL31 (see the review by Dullemond & Monnier, 2010, for details on various calculations of the location of the

dust inner rim). The smallest radii correspond to large grains ( $\sim$  a few  $\mu\text{m}$ ) at 1800 K, which because of their relative high efficiency in radiating away thermal emission compared to small grains ( $0.1\mu\text{m}$ ) can survive closer to the star before sublimating, while the largest radii correspond to small grains at 1500 K. We have no direct measurements of the grain properties of the inner disk, but the strong silicate emission feature at  $10\mu\text{m}$  is consistent with the presence of small amorphous grains rather than the large grains needed to get the disk down to 0.05 AU. Our measurements of the covering fraction for the inner disk find that it is consistently smaller than expected for a typical T Tauri star, which could be due to significant increase in the grain size for the inner disk versus the outer disk. Substantial grain growth in the inner disk would move the dust edge inward, making it more susceptible to oscillations of the stellar magnetosphere. We would expect to see variability from this process more often around systems with a slow rotation period, hence a much larger corotation radius and it would not preferentially occur around transition disks for which the type of infrared variability observed here is common (Espaillat et al., 2011). Without detailed information on the exact termination of the dusty disk, it is difficult to determine if oscillations in the stellar magnetosphere cause the observed variability.

#### 4.5 Conclusion

We present results from a large synoptic study of the transition disk variable LRL 31. The star itself stays relatively constant showing variability consistent with rotation of cool spots across its surface. We find large variations in the infrared excess and the accretion rate on timescales of weeks. The dust appears to stay at the dust destruction radius, while its scale height rapidly fluctuates by a factor of eight and the infrared flux changes by 0.3 mag. The accretion rate varies

by a factor of 5, and appears to be correlated with the strength of the infrared excess. However, the change in accretion rate is unlikely to be the direct cause for the change in infrared excess. It is also unlikely that the observed variations are due to the influence of a companion within 0.4 AU, based on the lack of periodicity in our Spitzer warm mission monitoring and the presence of an optically thick inner disk. The source of the variability may be related to a companion outside of, but still close to, 0.4 AU or to the dynamic interface between the disk and the stellar magnetic field, assuming the dust extends close enough to the star. Our observations are able to limit the list of plausible physical models, although they cannot exactly define what is happening to the disk. Further constraints on the radial velocity variations, and the exact position of the inner disk will help to select between these models.

Table 4.1. Observing Log

Date	MJD	Wavelength	Resolution	Note
Spex				
29 Dec 2005	53734.2	0.8-5 $\mu$ m	$\sim$ 1500	
09 Nov 2006	54049.3	0.8-5 $\mu$ m	$\sim$ 1500	
10 Oct 2008	54750.5	0.8-5 $\mu$ m	$\sim$ 1500	
11 Oct 2008	54751.5	0.8-5 $\mu$ m	$\sim$ 800	
18 Oct 2008	54757.4	0.8-5 $\mu$ m	$\sim$ 1500	
19 Oct 2009	54758.4	0.8-5 $\mu$ m	$\sim$ 1500	
08 Oct 2009	55112.6	0.8-2.5 $\mu$ m	$\sim$ 800	
09 Oct 2009	55113.6	0.8-2.5 $\mu$ m	$\sim$ 800	
31 Oct 2009	55137.3	0.8-5 $\mu$ m	$\sim$ 800	
04 Nov 2009	55141.5	0.8-5 $\mu$ m	$\sim$ 800	
08 Nov 2009	55144.5	0.8-5 $\mu$ m	$\sim$ 800	
Optical Spectra				
28 Nov 2006	54067	4700-9000Å	$\sim$ 33,000	Keck HIRES
29 Feb 2008	54526	6450-6650Å	$\sim$ 30,000	MMT Hectochelle
03 Dec 2008	54803	4700-9000Å	$\sim$ 33,000	Keck HIRES

Table 4.1—Continued

Date	MJD	Wavelength	Resolution	Note
13 Dec 2007	54447	4000-7500Å	~600	SPOL
16 Dec 2007	54450	4000-7500Å	~600	SPOL
06 Oct 2008	54745	4000-7500Å	~600	SPOL
09 Oct 2008	54748	4000-7500Å	~600	SPOL
28 Oct 2008	54767	4000-7500Å	~600	SPOL
24 Nov 2008	54794	4000-7500Å	~600	SPOL
12 Oct 2009	55116	6000-9500Å	~3500	CAFOS
IRS				
09 Oct 2007	54382	5-40 $\mu$ m	~600	
16 Oct 2007	54389	5-40 $\mu$ m	~600	
24 Feb 2008	54520	5-40 $\mu$ m	~600	
02 Mar 2008	54527	5-40 $\mu$ m	~600	
MIPS				
21 Feb 2004	53056	24 $\mu$ m	photometry	
19 Sep 2004	53267	24 $\mu$ m	photometry	
23 Sep 2007	53466	24 $\mu$ m	photometry	



Table 4.1—Continued

Date	MJD	Wavelength	Resolution	Note
24 Sep 2007	54367	24 $\mu$ m	photometry	
25 Sep 2007	54368	24 $\mu$ m	photometry	
26 Sep 2007	54369	24 $\mu$ m	photometry	
27 Sep 2007	54370	24 $\mu$ m	photometry	
12 Mar 2008	54537	24 $\mu$ m	photometry	
19 Mar 2008	54544	24 $\mu$ m	photometry	
IRAC				
11 Feb 2004	53046	3.6,4.5,5.8,8.0 $\mu$ m	photometry	Cold-mission
08 Sep 2004	53257	3.6,4.5,5.8,8.0 $\mu$ m	photometry	Cold-mission
19 Mar 2009	54910	3.6,4.5,5.8,8.0 $\mu$ m	photometry	Cold-mission
20 Mar 2009	54911	3.6,4.5,5.8,8.0 $\mu$ m	photometry	Cold-mission
21 Mar 2009	54912	3.6,4.5,5.8,8.0 $\mu$ m	photometry	Cold-mission
22 Mar 2009	54913	3.6,4.5,5.8,8.0 $\mu$ m	photometry	Cold-mission
23 Mar 2009	54914	3.6,4.5,5.8,8.0 $\mu$ m	photometry	Cold-mission
03 Oct-07 Nov 2009	55107-55142	3.6,4.5 $\mu$ m	photometry	Warm-mission

Table 4.2. Photometry

Date	J	H	K
2MASS	12.09	10.54	9.69
10 Oct 2008	12.19	10.71	9.95
11 Oct 2008	12.23	10.81	10.08
18 Oct 2008	12.26	10.81	10.07
19 Oct 2008	12.25	10.79	9.99
08 Oct 2009	12.34	10.92	10.29
09 Oct 2009	12.22	-	10.25
31 Oct 2009	12.26	10.83	10.14
04 Nov 2009	12.24	10.77	10.03
08 Nov 2008	12.15	10.68	9.92

Note. — Typical uncertainties in the photometry, dominated by the absolute uncertainty in the flux measurements, are 0.1 mag.

Table 4.3. IRAC photometry

Date	[3.6]	[4.5]	[5.8]	[8.0]
19 Mar 2009	$9.058 \pm 0.002$	$8.781 \pm 0.003$	$8.404 \pm 0.006$	$7.997 \pm 0.03$
20 Mar 2009	$9.064 \pm 0.002$	$8.721 \pm 0.003$	$8.403 \pm 0.006$	$8.033 \pm 0.03$
21 Mar 2009	$8.995 \pm 0.002$	$8.736 \pm 0.003$	$8.347 \pm 0.006$	$8.002 \pm 0.03$
22 Mar 2009	$8.968 \pm 0.002$	$8.639 \pm 0.003$	$8.343 \pm 0.006$	$7.941 \pm 0.03$
23 Mar 2009	$9.071 \pm 0.002$	$8.695 \pm 0.002$	$8.342 \pm 0.006$	$7.981 \pm 0.03$

Table 4.4. Extinction

Date	$A_V$	Wavelength Range
13 Dec 2007	8.8	Optical
06 Oct 2008	9.2	Optical
09 Oct 2008	8.9	Optical
10 Oct 2008	9.5	NIR
11 Oct 2008	8.2	NIR
18 Oct 2008	9.2	NIR
19 Oct 2008	9.2	NIR
28 Oct 2008	8.5	Optical
24 Nov 2008	8.1	Optical
08 Oct 2009	8.8	NIR
09 Oct 2009	8.3	NIR
31 Oct 2009	8.9	NIR
04 Nov 2009	8.7	NIR
08 Nov 2009	8.8	NIR

Note. — The uncertainty in the extinction is 0.5 mag.

Table 4.5. Stellar Luminosity

Date	Stellar Luminosity ( $L/L_{\odot}$ )
10 Oct 2008	$5.3 \pm 0.8$
11 Oct 2008	$3.6 \pm 0.6$
18 Oct 2008	$4.6 \pm 0.7$
19 Oct 2008	$4.6 \pm 0.7$
08 Oct 2009	$3.8 \pm 0.6$
09 Oct 2009	$3.8 \pm 0.6$
31 Oct 2009	$4.2 \pm 0.7$
04 Nov 2008	$4.1 \pm 0.6$
08 Nov 2009	$4.6 \pm 0.7$

Note. — Errors include the 0.1 mag uncertainty in the photometry and the 0.5 mag uncertainty in  $A_V$ .

Table 4.6. Infrared Excess

Date	Veiling	Dust Temperature	Covering Fraction
29 Dec 2005	$0.33 \pm 0.1$	-	-
09 Nov 2006	$0.20 \pm 0.1$	-	
10 Oct 2008	$0.20 \pm 0.1$	$1940 \pm 250$	0.039
11 Oct 2008	$0.32 \pm 0.1$	$2100 \pm 250$	0.084
18 Oct 2008	$0.17 \pm 0.1$	$1820 \pm 200$	0.037
19 Oct 2008	$0.16 \pm 0.1$	$1620 \pm 200$	0.031
08 Oct 2009	$-0.05 \pm 0.1$	-	$0.010^a$
09 Oct 2009	$0.02 \pm 0.1$	-	$0.012^a$
31 Oct 2009	$0.10 \pm 0.1$	$1540 \pm 250$	0.025
04 Nov 2009	$0.23 \pm 0.1$	$2020 \pm 300$	0.048
08 Nov 2009	$0.29 \pm 0.1$	$1780 \pm 250$	0.054

<sup>a</sup>Derived assuming a dust temperature of 1830 K and fitting to the IRAC photometry

Table 4.7. Polarimetry

Date	P(%)	q( $^{\circ}$ )
13 Dec 2007	$8.44 \pm 0.14$	$146.6 \pm 0.5$
16 Dec 2007	$7.66 \pm 0.25$	$144.0 \pm 0.9$
06 Oct 2008	$8.34 \pm 0.12$	$145.7 \pm 0.4$
09 Oct 2008	$7.70 \pm 0.07$	$144.9 \pm 0.3$
28 Oct 2008	$7.84 \pm 0.11$	$144.4 \pm 0.4$
24 Nov 2008	$7.77 \pm 0.23$	$143.2 \pm 0.8$

Table 4.8. Emission Line Tracers of Accretion Rate

Date	$\text{Pa}\beta$ EW ( $\text{\AA}$ )	$\text{Br}\gamma$ EW ( $\text{\AA}$ )	Veiling Corrected $\text{Br}\gamma$ EW ( $\text{\AA}$ )	Veiling
29 Dec 2005	$-3.36 \pm 0.08$ (0.50)	$-3.05 \pm 0.09$ (0.84)	$-2.56 \pm 0.09$ (0.71)	$0.33 \pm 0.1$
09 Nov 2006	$-4.29 \pm 0.04$ (0.37)	$-2.55 \pm 0.02$ (0.18)	$-2.08 \pm 0.02$ (0.15)	$0.20 \pm 0.1$
10 Oct 2008	$-2.74 \pm 0.07$ (0.49)	$-1.52 \pm 0.04$ (0.20)	$-1.20 \pm 0.04$ (0.17)	$0.20 \pm 0.1$
11 Oct 2008	$-2.69 \pm 0.07$ (0.45)	$-1.27 \pm 0.05$ (0.22)	$-0.80 \pm 0.05$ (0.16)	$0.32 \pm 0.1$
18 Oct 2008	$-1.54 \pm 0.04$ (0.12)	$-0.86 \pm 0.02$ (0.07)	$-0.59 \pm 0.02$ (0.05)	$0.17 \pm 0.1$
19 Oct 2008	$-1.78 \pm 0.06$ (0.30)	$-2.11 \pm 0.03$ (0.21)	$-1.84 \pm 0.03$ (0.19)	$0.16 \pm 0.1$
08 Oct 2009	$-1.12 \pm 0.12$ (0.31)	$-1.16 \pm 0.04$ (0.14)	$-1.16 \pm 0.04$ (0.14)	$-0.05 \pm 0.1$
09 Oct 2009	$-0.74 \pm 0.05$ (0.08)	$-1.39 \pm 0.03$ (0.11)	$-1.36 \pm 0.03$ (0.11)	$0.02 \pm 0.1$
31 Oct 2009	$-2.56 \pm 0.04$ (0.22)	$-2.04 \pm 0.02$ (0.14)	$-1.87 \pm 0.02$ (0.13)	$0.10 \pm 0.1$
04 Nov 2009	$-3.31 \pm 0.05$ (0.35)	$-2.29 \pm 0.03$ (0.21)	$-1.94 \pm 0.03$ (0.18)	$0.23 \pm 0.1$
08 Nov 2009	$-3.08 \pm 0.05$ (0.32)	$-2.30 \pm 0.03$ (0.18)	$-1.87 \pm 0.03$ (0.16)	$0.29 \pm 0.1$

Note. — Uncertainties in parenthesis include the uncertainties in the continuum



Table 4.9. Accretion Rates

Date	Flux ( $10^{-14}$ erg s $^{-1}$ cm $^{-2}$ )	$\log(L/L_{\odot})$	$\log(L_{acc}/L_{\odot})$	$\dot{M}$ ( $10^{-8}M_{\odot}yr^{-1}$ )
Pa $\beta$				
10 Oct 2008	$16.6 \pm 2.7$	$-3.28 \pm 0.07$	$-0.59 \pm 0.08$	$1.62 \pm 0.13$
11 Oct 2008	$11.2 \pm 1.8$	$-3.45 \pm 0.07$	$-0.78 \pm 0.08$	$1.05 \pm 0.08$
18 Oct 2008	$8.08 \pm 1.3$	$-3.59 \pm 0.07$	$-0.94 \pm 0.08$	$0.73 \pm 0.06$
19 Oct 2008	$9.43 \pm 1.6$	$-3.52 \pm 0.07$	$-0.86 \pm 0.08$	$0.87 \pm 0.07$
08 Oct 2009	$4.93 \pm 1.2$	$-3.81 \pm 0.11$	$-1.19 \pm 0.13$	$0.41 \pm 0.05$
09 Oct 2009	$3.21 \pm 0.6$	$-3.99 \pm 0.08$	$-1.40 \pm 0.09$	$0.25 \pm 0.02$
31 Oct 2009	$12.5 \pm 2.0$	$-3.40 \pm 0.07$	$-0.73 \pm 0.08$	$1.18 \pm 0.09$
04 Nov 2009	$15.5 \pm 2.5$	$-3.31 \pm 0.07$	$-0.62 \pm 0.08$	$1.52 \pm 0.12$
08 Nov 2009	$16.1 \pm 2.6$	$-3.29 \pm 0.07$	$-0.60 \pm 0.08$	$1.59 \pm 0.13$
Br $\gamma$				
10 Oct 2008	$3.10 \pm 0.38$	$-4.01 \pm 0.05$	$-0.62 \pm 0.06$	$1.52 \pm 0.09$
11 Oct 2008	$1.61 \pm 0.29$	$-4.29 \pm 0.08$	$-0.98 \pm 0.10$	$0.66 \pm 0.07$
18 Oct 2008	$1.32 \pm 0.18$	$-4.38 \pm 0.06$	$-1.09 \pm 0.08$	$0.51 \pm 0.04$
19 Oct 2008	$4.45 \pm 0.48$	$-3.85 \pm 0.05$	$-0.42 \pm 0.06$	$2.40 \pm 0.14$
08 Oct 2009	$2.04 \pm 0.26$	$-4.19 \pm 0.06$	$-0.85 \pm 0.08$	$0.89 \pm 0.07$

Table 4.9—Continued

Date	Flux ( $10^{-14}$ erg s $^{-1}$ cm $^{-2}$ )	log(L/L $_{\odot}$ )	log(L $_{acc}$ /L $_{\odot}$ )	$\dot{M}$ ( $10^{-8} M_{\odot} yr^{-1}$ )
09 Oct 2009	$2.35 \pm 0.26$	$-4.13 \pm 0.05$	$-0.77 \pm 0.06$	$1.09 \pm 0.06$
31 Oct 2009	$3.81 \pm 0.40$	$-3.92 \pm 0.05$	$-0.51 \pm 0.06$	$2.19 \pm 0.12$
04 Nov 2009	$4.28 \pm 0.46$	$-3.87 \pm 0.05$	$-0.45 \pm 0.06$	$2.76 \pm 0.13$
08 Nov 2009	$4.63 \pm 0.50$	$-3.83 \pm 0.05$	$-0.40 \pm 0.06$	$3.32 \pm 0.15$

Note. — Uncertainties include the uncertainty in the spectra and the J and K photometry, but do not include the uncertainty in the conversion from line flux to accretion luminosity. The Br $\gamma$  line fluxes are derived with veiling of the line taken into account.

Table 4.10.  $H\alpha$  EW

Date	$H\alpha$ EW( $\text{\AA}$ )
28 Nov 2006	11.5
13 Dec 2007	4.86
29 Feb 2008	12.0
06 Oct 2008	12.06
09 Oct 2008	10.32
28 Oct 2008	10.77
24 Nov 2008	13.56
03 Dec 2008	8.12
12 Oct 2009	4.02

Table 4.11. IRAC Warm Mission Photometry

MJD-55000	[3.6]	[4.5]
106.91	9.314	9.098
107.30	9.373	9.109
107.57	9.363	9.127
107.81	9.437	9.134
108.13	9.439	9.174
108.38	9.469	9.214
108.58	9.476	9.200
108.81	9.482	9.236
109.58	9.498	9.271
110.50	9.514	9.306
111.07	9.609	9.372
112.43	9.642	9.438
113.07	9.639	9.413
114.73	9.559	9.341
115.37	9.538	9.302
115.97	9.552	9.272
116.32	9.495	9.277
116.62	9.529	9.303
116.72	9.527	9.313
117.13	9.535	9.288

Table 4.11—Continued

MJD-55000	[3.6]	[4.5]
117.21	9.533	9.299
117.46	9.551	9.319
117.69	9.565	9.311
118.60	9.568	9.321
119.25	9.565	9.325
119.93	9.506	9.289
121.21	9.510	9.268
123.07	9.491	9.206
124.96	9.488	9.282
127.68	9.472	9.244
129.81	9.475	9.212
131.27	9.454	9.171
133.38	9.363	9.097
135.61	9.432	9.199
137.52	9.333	9.075
139.07	9.349	9.058
141.52	9.221	8.937
142.13	9.245	8.922

Note. — Uncertainties are 0.017 and 0.014 mag at [3.6] and [4.5] respectively based on the rms fluctuations of non-variable stars in the field

## CHAPTER 5

## TRANSITION DISK VARIABLES

We present results of a multi-wavelength multi-epoch survey of five transition disks in the cluster IC 348 that show significant infrared variability. Using  $3\text{-}8\mu\text{m}$  and  $24\mu\text{m}$  photometry along with  $5\text{-}40\mu\text{m}$  spectroscopy from the Spitzer space telescope, as well as ground-based  $0.8\text{-}5\mu\text{m}$  spectroscopy, optical spectroscopy and near-infrared photometry, covering timescales of days to years, we examine the variability in the disk, stellar and accretion flux. We find substantial variations at all infrared wavelengths on timescales of weeks to months for all of these young stellar objects. This behavior is consistent with changes in the structure of the inner disk, such as scale height fluctuations on a dynamical timescale. Previous observations, along with our near-infrared photometry, indicate that the stellar flux is relatively constant despite the large changes in the infrared flux. Based on our near-infrared spectroscopy of the  $\text{Pa}\beta$  and  $\text{Br}\gamma$  lines we find that the accretion rate is variable in most of the transition disks although it is unlikely that this is the cause of the infrared variability. The behavior observed in these transition disks is not unique when compared to the other cluster members. We discuss some possible physical causes for the variability, including the influence of a companion or of magnetic fields threading the disk.

## 5.1 Introduction

During the star formation process, the circumstellar material goes through many different stages. Early on a dense envelope surrounds the protostar and compact disk, which feeds the star. Eventually this envelope dissipates leaving only the disk behind. After a few million years this disk also disappears, either by

coagulating into planetesimals and planets, or by being removed by a photo-evaporative flow. Once the optically thick disk has been removed the system is left with only a small trace of optically thin dust constituting a debris disk caused by the collisions of planetesimals. While the different evolutionary stages of low mass star formation has been fairly well established, the physical process behind the movement from one stage to the next is not as well understood.

Transition disks represent a stage of disk evolution that is believed to lie between full optically thick disks and debris disks. They are characterized by spectral energy distributions (SEDs) that are deficient in flux at wavelengths typically less than  $10\mu\text{m}$  (e.g. Kim et al., 2009; Merín et al., 2010; Muzerolle et al., 2010). This lack of flux relative to a typical disk indicates a clearing of material from the inner few AU of the system (Andrews et al., 2011), possibly due to the presence of planets or a photo-evaporative flow (Bryden et al., 1999; Alexander et al., 2006). Understanding the gas and dust in this situation is crucial for a complete picture of planet formation and early stellar evolution.

Recently some transition disks have been found to have large infrared variability, which could potentially be related to the clearing of the disk. Muzerolle et al. (2009) study one member of the IC 348 cluster in which the flux shortward of  $8\mu\text{m}$  increases while the flux longward of  $8\mu\text{m}$  decreases, both in as little as one week. Espaillat et al. (2011) see this 'seesaw' behavior in a collection of 14 transition disks in Taurus and Chameleon observed with Spitzer 5-40 $\mu\text{m}$  IRS spectroscopy. The strength, speed, and wavelength dependence of the variability was surprising given the previously known sources of variability in pre-main sequence stars, such as starspots and stellar occultations. Fluctuations in the  $20\mu\text{m}$  flux on weekly timescales is unexpected given that this wavelength traces dust at a few AU where the dynamical timescale is closer to years. Geometric models of

the disk suggest that this variability may be due to changes in the scale height of the inner disk (Flaherty & Muzerolle, 2010; Espaillat et al., 2011), although multi-wavelength observations are needed to put constraints on the physical source of the variability (Flaherty et al., 2011).

Here we present multi-wavelength multi-epoch observations of five transition disks in IC 348 designed to constrain the properties of their variability. We also include results from a sixth previously published example (Flaherty et al., 2011). In section 5.2 we present our observations of the infrared variability, as traced by multiple epochs of 3-8 $\mu$ m, 24 $\mu$ m photometry and 5-40 $\mu$ m spectroscopy from Spitzer, as well as measurements of the accretion rate variability using ground-based near-infrared spectra. We then use this information to determine if the same process is operating in all of these stars, if this process is common among normal disks and what could be its physical cause.

## 5.2 Variability Observations

### 5.2.1 Data

We obtained multiple epochs (2007-2009) of data from 4000Å out to 40 $\mu$ m on the IC 348 transition disks LRL 2, 21, 58, 67, 1679 (Luhman et al., 2003; Muench et al., 2007) as part of the same program that observed the IC 348 transition disk LRL 31 (Flaherty et al., 2011). We also include previous infrared Spitzer observations taken as early as 2004 to extend our temporal coverage. Table 5.1 lists all of the observations for each source, including the days on which these measurements were taken. These observations include:

- 10 epochs of Spitzer 24 $\mu$ m photometry (Table 5.2). Two epochs were taken seven months apart in 2004 as part of the c2d map of IC 348 (Rebull et al., 2007) while another epoch was taken in 2004 as part of GTO observations



(Lada et al., 2006). We obtained five consecutive days of monitoring in Sep 2007 followed in Mar 2008 by two epochs separated by one week.

- 7 epochs of Spitzer IRAC cold-mission 3.6, 4.5, 5.8 and 8.0  $\mu\text{m}$  photometry (Table 5.3). One epoch was taken in 2004 as part of the c2d coverage (Jørgensen, et al., 2006) while GTO observations were also performed in 2004 (Lada et al., 2006). We obtained five consecutive days of photometry in Mar 2009.
- 4 epochs of Spitzer IRS 5-40  $\mu\text{m}$  spectra. Two spectra were taken a week apart in Oct 2007, while two more were taken in Mar 2008, also separated by one week
- 38 epochs of Spitzer IRAC warm-mission 3.6 and 4.5  $\mu\text{m}$  photometry spread over 40 days in fall 2009 (Table 5.4). The cadence for this photometry ranged from four observations a day to one observation every two days throughout the visibility window.
- One epoch of low-resolution optical spectra taken with CAFOS instrument on the 2.2-m telescope of the Calar-Alto Observatory of LRL 21, 58 and 1679 in fall 2009.
- Multiple epochs of 0.8-5  $\mu\text{m}$  spectroscopy with Spex on IRTF in fall 2008 (LRL 21, 1679) and fall 2009 (LRL 2, 21, 58, 1679). The exact number of epochs and the wavelength coverage of the spectra varies from source to source, with each object getting at least two 0.8-2.5  $\mu\text{m}$  spectra.
- One epoch of high-resolution optical spectra of LRL 21, 58, 67 and 1679 taken with Hectochelle on the MMT in Feb 2008.

Details on the data reduction can be found in Flaherty et al. (2011). We also observed four non-accreting diskless weak line T Tauri stars (WTTS) in Taurus (K0

star LkCa 19, A2 star HD 57928, M3 star LkCa21, M1 star JH 108) with Spex to use as standards for the 0.8-2.5 $\mu$ m spectroscopy. We have found that pre-main sequence stars provide a much better template than the dwarfs and giants in the IRTF spectral library (Rayner et al., 2009) when comparing the spectral shape and strength of the absorption lines. This is especially true for the spectral shapes of the late-type stars and the absorption lines in the early type stars. For the IRS spectra, unlike with LRL 31, we did not obtain both Short-Low (SL) and Long-Low (LL) spectra on every epoch, due to the significant background emission that made it difficult to extract the LL spectra. For LRL 2 and 58 we only obtained LL spectra in the first two epochs. These two sources, especially LRL 58, are the most susceptible to systematic uncertainties in the long wavelength end due to the large background. The background emission also leads to a systematic offset between the SL and LL spectra that is seen in LRL 2, 58 and 67. When comparing spectra taken on different epochs we have scaled down the LL spectra to match the SL spectra.

### 5.2.2 Stellar Properties

Here we summarize the stellar properties, and any evidence for variability in these properties, based on the literature and our own measurements.

#### 5.2.2.1 LRL 2

LRL 2 is a pre-main sequence A2 star with a bolometric luminosity of  $137L_{\odot}$ , a radius of  $5R_{\odot}$  (Luhman et al., 2003) with a mass of  $\sim 3.5M_{\odot}$  based on the Siess et al. (2000) 3 Myr isochrones. We can estimate the extinction using the shape of the 0.8-2.5 $\mu$ m spectra, ignoring the K-band whose shape may be influenced by dust emission. In our two epochs of near-infrared spectra we measure an average extinction of  $A_V=2.9$  (Table 5.5), which is consistent with previous estimates

(Luhman et al., 2003) given that we use a slightly different extinction law ( $R_V=5.5$  vs. 3.1, see Flaherty et al. (2011) for details). Previous studies have found no evidence for variability in the optical, suggesting that the photospheric flux is steady (Cohen et al., 2004; Littlefair et al., 2005).

#### 5.2.2.2 LRL 21

LRL 21 is a K0 star originally classified by Luhman et al. (2003), whose stellar flux varies substantially. We were able to obtain seven epochs of near-infrared photometry concurrent with our ground-based infrared spectra. This includes three epochs in 2008 separated by one week, 4 epochs in 2009 spread out over one month and 2MASS photometry taken in 1998. Details on the reduction of these data, along with how the luminosity is derived from the J band photometry, can be found in Flaherty et al. (2011). We find large year-to-year variations in the J band flux (Table 5.6), which is dominated by stellar emission, but no daily or weekly fluctuations. In 2009, when we have contemporaneous near-infrared and 3.6,4.5  $\mu\text{m}$  photometry, we find no significant change in the J band flux despite a large increase in the mid-infrared flux. Optical photometry from Luhman et al. (2003) ( $I=13.21$ ) and Cieza & Baliber (2006) ( $R=14.69$ ) is consistent with the low stellar flux state (Fig 5.3). Cieza & Baliber (2006) find small short-term optical fluctuations likely due to cool spots rotating across the surface of the star and use this to measure a rotation period of 2.5 days. This is consistent with the lack of large daily and weekly changes in the stellar flux in our near-infrared photometry. Our estimates of the luminosity from the J band fluxes range over 2.52-3.66  $L_\odot$  (Table 5.7), which corresponds to  $M \sim 1.8 M_\odot$  based on the Siess et al. (2000) isochrones. We measure a constant extinction ( $A_V=4.2$ , Table 5.5) during each epoch of near infrared photometry, suggesting that the obscuration is not variable, unless the obscuring source has large enough grains that it does not

reddden the central star.

There is also evidence that this system is a binary. Based on our high-resolution optical spectra, we find two peaks in the cross-correlation function, one at -15.7 km/sec and one at 66.8 km/sec (Table 5.8). Dahm (2008) measure a radial velocity of +17.01km/sec, but do not mention any sign of binarity. It is possible that Dahm (2008) observed the system during a phase when the two components were aligned along the line of sight and there was no significant difference in their radial velocity.

#### 5.2.2.3 LRL 58

LRL 58 is a M1.25 star with a luminosity of  $0.72L_{\odot}$  and a radius of  $2.1R_{\odot}$  (Luhman et al., 2003). Its mass is  $\sim 0.7M_{\odot}$  based on its position on the HR diagram relative to the Siess et al. (2000) 3 Myr isochrone. Cohen et al. (2004) and Cieza & Baliber (2006) detect periodic variability in the optical with a period of 7.4 days, consistent with the rotation of star spots across the stellar surface. The I band flux is roughly constant over years ( $I=14.10, 14.32, 14.18$  from Cohen et al. (2004), Cieza & Baliber (2006), Littlefair et al. (2005) respectively) suggesting that there are no large fluctuations in stellar flux. From our hectochelle data we measure a radial velocity of 14.2km/sec and an upper limit on the rotational velocity of 15.0 km/sec (Table 5.8). Based on two epochs of near-infrared spectra, its extinction is constant at  $A_V=3.4$  (Table 5.5). Unlike LRL 21, there is no substantial variation in the stellar flux of LRL 58.

#### 5.2.2.4 LRL 67

LRL 67 is a M0.75 star with a luminosity of  $0.48L_{\odot}$ , a radius of  $1.6R_{\odot}$  (Luhman et al., 2003), and a mass of  $\sim 0.6M_{\odot}$  (Siess et al., 2000). Dahm (2008) measured the radial velocity to be 15.09 km/sec, with  $v \sin i=13.59$  km/sec, Nordhagen et

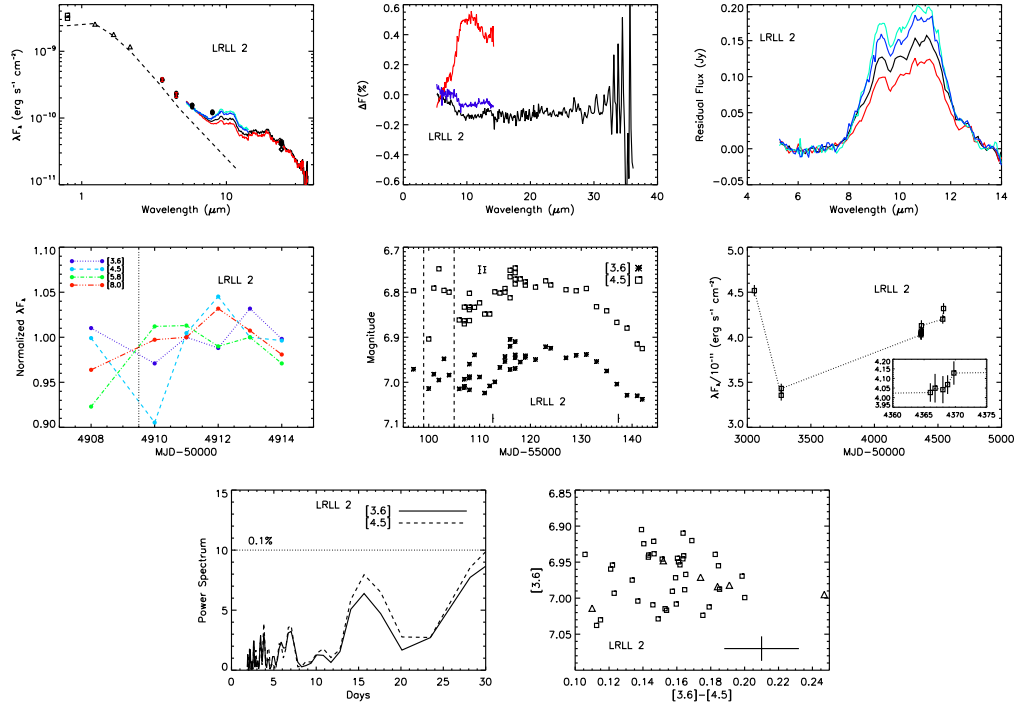


Figure 5.1 Spitzer data for LRL 2. *Top left*: The spectral energy distribution showing the IRS data (colored lines), the IRAC cold mission data (dots), JHK photometry (triangles), optical photometry (squares) and the range of the IRAC warm-mission photometry (error bars at 3.6,4.5 $\mu$ m). A reddened stellar photosphere from Kenyon & Hartmann (1995) is shown as the dashed line for comparison. *Top middle*: Difference spectra between different epochs of IRS spectra. Black line is the change from epoch 1 to epoch 2 (separated by one week), red line is the change from epoch 2 to epoch 3 (separated by 5 months) and the blue line is the change from epochs 3 to epoch 4 (separated by one week). *Top right*: Residual flux in the silicate feature after the continuum has been subtracted. *Middle left*: Cold mission light curves from our five consecutive days of monitoring along with earlier observations (left of dotted line). Different wavelengths are marked by different colors and lines, with the flux normalized to the median in each band. *center*: Warm-mission light curve. The error bars show the uncertainty in the 3.6 and 4.5 $\mu$ m warm-mission photometry (left and right error bar respectively). Vertical bars show the dates when near-infrared spectra were obtained. Points to the left of the dashed line are from our five consecutive days of monitoring, as well as previous observations during the Spitzer cold-mission. *Middle right*: MIPS 24 $\mu$ m light curve. Inset zooms in on the five consecutive days of photometry. *Bottom left* Lomb-Scargle normalized periodogram based on the warm-mission monitoring. The horizontal dotted line indicates a false alarm probability of 0.1%. *Bottom middle* Color-magnitude diagram with warm-mission photometry marked with squares, and cold-mission photometry marked with triangles. The error bar shows the uncertainty in the photometry.

al. (2006) find  $v_r=16.9$  km/sec with  $v_{\text{ sini}} < 11.0$  km/sec and our hectochelle data measure  $v_r=15.0$  km/sec and  $v_{\text{ sini}} < 15.0$  km/sec (Table 5.8). The lack of significant variation in the radial velocity, suggests that there is no massive companion in this system. Cieza & Baliber (2006) did not find evidence for periodic optical fluctuations. We do not have any near-infrared spectra of this star with which to estimate the extinction and we adopt the value from Luhman et al. (2003) ( $A_V=2.4$ ). As with LRL 2 and 58, there is no strong evidence for large fluctuations in the stellar flux.

#### 5.2.2.5 LRL 1679

LRL 1679 is the faintest star in our sample and was classified as a M3.5 star with  $L=0.21L_{\odot}$  and  $R_*=1.3R_{\odot}$  by Muench et al. (2007). We estimate its mass as  $\sim 0.3M_{\odot}$  using the Siess et al. (2000) isochrones. Based on five epochs of near-infrared spectra (3 in 2008, 2 in 2009) we find that its extinction is constant at  $A_V=5.8$  (Table 5.5). There is no mention of periodic optical fluctuations in the literature, although this source may have been too faint for these surveys or outside the field of view (at Dec=31:58:255 it is south of the cluster center).

#### 5.2.2.6 LRL 31

LRL 31 is a G6 star with a luminosity of  $4.3L_{\odot}$ ,  $R_*=2.1R_{\odot}$ ,  $M=1.5M_{\odot}$  and  $A_V = 8.8$  (Flaherty et al., 2011). Our multiple epochs of J-band photometry do not show significant fluctuations in the luminosity, although there may be long term trends in the stellar flux. The near-infrared spectra show that the extinction is constant on timescales of weeks and years. There is some evidence for variations in the radial velocity of the star, suggesting the presence of a companion, although with only three epochs this conclusion is not definitive.

### 5.2.2.7 Summary

Our sample represents a wide range of stellar masses, from  $0.3\text{--}3.5M_{\odot}$ , which allows us to look for correlations between properties of the infrared fluctuations and mass. Except for LRL 21, none of the sample show evidence for large changes in the stellar flux, either due to occultation events or hot spots rotating across the surface of the star. Some do show small fluctuations due to cold spots rotating across the surface of the star in previous optical monitoring surveys of IC 348. In the case of LRL 21, changes occur from one year to the next, but not on daily or weekly timescales.

### 5.2.3 Infrared Variability

Our infrared observations cover  $\lambda = 2 - 40\mu\text{m}$  on timescales of days to years allowing us to look for any wavelength dependence in the fluctuations, as well as constrain the variability timescale.

#### 5.2.3.1 LRL 2

The IRS spectra of LRL 2 show large ( $\sim 20\%$ ) variations in as little as one week and the change in the SED shows a wavelength dependence where the SED appears to pivot at  $\lambda = 6\mu\text{m}$  (Fig 5.1 summarizes all of the Spitzer data). There is a systematic offset between the LL and SL spectra ( $\sim 10\%$ ) and we reduce the LL spectra by this amount when comparing spectra from different epochs. In order to determine if the silicate flux changes in addition to the continuum we subtract a second order fit to the continuum, defined as  $5 < \lambda < 7\mu\text{m}$  and  $13 < \lambda < 14\mu\text{m}$ , from the silicate feature to produce the result in Figure 5.1. The flux of the silicate emission feature changes between these spectra, and is proportional to the long-wavelength continuum. The  $24\mu\text{m}$  photometry shows flux variations up to 25%, similar to that seen in the IRS spectra. Our five consecutive days of  $24\mu\text{m}$  mon-

itoring shows little change, suggesting that the largest variations are on longer timescales. This is consistent with the five consecutive days of  $3\text{--}8\mu\text{m}$  photometry, which show almost no variation. Our  $3.6, 4.5\mu\text{m}$  monitoring offers a more complete picture of the timescale and shows slow variations ( $\sim 0.1$  mag) on weekly timescales with no detectable periodicity.

These long-wavelength data trace material a few AU from the star while our ground-based spectroscopy is sensitive to much warmer dust close to the star, assuming thermal equilibrium temperatures. Based on the shape of the  $0.8\text{--}2.5\mu\text{m}$  spectra, there appears to be excess emission in K band (Fig 5.2). We estimate the veiling to be  $\sim 0.2$  in the K-band based on the shape of the spectra<sup>1</sup>. This is weaker than is typically seen around stars with dust in a puffed inner rim of a disk. We do not have enough spectral information to determine if the excess is due to hot dust at the dust destruction radius, or optically thin material further out, but we can say that the excess, including the  $3.6$  and  $4.5\mu\text{m}$  photometry, is consistent with optically thick dust at  $T > 1000\text{K}$ .

### 5.2.3.2 LRL 21

In the IRS spectra, LRL 21 displays large variations ( $\sim 40\%$ ) at  $\lambda < 15\mu\text{m}$  in observations separated by one week with no fluctuations ( $< 8\%$ ) at longer wavelengths (Fig 5.3). However, the  $24\mu\text{m}$  photometry does show fluctuations up to  $20\%$ , and this flux is systematically lower than the IRS spectra, suggesting that the long wavelength flux does vary. The flux of the silicate feature does not change with time, despite the change in the underlying continuum. Our five consecutive days of  $3\text{--}8\mu\text{m}$  photometry, as well as our  $3.6, 4.5\mu\text{m}$  monitoring show rapid variations even from one day to the next, although the predominate timescale appears

---

<sup>1</sup>Veiling cannot be determined from line EWs because of the absence of non-hydrogen photospheric absorption lines in the A2 stellar spectrum



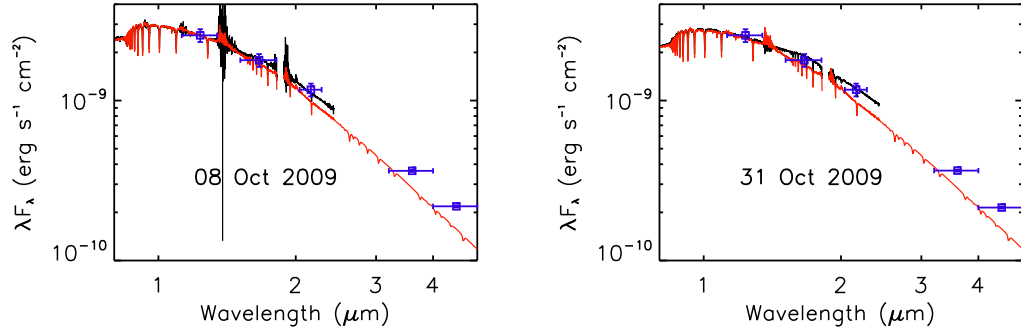


Figure 5.2 Spex spectra for LRL 2. Spectra have been scaled to 2MASS photometry. IRAC warm-mission photometry has been included where available. A stellar photosphere (HD 57928 + a kurucz model) shown in red has been reddened by  $A_V=2.9$  and scaled to J band of the spectra for comparison. Blue points are the photometry, and the error bars in the X-axis show the size of the passbands.

to be weeks and months. Of all the stars in our sample, this one shows the largest fluctuations, predominately on timescales of weeks to months, with no sign of periodicity.

For LRL 21 we have ground-based spectra (Fig 5.4) allowing us to measure the shape of the excess emission SED from 0.8-5 $\mu$ m. First we measure the veiling by comparing the LRL 21 spectra to that of a WTTS of the same spectral type (LkCa 19) in fifteen small bins from 0.8 to 2.5 $\mu$ m. We fit a line to these veiling measurements as a function of wavelength to derive the K-band (2.15 $\mu$ m) veiling. We use this value to normalize the LRL 21 spectra to the photosphere level, whose shape is estimated using our K0 WTTS standard along with a Kurucz model extension ( $T_{eff}=5250$ ,  $\log g = 2.5$ ) beyond 2.5 $\mu$ m. The LRL 21 spectra and the photosphere are then subtracted to produce a spectrum of the infrared excess, which in most T Tauri stars is dominated by emission from the optically thick inner wall at the dust destruction radius (Muzerolle et al., 2003). More details on this procedure can be found in Flaherty et al. (2011). The 0.8-5 $\mu$ m excess

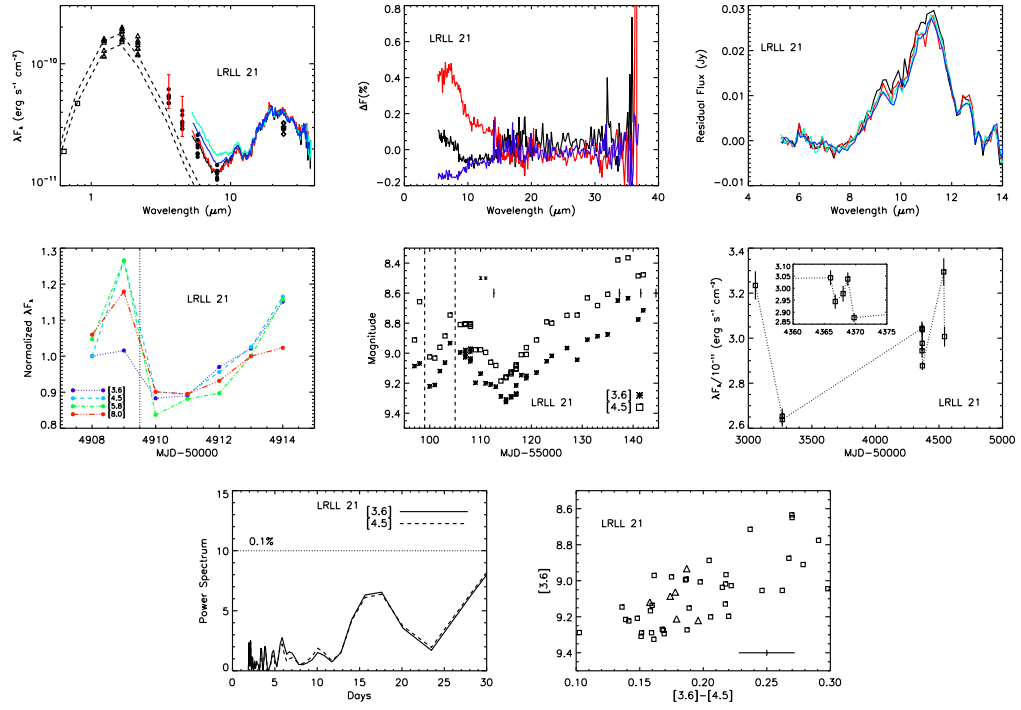


Figure 5.3 Same as Figure 5.1 but for LRL 21. Two photospheres are shown in the SED plot, corresponding to the high and low state of the stellar flux.

emission, shown in Figure 5.5, is consistent with an optically thick disk with a temperature of 1900 K at every epoch (Table 5.9), while the strength of the emission rapidly varies with K-band veiling measurements ranging from 0.19 to 0.56 (Table 5.9). The typical uncertainties in the derived temperature and veiling are 200K and 0.1 respectively. Not taking account of a possible massive companion (discussed above) could lead us to overestimate the dust temperature by  $\sim 100$  K and underestimate the K-band veiling by  $\sim 0.1$ . In 2009 we see a large increase in veiling from Oct 8 to Oct 31, which is consistent with the large increase in infrared flux seen in the  $3.6$  and  $4.5\mu\text{m}$  photometry at the same time. The constant temperature with changing flux suggests that the inner edge of the disk is set by dust sublimation and not the dynamical carving of a companion. It is also consistent with large changes in the scale height of the inner disk, since the flux is proportional to  $H/R$  where  $H$  is the height of the disk and  $R$  is its radius. The  $[3.6]\text{--}[4.5]$  color of the system gets redder as the flux increases (Fig 5.3), which is also consistent with blackbody emission from the dust destruction radius changing in strength, but not in temperature.

### 5.2.3.3 LRL 58

In the IRS spectra, LRL 58 displays no variations ( $< 5\%$  for  $\lambda < 14\mu\text{m}$  and  $< 20\%$  for  $\lambda \geq 14\mu\text{m}$ ), although the long-wavelength end has large systematic uncertainties due to uncertain background subtraction (Figure 5.7). These systematic uncertainties are the likely source of the mismatch between the SL and LL spectra at  $14\mu\text{m}$ , which we correct for by decreasing the LL spectra by a constant multiplicative factor when comparing different epochs. The  $24\mu\text{m}$  photometry shows significant fluctuations (14%), which fall below our detection limit in the IRS spectra, on predominately weekly and longer timescales. The five consecutive days of  $3\text{--}8\mu\text{m}$  photometry show a steady increase in flux, while the  $3.6$  and

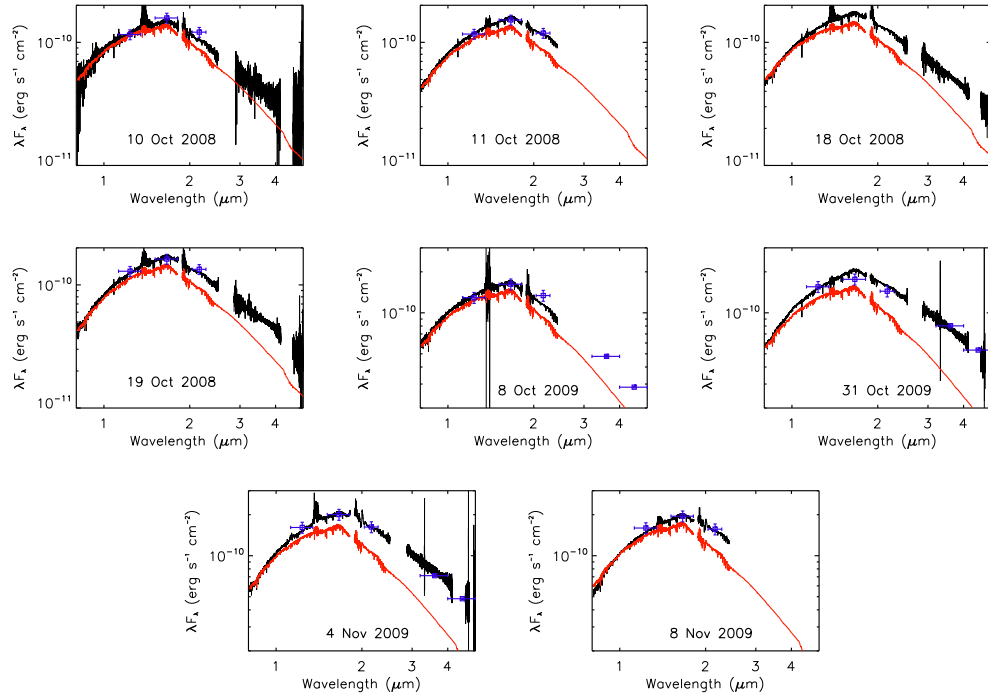


Figure 5.4 Spex spectra (black line) and photometry (blue points) for LRL 21. Spectra have been scaled to match photometry. A stellar photosphere (LkCa 19 + kurucz model) shown in red has been reddened by the  $A_V$  measured on each night to LRL 21 and scaled to the short wavelength flux of the spectra. Note the change in scale in 2009, when the star is brighter than in 2008.

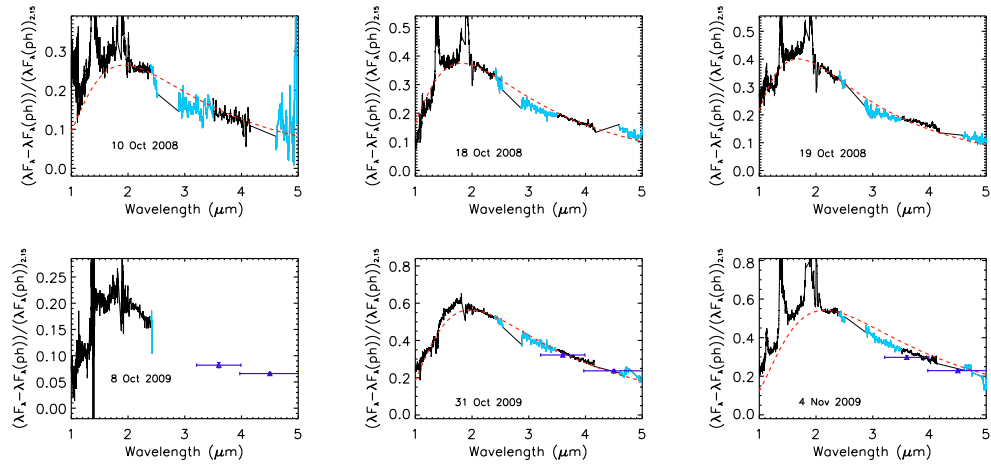


Figure 5.5 The infrared excess of LRL 21. Each plot shows the difference between LRL 21 and the standard, normalized to the photospheric flux at  $2.15\mu\text{m}$ . On each plot the best fit blackbody is shown with a red dashed line and the  $3.6, 4.5\mu\text{m}$  photometry is included when available. Each spectra has been smooth by a median filter  $0.01\mu\text{m}$  wide in order to reduce the noise in the continuum. The parts of the spectra marked in blue are strongly affected by the telluric correction. Note that the scale changes for each plot. The strength of the excess shows large variations from night to night, although the temperature stays roughly constant.

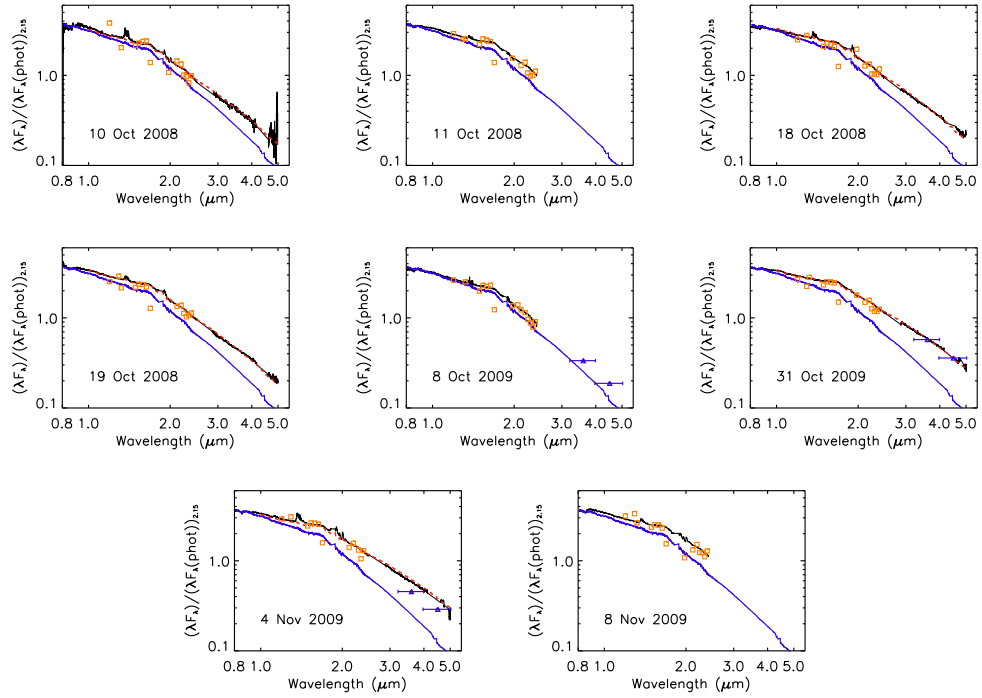


Figure 5.6 Dereddened spectra of LRL 21, along with the veiling measurements (orange squares), 3.6 and 4.5  $\mu\text{m}$  photometry where available (blue triangles) and a stellar photosphere for comparison (blue line). Red dashed line is the best fit photosphere+blackbody emission for those days where we have spectra beyond 2.5  $\mu\text{m}$ . LRL 21 shows a large range in the strength of the excess throughout our observations.

4.5 $\mu$ m photometry confirms that large (0.3 mag), daily fluctuations occur, with no evidence for periodicity. When comparing the IRS spectra with the 2-8 $\mu$ m photometry there appear to be very large fluctuations that have not been captured during any single monitoring campaign. The 3-8 $\mu$ m photometry shows a distinct excess in all but one epoch, while the IRS spectra is consistent with almost no excess at these wavelengths. Only at 8 $\mu$ m are the photometry and the spectra consistent with the same flux level. In the 3-8 $\mu$ m monitoring there is a distinct wavelength dependence: as the wavelength increases the size of the fluctuation decreases. This is consistent with the SED variations between the IRS spectra and the photometry suggesting that the SED pivots at  $\lambda = 8\mu\text{m}$ , similar to LRL 21 and 31. Significant veiling is present in the 0.8-2.5 $\mu$ m spectra ( $r_K=0.46, 0.48$ , Table 5.9, Fig 5.8, 5.9). As with LRL 2 we cannot constrain the exact source of this excess, but it is consistent with hot dust emission ( $> 1200\text{K}$ ) from close to the star.

#### 5.2.3.4 LRL 67

In the IRS spectra, LRL 67 displays no variations ( $< 3\%$  at  $\lambda < 14\mu\text{m}$  and  $< 10\%$  at  $\lambda \geq 14\mu\text{m}$ ) (Fig 5.10). LRL 67 also has a systematic offset between the SL and LL spectra at 14 $\mu$ m, as in LRL 2 and 58, which we account for when comparing different epochs. The 24 $\mu$ m photometry displays small fluctuations of 4%, with some changes even on daily timescales. The five consecutive days of 3-8 $\mu$ m photometry show no fluctuations ( $< 5\%$ ), while the 3.6 and 4.5 $\mu$ m monitoring does show large (0.4 mag) variations with no periodicity. Most of the change during the monitoring occurs during a brightening event over the last week. Prior to this the infrared flux varies by less than 0.2 mag, which is still significant given the small uncertainties in these data. The measurements are consistent with larger fluctuations at short wavelengths, similar to LRL 21, possibly involving periods of quiescence. During the 3.6, 4.5 $\mu$ m monitoring the [3.6]-[4.5] color gets redder

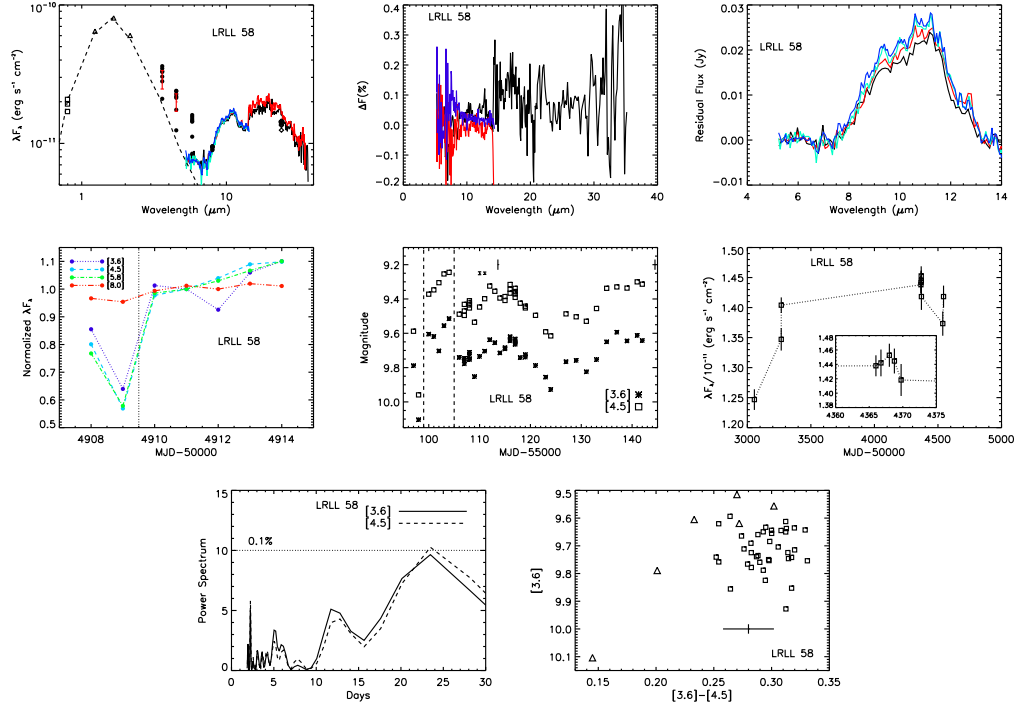


Figure 5.7 Same as Figure 5.1 but for LRL 58.

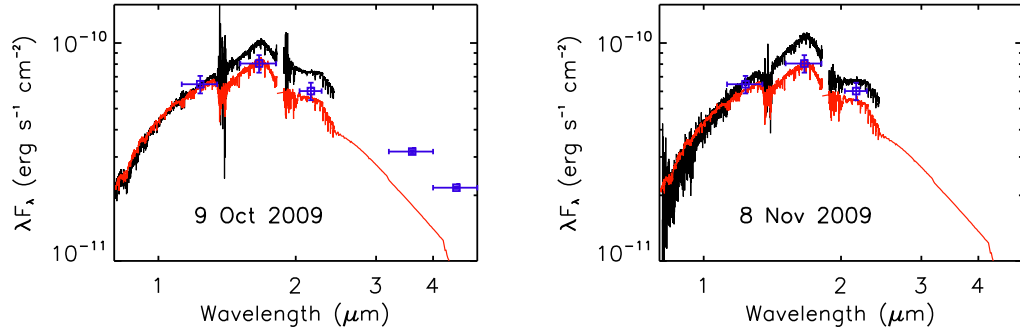


Figure 5.8 Spex spectra (black line) and photometry (blue points) for LRL 58. Spectra have been scaled to match 2MASS photometry. A stellar photosphere (JH 108 + kurucz model) shown in red has been reddened by the  $A_V$  measured on each night to LRL 58 and scaled to the short wavelength flux of the spectra. The mismatch between the spectra and the 2MASS photometry is likely a sign of variability between these epochs.



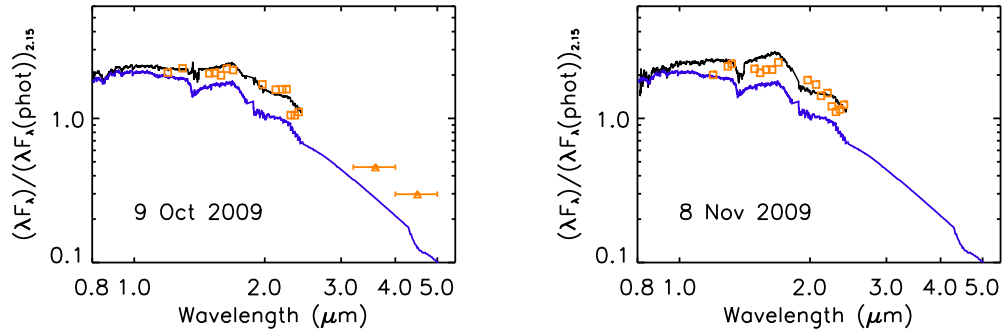


Figure 5.9 Dereddened spectra of LRL 58, along with the veiling measurements (orange squares), 3.6 and 4.5 $\mu$ m photometry where available (orange triangles) and a stellar photosphere for comparison (blue line). LRL 58 shows a strong excess throughout our spectra.

as the source gets brighter (Fig 5.10), consistent with a changing flux level from warm dust close to the star, similar to LRL 21.

#### 5.2.3.5 LRL 1679

In the IRS spectra, LRL 1679 displays large fluctuations ( $\sim 50\%$ ) on timescales of months, but no weekly changes ( $< 5\%$  for  $\lambda < 14\mu$ m and  $< 20\%$  for  $\lambda > 14\mu$ m) (Fig 5.11). The SED appears to pivot, similar to LRL 2, 21, 31 and 58, at  $\lambda = 14\mu$ m. The 24 $\mu$ m photometry displays fluctuations (50%) that are consistent with those seen in the IRS spectra. Despite the large fluctuations in the continuum, there is no change in the flux of the silicate feature (although it is the weakest feature in our sample). The five consecutive days of 3-8 $\mu$ m photometry show no variation ( $< 5\%$ ), consistent with the longer variability timescale. This is also confirmed in the 3.6 and 4.5 $\mu$ m monitoring, which shows a steady increase in the flux of 0.1 mag over the course of 40 days with no evidence for periodicity. The change in [3.6]-[4.5] color between the 3-8 $\mu$ m photometry and the 3.6,4.5 $\mu$ m monitoring, where the source gets redder as it gets brighter, is consistent with optically thick dust in the inner disk getting brighter with time, although there is

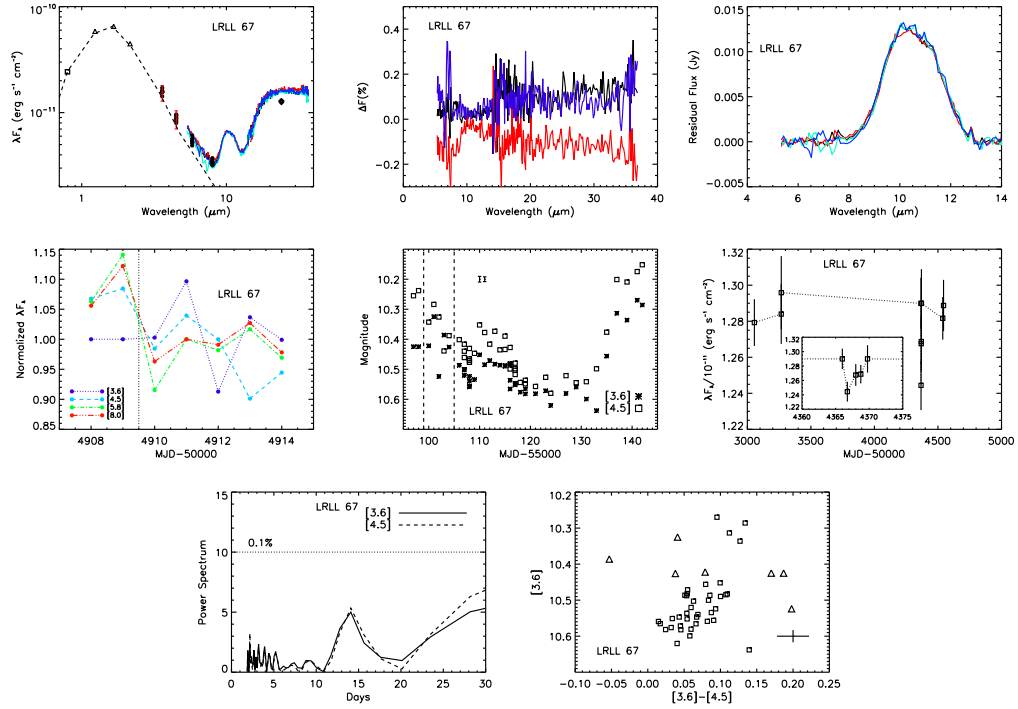


Figure 5.10 Same as Figure 5.1 but for LRL 67.

no evidence of veiling in the  $0.8\text{--}2.5\mu\text{m}$  spectra (Fig 5.12). The short-wavelength excess can be very small, almost at the level of the photosphere in some epochs, and it is possible that when we obtained our near-infrared spectra the excess was below our detection limit. The non-zero  $[3.6]\text{--}[4.5]$  color suggests that there is some hot dust close to the star creating a weak excess.

#### 5.2.3.6 LRL 31

Here we summarize previously published results on LRL 31 (Muzerolle et al., 2009; Flaherty et al., 2011) to compare with these other transition disks. In the IRS spectra, LRL 31 displays large fluctuations ( $\sim 60\%$ ) in as little as one week with a clear wavelength dependence in which the SED appears to pivot around  $8\mu\text{m}$ . The  $24\mu\text{m}$  photometry displays large fluctuations (30%) consistent with those seen in the IRS spectra. The flux of the silicate feature also changes with

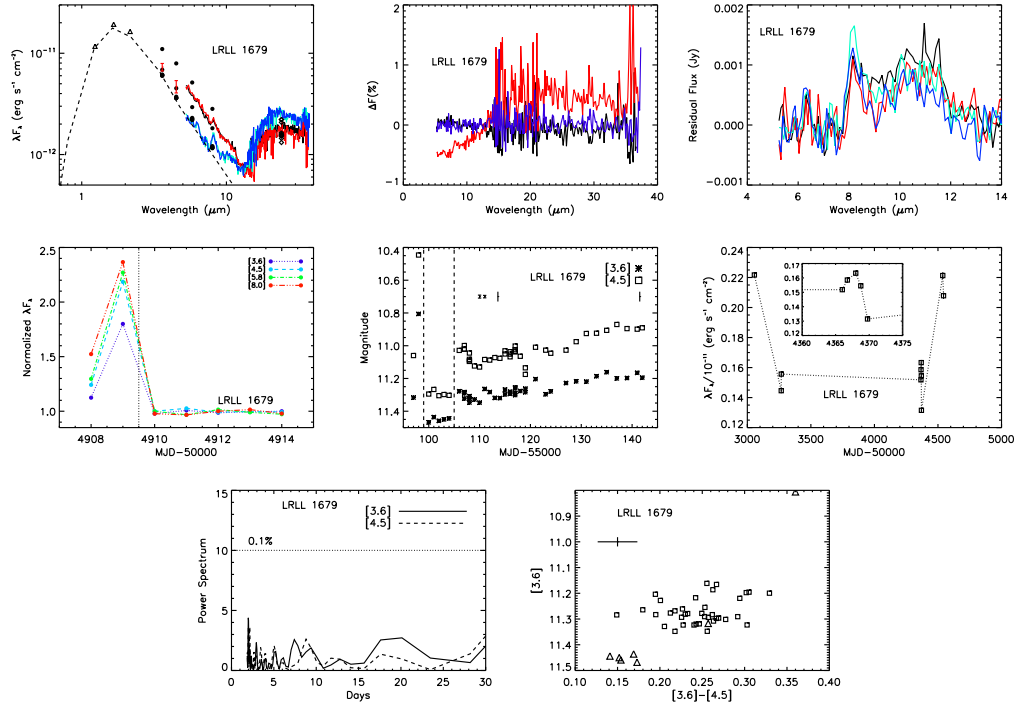


Figure 5.11 Same as Figure 5.1 but for LRL 1679.

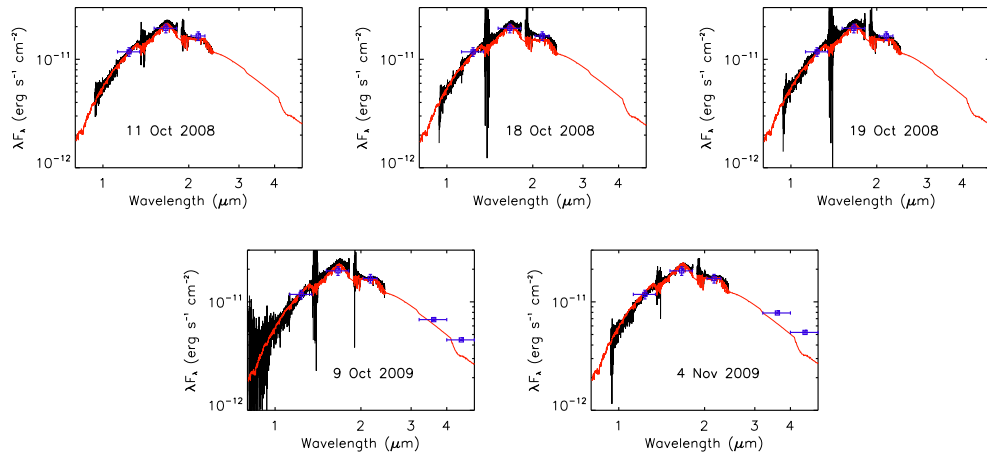


Figure 5.12 Spex spectra (black line) and photometry (blue points) for LRL 1679. Spectra have been scaled to match 2MASS photometry. A stellar photosphere (LkCa 21 + kurucz model) shown in red has been reddened by the  $A_V$  measured on each night to LRL 1679 and scaled to the short wavelength flux of the spectra. Very little excess is seen throughout the observations.

time, and the changes are correlated with the long-wavelength fluctuations. The 3.6 and 4.5 $\mu\text{m}$  monitoring shows large (0.3 mag) fluctuations predominately on weekly timescales and a light curve shape almost identical to LRL 21. Multiple epochs measuring the shape of the 2-5 $\mu\text{m}$  excess find that this excess looks like a single temperature blackbody at  $\sim 1700\text{K}$  whose strength rapidly varies with time. The [3.6]-[4.5] color of the system appears to get redder as it gets brighter, similar to LRL 21, 67 and 1679. There was no evidence for periodicity in the light curve.

#### 5.2.3.7 Summary

The exact size, wavelength dependence and timescale of the fluctuations varies from source to source, but overall all six sources show variability at all wavelengths on weekly to monthly timescales. Some show very large flux changes, up to 50%, while others show much smaller variations. The timescales range from weeks to months, with no evidence for long year-to-year changes, suggesting that we are not observing the remnants of a single burst or the slow removal/addition of dust to the disk. None of them show strong evidence for periodicity in the warm mission data, which is sensitive to  $P=2\text{-}25$  days.

#### 5.2.4 Gas Properties

Our optical and near-infrared spectroscopy of the hydrogen emission lines ( $\text{H}\alpha$ ,  $\text{Pa}\beta$  and  $\text{Br}\gamma$ ) whose flux is directly related to the accretion rate, as well as measurements from the literature, allow us to characterize the level of variability in the accretion rate and look for any connection with the infrared variability. Here we summarize the observations for each of our six transition disks.

#### 5.2.4.1 LRL 2

During two epochs of observations in 2009 separated by 3 weeks we see little change in the strength of the  $\text{Pa}\beta$  and  $\text{Br}\gamma$  lines (Fig 5.13). The line strengths are weaker than simple photospheric absorption, suggesting additional emission within the system, most likely due to hot gas in the accretion flow, and in Figure 5.13 we display the lines after the photosphere has been subtracted, showing the emission more clearly, while Table 5.10 lists the measured equivalent widths (EW). The difference in EW between the two epochs is most likely due to a difference in our determination of the continuum rather than real fluctuations in the accretion rate. A slight mismatch in spectral type can have a significant effect on our subtraction of the line, especially in the line wings, but does not strongly affect the conclusion that there is some emission in the line due to an accretion flow. We can convert from EW to line flux using the JHK photometry combined with the veiling to estimate the continuum level and then convert from line flux to accretion rate (Muzerolle et al., 1998). The results are listed in Table 5.11. More detail on this process as applied to LRL 31 can be found in Flaherty et al. (2011). The average accretion rate is  $3 \times 10^{-7} M_{\odot} \text{yr}^{-1}$  and the accretion luminosity is small relative to the stellar luminosity ( $L_{\text{acc}}/L_{*}=0.06$ ). The uncertainty in the accretion rate is a factor of 2 due to possible spectral type mismatch, uncertainties in the location of the continuum and the uncertainty in the conversion from line flux to accretion rate.

#### 5.2.4.2 LRL 21

Based on eight total epochs of near infrared spectra, including four in 2008 over the course of 8 days and four in 2009 over the course of one month, we find large fluctuations in the  $\text{Pa}\beta$  and  $\text{Br}\gamma$  lines, often changing from absorption to emission (Fig 5.14). While in emission the  $\text{Pa}\beta$  and  $\text{Br}\gamma$  lines reach a peak of

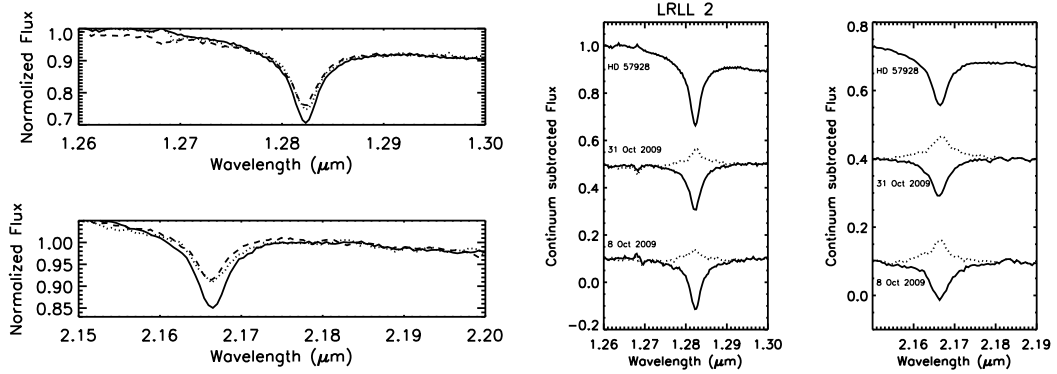


Figure 5.13  $\text{Pa}\beta$  and  $\text{Br}\gamma$  lines for LRL 2. On the left the two epochs are directly compared, along with a WTTs standard. There is little evidence for variability between these two epochs. On the right the spectra are shown after the photospheric absorption has been subtracted (dotted line). Once the strong intrinsic absorption has been removed, there is evidence for emission indicating ongoing accretion.

1.25 and 1.11Å respectively, with accretion rates varying from undetectable to  $10^{-8} M_{\odot} \text{yr}^{-1}$ . There are no day-to-day changes seen in the 2008 spectra but there are large changes from one week to the next, which is also seen in the 2009 data. Dahm (2008) and Luhman et al. (2003) measure the EW of the  $\text{H}\alpha$  line to be 4.48 and 4.7Å respectively, while our high-resolution MMT spectrum (Fig 5.15) has an EW of 7.1Å and our low-resolution spectrum measures 1.59Å. The high-resolution profiles of the  $\text{H}\alpha$  line from Dahm (2008) and our MMT spectra show strong central absorption, possibly consistent with two separate  $\text{H}\alpha$  emission lines, from the two components of the binary system. Our low-resolution spectrum, taken in 2009 when the  $\text{Pa}\beta$  line is in absorption, shows especially weak  $\text{H}\alpha$  emission compared to what is typically seen around actively accreting stars and is consistent with being entirely from chromospheric emission (White & Basri, 2003), although it is possible that unresolved absorption leads to a very small EW even with ongoing accretion. This very weak accretion measure is similar to the infrared lines that show no emission in some epochs, which may also be

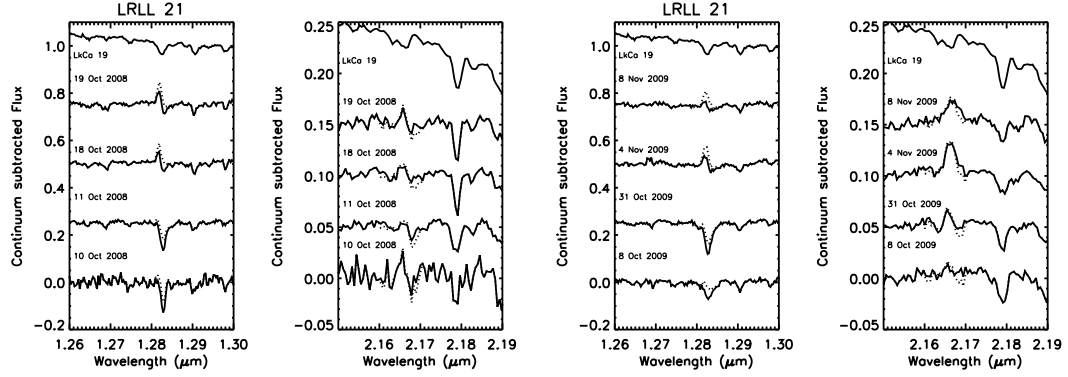


Figure 5.14 Line measurements from 2008 (left two panels) and 2009 (right two panels). Both the  $\text{Pa}\beta$  line ( $\lambda = 1.282\mu\text{m}$ ) and the  $\text{Br}\gamma$  line ( $\lambda = 2.166\mu\text{m}$ ) are shown for each day. The solid line is the observed spectrum while the dashed line has had the photospheric absorption subtracted from the line. At the top of each panel is the K0 WTTs standard. There are large variations in the emission lines, mainly on timescales of weeks.

due to unresolved absorption. Even during the most active accretion, the ratio of accretion to stellar luminosity ( $L_{\text{acc}}/L_{*}=0.06$ ) is small.

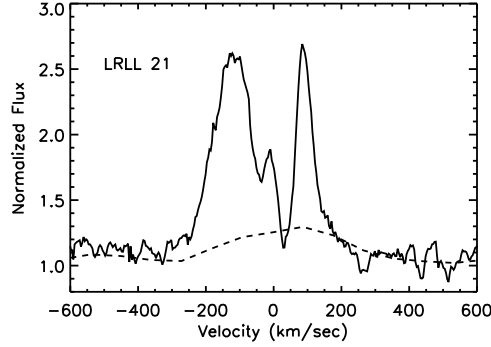


Figure 5.15 Optical spectra of the  $H\alpha$  line for LRL 21. Solid line is high-resolution spectra while dashed line is the low-resolution spectra, both normalized to the continuum.

#### 5.2.4.3 LRL 58

During our two near-infrared observations in 2009 separated by roughly one month the  $\text{Pa}\beta$  and  $\text{Br}\gamma$  appears to change. Fig 5.16 shows that in the second epoch the lines are slightly stronger, although the noisy continuum make it difficult to calculate accurate EWs. An additional complication is that our M1 WTTS standard JH 108, which is used to estimate the photospheric absorption, appears to show emission near the  $\text{Br}\gamma$  line (Fig 5.16), which makes it difficult to estimate the emission for these lines. The equivalent width of the  $H\alpha$  line varies from  $9\text{\AA}$  (Herbig, 1998) to  $20.8\text{\AA}$  from our low-resolution spectra and  $14.9\text{\AA}$  in our high-resolution spectra (Fig 5.17), indicating that there have been large fluctuations in the accretion flux. The small  $H\alpha$  line strength measured by Herbig (1998) is close to the boundary between accreting and non-accreting sources (White & Basri, 2003), suggesting that the accretion rate can drop to very low levels. Our high-resolution spectra displays a broad line width indicative of ongoing accretion. Based on our measured accretion rate ( $\dot{M} \sim 5 \times 10^{-9} M_{\odot} \text{yr}^{-1}$ ), the accretion luminosity is a small factor ( $L_{\text{acc}}/L_{*} \lesssim 0.1$ ) of the total luminosity that is responsible for heating the disk.



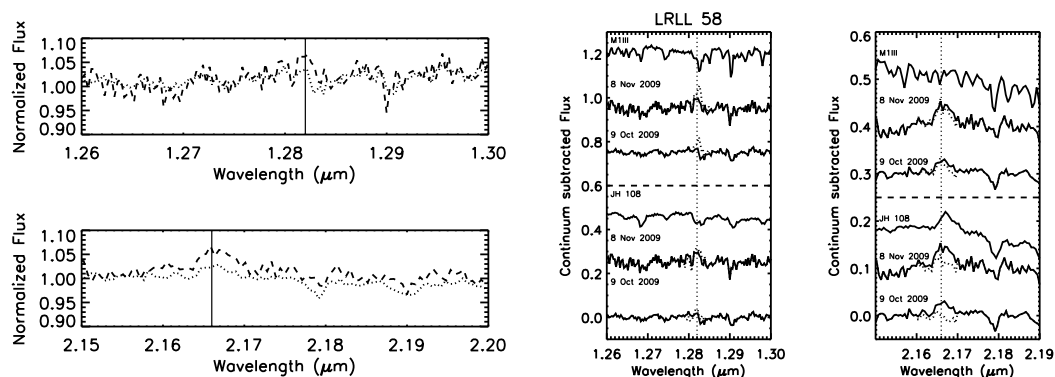


Figure 5.16 Same as Figure 5.13, but for LRL 58. There is some evidence for a change in the line strengths between the two epochs, and ongoing accretion in both epochs, although the uncertainties in the derived accretion rates are large. When subtracting by a photospheric standard we consider both a WTTS and a giant from the IRTF spectral library, since the WTTS seems to exhibit Br $\gamma$  emission.

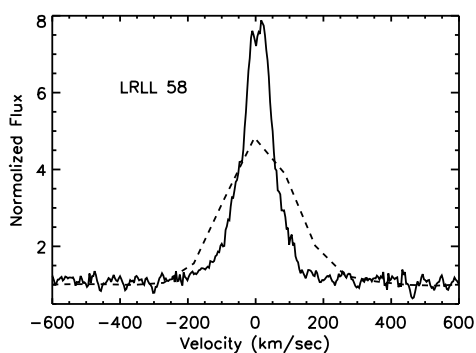


Figure 5.17 Optical spectra of the H $\alpha$  line for LRL 58. Solid line is high-resolution spectra while dashed line is the low-resolution spectra, both normalized to the continuum.

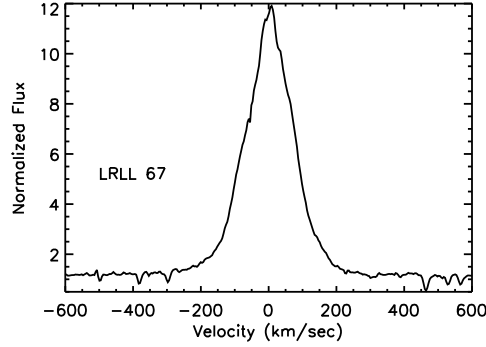


Figure 5.18 High-resolution optical spectra of the  $H\alpha$  line for LRL 58 normalized to the continuum.

#### 5.2.4.4 LRL 67

We have no near-infrared spectra of LRL 67, but Dahm (2008) measure an  $H\alpha$  equivalent width of  $28.32\text{\AA}$  with an accretion rate of  $2 \times 10^{-9} M_{\odot}\text{yr}^{-1}$  while Luhman et al. (2003) measure an  $H\alpha$  line strength of  $35\text{\AA}$  and we find  $\text{EW}=31.4\text{\AA}$  in our high-resolution spectra (Fig 5.18). LRL 67 appears to be actively accreting, with a variable accretion rate, whose accretion luminosity is small ( $L_{\text{acc}}/L_{*}=0.06$ ) compared to the stellar luminosity.

#### 5.2.4.5 LRL 1679

During our five epochs of near-infrared observations, three in 2008 over the course of a week and two in 2009 separated by a month, we find no evidence for  $\text{Pa}\beta$  or  $\text{Br}\gamma$  emission (Fig 5.19). Our low resolution optical spectrum taken in 2009 during the  $3.6, 4.5\mu\text{m}$  monitoring measures an EW of the  $H\alpha$  line of  $3.3\text{\AA}$ , which is below the accretion boundary for a star of this spectral type (White & Basri, 2003). The high-resolution spectrum has an EW of only  $1.7\text{\AA}$  and show very weak, narrow emission, suggesting that any ongoing accretion must be at a very low rate (Fig 5.20). In no epoch do we detect evidence for ongoing accretion in this star.

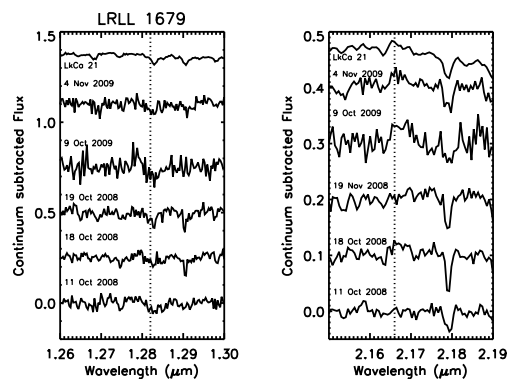


Figure 5.19 Same as Figure 5.14, but for LRL 1679. We do not subtract the photospheric absorption since it is very weak and would only add to the uncertainty in the spectra. There is no evidence for either  $\text{Pa}\beta$  or  $\text{Br}\gamma$  emission in any epoch.

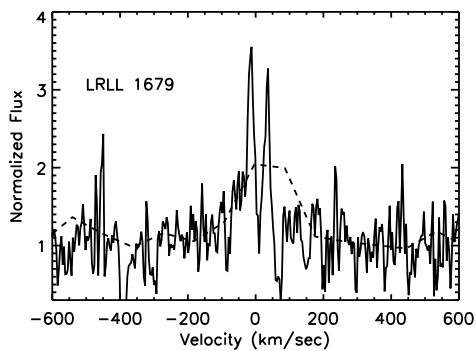


Figure 5.20 Optical spectra of the  $\text{H}\alpha$  line for LRL 1679. Solid line is high-resolution spectra while dashed line is the low-resolution spectra, both normalized to the continuum.

#### 5.2.4.6 LRL 31

Based on multiple epochs of the Pa $\beta$  and Br $\gamma$  emission lines the accretion rate in LRL 31 changes by a factor of five, from  $0.3$  to  $1.6 \times 10^{-8} M_{\odot} \text{yr}^{-1}$ . This behavior is also seen in multiple epochs of H $\alpha$  spectroscopy, which show large fluctuations in the EW. Similar to the other transition disks, the accretion luminosity is small ( $L_{\text{acc}}/L_{*} < 0.1$ ) compared to the stellar flux.

#### 5.2.4.7 Summary

In most of the sources there is evidence for variable accretion, with some epochs dipping below our ability to measure ongoing accretion. The only exception is LRL 1679 in which there is no evidence of ongoing accretion above our detection limits at any epoch. Overall the accretion luminosity is small relative to the stellar luminosity even when the stars are actively accreting.

### 5.3 Perturbation of the Disk

Given all of this information, we seek to address a number of questions: Is the variability in all of these systems caused by similar perturbations to the disk? Is the type of perturbation common among cluster members? What are the possible physical causes of the perturbation, particularly what is the effect of variable illumination from the star and the accretion luminosity?

#### 5.3.1 Is the infrared variability in all of these stars caused by a similar perturbation to the disk?

There is a bewildering array of infrared variability for our six sources. Some show large infrared fluctuations with a clear wavelength dependence in every epoch, some do not. Some (LRL 58,67,1679) show almost no excess emission for  $\lambda < 8 \mu\text{m}$  in some epochs, while others (LRL 21) always have a significant

excess. Here we try to determine if these sources can be included together as one coherent type of object based on the infrared variability.

As a starting point we consider the model for the variability of LRL 31. This model consisted of an optically thick inner disk whose scale height was rapidly varying (Flaherty & Muzerolle, 2010; Flaherty et al., 2011), which has also been successful in explaining the infrared variability of other transition disks (Espaillat et al., 2011). The consequences of this model are:

- An SED that varies at all infrared wavelengths and appears to pivot around a certain wavelength between different epochs. As the scale height of the inner disk increases it produces more short wavelength flux while also shadowing the outer disk, causing the long-wavelength flux to decrease. In the case of the LRL 31, the flux shortward of  $8\mu\text{m}$  would decrease when the long-wavelength flux increased. The pivot point may change depending on the geometry of the disk (Espaillat et al., 2011), but it is difficult to produce this wavelength dependence without a variable inner disk scale height (Flaherty & Muzerolle, 2010).
- Changes in infrared flux on the dynamical timescale of the inner disk. These rapid variations can even be seen at the longest wavelengths, which probe material at a few AU from the star where the dynamical timescales are closer to years.
- The [3.6]-[4.5] color gets redder as it gets brighter. Increasing the size of the inner disk will cause a larger increase at  $4.5\mu\text{m}$  than at  $3.6\mu\text{m}$  because the relative contribution of the stellar flux at  $4.5\mu\text{m}$  is smaller.
- Correlated changes between the silicate feature flux and the long-wavelength flux. Variable shadowing of the silicate emission zone and the source of the

long wavelength flux can explain this behavior.

Overall each source displays some of the signs of a variable inner disk suggesting that all of these sources are experiencing the same type of variability. LRL 2 displays a SED that pivots around  $\lambda = 6\mu\text{m}$  and its silicate feature flux is correlated with the long-wavelength flux. LRL 21 has a light curve that is almost identical to LRL 31, its [3.6]-[4.5] color gets redder as it gets brighter and direct observations of the emission from the inner disk show that it is optically thick and the size of the emitting region gets larger while its temperature stays the same. The  $24\mu\text{m}$  photometry shows that the source is variable at this wavelength. LRL 58 shows a pivot in the SED at  $\lambda = 8\mu\text{m}$  when comparing the photometry and the IRS spectra, and the  $24\mu\text{m}$  photometry shows significant fluctuations. It also shows variations on short timescales, consistent with the dynamical timescale of the inner disk (5 days). LRL 67 shows rapid fluctuations consistent with the dynamical timescale of the inner disk (4 days) and the [3.6]-[4.5] color gets redder as it gets brighter. The  $24\mu\text{m}$  photometry varies slightly, suggesting that there is some long-wavelength variation. LRL 1679 clearly displays a pivot in its IRS spectra at  $\lambda = 13\mu\text{m}$  and there is some evidence that the [3.6]-[4.5] color gets redder as it gets brighter. The small change in optical flux on short timescales in all of these sources suggests that the radius of the inner disk, which if set by dust sublimation is proportional to the stellar and accretion luminosity, is not changing. The rapid infrared fluctuations imply changes in the emitting area of the disk, but since the radius of this dust does not change then the scale height must be variable. That none of them show all of the hallmarks of a variable inner disk may be a sign of differences in the exact geometry of the disk (optically thin vs. optically thick inner disk, location of the outer disk, grain size/composition) rather than differences in the perturbation.

### 5.3.2 LRL 67

One key tenant of this model for the inner variability is an optically thick inner disk. LRL 21 and 31 show direct evidence for optically thick inner disks based on the shape of the 2-5 $\mu$ m excess. The strength of the veiling observed at K band in LRL 58 is also consistent with strong emission for an optically thick inner disk, rather than the weak emission from an optically thin disk. LRL 2 and 1679 show a pivot when comparing IRS spectra, while LRL 58 shows a pivot between the spectra and photometry, which is difficult to explain without shadowing from an optically thick inner disk. For LRL 67 the evidence for an optically thick inner disk is weaker than in any other star. Its SED is reminiscent of sources such as GM Aur, DM Tau, CS Cha and Coku Tau/4, which have been modeled using only optically thin dust in the inner disk (Espaillat et al., 2007; D'Alessio et al., 2005; Calvet et al., 2005). We have no near-infrared spectra to look for a sign of hot dust, but the weak 3-8 $\mu$ m excess at all epochs is difficult to explain with optically thick dust. A perfectly flat disk extending inward to the dust destruction radius at  $T=1500$  K oriented at  $i < 85^\circ$  would produce an excess that is larger than we observe in this system. If the inner disk is optically thin then changing the scale height will have no effect on the short wavelength flux, since the emission is proportional to the total column density of material and not its exact geometry. The inner disk will also not be able to shadow the outer disk, leading to no variation in the long-wavelength flux.

LRL 67 has a substantial accretion rate, indicating that some material must be traveling from the massive outer disk, through the inner disk, and onto the star. The measured accretion rate of  $2 \times 10^{-9} M_\odot \text{ yr}^{-1}$  corresponds to a gas surface density of  $\sim 10 \text{ g cm}^{-2}$  at 1 AU (D'Alessio et al., 1999). If the gas to dust mass ratio is 100, then the dust emission should be optically thick. Rice et al. (2006)

find that the outer edge of the gap can block some of the inward flowing dust resulting in very high gas to dust ratio and a much lower dust mass in the inner disk. If the inner disk were radially optically thick while vertically optically thin it would be able to shadow the outer disk, while still producing very weak emission, although this model has difficulty explaining the variability at 3.6 and  $4.5\mu\text{m}$ . If the inner disk were optically thin then a change in its temperature could lead to substantially changes in the infrared flux. This variable heating could be due to changes in the accretion rate, although for LRL 67 the heating of the disk is dominated by the stellar flux, or an unseen companion in the disk (Nagel et al., 2010). Another possibility is that the inner disk is non-axisymmetric, with the majority of it optically thin with only thin trails of optically thick dust. The small covering fraction of these trails would create a very weak excess, similar to what is observed (Dodson-Robinson & Salyk, 2011). A completely optically thin inner disk would produce no shadowing of the outer disk, and the associated 'seesaw' behavior in the SED. Of the transition disks, LRL 67 shows the least amount of evidence for a pivot in the SED or any 'seesaw' behavior in the IRS spectra, leaving open the possibility that the outer disk is not shadowed, although the variable  $24\mu\text{m}$  emission is difficult to explain without shadowing of the outer disk. Observations of the near-infrared excess to determine if it is optically thick, as has been done for LRL 21 and 31, as well as detailed modeling of the SED are needed to better understand this source.

### 5.3.3 Comparing Transition Disk Variables to Other Variables

Do these stars represent a unique class of objects, or is the physical mechanism responsible for their variability common to other young stellar objects? We can start by comparing the dust grain properties, as traced by the  $10\mu\text{m}$  silicate emission, in our transition disks to a less evolved disk population. The emission can



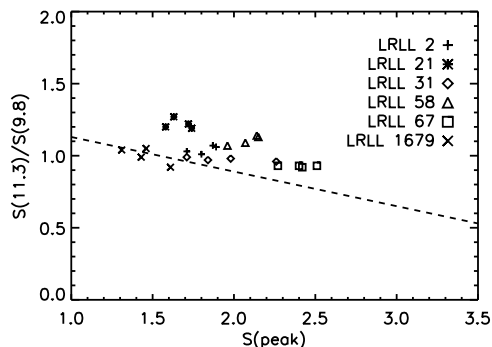


Figure 5.21 Strength versus shape of the  $10\mu\text{m}$  silicate feature for the transition disks. Definitions of the axes are from Kessler-Silacci et al. 2006. The dashed line shows a fit to stars from c2d and demonstrates the correlation between strength and shape found for typical stars. The transition disks tend to lie slightly above this relation, but are not substantially different than other T Tauri stars.

be characterized by the continuum normalized peak flux ( $S(\text{peak})$ ) and the ratio of the continuum normalized flux on two sides of the feature ( $S_{11.3}/S_{9.8}$ ) as in Kessler-Silacci et al. (2006). The wavelengths  $11.3$  and  $9.8\mu\text{m}$  correspond to the peak of the emission profiles from crystalline and amorphous silicates, allowing us to distinguish processing of the dust grains. In Figure 5.21 we compare the strength and shape of the silicate feature for each observation of the transition disks with the trend previously observed by Kessler-Silacci et al. (2006). A similar conclusion is found when using the method of Manoj et al. (2011) and Furlan et al. (2009), which apply slightly different indices to trace the strength of the feature and the strength of the continuum, and comparing to the Taurus, Chameleon and Ophiuchus cluster members studied in those papers. Although our sample consists entirely of transition disks, and by definition the structure of the dust within the disk is different from a typical T Tauri star, there is no clear distinction in their dust properties.

Our photometry taken with IRAC during both the cold-mission and the warm-

mission, as well as with MIPS allow us to compare the size and timescale of the fluctuations between the transition disks and the rest of the cluster members. One way of characterizing the fluctuations is with the rms, which traces the typical size of the infrared changes. The rms is defined as (Carpenter et al., 2001):

$$(rms)^2 = \frac{n \sum_{i=1}^n w_i (m_i - \bar{m})^2}{(n-1) \sum_{i=1}^n w_i} \quad (5.1)$$

where  $n$  is the number of observations,  $m_i$  is the magnitude on a given epoch,  $w_i = 1/\sigma_i^2$  and  $\sigma_i$  is the photometric noise. In Figure 5.22 we show the rms of the fluctuations at every wavelength for which we have photometry, with the size and color of each point scaled to the slope,  $\alpha$ , of the IRAC SED, defined as  $\lambda F_\lambda \propto \lambda^\alpha$ , in order to show any changes in strength of the variability with SED classification. For the [3.6] and [4.5] photometry we only include the warm mission photometry since any systematic uncertainties may differ between the cold mission and warm mission photometry. For the [5.8] and [8.0] photometry we exclude the c2d photometry because the different observing strategy prevented them from measuring accurate photometry of many of the brightest members. We also mark the transition disks in IC 348 identified by Muzerolle et al. (2010) for a comparison between evolved disks. The rms for the transition disks studied here does not stand out from the rest of the cluster members at any wavelength. The number of epochs of data available at each wavelength varies (38 for [3.6] and [4.5], 6 for [5.8] and [8.0] and 10 for [24]) but the conclusion is the same. The fluctuations of our sample of six are larger than average, but this is mainly because these sources were chosen as the transition disks that showed the largest fluctuations.

The rms is limited to tracing the size of the fluctuation and offers no information on the timescale of the fluctuations. There are a number of statistical tools that allow us to study the variability as a function of timescale, such as the power-

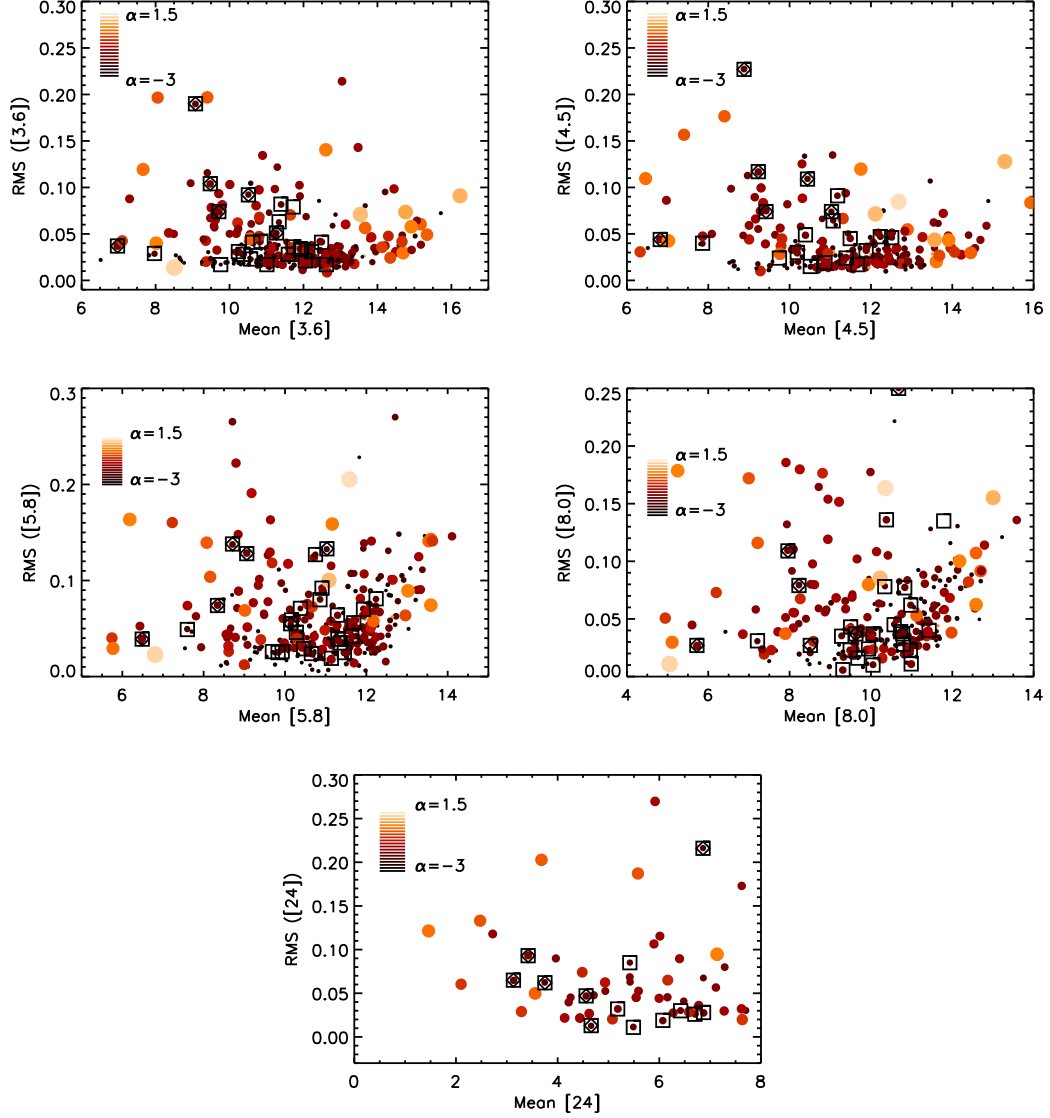


Figure 5.22 RMS of the fluctuations versus average magnitude for the cluster members. We show the 3.6 and 4.5  $\mu\text{m}$  photometry from the warm-mission monitoring as well as the 5.8, 8.0 and 24  $\mu\text{m}$  photometry from our cold-mission monitoring. The size and color of each points scales with the power law slope of the SED from 3.6 to 8.0  $\mu\text{m}$  (Large, light symbols have rising SEDs while small dark points are stellar photospheres. Small, light points do not have enough information determine the slope of the SED). Transition disks are marked with squares and the transition disks studied in this paper are marked with triangles. The size of the fluctuations of the transition disks is similar to other stars in the sample.

spectrum, the auto-correlation function and the structure function. Here we focus on the structure function because it is not affected by period-aliasing and it is able to evaluate variability on a large range of time scales. Detailed modeling of the light curve (e.g. Kelly et al., 2011) is difficult given the lack of data, and here we restrict ourselves to a more qualitative analysis. The structure function (Simonetti et al., 1985) is defined as :

$$SF(\tau) = \langle (m(t + \tau) - m(t))^2 \rangle \quad (5.2)$$

where  $m(t)$  is the measurement taken at time  $t$  and  $\tau$  is the lag between the two measurements. If the light curve varies on a range of timescales from  $t_0$  to  $t_1$  then for  $t \gg t_1$  the structure function will flatten out at a value of  $2(\text{rms})^2$ . For  $t \ll t_0$  the structure function rises as  $t^2$ , although in reality it flattens out as it approaches the noise level. For  $t_0 < t < t_1$  the shape of the structure function will lie somewhere between these boundary conditions. If the light curve is periodic then the structure function will return to the noise level at  $t = nP$  where  $n$  is an integer and  $P$  is the period<sup>2</sup>. This behavior makes a structure function a useful tool for characterizing the variability timescale. We focus on the 3.6 and 4.5 $\mu\text{m}$  monitoring since these data have the density necessary for this type of analysis. With these data we are most sensitive to timescale in the range of 2 to 25 days. In Figure 5.23 we compare the structure function for each of the transition disks with the average structure function of all of the variable cluster members (chosen to have reduced  $\chi^2 > 3$ , e.g. Carpenter et al. (2001)). There is no significant difference between the two samples, suggesting that the variability timescales seen in the transition disks is similar to the range of timescales seen in the rest of the sample. A similar analysis can be performed with the auto-correlation

---

<sup>2</sup>A periodogram is more effective at searching for periodicity, and we find none in any of these sources.

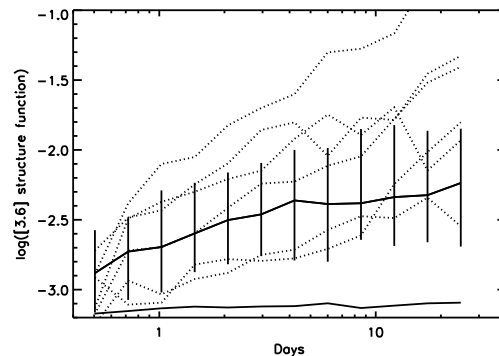


Figure 5.23 [3.6] structure function showing the median of the variables stars, along with the quartiles of the distribution (solid line with error bars) the median of the non-variable stars (solid line without error bars) along with the transition disk variables considered here (dotted lines). The shape of the structure function for the transition disk variables is similar to that of the other variables in the cluster, suggesting that these stars are not unique.

function or power spectrum with similar results.

Despite the lack of ancillary data for the IC 348 normal disks, there is some evidence for varying, non-axisymmetric structure in inner disks around other stars in the literature, suggesting that this phenomenon is not unique to the transition disks studied here. Hutchinson et al. (1994) find a wavelength dependence in the variability of UX Ori and AK Sco that can be explained by changing the scale height of the inner disk (Flaherty & Muzerolle, 2010). Juhász et al. (2007) see infrared variability in SV Cep that they are able to successfully model with a disk whose inner scale height is rapidly varying. None of these objects are characterized by transition disk SEDs.

Other systems show evidence for non-axisymmetric structure in the inner disk, based on the occasional obscuration of the star by this material. Morales-Calderón et al. (2011) find a significant fraction of the variables in Orion display rapid dips in their light curves due to brief stellar occultations by the disk. The Corot satellite monitored the young cluster NGC 2264 for 23 straight days and

found that 28% of the young stellar objects exhibit this behavior (Alencar et al., 2010). AA Tau is a well-studied example of a star with periodic occultations due a warp in the inner disk (Bouvier et al., 2007a). The structure that causes these occultations may be long-lived, or it may rapidly appear and disappear on an orbital timescale. In fact UX Ori, which shows strong evidence for an inner disk with a variable scale height based on its infrared fluctuations, is the canonical member of the UX-Ori class of variables that are characterized by brief drops in their optical flux, similar to those seen in Orion, NGC 2264 and AA Tau.

This suggests that structural changes in disks similar to that seen in the transition disks studied here, are common among young stellar objects. Roughly 50% of the IC 348 cluster members with an infrared excess show variability at 3.6 and 4.5 $\mu\text{m}$  larger than 0.05 mag (Flaherty et al in prep.). Morales-Calderón et al. (2011) find that 70% of the stars in Orion with an infrared excess are variable at 3.6 and 4.5 $\mu\text{m}$  with amplitudes similar to those studied here. The amplitude of the flux variations is very similar between the transition disks studied here and the other variable disks, which make up a majority of the members with disks. This suggests that the transition disks are undergoing structural changes in their circumstellar material that are similar in amplitude to many of the other cluster members with disks. The commonality implies that we are observing a fundamental property of young stellar objects that has been previously been unaccounted for. Further work is needed to determine if the structural changes are identical for a wide range of sources, and if they are all caused by the same physical mechanism.

## 5.4 What could be causing these variations?

### 5.4.1 No Apparent Connection between the Infrared Variability and the Stellar/Accretion flux

One possible explanation for the observed infrared variability is that the illumination of the disk changes rapidly. As the flux striking the disk increases the temperature of the disk rises. If the inner edge is set by dust sublimation then the location of the inner edge will move outward, increasing its emitting area and hence flux. The increased heating may also raise the temperature of the mid-plane resulting in an increase in the disk scale height, shadowing the outer disk. The illumination of the disk is dominated by the stellar and accretion luminosity, which we can trace using our near-infrared photometry and our measurements of the  $\text{Pa}\beta$  and  $\text{Br}\gamma$  lines as well as measurements from the literature. The observations of the stellar and accretion flux for these stars are not as dense as the infrared coverage, but we can still look for variability in these properties.

In terms of stellar flux, none of the six transition disks show evidence for strong fluctuations on timescales similar to that of the infrared variability. LRL 2, 58, 67 and 1679 display, at the most, small changes due to cold spots rotating across the face of the star. These fluctuations are not large enough to substantially change the heating of the disk. LRL 21 and 31 show evidence for year-to-year changes in stellar flux, which is much longer than the timescale for the infrared variability. For both stars we have contemporaneous J band and  $3.6, 4.5\mu\text{m}$  photometry in 2009 and we find that the J band flux stays relatively constant despite the large changes in the infrared flux.

The accretion rate does show large variations in most of these stars, with the only exception being LRL 1679 for which we do not detect any strong ongoing accretion ( $< 10^{-7} M_{\odot} \text{ yr}^{-1}$ ). Despite the accretion rate variability, the average ac-

accretion luminosity is small compared to the stellar flux and is not an important source of heating in the disk surface layer. In none of the transition disks is the accretion luminosity larger than 10% of the total flux striking the disk. The size of the inner disk emitting area is proportional to the luminosity striking its surface (Dullemond & Monnier, 2010) and the variations in the accretion luminosity need to be larger than has been observed to explain the infrared variability. This suggests that even though the accretion luminosity changes significantly, the heating of the disk will not vary at an observable level.

For LRL 21 and 31 we have enough contemporaneous data in 2009 to look for any correlation between the accretion rate and infrared flux. Both of these stars show similar infrared light curves, with a sharp drop during the first week of observations followed by a slow increase over the next four weeks. We were able to obtain  $\text{Pa}\beta$  and  $\text{Br}\gamma$  measurements during the IR minimum as well as a few weeks later after the infrared flux had increased for both stars. In LRL 31, the  $\text{Pa}\beta$  line shows almost no emission during the infrared minimum while it has strong emission after the infrared flux has increased, suggesting a strong correlation between the gas and dust. In LRL 21, the  $\text{Pa}\beta$  line shows absorption during the infrared minimum (Oct 8) as well as 3 weeks later (Oct 31) after the infrared flux has increased by 0.7 mag. One week later (Nov 4) the  $\text{Pa}\beta$  line is in emission even though the infrared flux has only increased by 0.1 mag. It is possible that unresolved absorption on Oct 31 makes the line appear very weak. The  $\text{HeI}$  line, which traces the inflow and outflow of gas near the star, shows very strong red-shifted absorption due to the accretion in this epoch, but not during any other epoch (Fig 5.24). There is also evidence for red-shifted absorption in the  $\text{Pa}\gamma$  line. This suggests that there may be additional absorption that suppresses the  $\text{Pa}\beta$  emission making it appear very weak. If this is the case then the  $\text{Pa}\beta$



flux may be correlated with the infrared flux as in LRL 31. Even if these two properties are correlated it is unlikely that the accretion variability is the source of the infrared fluctuations. As discussed earlier, the accretion luminosity is small compared to the stellar flux heating the disk. It is also unlikely that a variable accretion flow through the disk leads to the variable disk emission because the timescale for an over-dense clump of dust and gas to move through the disk is the viscous timescale, which is on the order of hundreds of years at the location of the inner disk edge for the objects.

### 5.4.2 Winds

A highly variable wind, carrying both gas and dust out of the disk, could lead to variable infrared emission (Konigl & Pudritz, 2000; Vinković & Jurkić, 2007). As material is lifted out of the disk its emitting area increases and it may shadow the outer disk, creating the observed infrared variability. It is also possible that the wind is asymmetric about the midplane, likely due to a misaligned stellar magnetic field (Lovelace et al., 2010). If the mass flow in the wind is larger on one side of the disk than the other, then the asymmetric loss of angular momentum will lead to warping of the inner disk. We can trace the wind using the infrared spectra of the HeI ( $1.08\mu\text{m}$ ) line whose blue-shifted absorption/emission is connected with a wind (Edwards et al., 2006). When a clump of material is lifted out of the midplane by a wind (Suzuki et al., 2010) the clump needs to be optically thick to stellar photons to shadow the outer disk and produce the observed wavelength dependence of the variability. This sets a lower limit on the column density of material in the clump of  $A_V \sim 1$ , which corresponds to  $\log(N_H) \sim 21$  (Draine, 2003) and a wind with this column density that arose from  $\sim 0.5\text{AU}$  and was able to remove material in a week would have an outflow rate of  $\dot{M}_w \sim 10^{-9} M_\odot \text{yr}^{-1}$ . This is comparable to the accretion rates detected in the transition disks, and should produce detectable HeI emission (Kwan & Fischer, 2011). In LRL 2, 58 and 1679 we see no evidence for absorption or emission in the HeI line (Fig 5.24). Only LRL 21 shows blue-shifted emission in some epochs, but not nearly at the strength relative to the continuum expected for such a high column density of material. This suggests that any wind that is present in the system is not dense enough to shadow the outer disk.

An asymmetric wind does not require the density in the wind to be as high, since it is the warped disk that is doing the shadowing of the outer disk, rather

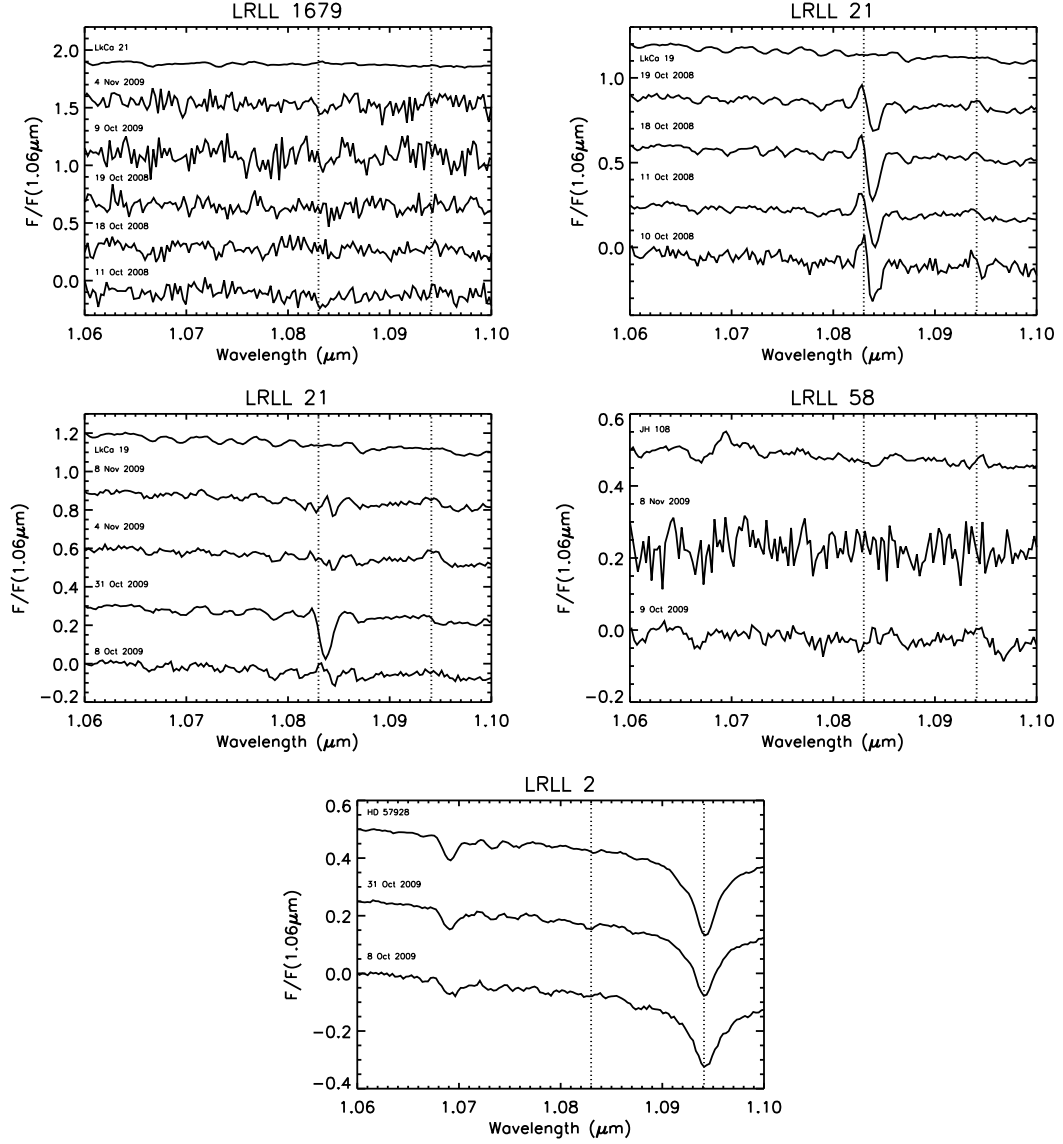


Figure 5.24 HeI ( $\lambda = 1.083\mu\text{m}$ ) and Pa $\gamma$  ( $\lambda = 1.0941\mu\text{m}$ ) lines in the transition disks. LRL 21 is the only source that shows strong absorption or emission in the HeI line, and this line is highly variable.

than the wind itself. With this model we would expect the strongest blue-shifted absorption/emission, corresponding to the strongest wind, to occur during the epochs when the infrared flux, and hence the warping of the disk, is the largest. For LRL 21 in 2009, when we have contemporaneous measurements of HeI and infrared flux, there is no sign of a correlation between HeI and the infrared flux (Fig 5.24). In LRL 31, in 2009, the strongest blue-shifted absorption occurs during the minimum of the infrared light curve, which is the opposite of the expected correlation (Flaherty et al., 2011). This suggests that an asymmetric wind is not the source of the observed infrared variability.

#### 5.4.3 Companion

A companion on an orbit that is misaligned with the disk will lead to a warp whose height varies as the companion drags material out of the midplane (Fragner & Nelson, 2010). If a companion were coplanar with the disk, then it could lead to variable heating of the disk (Nagel et al., 2010) or variable mass flow through the disk in the gap surrounding the planet (Artymowicz & Lubow, 1996). The fluctuating mass flow through a gap could lead to variable shock heating of the inner disk which would then change the scale height of the inner disk. The perturbation from such an object would occur on a timescale equal to the companion's orbital period, which could be as little as a few days. There is evidence for radial velocity variations in the optical spectra of LRL 21 and 31, which are consistent with the presence of a massive companion. We can put some constraints on the possible location of a companion based on two observations: (1) the existence of hot dust, responsible for the 2-5 $\mu$ m excess and (2) the lack of periodicity in the infrared for  $P=2-25$  days. The first constraint prevents a companion from being located within  $0.3a < r < 1.7a$  where  $a$  is the location of the inner dust, or else the inner disk would be removed (Artymowicz & Lubow, 1996). It is

possible the the inner disk has a finite radial extent, in which case the companion is excluded from  $0.3a_0 < r < 1.7a_1$  where  $a_0$  and  $a_1$  are the inner and outer edges of the inner disk. We assume that the inner disk is infinitesimally thin in order to place the most conservative constraints on the location of a companion. We estimate the location of the dust destruction radii assuming  $T_{inner}=1500$  K and ISM like grains (Dullemond & Monnier, 2010). Here we have assumed that every system has optically thick dust at the dust sublimation radius. For LRL 21 and 31 we have direct measurements of this excess, while in LRL 2, 58 and 1679 we have indirect evidence based on the strength of the K-band veiling and the ‘see-saw’ behavior in the IRS spectra. As discussed earlier, the evidence for optically thick dust close to LRL 67 is weak, although we include it here for completeness. The large spectral type range for our sample results in a large range of inner disk radii, from 0.76AU for LRL 2 down to 0.03 AU for LRL 1679. The second constraint excludes companion from orbits with that same range of periods, assuming that a companion would perturb the material on every orbit. In Figure 5.25 we indicate the radii for which a companion is excluded in these transition disks. For LRL 2 we can place the tightest constraints, and exclude a companion from 0.05-1.3AU. More direct tracers of the presence of a companion are needed to rule out or confirm the perturbation of the disk by a companion.

#### 5.4.4 Magnetic Fields

Magnetic fields play an important role in channeling material from the disk onto the star (Bouvier et al., 2007b) and possibly for driving the turbulence within the disk that leads to the inward flow of material (Balbus & Hawley, 1991). Many theoretical models predict that the structure of the magnetic field in these young systems should not be constant and these fluctuations may be the source of the variable inner disk scale height. Magnetic fields in the turbulent disk may occa-

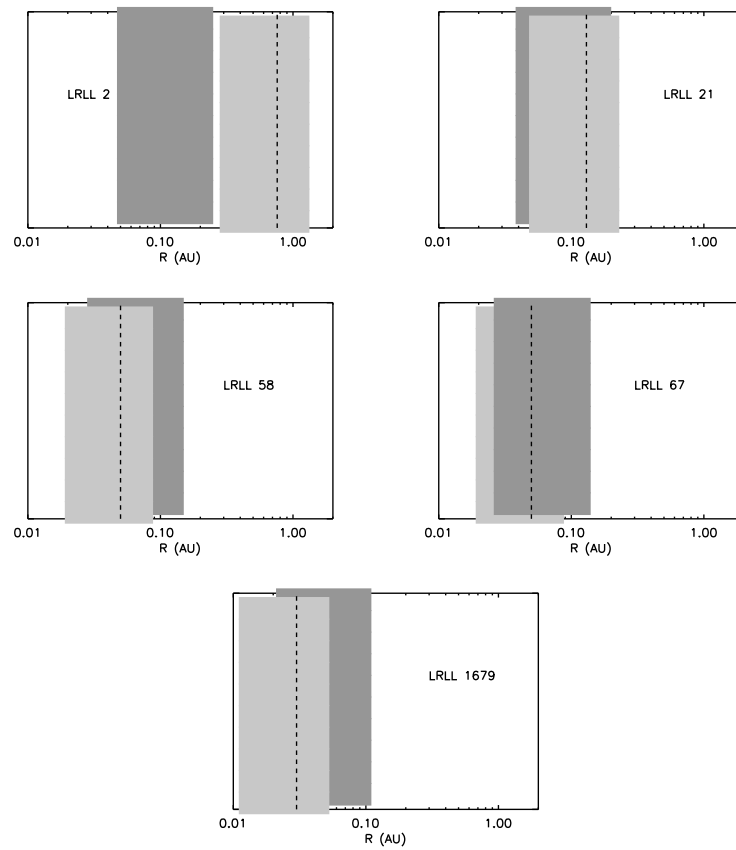


Figure 5.25 Areas near the star that are excluded from having a companion. Dark grey box has been excluded based on the lack of periodicity in the  $3.6$  and  $4.5\mu\text{m}$  monitoring while the light grey box has been excluded based on the presence of hot dust in the inner disk (dust destruction radius is marked with a dashed line).

sionally become buoyant, lifting dust and gas off the disk on very short timescales (Turner et al., 2010; Hirose & Turner, 2011). The stellar magnetic field, and where it intersects the disk, may also be important for variability. As material from the disk flows inward it eventually is loaded onto the stellar magnetic field lines, is lifted out of the midplane, and free-fall onto the stars. A highly dynamic interface between the stellar magnetic field and the disk may lead to rapid changes in disk structure. The stellar magnetic field may expand and contract on weekly timescales, leading to a warping of the disk as the field expands (Goodson & Winglee, 1999). If the stellar magnetic field is misaligned with the disk, then this could also cause a warp (Lai & Zhang, 2008). Simulations also show that the inflow of material along field lines is unstable and very patchy (Romanova et al., 2009). If dust is entrained in this patchy inflow then it could occasionally create a large short-wavelength excess as it is lifted out of the midplane as well as shadow the outer disk.

These last two models (tilted magnetic field and patchy inflow) require dust to extend inwards toward the point at which material is loaded onto the magnetic field lines. This radius is typically taken as near the co-rotation radius, where the period of the star and the disk are equal, since outside of this radii the angular momentum of the gas and dust is large enough that it would be flung out of the system rather than accreted onto the star. The innermost radius of the dust is set by the point at which the dust is hot enough to sublime, which depends on the luminosity of the central star, as well as the dust composition (Dullemond & Monnier, 2010). Table 5.13 lists estimates of the co-rotation radii, calculated using either measured rotation periods or the observed range of rotation periods for pre-main sequence stars in IC 348 (Cieza & Baliber, 2006), as well as the dust sublimation radii, calculated earlier. For the low-luminosity sources (LRL

58, 67, 1679) dust can extend close enough to the star to be loaded onto the stellar magnetic field lines and lifted out of the midplane. For the high-luminosity sources the dust disk is truncated at a much larger radii, even if we assume that the disk is entirely composed of very large ( $> 10\mu\text{m}$ ) grains, which can extend closer to the star than small ( $0.1\mu\text{m}$ ) grains. Lifting dust out of the midplane would occasionally lead to higher extinction and decreased stellar flux coincident with changes in the infrared flux as our line of sight passes through one of these dense clumps. In none of our stars do we see evidence for an increase in extinction or a decrease in stellar flux associated with the infrared flux variations. It is unlikely that for all of these six systems we have been lucky enough that our line of sight never intersects the dusty clump, although the paucity of measurements of the extinction of stellar flux make it difficult for us to say that the stars are never occulted. For LRL 21 and 31, where we have the densest coverage of the extinction contemporaneous with the 2009 infrared monitoring, we do not see any correlation between these properties. This suggests that the coverage of the sky by the clump as seen from the star is small. Additional monitoring for extinction events associated with material being lifted out of the midplane would help to further constrain this theory.

## 5.5 Conclusion

We have studied the mid-infrared variability of six transition disk systems in the young stellar cluster IC 348.

- We find strong infrared variability at all wavelengths in every source. These fluctuations are typically rapid (days to weeks) and sometimes show a wavelength dependence where the short-wavelength flux increases as the long-wavelength flux decreases.



- The most likely source of this infrared variability is a perturbation in the scale height of the inner disk.
- The strength and timescale of the infrared variability in these transition disks is not unlike that seen in the rest of the IC 348 cluster members of which at least 40% are variable. This result suggests that these types of perturbations are common.
- It is unlikely that variable heating from fluctuations in the stellar flux or accretion rate are responsible for the infrared variability. We do not observe strong stellar flux changes on the same timescale as the infrared variability, and the accretion luminosity is not a significant component of the flux striking the disk.
- We can also exclude the influence of strong winds and companions at certain radii within the disk.
- Possible explanations for the behavior are either companions at permitted radii or effects from the system magnetic field. However both make predictions that are not yet confirmed - in the first case of periodicities and in the second of the variable extinction of the star.

The size and timescale of the infrared flux variations seen in the six transition disks studied here are very similar to the other variable disks in IC 348, which make up roughly half of the cluster members with disks. This suggests that many young stellar objects undergo similar perturbations to the structure of their inner disks. Further observations are needed to determine if the physical causes of the variability are similar between these two samples, but the similarity in the size of the fluctuations suggest that variability could be a useful tool for studying the inner disks around many young stellar objects.

Table 5.1. Observing Log

Date	MJD	Wavelength	Resolution	Instrument
LRL 2				
08 Oct 2007	54381.9	5-40 $\mu$ m	$\sim$ 600	IRS spectra
15 Oct 2007	54388.9	5-40 $\mu$ m	$\sim$ 600	IRS spectra
24 Mar 2008	54549.2	5-40 $\mu$ m	$\sim$ 600	IRS spectra
31 Mar 2008	54556.7	5-40 $\mu$ m	$\sim$ 600	IRS spectra
08 Oct 2009	55112.6	0.8-2.5 $\mu$ m	$\sim$ 800	Spex
31 Oct 2009	55137.3	0.8-2.5 $\mu$ m	$\sim$ 800	Spex
LRL 21				
09 Oct 2007	54382.3	5-40 $\mu$ m	$\sim$ 600	IRS spectra
15 Oct 2007	54388.8	5-40 $\mu$ m	$\sim$ 600	IRS spectra
24 Feb 2008	54520.3	5-40 $\mu$ m	$\sim$ 600	IRS spectra
29 Feb 2008	54525.1	6460-6650 $\text{\AA}$	$\sim$ 35000	Hectochelle
01 Mar 2008	54526.9	5-40 $\mu$ m	$\sim$ 600	IRS spectra
10 Oct 2008	54750.5	0.8-5 $\mu$ m	$\sim$ 1500	Spex
11 Oct 2008	54751.5	0.8-2.5 $\mu$ m	$\sim$ 800	Spex
18 Oct 2008	54757.4	0.8-5 $\mu$ m	$\sim$ 1500	Spex
19 Oct 2008	54758.4	0.8-5 $\mu$ m	$\sim$ 1500	Spex
08 Oct 2009	55112.6	0.8-5 $\mu$ m	$\sim$ 800	Spex
12 Oct 2009	55116.1	6000-9000 $\text{\AA}$	$\sim$ 3500	CAFOS
31 Oct 2009	55137.3	0.8-5 $\mu$ m	$\sim$ 800	Spex
04 Nov 2009	55141.5	0.8-5 $\mu$ m	$\sim$ 800	Spex
08 Nov 2009	55144.5	0.8-2.5 $\mu$ m	$\sim$ 800	Spex
LRL 58				
08 Oct 2007	54381.9	5-40 $\mu$ m	$\sim$ 600	IRS spectra
15 Oct 2007	54388.9	5-40 $\mu$ m	$\sim$ 600	IRS spectra
29 Feb 2008	54525.1	6460-6650 $\text{\AA}$	$\sim$ 35000	Hectochelle

Table 5.1—Continued

Date	MJD	Wavelength	Resolution	Instrument
24 Mar 2008	54549.2	5-40 $\mu$ m	$\sim$ 600	IRS spectra
31 Mar 2008	54556.8	5-40 $\mu$ m	$\sim$ 600	IRS spectra
09 Oct 2009	55113.6	0.8-2.5 $\mu$ m	$\sim$ 800	Spex
13 Oct 2009	55117.1	6000-9000Å	$\sim$ 3500	CAFOS
08 Nov 2009	55144.5	0.8-2.5 $\mu$ m	$\sim$ 800	Spex
LRL 67				
09 Oct 2007	54382.4	5-40 $\mu$ m	$\sim$ 600	IRS spectra
15 Oct 2007	54388.9	5-40 $\mu$ m	$\sim$ 600	IRS spectra
24 Feb 2008	54520.3	5-40 $\mu$ m	$\sim$ 600	IRS spectra
29 Feb 2008	54525.1	6460-6650Å	$\sim$ 35000	Hectochelle
03 Mar 2008	54527.0	5-40 $\mu$ m	$\sim$ 600	IRS spectra
LRL 1679				
08 Oct 2007	54381.9	5-40 $\mu$ m	$\sim$ 600	IRS spectra
15 Oct 2007	54388.9	5-40 $\mu$ m	$\sim$ 600	IRS spectra
29 Feb 2008	54525.1	6460-6650Å	$\sim$ 35000	Hectochelle
24 Mar 2008	54549.1	5-40 $\mu$ m	$\sim$ 600	IRS spectra
31 Mar 2008	54556.8	5-40 $\mu$ m	$\sim$ 600	IRS spectra
11 Oct 2008	54751.5	0.8-2.5 $\mu$ m	$\sim$ 800	Spex
13 Oct 2009	55117.1	6000-9000Å	$\sim$ 3500	CAFOS
18 Oct 2008	54757.4	0.8-2.5 $\mu$ m	$\sim$ 1500	Spex
19 Oct 2008	54758.4	0.8-2.5 $\mu$ m	$\sim$ 1500	Spex
09 Oct 2009	55113.6	0.8-2.5 $\mu$ m	$\sim$ 800	Spex
04 Nov 2009	55141.5	0.8-2.5 $\mu$ m	$\sim$ 800	Spex
All Stars				
21 Feb 2004	53056.6	24 $\mu$ m	photometry	MIPS
19 Sep 2004	53267.9	24 $\mu$ m	photometry	MIPS

Table 5.1—Continued

Date	MJD	Wavelength	Resolution	Instrument
23 Sep 2007	54366.9	24 $\mu$ m	photometry	MIPS
24 Sep 2007	54367.9	24 $\mu$ m	photometry	MIPS
25 Sep 2007	54368.9	24 $\mu$ m	photometry	MIPS
26 Sep 2007	54369.9	24 $\mu$ m	photometry	MIPS
27 Sep 2007	54370.8	24 $\mu$ m	photometry	MIPS
12 Mar 2008	54538.7	24 $\mu$ m	photometry	MIPS
19 Mar 2008	54544.8	24 $\mu$ m	photometry	MIPS
11 Feb 2004	53046	3-8 $\mu$ m	photometry	IRAC cold-mission
08 Sep 2004	53257	3-8 $\mu$ m	photometry	IRAC cold-mission
19 Mar 2009	54910	3-8 $\mu$ m	photometry	IRAC cold-mission
20 Mar 2009	54911	3-8 $\mu$ m	photometry	IRAC cold-mission
21 Mar 2009	54912	3-8 $\mu$ m	photometry	IRAC cold-mission
22 Mar 2009	54913	3-8 $\mu$ m	photometry	IRAC cold-mission
23 Mar 2009	54914	3-8 $\mu$ m	photometry	IRAC cold-mission
03 Oct-07 Nov 2009	55107-55142	3.6,4.5 $\mu$ m	photometry	IRAC warm-mission

Table 5.2. MIPS photometry

Date	LRLL 2	LRLL 21	LRLL 58	LRLL 67	LRLL 1679
3056.06	$3.288 \pm 0.015$	$3.651 \pm 0.021$	$4.686 \pm 0.015$	$4.658 \pm 0.011$	$6.561 \pm 0.009$
3267.37	$3.611 \pm 0.019$	$3.866 \pm 0.014$	$4.602 \pm 0.015$	$4.654 \pm 0.014$	$7.025 \pm 0.013$
3267.59	$3.587 \pm 0.017$	$3.872 \pm 0.013$	$4.557 \pm 0.010$	$4.644 \pm 0.017$	$6.945 \pm 0.014$
4366.38	$3.413 \pm 0.013$	$3.717 \pm 0.011$	$4.531 \pm 0.011$	$4.649 \pm 0.012$	$6.972 \pm 0.012$
4367.36	$3.407 \pm 0.020$	$3.753 \pm 0.011$	$4.528 \pm 0.014$	$4.688 \pm 0.012$	$6.925 \pm 0.014$
4368.41	$3.409 \pm 0.019$	$3.741 \pm 0.012$	$4.520 \pm 0.012$	$4.668 \pm 0.013$	$6.893 \pm 0.012$
4369.36	$3.402 \pm 0.013$	$3.719 \pm 0.010$	$4.526 \pm 0.013$	$4.667 \pm 0.011$	$6.953 \pm 0.011$
4370.30	$3.386 \pm 0.016$	$3.778 \pm 0.007$	$4.546 \pm 0.017$	$4.649 \pm 0.016$	$7.128 \pm 0.013$
4538.16	$3.367 \pm 0.013$	$3.631 \pm 0.020$	$4.581 \pm 0.016$	$4.656 \pm 0.010$	$6.563 \pm 0.011$
4544.28	$3.337 \pm 0.015$	$3.730 \pm 0.016$	$4.546 \pm 0.014$	$4.650 \pm 0.012$	$6.631 \pm 0.011$

Table 5.3. IRAC Photometry

Date	[3.6]	[4.5]	[5.8]	[8.0]
LRL 2				
11 Feb 2004	$6.971 \pm 0.002$	$6.797 \pm 0.002$	$6.555 \pm 0.002$	$5.761 \pm 0.004$
08 Sep 2004	-	-	-	-
19 Mar 2009	$7.015 \pm 0.002$	$6.905 \pm 0.003$	$6.455 \pm 0.002$	$5.724 \pm 0.005$
20 Mar 2009	$6.982 \pm 0.002$	$6.791 \pm 0.002$	$6.454 \pm 0.002$	$5.721 \pm 0.005$
21 Mar 2009	$6.995 \pm 0.002$	$6.748 \pm 0.002$	$6.479 \pm 0.002$	$5.687 \pm 0.004$
22 Mar 2009	$6.948 \pm 0.002$	$6.796 \pm 0.002$	$6.468 \pm 0.002$	$5.713 \pm 0.003$
23 Mar 2009	$6.984 \pm 0.002$	$6.800 \pm 0.002$	$6.500 \pm 0.002$	$5.742 \pm 0.004$
LRL 21				
11 Feb 2004	$9.086 \pm 0.003$	$8.912 \pm 0.003$	$8.619 \pm 0.006$	$8.130 \pm 0.02$
08 Sep 2004	$9.069 \pm 0.004$	$8.657 \pm 0.003$	$8.413 \pm 0.006$	$8.014 \pm 0.02$
19 Mar 2009	$9.221 \pm 0.003$	$9.025 \pm 0.003$	$8.862 \pm 0.007$	$8.306 \pm 0.03$
20 Mar 2009	$9.212 \pm 0.003$	$9.033 \pm 0.003$	$8.806 \pm 0.006$	$8.313 \pm 0.03$
21 Mar 2009	$9.119 \pm 0.003$	$8.961 \pm 0.003$	$8.787 \pm 0.006$	$8.270 \pm 0.03$
22 Mar 2009	$9.063 \pm 0.003$	$8.885 \pm 0.003$	$8.669 \pm 0.005$	$8.193 \pm 0.02$
23 Mar 2009	$8.934 \pm 0.003$	$8.746 \pm 0.003$	$8.511 \pm 0.005$	$8.168 \pm 0.02$
LRL 58				
11 Feb 2004	$9.789 \pm 0.004$	$9.588 \pm 0.004$	$9.330 \pm 0.015$	$8.543 \pm 0.05$
08 Sep 2004	$10.104 \pm 0.004$	$9.959 \pm 0.004$	$9.637 \pm 0.017$	$8.557 \pm 0.05$
19 Mar 2009	$9.605 \pm 0.004$	$9.372 \pm 0.003$	$9.059 \pm 0.014$	$8.513 \pm 0.04$
20 Mar 2009	$9.619 \pm 0.003$	$9.347 \pm 0.003$	$9.043 \pm 0.012$	$8.493 \pm 0.04$
21 Mar 2009	$9.703 \pm 0.004$	$9.305 \pm 0.003$	$9.011 \pm 0.014$	$8.506 \pm 0.05$
22 Mar 2009	$9.556 \pm 0.004$	$9.254 \pm 0.004$	$8.973 \pm 0.012$	$8.484 \pm 0.05$
23 Mar 2009	$9.515 \pm 0.003$	$9.245 \pm 0.004$	$8.939 \pm 0.012$	$8.494 \pm 0.05$
LRL 67				

Table 5.3—Continued

Date	[3.6]	[4.5]	[5.8]	[8.0]
11 Feb 2004	$10.425 \pm 0.003$	$10.255 \pm 0.003$	$10.063 \pm 0.007$	$9.575 \pm 0.010$
08 Sep 2004	$10.425 \pm 0.003$	$10.238 \pm 0.004$	$9.986 \pm 0.007$	$9.509 \pm 0.011$
19 Mar 2009	$10.422 \pm 0.003$	$10.343 \pm 0.003$	$10.225 \pm 0.008$	$9.675 \pm 0.010$
20 Mar 2009	$10.325 \pm 0.002$	$10.284 \pm 0.003$	$10.129 \pm 0.008$	$9.633 \pm 0.010$
21 Mar 2009	$10.524 \pm 0.003$	$10.325 \pm 0.003$	$10.149 \pm 0.008$	$9.644 \pm 0.010$
22 Mar 2009	$10.386 \pm 0.003$	$10.439 \pm 0.004$	$10.111 \pm 0.008$	$9.605 \pm 0.009$
23 Mar 2009	$10.426 \pm 0.003$	$10.388 \pm 0.004$	$10.163 \pm 0.008$	$9.658 \pm 0.012$
LRL 1679				
11 Feb 2004	$11.317 \pm 0.004$	$11.060 \pm 0.004$	$10.781 \pm 0.011$	$10.287 \pm 0.010$
08 Sep 2004	$10.806 \pm 0.003$	$10.446 \pm 0.003$	$10.173 \pm 0.008$	$9.809 \pm 0.007$
19 Mar 2009	$11.468 \pm 0.004$	$11.295 \pm 0.005$	$11.063 \pm 0.012$	$10.769 \pm 0.014$
20 Mar 2009	$11.436 \pm 0.004$	$11.267 \pm 0.005$	$11.099 \pm 0.013$	$10.781 \pm 0.014$
21 Mar 2009	$11.459 \pm 0.004$	$11.305 \pm 0.005$	$11.047 \pm 0.012$	$10.744 \pm 0.015$
22 Mar 2009	$11.449 \pm 0.004$	$11.298 \pm 0.005$	$11.074 \pm 0.013$	$10.728 \pm 0.016$
23 Mar 2009	$11.444 \pm 0.004$	$11.303 \pm 0.005$	$11.093 \pm 0.013$	$10.769 \pm 0.015$

Table 5.4. IRAC Warm Mission Photometry

MJD-55000	LRL 2		LRL 21		LRL 58		LRL 67		LRL 1679	
	[3.6]	[4.5]	[3.6]	[4.5]	[3.6]	[4.5]	[3.6]	[4.5]	[3.6]	[4.5]
106.91	7.015	6.862	8.996	8.809	9.741	9.489	10.487	10.401	11.278	11.029
107.30	7.009	6.863	8.979	8.804	9.778	9.496	10.500	10.417	11.323	11.020
107.57	7.012	6.833	9.027	8.805	9.759	9.469	10.503	10.439	11.291	10.999
107.81	6.993	6.870	9.006	8.809	9.746	9.431	10.521	10.461	11.283	11.021
108.13	7.017	6.863	8.991	8.805	9.711	9.435	10.559	10.477	11.308	11.045
108.38	6.959	6.838	8.971	8.809	9.724	9.410	10.556	10.465	11.348	11.092
108.58	6.991	6.833	9.054	8.808	9.754	9.423	10.540	10.471	11.323	11.083
108.81	6.988	6.802	9.037	8.822	9.749	9.452	10.524	10.431	11.323	11.096
109.58	6.939	6.833	9.197	8.977	9.853	9.536	10.534	10.447	11.329	11.124
110.50	6.988	6.823	9.137	8.977	9.735	9.447	10.452	10.352	11.348	11.130
111.07	7.024	6.849	9.201	8.995	9.704	9.398	10.485	10.378	11.264	11.084
112.43	7.008	6.848	9.209	9.060	9.638	9.325	10.471	10.416	11.283	11.088
113.07	6.999	6.799	9.223	9.082	9.655	9.355	10.483	10.374	11.319	11.072
114.73	6.967	6.802	9.288	9.185	9.715	9.395	10.486	10.435	11.319	11.077
115.37	6.943	6.799	9.325	9.164	9.691	9.409	10.488	10.434	11.298	11.031
115.97	6.954	6.792	9.309	9.158	9.684	9.386	10.489	10.389	11.268	11.050
116.32	6.905	6.766	9.294	9.125	9.620	9.366	10.482	10.427	11.281	11.051
116.62	6.920	6.751	9.289	9.129	9.635	9.316	10.537	10.483	11.294	11.036
116.72	6.972	6.812	9.290	9.138	9.644	9.344	10.565	10.499	11.293	11.068
117.13	6.954	6.746	9.269	9.102	9.649	9.357	10.552	10.498	11.291	11.038
117.21	6.969	6.771	9.275	9.107	9.633	9.338	10.547	10.479	11.261	11.034
117.46	6.945	6.782	9.273	9.086	9.659	9.371	10.547	10.504	11.255	11.002
117.69	6.939	6.757	9.215	9.076	9.665	9.391	10.551	10.517	11.301	11.024
118.60	6.909	6.771	9.146	9.010	9.742	9.425	10.576	10.544	11.277	11.064
119.25	6.955	6.784	9.167	9.008	9.725	9.442	10.565	10.548	11.263	11.175
119.93	6.944	6.777	9.151	8.963	9.739	9.452	10.582	10.537	11.284	11.135
121.21	6.949	6.789	9.129	8.912	9.788	9.495	10.582	10.557	11.204	11.009
123.07	6.921	6.775	9.054	8.792	9.856	9.591	10.572	10.529	11.296	11.027
124.96	6.924	6.784	9.018	8.800	9.928	9.615	10.620	10.580	11.279	11.046
127.68	6.945	6.794	8.966	8.748	9.766	9.487	10.581	10.521	11.228	11.027
129.81	6.940	6.797	9.044	8.746	9.758	9.504	10.559	10.545	11.217	10.975



Table 5.4—Continued

MJD-55000	LRL 2		LRL 21		LRL 58		LRL 67		LRL 1679	
	[3.6]	[4.5]	[3.6]	[4.5]	[3.6]	[4.5]	[3.6]	[4.5]	[3.6]	[4.5]
131.27	6.938	6.792	8.910	8.632	9.825	9.529	10.599	10.541	11.219	10.925
133.38	6.954	6.832	8.887	8.683	9.753	9.456	10.638	10.498	11.186	10.924
135.61	6.975	6.841	8.875	8.608	9.649	9.338	10.456	10.377	11.162	10.906
137.52	7.004	6.867	8.649	8.379	9.594	9.329	10.314	10.201	11.199	10.870
139.07	7.029	6.879	8.634	8.364	9.645	9.337	10.336	10.209	11.197	10.895
141.52	7.030	6.915	8.776	8.485	9.612	9.300	10.269	10.175	11.166	10.899
142.11	7.038	6.925	8.715	8.478	9.643	9.314	10.286	10.152	11.196	10.890

Table 5.5. Extinction

Date	$A_V$
LRL 2	
08 Oct 2009	2.8
31 Oct 2009	3.0
LRL 21	
10 Oct 2008	4.1
11 Oct 2008	4.4
18 Oct 2008	4.2
19 Oct 2008	4.6
08 Oct 2009	3.9
31 Oct 2009	4.1
04 Nov 2009	4.2
08 Nov 2009	4.3
LRL 58	
09 Oct 2009	3.4
08 Nov 2009	3.4
LRL 1679	
11 Oct 2008	5.8
18 Oct 2008	5.8
19 Oct 2008	5.8
09 Oct 2009	5.8
04 Nov 2009	5.8

Table 5.6. LRL 21 NIR Photometry

Date	J	H	K
2MASS	11.02	9.99	9.47
10 Oct 2008	11.31	10.17	9.71
11 Oct 2008	11.30	10.21	9.73
19 Oct 2008	11.19	10.14	9.60
8 Oct 2009	10.96	9.98	9.59
31 Oct 2009	10.99	10.05	9.52
4 Nov 2009	10.95	9.91	9.39
8 Nov 2009	10.96	9.94	9.43

Table 5.7. LRL 21 Stellar Luminosity

Date	$L_*$ ( $L_\odot$ )
10 Oct 2008	2.52 pm 0.39
11 Oct 2008	2.75 pm 0.43
19 Oct 2008	3.20 pm 0.50
08 Oct 2009	3.30 pm 0.52
31 Oct 2009	3.38 pm 0.53
04 Nov 2009	3.60 pm 0.56
08 Nov 2009	3.66 pm 0.57

Table 5.8. Radial and Rotational Velocity

ID	$v_r$	$v \sin i$	Reference
LRL 21	17.01	17.84	1
	-15.7 <sup>a</sup>	21.9 <sup>a</sup>	2
	66.8 <sup>a</sup>	<15 <sup>a</sup>	2
LRL 58	14.2	<15	2
LRL 67	15.0	<15	2
	15.09	13.6	1
	16.9	<11	3

<sup>a</sup>In our high-resolution spectra of LRL 21 we find two peaks in the cross-correlation function and report the radial and rotational velocity of each component.

Note. — References: (1) Dahm (2008) (2) This paper (3) Nordhagen et al. (2006).

Table 5.9. Infrared Excess

Date	$r_J$	$r_H$	$r_K$	$T_{dust}$	Covering Fraction
LRL 21					
10 Oct 2008	0.13	0.19	0.26	1900	0.06
11 Oct 2008	0.10	0.22	0.35	-	-
18 Oct 2008	0.01	0.17	0.36	2020	0.08
19 Oct 2008	0.01	0.17	0.37	2180	0.08
08 Oct 2009	0.02	0.09	0.19	-	-
31 Oct 2009	0.06	0.29	0.56	1860	0.13
04 Nov 2009	0.07	0.29	0.54	1700	0.13
08 Nov 2009	0.15	0.29	0.46	-	-
LRL 58 <sup>a</sup>					
09 Oct 2009	0.12	0.28	0.46	-	-
08 Nov 2009	0.18	0.32	0.48	-	-
LRL 1679					
11 Oct 2008	-0.02	-0.004	0.01	-	-

Table 5.9—Continued

Date	$r_J$	$r_H$	$r_K$	$T_{dust}$	Covering Fraction
18 Oct 2008	-0.09	-0.07	-0.04	-	-
19 Oct 2008	-0.16	-0.11	-0.05	-	-
09 Oct 2009	-0.11	-0.02	0.07	-	-
04 Nov 2009	-0.04	0.02	0.09	-	-

<sup>a</sup>For LRL 58 we use to standard JH 108 to measure the veiling even though it shows emission near the Br $\gamma$  line, which may indicate accretion and possibly a disk. The line strengths fit better than an M1 giant or dwarf standard. The measured veiling is only a lower limit, although the lack of infrared excess for JH 108 indicates that within our uncertainties we are measuring the true veiling

Note. — Uncertainties on the veiling measurements are  $\sim 0.1$ . No veiling is measured for LRL 2 since the only photospheric absorption lines are the hydrogen series, which will be contaminated from emission by the accretion flow.

Table 5.10. Emission Lines

Date	Pa $\beta$ EW ( $\text{\AA}$ )	Br $\gamma$ EW ( $\text{\AA}$ )	Corrected Br $\gamma$ EW ( $\text{\AA}$ )
LRL 2			
9 Oct 2009	$0.46 \pm 0.04$	$3.45 \pm 0.27$	$1.85 \pm 0.17$
31 Oct 2009	$3.40 \pm 0.03$	$5.23 \pm 0.17$	$3.16 \pm 0.10$
LRL 21			
10 Oct 2008	$-0.63 \pm 0.35$	$0.01 \pm 0.27$	$0.07 \pm 0.26$
11 Oct 2008	$-0.96 \pm 0.07$	$-0.32 \pm 0.05$	$-0.27 \pm 0.04$
18 Oct 2008	$1.21 \pm 0.05$	$-0.16 \pm 0.04$	$-0.09 \pm 0.03$
19 Oct 2008	$1.25 \pm 0.08$	$-0.07 \pm 0.05$	$-0.02 \pm 0.04$
8 Oct 2009	$-0.83 \pm 0.06$	$0.29 \pm 0.05$	$0.33 \pm 0.05$
31 Oct 2009	$-1.90 \pm 0.07$	$0.14 \pm 0.04$	$0.22 \pm 0.03$
4 Nov 2009	$0.70 \pm 0.07$	$1.02 \pm 0.08$	$1.11 \pm 0.08$
8 Nov 2009	$0.56 \pm 0.06$	$0.88 \pm 0.09$	$0.94 \pm 0.09$
LRL 58			
9 Oct 2009	$0.96 \pm 0.09$	$0.66 \pm 0.09$	$0.86 \pm 0.09$
8 Nov 2009	$1.95 \pm 0.51$	$1.63 \pm 0.45$	$1.84 \pm 0.47$
LRL 1679			
11 Oct 2008	$-0.58 \pm 0.22$	$-0.12 \pm 0.07$	-
18 Oct 2008	$-0.23 \pm 0.24$	$0.66 \pm 0.20$	-
19 Oct 2008	$-1.03 \pm 0.33$	$0.13 \pm 0.15$	-
9 Oct 2009	$-0.89 \pm 0.49$	$0.51 \pm 0.42$	-
4 Nov 2009	$-0.78 \pm 0.31$	$0.17 \pm 0.13$	-

Table 5.11. Accretion Rates

Date	Flux ( $10^{-14}$ erg s $^{-1}$ cm $^{-2}$ )	$\log(L/L_{\odot})$	$\log(L_{acc}/L_{\odot})$	$L_{acc}/L_{*}$	$\dot{M}$ ( $10^{-8} M_{\odot} yr^{-1}$ )
LRL 2 Pa $\beta$					
9 Oct 2009	$25.2 \pm 6.8$	$-3.09 \pm 0.12$	$-0.37 \pm 0.14$	0.003	$3.14 \pm 0.44$
31 Oct 2009	$185 \pm 29$	$-2.23 \pm 0.07$	$0.61 \pm 0.08$	0.03	$29.9 \pm 2.4$
LRL 2 Br $\gamma$					
9 Oct 2009	$29.2 \pm 3.6$	$-3.03 \pm 0.05$	$0.61 \pm 0.06$	0.03	$29.9 \pm 1.8$
31 Oct 2009	$49.8 \pm 5.2$	$-2.80 \pm 0.04$	$0.90 \pm 0.05$	0.06	$58.4 \pm 2.9$
LRL 58 Pa $\beta$					
9 Oct 2009	$1.35 \pm 0.24$	$-4.37 \pm 0.08$	$-1.83 \pm 0.09$	0.02	$0.23 \pm 0.02$
8 Nov 2009	$2.81 \pm 0.56$	$-4.05 \pm 0.09$	$-1.47 \pm 0.10$	0.05	$0.52 \pm 0.05$
LRL 58 Br $\gamma$					
9 Oct 2009	$0.74 \pm 0.09$	$-4.63 \pm 0.06$	$-1.40 \pm 0.08$	0.06	$0.62 \pm 0.05$
8 Nov 2009	$1.57 \pm 0.23$	$-4.30 \pm 0.06$	$-0.99 \pm 0.08$	0.14	$1.58 \pm 0.13$
LRL 21 Pa $\beta$					
18 Oct 2008	$4.68 \pm 0.74$	$-3.83 \pm 0.07$	$-1.22 \pm 0.08$	0.02	$0.388 \pm 0.031$
19 Oct 2009	$5.33 \pm 0.86$	$-3.77 \pm 0.07$	$-1.15 \pm 0.08$	0.02	$0.455 \pm 0.036$
4 Nov 2009	$3.36 \pm 0.57$	$-3.97 \pm 0.07$	$-1.38 \pm 0.09$	0.01	$0.268 \pm 0.024$
8 Nov 2009	$2.75 \pm 0.49$	$-4.06 \pm 0.08$	$-1.48 \pm 0.10$	0.01	$0.212 \pm 0.021$
LRL 21 Br $\gamma$					
8 Oct 2009	$0.663 \pm 0.164$	$-4.68 \pm 0.11$	$-1.47 \pm 0.14$	0.01	$0.218 \pm 0.031$
31 Oct 2009	$0.501 \pm 0.103$	$-4.79 \pm 0.09$	$-1.61 \pm 0.11$	0.007	$0.158 \pm 0.017$



Table 5.11—Continued

Date	Flux ( $10^{-14}$ erg s $^{-1}$ cm $^{-2}$ )	log(L/L $_{\odot}$ )	log(L $_{acc}$ /L $_{\odot}$ )	L $_{acc}$ /L $_{*}$	$\dot{M}$ ( $10^{-8}$ M $_{\odot}$ yr $^{-1}$ )
4 Nov 2009	$2.78 \pm 0.31$	$-4.05 \pm 0.05$	$-0.67 \pm 0.06$	0.06	$1.38 \pm 0.08$
8 Nov 2008	$2.30 \pm 0.29$	$-4.13 \pm 0.05$	$-0.77 \pm 0.06$	0.05	$1.09 \pm 0.07$

Table 5.12. Strength and shape of silicate feature

Epoch	EW(10 $\mu$ m)	$S(\text{peak})$	$S(11.3)/S(9.8)$
LRL 2			
1	2.98	0.97	1.00
2	2.71	0.91	1.06
3	2.97	0.96	1.11
4	2.96	0.96	1.13
LRL 21			
1	2.19	0.76	1.39
2	2.13	0.80	1.52
3	1.87	0.65	1.53
4	1.89	0.68	1.81
LRL 31			
1	2.37	1.98	0.98
2	3.31	2.26	0.96
3	2.37	1.84	0.97

Table 5.12—Continued

Epoch	EW(10 $\mu$ m)	$S(\textit{peak})$	$S(11.3)/S(9.8)$
4	2.37	1.71	0.99
LRL 58			
1	2.51	0.79	1.13
2	2.76	0.87	1.18
3	3.07	1.03	1.27
4	3.21	1.05	1.24
LRL 67			
1	3.73	1.62	0.87
2	3.51	1.49	0.87
3	3.92	1.72	0.87
4	3.77	1.63	0.86
LRL 1679			
1	1.68	0.69	0.93
2	1.33	0.47	1.16

Table 5.12—Continued

Epoch	EW(10 $\mu$ m)	$S(\textit{peak})$	$S(11.3)/S(9.8)$
3	1.74	0.69	0.70
4	1.19	0.53	1.21

Note. — These parameters have been derived based on a dereddened silicate feature. The extinction is assumed to be constant between each epoch and the spectra are dereddened using the McClure (2009) extinction law

Table 5.13. Inner radii of disk

ID	Co-rotation Radius (AU)	Sublimation Radius (AU)
LRL 2	(0.03-0.18)	0.76 (>0.41)
LRL 21	0.04	0.13 (>0.07)
LRL 31	0.05	0.13 (>0.07)
LRL 58	0.07	0.05 (>0.03)
LRL 67	(0.02-0.10)	0.04 (>0.02)
LRL 1679	(0.01-0.08)	0.03 (>0.02)

Note. — Co-rotation radii are calculated based on observed rotational periods estimated from optical light curves. When not observed period is available we estimate the co-rotation radius for periods of 1 and 15 days, which span the typical periods observed for pre-main sequence stars in IC 348 (Cieza & Baliber, 2006). The lower limit on the sublimation radius, included in parenthesis, assumes very large grains ( $> 10\mu\text{m}$ ) at 1500K.

## CHAPTER 6

## CONCLUSION

We now summarize the key results of the previous chapters and discuss areas of future study.

### 6.1 Disk Evolution in NGC 2068/71

The first step towards understanding how disks evolve is identifying the disks in the process of being removed and putting them in context with other less evolved disks. To this end, in Chapter 2 we used low-resolution optical spectra to select a sample of pre-main sequence members of the cluster NGC 2068/71 and then used 3-24 $\mu$ m infrared photometry to characterize the disks in these systems. We were able to catalog 69 cluster members, 79% of which have an infrared excess, and estimate a median age for the cluster of 2 Myr. Based on high-resolution H $\alpha$  spectra, we find that all but one of the stars with an infrared excess are actively accreting.

The 3-24 $\mu$ m photometry provides detailed sampling of the infrared SED which allows us to distinguish evolved disks from fully flared optically thick disks. We identify three groups of evolved disks: IRAC-weak, MIPS-weak and transition disks. The IRAC-weak disks are defined as having  $-2.5 < \alpha_{IRAC} < -1.6$ , the MIPS-weak disks have  $[8.0]-[24] < 2.4$  while the transition disks have  $[8.0]-[24] > 4$  and  $[3.6]-[4.5] < 0.1$ . All three groups have much weaker excesses than a typical primordial disk, indicating a change in the dust structure. The IRAC-weak disks have weaker 3-8 $\mu$ m emission, and generally weaker 24 $\mu$ m emission. The transition disks have almost no 3-8 $\mu$ m emission, but strong 24 $\mu$ m emission and the MIPS-weak disks have overall weaker 3-24 $\mu$ m emission. By combining this

SED information with the  $H\alpha$  profiles we can study the simultaneous evolution of the gas and dust. We find that the evolved disks are still actively accreting, but at a lower level than the less evolved disks. In general both the  $H\alpha$  EW and the velocity width of the line are lower relative to the strong disks. This indicates that the evolution of the gas and the dust is tightly connected in these systems and whatever process changes the dust distribution also affects the flow and/or the surface density of gas.

## 6.2 Modeling Infrared Variability

Once evolved disks have been selected, they can be studied in detail to further understand their structure and how it differs from a normal disk. One unexplored avenue for understanding the disk is infrared variability. Anecdotal evidence in the past suggested that some disks did show large changes in their infrared SED, consistent with perturbations to the traditional picture of an axisymmetric, flared, optically thick disk (Juhász et al., 2007; Hutchinson et al., 1994). Recently this behavior has been seen in transition disks (Muzerolle et al., 2009; Espaillat et al., 2011). If the variability is due to changes in the disk then it may be useful in understanding disk structure. To further explore this possibility, in chapter 3 we constructed simple geometric models of non-axisymmetric structure within a disk in order to understand if it could explain the observed infrared variability.

These models were motivated by observations that found a unique wavelength dependence to the infrared variability. Muzerolle et al. (2009) present IRS spectra of one transition disk, LRL 31, in which the  $\lambda < 8\mu\text{m}$  flux decreases as the  $\lambda > 8\mu\text{m}$  flux increases, all in one week. Traditional theories of pre-main sequence variability typically involve hot or cold spots rotating across the stellar surface, which alone cannot reproduce this wavelength dependence. We instead

considered non-axisymmetric perturbations to the disk, such as a warp or a spiral wave. We found that the precession of this structure created very weak infrared fluctuations ( $< 2\%$ ) without reproducing the observed wavelength dependence. Previous models only studied axisymmetric changes in the disk structure and were not able to analyze precession. We did find that changing the scale height of a warp or spiral wave at the inner edge of the disk from  $h/r=0.01$  to  $0.10$  was able to reproduce the observations. As the warp grows in size the emitting area of the hot dust increases, while the temperature rises as it becomes more directly illuminated, creating more short wavelength flux. At the same time the warp shadows the outer disk, decreasing its temperature and as a consequence the long-wavelength flux decreases. Placing the warp at the inner edge of the disk is consistent with the timescale for this variability, since the dynamical timescale of the inner disk is roughly a week for many pre-main sequence stars.

### 6.3 Multi-wavelength, Multi-epoch observations of Transition Disks

Our modeling suggests structural changes in the scale height of the inner disk are the source of the infrared variability, a conclusion that has been reached by others using more detailed, but axisymmetric, radiative transfer models (Juhász et al., 2007; Espaillat et al., 2011). These models are limited in their ability to determine the physical source of these changes in the disk. In chapter 4 and 5 we describe observations of a sample of six transition disks in the nearby ( $\sim 320$ pc), young ( $\sim 3$ Myr) cluster IC 348. These observations include more concentrated monitoring of the  $3.6$  and  $4.5\mu\text{m}$  emission in order to better determine the variability timescale,  $0.8\text{--}5\mu\text{m}$  infrared spectra to characterize the presence and behavior of any hot dust close to the star as well as measure the accretion using the  $\text{Pa}\beta$  and  $\text{Br}\gamma$  emission lines, near-infrared photometry to trace the photospheric flux and



optical spectroscopy to follow accretion rate fluctuations. Including measures of the accretion rate is crucial because of the importance of the gas within primordial disks. As we found in chapter 2 the gas and dust appear to evolve together and it is possible that in these variable transition disks changes in the gas and dust structure are strongly related.

In chapter 4 we focus on the transition disk LRL 31, a  $\sim 2M_{\odot}$  star that shows substantial variation in the IRS spectra, and for which we have the most extensive ancillary data among the transition disks. We found consistent fluctuations of the infrared flux on timescales of weeks, suggesting that we are not observing a single burst but rather continuous variability of the disk. Spectra of the 2-5  $\mu\text{m}$  excess, taken over the course of two years found that the excess is well fit by a single temperature blackbody, indicative of optically thick dust at the dust destruction radius. The strength of this excess varies substantially due to changes in the scale height of the inner disk, consistent with the simple models from chapter 3. The accretion rate also appears to vary by a factor of 5, and in 2009 when we have contemporaneous monitoring of the accretion rate and infrared flux, we find a correlation between these properties. Despite this correlation, the variable accretion rate is unlikely to be the cause of the changes in disk structure. The accretion luminosity is small compared to the stellar flux, indicating that heating of the disk does not substantially change during periods of fluctuating accretion rate. The lack of periodicity in the infrared monitoring also suggests that it is unlikely that a companion within 0.4 AU perturbs the disk on every orbit. The most promising explanations are either a companion beyond 0.4 AU or a dynamic stellar or disk magnetic field.

In chapter 5 we expand this sample to include five more transition disks in IC 348 including observations from 4000  $\text{\AA}$  to 40  $\mu\text{m}$  on timescales of days to

years. We find infrared variability in all of these sources and the observations are consistent with an inner disk whose scale height is varying rapidly. We see a wavelength dependence, with anti-correlated changes in the short and long-wavelength infrared flux, in some of the sources similar to what was seen in LRL 31. For one source we have multi-epoch observations of the  $2\text{--}5\mu\text{m}$  excess and we find that the strength changes while the shape stays the same, again similar to LRL 31. We find little change in the stellar flux and large fluctuations in the accretion rate, although the accretion luminosity is small compared to the stellar luminosity indicating that the overall heating of the disk does not change rapidly. Unlike in LRL 31, we do not see a strong correlation between the infrared flux and the accretion rate in any of our sources during our 40 days of intense monitoring. While accretion is unlikely to be the source of the variability, the most promising sources of the variability continue to be either an unseen companion or a dynamic magnetic field.

#### 6.4 Future Directions

Throughout our work we have seen a tight connection between the gas and dust in circumstellar disks. In chapter 2 we found that during the removal of the primordial disk, the accretion activity also decreases. In chapter 4 we found that the perturbation to the dust also affected the flow of gas onto the star. Both of these observational results indicate a close connection between the flow of gas and the dust structure, even when the dust is perturbed on very short timescales. The strongest connection was seen in LRL 31, although it is not clear if this behavior is common to all young stellar objects. We limited ourselves to synoptic monitoring of a small sample of transition disks but extending the accretion rate monitoring with multi-object spectroscopy would help to determine if this be-

havior is common among all of the disks, or if it is only present in systems with evolved disks.

We have also found that infrared variability is common among transition disks and is indicative of fluctuations in the inner disk structure. The commonality of the variability is a sign that it represents a fundamental property of these systems. This hints at the potential for using infrared variability to study disk structure. From our observations we have already learned that the scale height of the inner disk can change by a factor of a few over the course of a week. We found that previously unaccounted for phenomena, such as low-mass companions or dynamic stellar magnetic fields, can strongly influence the disk structure and ruled out a variable accretion luminosity as the source of the changes in the disk structure. Future studies of variability will have the potential to reveal more details about the structural changes around many young stellar objects, not just transition disks, as well as put further constraints on the physical mechanism responsible for this variability.

We have found that coordinated multi-wavelength campaigns are powerful tools for studying the cause of the infrared flux variations. Our coverage of the stellar and accretion luminosity ruled these properties out as a potential cause of the infrared variability. Unfortunately they were not able to completely restrict the theoretical cause and additional observations are needed. X-ray monitoring would be a valuable addition to this type of study, especially given the possible role of magnetic fields. X-ray flares may heat the disk to very high temperatures, or they may extend far enough for the plasma to directly disrupt the dust. An expanding and contracting stellar magnetic field will create periodic reconnection events that would be detected as X-ray flares (Goodson & Winglee, 1999) while disrupting the disk when in its bloated state. The relative timing of the X-ray

and infrared changes, along with the characteristics of the X-ray flares, should distinguish between these models.

While X-ray monitoring would reveal clues to the interaction of the magnetic field and the disk, other measurements are needed to look for unseen companions. Radial velocity monitoring would help to determine if a close in companion exists in many of these systems. While it is difficult to put strong constraints on the radial velocity perturbations from a companion in young stars due to their highly variable spectra, stellar mass companions can still be detected. Extending the baseline of infrared monitoring would also allow us to look for periodicity, a sign of a companion, on much longer timescales. Our previous infrared monitoring was confined to a single 40 day window, which limited us to studying periods of 2-25 days. Further monitoring will allow us to look for long-term periodicity and determine if the properties of the fluctuations are constant with time. The advent of wide-field infrared cameras, efficient survey instruments, and multi-object spectrographs will allow us to use variability as a powerful tool in the future.

## APPENDIX A

## DETAILED CALCULATION OF THE SED

## A.1 Outer Warp + Flat Extension

A.1.1 Adding  $\alpha$  Dependence to Outer Warp

TB96 describe how to calculate the SED for an outer warp seen at various inclination angles. Their general method for calculating the SED also includes a dependence on azimuthal viewing angle, although their detailed treatment of various occultation effects (the star blocking the far side of the disk, the disk blocking the star, etc.) does not include this dependence. Since these disks are non-axisymmetric the SED can depend substantially on the azimuthal viewing angle,  $\alpha$ , of the observer. In this section we describe how we have added this dependence into the equations of TB96. We do not include a detailed description of the derivation of the equations, but merely state most of them and some of the geometric logic behind their modification.

The first modification is to equation (6) of TB96, which describes the calculation of the flux from the disk based on the temperature of the disk. This equation assumes that the disk is viewed along  $\alpha = 0$  so that the upper disk from 0 to  $\pi/2$  looks the same as the upper disk from  $3\pi/2$  to  $2\pi$ . When  $\alpha \neq 0$  this symmetry is broken and the individual components of the disk must be considered. While the temperature of a concave, or convex, piece of the disk does not change with viewing angle, the orientation of each of the concave, or convex pieces, changes and must be treated separately. For the outer warp this becomes:

$$F_{\nu, \mathbf{u}} = \int_{r_{min}}^{R_{disk}} \left[ \int_0^{\pi/2} (B(T_{concave})f_{up} + B(T_{convex})f_{low}) \right]$$

$$\begin{aligned}
& + \int_{r_{min}}^{R_{disk}} \left[ \int_{\pi/2}^{\pi} (B(T_{concave})f_{low} + B(T_{convex})f_{up}) \right] \\
& + \int_{r_{min}}^{R_{disk}} \left[ \int_{\pi}^{3\pi/2} (B(T_{convex})f_{up} + B(T_{concave})f_{low}) \right] \\
& + \int_{r_{min}}^{R_{disk}} \left[ \int_{3\pi/2}^{2\pi} (B(T_{concave})f_{up} + B(T_{convex})f_{low}) \right]
\end{aligned} \tag{A.1}$$

The next change comes in the appendix to the functional form of the parameter  $C$ . The function  $C$  is used to define the points that are along the line of sight with the star. If the line intersects the star then we need to worry about whether the disk blocks the star or the star blocks the disk. If this line does not intersect the star then the disk cannot block the star and the star cannot block the disk. The definition of  $C$  changes from  $C = r \sin \theta$  to  $C = r \sin(\theta - \alpha)$ . Also the radial part of the deformation used in equation (A6) of TB96 is taken to be  $H(r) = gR_{disk} \left( \frac{r}{R_{disk}} \right)^n \cos \alpha$ . For  $\alpha = \pi/2$  the disk along the line of sight is flat and the radial part of the height will remain at zero, while along  $\alpha = \pi$  the disk curves below the midplane as expected.

The final change comes when calculating the stellar flux. In equation (A12) of TB96 we take  $h(r, \theta)$  to be  $h(r, \alpha)$  since this represents the part of the disk that will block the star. As the azimuthal angle increases the disk blocks less of the star because the height of the disk is smaller. We make more changes to how the stellar flux is calculated, which are described below, but when it comes to the occultation of the star by the disk this is the only change.

In the end we are able to run our models from  $0 < i < \pi$  and  $-\pi/2 < \alpha < \pi/2$ . Due to the symmetry of the disk this covers all possible viewing angles allowing us to accurately model the precession of the warp, as well as observe the warp from an arbitrary angle.

### A.1.2 Flat Extension of Outer Warp

We have taken the outer warp model and added a flat extension beyond it in order to treat disks where the warp is not at the outer edge of the disk. The warp will shadow the outer disk, changing its temperature structure. For simplicity we assume that the outer disk is a flat blackbody. The temperature can be derived using the same formula as with the warped disk (Equation 6), but with different definitions for the integration boundaries. Half of the flat extension will be shadowed while half will not be shadowed. For the side of the flat extension that is beyond the part of the warp the goes below the midplane there is no shadowing of the disk and the integration ranges over:

$$\begin{aligned}
 \varepsilon_{min} &= 0 \\
 \varepsilon_{max} &= \pi/2 \\
 \delta_{min} &= 0 \\
 \delta_{max} &= \arcsin(R_*/d) \\
 d^2 &= r^2 + h^2
 \end{aligned}
 \tag{A.2}$$

For the part of the flat extension that lies behind the warp that stretches above the midplane the definition of  $\delta_{min}$  changes. In this case  $\delta_{min}$  is set by the angle between the warp and the point  $P(r, \theta)$  in the disk.

$$\delta_{min} = \arctan\left(\frac{gR_{warp} \cos(\theta)}{(r - R_{warp})}\right)
 \tag{A.4}$$

This takes into account shadowing of the flat extension to the disk due to the warp. Once the temperature structure has been determined the flux can be derived using the equation for the flux from a disk (Equation 5).

## A.2 Inner Warp

### A.2.1 Temperature Profile of Inner Warp

In this section we describe the method for calculating the SED of a disk with an inner warp. In the text we laid out the basic equations from TB96 that are needed to calculate the temperature structure. As mentioned in the text the essential difference between the inner warp and outer warp comes in calculating  $\delta_{max}, \delta_{min}, \varepsilon_{min}, \varepsilon_{max}$  for each point  $P(r, \theta)$ , which are used in equation 6. From here the disk is split into two sides that are treated separately. The convex side is the side of the disk that faces the star on the inner edge and receives the most direct heating from the star. For this side, the integration ranges over:

$$\begin{aligned}\varepsilon_{min} &= 0 \\ \varepsilon_{max} &= \pi/2\end{aligned}\tag{A.5}$$

$$\begin{aligned}\delta_{min} &= -\arctan(\partial h / \partial r) \\ \delta_{max} &= \arcsin(R_*/d) \\ d^2 &= r^2 + h^2\end{aligned}\tag{A.6}$$

Figure A.1 demonstrates the limits on  $\delta$  for the convex side of the disk. The definition of  $\delta_{min}$ , demonstrated in figure A.2, comes from the inner disk blocking light from the top of the star. The inner disk will limit the field of view of the point  $P(r, \theta)$  as it looks toward the star. Traveling out from the star, less of the star will be seen by the disk because the shallower slope of the disk will cause more of the star to be blocked. In the limit of a flat disk far from the star  $\delta_{min}$  approaches



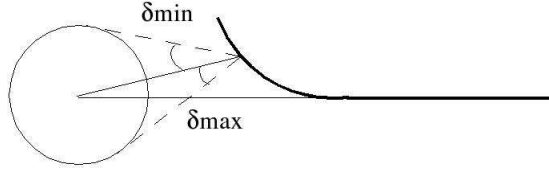


Figure A.1 Schematic diagram of the limits on  $\delta$  for the convex side of the disk.

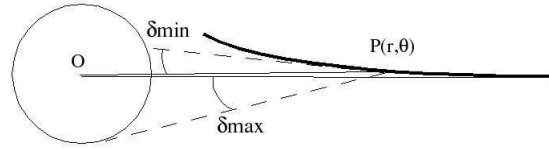


Figure A.2 Schematic diagram of the limits on  $\delta$  for the convex side of the disk. In this case the star is blocked by some of the disk. The shallow slope of the disk prevents all of the star from being seen.

zero and the disk can only see half of the star. If the point  $P(r, \theta)$  on the disk is close enough to the star then the disk can see all of the star and  $\delta_{min} = -\delta_{max}$ . The limits on  $\varepsilon$  assume that the scale height of the disk does not change across the face of the disk, which will be an accurate approximation far from the star.

The concave side of the disk is the side that does not directly face the star. Since it does not face the star much of the inner parts of the disk will be blocked by the warp and will only be heated by viscous dissipation. The condition for the point  $P(r, \theta)$  on the concave part of the disk to see any of the star is:

$$\frac{h(r_{min}, \theta)}{r - r_{min}} < \frac{R_*}{r} \quad (\text{A.7})$$

If the point  $P(r, \theta)$  meets this condition then this point can see some of the star and  $\delta_{min}$  becomes (fig A.3)

$$\delta_{min} = \arctan\left(\frac{h(r_{min}, \theta)}{r - r_{min}}\right) \quad (\text{A.8})$$

The rest of the limits stay the same. In the limit of a perfectly flat disk  $\delta_{min}$  approaches 0 and the point  $P(r, \theta)$  is irradiated by only half of the star. For a large

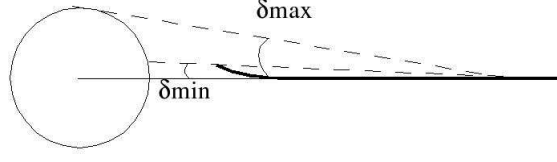


Figure A.3 Schematic diagram of the limits on  $\delta$  for the concave side of the disk.

warp the only heating by this side of the disk will be from viscous dissipation because the warp will block the star over most of the disk.

### A.2.2 Calculating the SED for an Inner Warp

In this section we describe the procedure for converting the temperature structure into a spectral energy distribution (SED). From TB96, the flux emitted by the disk is

$$F_{\nu, \mathbf{u}} = \int \int_{\text{disk surface}} B_{\nu}(T(r, \theta)) dS \mathbf{n}_d \cdot \mathbf{u} \quad (\text{A.9})$$

In this case  $\mathbf{u}$  is the vector along the line of sight to the observer from the center of the star and  $\mathbf{n}_d$  is the normal to the disk at the point  $P(r, \theta)$ . The vector  $\mathbf{u}$  can be defined in terms of the azimuthal and polar angles to the line of sight,  $\alpha$  and  $i$  respectively. The area of the disk along the line of sight is given by

$$dS \mathbf{n}_d \cdot \mathbf{u} = r \left[ \left( \frac{1}{r} \frac{\partial h}{\partial \theta} \sin \theta - \frac{\partial h}{\partial r} \cos \theta \right) \cos \alpha \sin i - \left( \frac{1}{r} \frac{\partial h}{\partial \theta} \cos \theta + \frac{\partial h}{\partial r} \sin \theta \right) \sin \alpha \sin i + \cos i \right] dr d\theta \quad (\text{A.10})$$

The angle  $\alpha$  ranges from  $-\pi/2$  to  $\pi/2$  while the inclination  $i$  ranges from 0 to  $\pi$ . This covers all possible viewing angles of the disk, since the symmetry of the disk makes some viewing angles redundant.

Splitting up the equation for the flux from the disk helps to make the problem simpler to understand and more tractable. It also fits with the fact that we do not need to calculate the temperature structure of the entire disk. The symmetry of

the disk allows us to calculate the temperature of the convex and concave side from  $0 < \theta < \pi/2$  and then apply this temperature profile to the rest of the disk. The integral is split into eight parts:

$$\begin{aligned}
 F_{\nu, \mathbf{u}} = & \int_{r_{min}}^{R_{disk}} \left[ \int_0^{\pi/2} (B(T_{concave})f_{up} + B(T_{convex})f_{low}) \right] \\
 & + \int_{r_{min}}^{R_{disk}} \left[ \int_{\pi/2}^{\pi} (B(T_{concave})f_{low} + B(T_{convex})f_{up}) \right] \\
 & + \int_{r_{min}}^{R_{disk}} \left[ \int_{\pi}^{3\pi/2} (B(T_{convex})f_{up} + B(T_{concave})f_{low}) \right] \\
 & + \int_{r_{min}}^{R_{disk}} \left[ \int_{3\pi/2}^{2\pi} (B(T_{concave})f_{up} + B(T_{convex})f_{low}) \right] \quad (A.11)
 \end{aligned}$$

where  $f(r, \theta) = dS \mathbf{n}_d \cdot \mathbf{u} p(r, \theta)$ , and  $p(r, \theta)$  is a binary function used to determine if the point  $P(r, \theta)$  is visible to the observer. The integration is done over both the upper and lower sides of the disk in order to account for inclination angles greater than  $90^\circ$  where the lower half of the disk is visible. If the inclination is 0 then the observer is face on to the upper half of the disk, which has both a concave and convex side. If the inclination is  $180^\circ$  then the observer is face on to the lower half of the disk, which includes both a concave and a convex side. Treating each quarter of the disk separately allows us to use the symmetry of the temperature profile but still treat general azimuthal viewing angles.

#### A.2.2.1 Calculating the value of p

The above description sets out the basics for how to calculate the temperature structure and SED for a warped inner disk. Most of this is derived from TB96, which treated these situations generally enough to apply to any type of warp. The main differences between this inner warp and the outer warp from TB96 comes from the calculation of  $p(r, \theta)$ . This section describes the conditions used to calculate  $p(r, \theta)$  for the particular warp used here.

The first condition is that the observer is facing the point  $P(r, \theta)$ . For inclinations less than  $90^\circ$  the observer will see mostly the upper half of the disk, while at inclinations greater than  $90^\circ$  the observer will see mostly the lower half of the disk. There are select inclinations close to edge on where at inclinations less than  $90^\circ$  some of the lower disk can be seen. For example, if figure A.2 had an observer in the upper left viewing the disk close to edge on they would be able to see some of the lower convex side that is illustrated in the figure. In general it can be determined if the observer is facing the point  $P(r, \theta)$  based on the dot product  $\mathbf{n}_d \cdot \mathbf{u}$ . The normal is defined as extending on the upper side of the disk and the dot product will be greater than zero if  $\mathbf{n}_d$  and  $\mathbf{u}$  lie along the same direction. Therefore, the upper part of the disk can be seen if the dot product is greater than 0 while the lower part of the disk can be seen when the dot product is negative.

Now we determine if the point  $P(r, \theta)$  is blocked by either the star or the disk. First we consider whether the star blocks the far side of the disk. This applies for inclinations less than  $90^\circ$  where the star may block part of the upper convex side, as is demonstrated in figure A.4. The limit at which this condition applies is given by

$$\tan i_{lim} = \frac{r_{min} - R_* \cos i_{lim}}{gr_{min} \cos \alpha + R_* \sin i_{lim}} \quad (\text{A.12})$$

If the inclination is greater than  $i_{lim}$  then part of the disk is blocked by the star. In this case we can use the discussion of TB96 to determine if the point  $P(r, \theta)$  is blocked by the star (figure A.5 and table A.1). Defining  $C = r \sin(\theta - \alpha)$  the only time the star can block the disk is when  $C < R_*$  otherwise  $p(r, \theta) = 1$ . If  $C < R_*$  then  $p(r, \theta) = 1$  only if  $r \cos \theta < r_D \cos \theta_D$ , where  $\theta_D = \pi - \arcsin(C/r_D)$  and  $r_D$  is the positive root of the following equation:

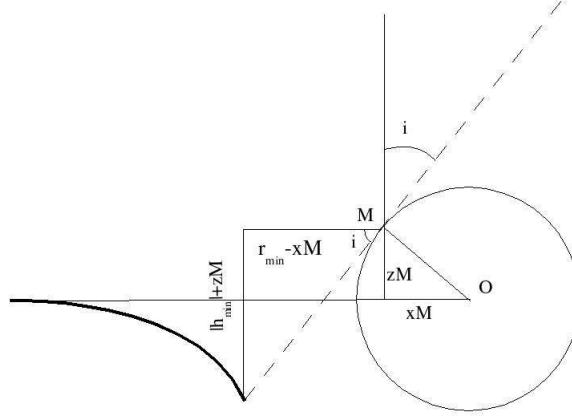


Figure A.4 Schematic diagram demonstrating when the star starts to block some of the disk.

Table A.1. Limiting inclination for occultation of disk by star

$g$	$r_{min} = 2R_*$	$r_{min} = 5R_*$	$r_{min} = 10R_*$
0.005	59.7	78.2	83.9
0.01	59.4	77.9	83.7
0.03	59.3	76.7	82.5
0.05	57.2	75.6	81.4
0.07	56.1	74.5	80.3
0.1	54.5	72.8	78.6
0.3	44.7	62.3	67.8
0.5	36.7	53.1	58.3

Note. — The limit on the inclination for the star to begin occulting the disk and for the disk to begin occulting the star.

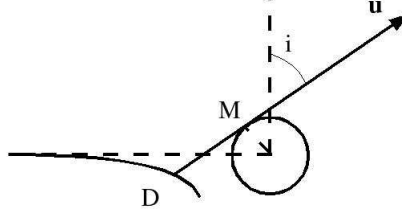


Figure A.5 Schematic diagram demonstrating the part of the disk that gets blocked by the star.

$$\left( -H(r_D) \sqrt{1 - \left( \frac{C}{r_D} \right)^2} - z_M \right) \sin i + \left( r_D \sqrt{1 - \left( \frac{C}{r_D} \right)^2} + x_M \right) \cos i = 0 \quad (\text{A.13})$$

where  $H(r) = gr_{\min} \left( \frac{r}{r_{\min}} \right)^{-n} \cos \alpha$  and M is the point on the northern hemisphere of the star in the plane (P, **u**, z) such that **u** is tangent to the star at this point:

$$x_M = -\sqrt{R_*^2 - C^2} \cos i \quad (\text{A.14})$$

$$y_M = C \quad (\text{A.15})$$

$$z_M = \sqrt{R_*^2 - C^2} \sin i \quad (\text{A.16})$$

Now consider inclinations greater than  $90^\circ$ . In this case the disk can still be blocked by the star if the warp is small enough and the inclination angle is close enough to 90 degrees (figure A.6). This affects both the upper and lower part of the disk, but only from  $\theta \in [\alpha + \pi/2, \alpha + 3\pi/2]$ . The condition for the point P to be hidden by the star is:

$$|h(r, \theta)| < \frac{R_* \cos(i - \pi/2) \tan(\pi - i) - r}{\tan(\pi - i)} \quad (\text{A.17})$$

As above this only applies when  $C = R_* \sin(\theta - \alpha) < R_*$ .

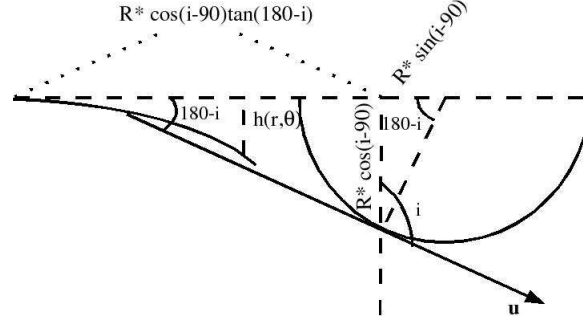


Figure A.6 Schematic diagram demonstrating the part of the disk that gets blocked by the star.

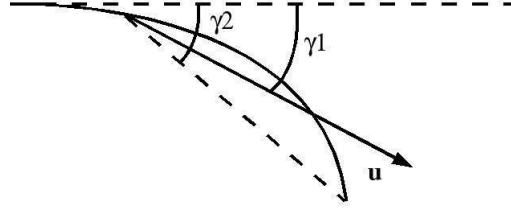


Figure A.7 Schematic diagram demonstrating when the disk is steep enough to block itself.

Another possibility to consider when the inclination is greater than  $90^\circ$  is that the warp on the lower concave side is steep enough that it blocks part of this side of the disk (figure A.7). This condition only applies to parts of the lower concave side, from  $\theta \in [\alpha + \pi/2, \alpha + 3\pi/2]$ . The condition is that  $\gamma_1 < \gamma_2$  where  $\gamma_1 = i - \pi/2$  and

$$\gamma_2 = \arcsin \left( \frac{h_m - h(r, \theta)}{PM} \right) \quad (\text{A.18})$$

In this case M is the highest point on the disk on the line of sight to point P. For  $r \sin(\pi - \theta) > r_{min}$  the disk does block itself, but for  $r \sin(\pi - \theta) < r_{min}$  we have  $r_m = r_{min}$  and  $\theta_m = \arcsin(r \sin(\theta - \alpha)/r_m)$ . The quantity PM is the distance between the point P and the point M ( $\sqrt{(h_m - h)^2 + (r_m - r)^2}$ ).

Once all of the conditions have been considered the flux from the disk can

be calculated using equation A.11. These conditions would apply to any type of warp whose maximum height above the midplane occurs at the inner edge of the disk, as opposed to at the outer edge of the disk, regardless of the exact functional form of the warp (ie. power law vs. exponential).

### A.3 Spiral Wave

#### A.3.1 Temperature Profile of Spiral Wave

The third type of disk that we attempt to model contains a spiral wave. As with the warped disks we follow the derivation of TB96 to derive the temperature structure and SED for this disk. The derivation for the temperature structure is very similar to that of the inner warp, only with slightly different definitions of the boundaries. For the part of the disk inside the wave, the disk is not blocked by the wave but the amount of the star seen can change. For points far from the wave, the disk is like a flat disk and  $\delta_{min} = 0$ . For points on the wave, as it rises above the midplane, more of the lower half of the star will become visible. How much of the lower half of the star is visible depends on the location and height of the point on the wave. In this case the lower limit on  $\delta$  is:

$$\delta_{min} = -\arctan(h/(r - r_{min})) \quad (\text{A.19})$$

This limit will continue to increase until the point on the wave can see the entire star and then  $\delta_{min} = -\delta_{max}$ . The other limits stay the same as in the previous models:

$$\varepsilon_{min} = 0$$

$$\varepsilon_{max} = \pi/2$$



(A.20)

$$\delta_{max} = \arcsin(R_*/d)$$

$$d^2 = r^2 + h^2$$

(A.21)

For the parts of the disk behind the wave, some of the star may be obscured. In this case:

$$\delta_{min} = \arctan(h_{sw}/(r - r_{sw})) \quad (A.22)$$

$$h_{sw} = gr_{min-sw}(1 - m\theta/2\pi)$$

$$r_{sw} = r_{min-sw}(1 + n\theta)$$

(A.23)

This is similar to the concave side of the inner warp, where the warp can obscure part of the star. The only difference is that the maximum height of the disk does not occur at the inner edge of the disk, but instead occurs at the location of the spiral wave. When  $\delta_{min} > \delta_{max}$  then the entire star is blocked and that point on the disk is only heated by viscous dissipation. With these definitions and equation (6) we can calculate the temperature of the disk.

### A.3.2 Calculating SED of Spiral Wave

The flux from the disk is given by:

$$F_{\nu, \mathbf{u}} = \int_{r_{min}}^{R_{disk}} \int_0^{2\pi} B(T_{disk}) f_{up} \quad (A.24)$$

There is no symmetry in the disk that allows us to split the disk into different parts, as with the concave and convex pieces of the inner warp. We also only

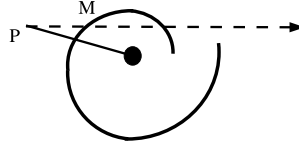


Figure A.8 Schematic diagram demonstrating the position of M and P in the disk when the wave can block part of the disk.

consider inclinations less than  $90^\circ$ , where we only see the upper disk, since the lower disk will look the same as the upper disk.

The one occultation effect we include is the blocking of the disk by the wave. For  $\alpha - \pi/2 < \theta < \alpha + \pi/2$ , the near side of the disk, the wave can block the part of the disk that is at smaller radius than the wave. For  $\alpha + \pi/2 < \theta < \alpha + 3\pi/2$ , the side of the disk on the other side of the star from the observer, the outer disk can be blocked by the wave. This effect can become important for modest inclinations, given the typical wave heights we consider here. To determine if a point on the disk is blocked by the wave we first need to determine where the line of sight intersects the wave. This is illustrated in figure A.8 and is given by:

$$x = r \sin \theta = r_{min-sw}(1 + n\theta_M) \sin(\theta_M) \quad (\text{A.25})$$

Here  $\theta_m$  is the azimuthal coordinate of the point where the wave intersects the line of sight. We assume that the point M lies at the peak of the spiral wave. This is only an approximation, although the narrowness of the wave make it an accurate one. The angle between the line connecting the points P and M and the midplane is  $\gamma$  (Fig. A.9). When  $\gamma > \pi/2 - i$  then point  $P(r, \theta)$  is blocked.

$$\tan \gamma = \left( \frac{h_M - h_P}{r_M - r_P} \right) \quad (\text{A.26})$$

We ignore occultation effects due to the star blocking the disk, which we did consider in the inner and outer warp model. Based on our experience with the

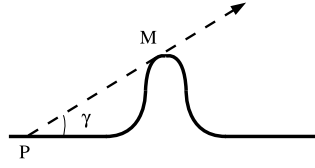


Figure A.9 Schematic diagram demonstrating how the spiral wave can block part of the disk.

warped disks and the typical dimensions of the disk, these are negligible effects that will only play a role very close to edge on. We also do not consider situations where the wave on the near side of the disk can block the far side of the disk. The exclusion of these two effects prevents us from considering the spiral wave at inclinations very close to  $90^\circ$ .

#### A.4 Stellar Flux

Next we consider the flux coming from the star. We follow a similar procedure as above where the equation for the stellar flux is modulated by a binary function ( $\varepsilon(\phi, \psi)$ ) which equals 1 when that part of the star is not blocked by the disk and it equals zero when the star is blocked by the disk. The angles  $\phi, \psi$ , shown in figure A.10, are the azimuthal and polar angles of a point on the surface of the star relative to the center of the star and the  $z$  axis (the same  $z$  axis as for the disk). The  $x$ -axis of this coordinate system is in the same direction as the line of sight, and will differ from the  $x$ -axis of the disk by the angle  $\alpha$ . The flux from the star is:

$$F_* = B_\nu \int \int_{\text{surface}} \varepsilon(\phi, \psi) d\mathbf{A} \quad (\text{A.27})$$

To determine the surface over which we integrate, we need to know the points of the star that are seen by the observer (ie. which side of the star is facing the observer). These points will be those that have  $\mathbf{u} \cdot d\mathbf{A} \geq 0$  where

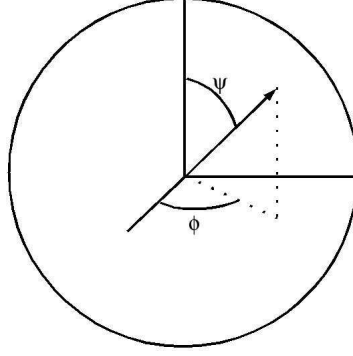


Figure A.10 Schematic diagram defining the angles  $\phi, \psi$

$$\mathbf{u} = \sin i \hat{x} + \cos i \hat{z} \quad (\text{A.28})$$

$$d\mathbf{A} = R_*^2 \sin \psi d\psi d\phi (\cos \phi \sin \psi \hat{x} + \sin \phi \cos \psi \hat{y} + \cos \psi \hat{z}) \quad (\text{A.29})$$

The evaluation of  $\varepsilon(\phi, \psi)$  will depend on the type of warp/wave and the orientation of the observer. First consider inclinations less than  $90^\circ$ . In this case the warp/wave stretching above the midplane may block some of the star. The entire star will be blocked if the following condition is met:

$$h(r, \alpha) - r \tan(\pi/2 - i) > R_* \quad (\text{A.30})$$

where  $r$  is location of the peak of the vertical disturbance and  $h$  is the maximum height of the warp or wave at the angle  $\alpha$ . The exact value of  $r$  and  $h$  will depend on whether we are considering the outer warp, inner warp, or spiral wave (ie.  $r = r_{min}$ ,  $h(r, \alpha) = gr_{min} \cos(\alpha)$  for the inner warp). This condition is illustrated in figure A.11 for the inner warp, which is the disk that is the most likely to occult the star.

None of the star will be blocked if the inclination is less than  $i_{lim}$  (discussed earlier). A generic version of the equation for  $i_{lim}$  that can be applied to all of the disks is:

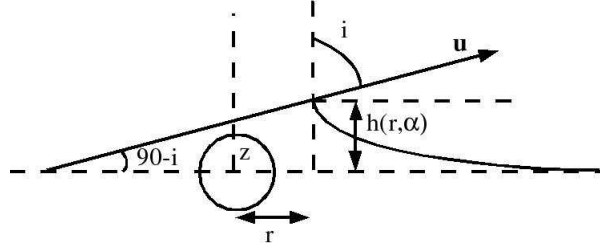


Figure A.11 Schematic diagram showing the case where  $i < 90^\circ$  and the disk can block the star.

$$\tan i_{lim} = \frac{r - R_* \cos i_{lim}}{h(r, \alpha) + R_* \sin i_{lim}} \quad (\text{A.31})$$

When the inclination falls between these two limits only a fraction of the star is blocked. We can use the discussion of TB96 section A2.2 to determine if a point of the star's surface is hidden by the star

The point Q is a point on the surface of the star that intersects the line of sight and the upper edge of the disk. If the point  $N(\phi, \psi)$  lies above Q then the observer can see this part of the star, otherwise it is hidden and  $\varepsilon(\phi, \psi) = 0$ . The vertical coordinate of Q,  $z_Q$ , is the greatest root of the following equation:

$$(1 + \tan^2 i) z_Q^2 - 2 \tan i (h \tan i - r \cos \alpha) z_Q + (h \tan i - r \cos \alpha)^2 - R_*^2 + R_*^2 \sin^2 \psi \cos^2 \phi = 0 \quad (\text{A.32})$$

If  $z_N \geq z_Q$  then  $\varepsilon(\phi, \psi) = 1$  otherwise  $\varepsilon(\phi, \psi) = 0$  with  $z_N$  being given by:

$$z_N = -R_* \sin \psi \sin \phi \sin i + R_* \cos \psi \cos i \quad (\text{A.33})$$

For the inner and outer warp we consider inclinations greater than  $90^\circ$  where the disk can still block part of the star, although it is less likely because the disk curves away from the observer. This is illustrated in figure A.12 for the inner warp, but can also apply to the outer warp in the limit that  $h$  goes to zero. The

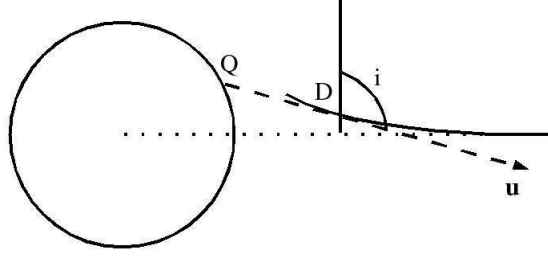


Figure A.12 Schematic diagram showing the case where  $i > 90$  and the disk can block the star.

point at which the line of sight is perpendicular to the normal of the disk sets a limit to the distance  $z$  above the midplane that an observer can see. If this distance is less than the radius of the star then some of the star is blocked by the disk. The point D at which the the line of sight is perpendicular to the disk occurs when  $\mathbf{u} \cdot \mathbf{n} = 0$  (figure A.12). If this condition is met at a radius  $r_D$  then a point  $N(\phi, \psi)$  on the stellar surface will be blocked if

$$R_* \cos \psi > h(r_D, \alpha) + r_D \tan(i - \pi/2) \quad (\text{A.34})$$

If there is no point at which  $\mathbf{u} \cdot \mathbf{n} = 0$  then  $r_D = r_{min}$  and the same condition for being able to see the star is used. When this condition is met  $\varepsilon(\phi, \psi) = 0$ , otherwise  $\varepsilon(\phi, \psi) = 1$ .

All of these different occultations are combined to determine  $\varepsilon(\phi, \psi)$ . The flux is determined by integrating over the entire surface and added to the flux from the disk to create the observed SED.

## REFERENCES

- Ábrahám, P., et al. 2009, *Nature*, 459, 224
- Alencar, S.H.P., et al. 2010, *A&A*, 519, 88
- Alexander, R.D., Clarke, C.J & Pringle, J.E. 2006, *MNRAS*, 369, 229
- Allen, L.E. & Strom, K.M. 1995 *AJ*, 109, 1379
- Alves de Oliveira, C., & Casali, M. 2008, *A&A*, 485, 155
- Andrews, S.M., & Williams, J.P. 2005, *ApJ*, 631, 1134
- Andrews, S.M. & Williams, J.P. 2007, *ApJ*, 659, 705
- Andrews, S.M., Wilner, D.J., Espaillat, C., Hughes, A.M., Dullemond, C.P., McClure, M.K., Qi, C., & Brown, J.M. 2011, *ApJ*, 732, 42
- Anthony-Twarog, B.J. 1982, *AJ*, 87, 1213
- Artymowicz, P., & Lubow, S.H. 1994, *ApJ*, 421, 651
- Artymowicz, P., & Lubow, S.H. 1996, *ApJ*, 467, L77
- Augereau, J.C., Nelson, R.P., Lagrange, A.M., Papaloizou, J.C.B., & Mouillet, D. 2001, *A&A*, 370, 447
- Balbus, S.A., & Hawley, J.F. 1991, *ApJ*, 376, 214
- Bally, J. 1982, *ApJ*, 261, 558
- Balog, Z., Muzerolle, J., Rieke, G.H., Su, K.Y.L., Young, E.T. & Megeath, S.T. 2007 *ApJ*, 660, 1532

- Baraffe, I., Chabrier, G., Allard, F. & Hauschildt, M.H. 1998, *A&A*, 337, 403
- Barsony, M., Ressler, M.E., & Marsh, K.A. 2005, *ApJ*, 630, 381
- Bary, J.S., Leisenring, J.M., & Skrutskie, M.F. 2009, *ApJ*, 706, L168
- Basri, G. & Batalha, C. 1990, *ApJ*, 363, 654
- Beckwith, S.V.W. & Sargent, A.N. 1991, *ApJ*, 381, 250
- Blandford, R.D., & Payne, D.G. 1982, *MNRAS*, 199, 883
- Boley, A.C., & Durisen, R.H. 2006, *ApJ*, 641, 534
- Borucki, W.J., et al. *ApJ*submitted arXiv/1102.0541
- Bouvier, J., et al. 2003, *A&A*, 409, 169
- Bouvier, J., et al. 2007a, *A&A*, 463, 1017
- Bouvier, J., Alencar, S.H.P., Harries, T.J., Johns-Krull, C.M., Romanova, M.M. 2007b in *Protostars and Planets V*, ed. Reipurth, B., Jewitt, D., Keil, K. (Tucson, AZ: Univ. Arizona Press), 479
- Bouwman, J., Meeus, G., de Koter, A., Hony, S., Dominik, C. & Waters, L.B.F.M. 2001, *A&A*, 375, 950
- Bričeno, C., Calvet, N., Hernández, J., Vivas, A.K., Hartmann, L., Downes, J.J. & Berlind, P. 2005, *ApJ*, 129, 907
- Bryden, G., Chen, X., Lin, D.N.C., Nelson, R.P., & Papaloizou, J.C.B. 1999, *ApJ*, 514, 344
- Calvet, N., D'Alessio, P., Hartmann, L., Wilner, D., Walsh, A., & Sitko, M. 2002, *ApJ*, 568, 1008



- Calvet, N., et al. 2005, *ApJ*, 630, L185
- Castelli, F., & Kurucz, R.L. 2004, <http://adsabs.harvard.edu/abs/2004astro.ph..5087C>
- Cardelli, J.A., Clayton, G.C. & Mathis, J.S. 1989, *ApJ*, 345, 245
- Carpenter, J.M., Hillenbrand, L.A., & Skrutskie, M.F. 2001, *AJ*, 121, 3160
- Carpenter, J.M., Mamajek, E.E., Hillenbrand, L.A., & Meyer, M.R. 2006, *ApJ*, 651, L49
- Caproni, A., Livio, M., Abraham, Z., & Mosquera Cuesta, H.J. 2006, *ApJ*, 653, 112
- Chiang, E.I., & Goldreich, P. 1997, *ApJ*, 490, 368
- Cieza, L., & Baliber, N. 2006, *ApJ*, 649, 878
- Clarke, C.J., & Bouvier, J. 2000, *MNRAS*, 319, 457
- Clarke, C.J., Gendrin, A. & Sotomayor, M. 2001, *MNRAS*, 328, 485
- Cohen, R.E., Herbst, W., & Williams, E.C. 2004 *AJ*, 127, 1602
- Currie, T. et al. 2007, *ApJ*, 659, 599
- Currie, T., Lada, C.J., Plavchan, P., Robitaille, T.P., Irwin, J., & Kenyon, S.J. 2009, *ApJ*, 698, 1
- Cushing, M.C., Vacca, W.D., & Rayner, J.T. 2004, *PASP*, 116, 362
- Dahm, S.E. 2008, *AJ*, 136, 521
- Dahm, S.E. & Hillenbrand, L.A. 2007, *AJ*, 133, 2072
- D'Alessio, P., Canto, J., Calvet, N., & Lizano, S. 1998, 500, 411

- D'Alessio, P., Cantó, J., Hartmann, L., Calvet, N., & Lizano, S. 1999, *ApJ*, 511, 896
- D'Alessio, P.D., et al. 2005, *ApJ*, 621, 461
- D'Alessio, P., Calvet, N., Hartmann, L., Franco-Hernández, R., & Servín, H. 2006, *ApJ*, 638, 314
- D'Antona, F. & Mazzitelli, I. 1997, *Mem. Soc. Astron. Italiana*, 68, 807
- Dobashi, K., Uehara, H., Kandori, R., Sakurai, T., Kaiden, M., Umemoto, T. & Sato, F. 2005, *PASJ*, 57, 1
- Dodson-Robinson, S.E., & Salyk, C. 2011, *arXiv:1106.4824*
- Draine, B.T. 2003, *ARA&A*, 41, 241
- Dullemond, C.P. 2001, *A&A*, 361, L17
- Dullemond, C.P., Dominik, C., & Natta, A. 2001, *ApJ*, 560, 957
- Dullemond, C.P. & Dominik, C. 2004, *A&A*, 421, 1075
- Dullemond, C.P. & Dominik, C. 2005, *A&A*, 434, 971
- Dullemond, C.P., Natta, A. & Testi, L. 2006, *ApJ*, 645, L69
- Dullemond, C.P., & Monnier, J.D. 2010, *ARA&A*, 48, 205
- Dullemond, C.P., van den Ancker, M.E., Acke, B., & van Boekel, R. 2003, *ApJ*, 594, L47
- Edgar, R.G., & Quillen, A.C. 2008, *MNRAS*, 387, 387
- Edwards, S., Fischer, W., Hillenbrand, L., Kwan, J. 2006, *ApJ*, 646, 319
- Eiroa, C., et al. 2002, *A&A*, 384, 1038

- Engelbracht, C.W., et al. 2007, *PASP*, 119, 994
- Espaillat, C., Calvet, N., D'Alessio, P., Derández, J., Qi, C., Hartmann, L., Furlan, E., & Watson, D.M. 2007, *ApJ*, 670, L135
- Espaillat, C., et al. 2010, *ApJ*, 717, 441
- Espaillat, C., Furlan, E., D'Alessio, P., Sargent, B., Nagel, E., Calvet, N., Watson, D.M., & Muzerolle, J. 2011, *ApJ*, 728, 49
- Fabricant, D. et al., 2005, *PASP*, 117, 1411
- Fazio, G.G., et al. 2004, *ApJS*, 154, 10
- Finkbeiner, D., et al. 2004, *AJ*, 128, 2577
- Fischer, W., Kwan, J., Edwards, S., & Hillenbrand, L. 2008, *ApJ*, 687, 1117
- Flaherty, K.M., Pipher, J.L., Megeath, S.T., Winston, E.A., Gutermuth, R.A., Muzerolle, J., Allen, L.E. & Fazio, G.G. 2007, *ApJ*, 663, 1069
- Flaherty, K.M., & Muzerolle, J. 2008, *AJ*, 135, 966
- Flaherty, K.M., & Muzerolle, J. 2010, *ApJ*, 719, 1733
- Flaherty, K.M., Muzerolle, J., Rieke, G., Gutermuth, R., Balog, Z., Herbst, W., Megeath, S.T., & Kun, M. 2011, *ApJ*, 732, 83
- Forrest, W.J., et al. 2004, *ApJS*, 154, 443
- Fragner, M.M., & Nelson, R.P. 2010, *A&A*, 511, 77
- Fukui, Y., Sugitani, K., Takaba, H., Iwata, T., Mizuno, A., Ogawa, H. & Kawabata, K. 1986, *ApJ*, 311, L85

- Furlan, E. et al. 2006 ApJS, 165, 568
- Furlan, E., et al. 2009, ApJ, 703, 1964
- Gerakines, P.A., Whittet, D.C.B., & Lazarian, A. 1995, ApJ, 455, L171
- Goldreich, P., & Tremaine, S. 1979, ApJ, 233, 857
- Goetz, J., Gutermuth, R., Pipher, J.L., Forrest, W.J. & Howard, E.M. 2003, ApJ, 599, 1173
- Goodson, A.P., & Winglee, R.M. 1999, 524, 159
- Gordon, K. D., et al. 2005, PASP, 117, 503
- Gorlova, N., Balog, Z., Rieke, G.H., Muzerolle, J., Su, K.Y.L., Ivanov, V.D. & Young, E.T. 2007, ApJ, 670, 516
- Gullbring, E., Petrov, P.P., Ilyin, I., Tuominen, I., Gahm, G.F., & Loden, K. 1996, A&A, 314, 835
- Gullbring, E., Hartmann, L., Briceno, C. & Calvet, N. 1998, ApJ, 492, 323
- Gutermuth, R.A. et al. 2004, ApJ, 154, 374
- Gutermuth, R.A., Megeath, S.T., Myers, P.C., Allen, L.E., Pipher, J.L., & Fazio, G.G. 2009, ApJS, 184, 18
- Haisch, K.E., Lada, E.A. & Lada, C.J. 2001, AJ, 121, 2065
- Hartigan, P., Hartmann, L., Kenyon, S., Hewett, R. & Stauffer, J. 1989, ApJS, 70, 899
- Hartigan, P., Kenyon, S.J., Hartmann, L., Strom, S.E., Edwards, S., Welty, A.D., & Stauffer, J. 1991, ApJ, 382, 617

- Hartmann, L., Hewett, R., Stahler, S & Mathieu, R.D. 1986, *ApJ*, 309, 275
- Hartmann, L., & Kenyon, S.J. 1996, *ARA&A*, 34, 207
- Hartmann, L., Megeath, S.T., Allen, L., Luhman, K., Clavet, N., D'Alessio, P., Franco-Hernandez, R. & Fazio, G.G. 2005, *ApJ*, 629, 881
- Herbig, G.H. 1998, *ApJ*, 497, 736
- Herbig, G.H. 2007, *AJ*, 133, 2679
- Herbst, W., Herbst, D.K., Grossman, E.J., & Weinstein, D. 1994, *AJ*, 108, 1906
- Herbst, W., LeDuc, K., Hamilton, C.M., Winn, J.N., Ibrahimov, M., Mundt, R., Johns-Krull, C.M. 2010, *AJ*, 140, 2025
- Hernandez, J., et al. 2007, *ApJ*, 662, 1067
- Higdon, S.J.U., et al. 2004, *PASP*, 116, 975
- Hillenbrand, L.A. 1997, *AJ*, 113, 1733
- Hillenbrand, L.A. & White, R.J., 2004, *ApJ*, 604, 741
- Hirose, S. & Turner, N.J. 2011, *ApJ*, 732, 30L
- Houck, J.R., et al. 2004, *ApJS*, 154, 18
- Hutchinson, M.G., Albinson, J.S., Barrett, P., Davies, J.K., Evans, A., Goldsmith, M.J., & Maddison, R.C. 1994, *A&A*, 285, 883
- Indebetouw, R., et al. 2005, *ApJ*, 619, 931
- Ireland, M.J., & Krause, A.L. 2008, *ApJ*, 678, L59
- Isella, A., & Natta, A. 2005, *A&A*, 899, 907

- Jang-Condell, H. 2009, *ApJ*, 700, 820
- Jayawardhana, R., Coffey, J., Scholz, A., Brandeker, A. & van Kerkwijk, M.H. 2006, *ApJ*, 648, 1206
- Johns, C.M. & Basri, G. 1995, *AJ*, 109, 2800
- Johnstone, D., Hollenbach, D., & Bally, J. 1998, *ApJ*, 499, 758
- Johnstone, D., Fich, M., Mitchell, G.F. & Moriarty-Schieven, G. 2001, *ApJ*, 559, 307
- Jordi, K., Grebel, E.K. & Ammon, K. 2006, *A&A*, 460, 339
- Jørgensen, J.K., et al. 2006, *ApJ*, 645, 1246
- Joy, A.H. 1945, *ApJ*, 102, 168
- Juhász, A., Prusti, T., Ábrahám, P., & Dullemond, C.P. 2007, *MNRAS*, 274, 1242
- Kama, M., Min, M., & Dominik, C. 2009, *A&A*, 506, 1199
- Kelly, B.C., Sobolewska, M., Siemiginowska, A. 2011, *ApJ*, 730, 52
- Kenyon, S.J., & Hartmann, L. 1995, *ApJS*, 101, 117
- Kenyon, S.J., Yi, I. & Hartmann, L.W. 1996, *ApJ*, 462, 439
- Kessler-Silacci, J. et al. 2006, *ApJ*, 639, 275
- Kessler-Silacci, J.E., et al. 2007, *ApJ*, 659, 680
- Kim, K.H., et al. 2009, *ApJ*, 700, 1017
- Kley, W. 1999, *MNRAS*, 303, 696
- Konigl, A., Pudritz, R.E. 2000 in *Protostars and Planets IV*, ed. Mannings, V., Boss, A.P., Russell, S.S. (Tucson, AZ: Univ. Arizona Press), 759

- Kulkarni, A.K., & Romanova, M.M. 2008, MNRAS, 386, 673
- Kwan, J., & Fischer, W. 2011, MNRAS, 411, 2383
- Lada, E.A., Bally, J. & Stark, A.A. 1991, ApJ, 368, 432
- Lada, C., et al. 2006, AJ, 131, 1574
- Lai, D. 1999, ApJ, 524, 1030
- Lai, D., & Zhang, H. 2008, ApJ, 683, 949
- Larwood, J.D., Papaloizou, J.C.B. 1997, MNRAS, 285, 288
- Liu, M.C., et al. 1996, ApJ, 461, 334
- Littlefair, S.P., Naylor, T., Burningham, B., & Jeffries, R.D. 2005, MNRAS, 358, 341
- Lovelace, R.V.E., Romanova, M.M., Ustyugova, G.V., & Koldoba, A.V. 2010, MNRAS, 408, 2083
- Lubow, S.H. & D'Angelo G. 2006, ApJ, 641, 526
- Luhman, K.L., Stauffer, J.R., Muench, A.A., Rieke, G.H., Lada, E.A., Bouvier, J., & Lada, C.J. 2003, ApJ, 593, 1093
- Manoj, P., et al. 2011, ApJS, 193, 11
- Mathieu, R.D. 1994, ARA&A, 32, 465
- Mathieu, R.D., Ghez, A.M., Jensen, E.N. & Simon, M. 2000 in Protostars and Planets IV ed V. Mannings, V., Boss, A.P., Russell, S.S. (Tucson, Univ. Arizona Press), 703
- Mathis, J.S. 1990, ARA&A, 28, 37

- McClure, M. 2009, *ApJL*, 693, 81L
- McClure, M.K., et al. 2010, *ApJS*, 188, 75
- Megeath, S.T., Hartmann, L., Luhman, K.L. & Fazio, G.G. 2005, *ApJ*, 634L, 113
- Merín, B., et al. 2010, *ApJ*, 718, 1200
- Meyer, M., Calvet, N. & Hillenbrand, L.A. 1997, *AJ*, 114, 288
- Milan-Gabet, R., Malbet, F., Akeson, R., Leinert, C., Monnier, J., & Waters, R. 2007 in *Protostars and Planets V*, ed. B. Reipurth, D. Jewitt, & K. Keil (Tucson, AZ: Univ. Arizona Press), 539
- Miyake, K. & Nakagawa, Y., 1993, *Icarus*, 106, 20
- Morales-Calderón, et al. 2009 *ApJ*, 702, 1507
- Morales-Calderón, M., et al. 2011, *arXiv/1103.5238*
- Muench, A.A., Lada, C.J., Luhman, K.L., Muzerolle, J., & Young, E. 2007, *AJ*, 134, 411
- Muzerolle, J., Hartmann, L., & Calvet, N. 1998, *AJ*, 116, 2965
- Muzerolle, J., Calvet, N., Briceno, C., Hartmann, L. & Hillenbrand, L. 2000, *ApJ*, 535, 47
- Muzerolle, J., Clavet, N., Hartmann, L., & D'Alessio, P. 2003, *ApJ*, 597, L149
- Muzerolle, J., et al. 2009 *ApJL* 704, 15
- Muzerolle, J., Allen, L.E., Megeath, S.T., Hernández, J., & Gutermuth, R.A. 2010, *ApJ*, 708, 1107



- Nagel, E., D'Alessio, Calvet, N., Espaillat, C., Sargent, B., Hernández, J., & Forrest, W. 2010, *ApJ*, 708, 38
- Najita, J.R., Strom, S.E. & Muzerolle, J. 2007, *MNRAS*, 378, 369
- Nordhagen, S., Herbst, W., Rhode, K.L., & Williams, E.C. 2006, *AJ*, 132, 1555
- Ogilvie, G.I., & Lubow, S.H. 2002, *MNRAS*, 330, 950
- Owen, J.E., Ercolano, B., Clarke, C.J., & Alexander, R.D. 2010, *MNRAS*, 401, 1415
- Padgett, D.L., Strom, S.E. & Ghez, A. 1997, *ApJ*, 477, 705
- Palla, F., & Stahler, S.W. 1999, *ApJ*, 525, 772
- Pascucci, I., & Sterzik, M. 2009, *ApJ*, 702, 724
- Pacucci, I., et al. 2006, *ApJ*, 651, 1177
- Papaloizou, J.C.B., Nelson, R.P., Kley, W., Masset, F.S., Artymowicz, P. 2007, in *Protostars and Planets V*, ed. B. Reipurth, D. Jewitt, & K. Keil (Tucson: Univ. Arizona Press), 655
- Pardekooper, S.J. & Mellema, G. 2004, *A&A*, 425, L9
- Plavchan, P., Gee, A.H., Stapelfeldt, K., & Becker, A. 2008, *ApJL*, 684, L37
- Plavchan, P., Werner, M.W., Chen, C.H., Stapelfeldt, K.R., Su, K.Y.L., Stauffer, J.R., & Song, I. 2009, *ApJ*, 698, 1068
- Pollack, P.B., Hollenbach, D., Beckwith, S., Simonelli, D.P., Roush, T., & Fong, W. 1994, *ApJ*, 421, 615
- Pontoppidan, K.M., Dullemond, C.P., Blake, G.A., Boogert, A.C.A., van Dishoeck, E.F., Evans, N.J. II, Kessler-Silacci, J., & Lahuis, F. 2007, *ApJ*, 656, 980

- Pontoppidan, K.M., Blake, G.A., van Dishoeck, E.F., Smette, A., Ireland, M.J., & Brown, J. 2008, *ApJ*, 684, 1323
- Quillen, A.C., Blackman, E.G., Frank, A. & Varnière, P. 2004, *ApJ*, 612, L137
- Rayner, J.T., Toomey, D.W., Onaka, P.M., Denault, A.J., Stahlberger, W.E., Vacca, W.D., Cushing, M.C., Wang, S. 2003, *PASP*, 115, 362
- Rayner, J.T., Cushing, M.C., & Vacca, W.D. 2009, *ApJS*, 185, 289
- Rebull, L.M., Wolff, S.C. & Strom, S.E. 2004, *AJ*, 127, 1029
- Rebull, L.M., et al. 2007, *ApJS*, 171, 447
- Reipurth, B. 1999, *General Catalogue of Herbig-Haro Objects* (2d e.; Boulder: Cent. Astrophys. Space Aston.)
- Rice, W.K.M., Wood, K., Armitage, P.J., Whitney, B.A. & Bjorkman, J.E. 2003, *MNRAS*, 342, 79
- Rice, W.K.M., Armitage, P.J., Wood, K. & Lodato, G. 2006, *MNRAS*, 373, 1619
- Rieke, G.H. & Lebofsky, M.J. 1985, *ApJ*, 288, 618
- Rieke, G.H., et al. 2004, *ApJS*, 154, 25
- Roccatagliata, V., Henning, T., Wolk, S., Rodmann, J., Corder, S., Carpenter, J.M., Meyer, M.R., & Dowell, D. 2009, *A&A*, 497, 409
- Romanova, M.M., Ustyugova, G.V., Koldoba, A.V., & Lovelace, R.V.E. 2009, *MNRAS*, 399, 1802
- Salyk, C., Blake, G.A., Boogert, A.C.A., & Brown, J.M. 2009, *ApJ*, 699, 330
- Sargent, B. et al., 2006, *ApJ*, 645, 395

- Schisano, E., Covino, E., Alcalá, J.M., Esposito, M., Gandolfi, D., Guenther, E.W. 2009, *A&A*, 501, 1013
- Schmidt, G.D., Stockman, H.S., & Smith, P.S. 1992, *ApJ*, 398, L57
- Sicilia-Aguilar, A., Hartmann, L.W., Briceno, C., Muzerolle, J. & Calvet, N. 2004, *AJ*, 128, 805
- Sicilia-Aguilar, A., et al. 2005 *AJ*, 129, 363
- Sicilia-Aguilar, A., et al. 2006 *ApJ*, 638, 897
- Siess, L., Dufour, E., & Forestini, M. 2000, *A&A*, 358, 593
- Simonetti, J.H., Cordes, J.M., Heeschen, D.S. 1985, *ApJ*, 296, 46
- Sitko, M.L., et al. 2008, *ApJ*, 678, 1070
- Skemer, A., Close, L., Hinz, P., Hoffmann, W., Greene, T., Males, & Beck, T. 2010 *ApJ*, 711, 1280
- Skinner, S.L., Simmons, A.E., Audard, M. & Güdel, M. 2007, *ApJ*, 658, 1144
- Skrutskie, M.F., Meyer, M.R., Whalen, D., & Hamilton, C. 1996, *AJ*, 112, 2168
- Smith, P.S., Schmidt, G.D., Hines, D.C., & Foltz, C.B. 2003, *ApJ*, 593, 676
- Snell, R.L. & Edwards, S. 1982, *ApJ*, 223, 884
- Strom, K.M., Strom, S.E., Edwards, S., Cabrit, S., & Skrutskie, M. 1989, *AJ*, 97, 1451
- Suzuki, T.K., Muto, T., & Inutsuka, S. 2010, *ApJ*, 718, 1289

- Szentgyorgyi, A.H., Cheimets, P., Eng, R., Fabricant, D.G., Geary, J.C., Hartmann, L., Pieri, M.R., & Roll, J.B. 1998, SPIE, 3355, 242
- Tanaka, H., Himerno, Y., & Ida, Shigeru 2005, ApJ, 625, 414
- Terquem, C, & Bertout, C. 1993, A&A, 274, 291
- Terquem, C, & Bertout, C. 1996, MNRAS, 279, 415
- Tonry, J. & Davis, M. 1979, AJ, 84, 1511
- Turner, N.J., Carballido, A., & Sano, T. 2010, ApJ, 708, 188
- Vacca, W.D., Cushing, M.C., Rayner, J.T. 2003, PASP, 115, 389
- van Boekel, R., et al. 2004, Nature, 432, 479
- Vinković, D., & Jurkić, T. 2007, ApJ, 658, 462
- Vogt, S.S., eet al. 1994, SPIE, 2198, 362
- Watanabe, S., & Lin, D.N.C. 2008, ApJ, 672, 1183
- Watson, A.M., & Stapelfeldt, K.R. 2007, AJ, 133, 845
- Weingartner, J.C., & Draine, B.T. 2001, ApJ, 548, 296
- White, R.J. & Basri,G. 2003, ApJ, 582, 1109
- White, R.J. & Hillenbrand, L.A. 2004, ApJ, 616, 998
- White, G.J. & Phillips, J.P. 1981, MNRAS, 194,947
- Whittet, D.C.B., Gerakines, P.A., Hough, J.H. & Shenoy, S.S. 2001, ApJ, 547, 872
- Wiling, B.A., Meyer, M.R., Robinson, J.G., Greene, T.P. 2005, AJ, 130, 1733

Wilson, B.A., Dame, T.M., Mashedier, M.R.W. & Thaddeus, P. 2005, *A&A*, 430, 523

Winston, E. et al. 2007 *ApJ*, 669, 493

Wisniewski, J.P., Clampin, M., Grady, C.A., Ardila, D.R., Ford, H.C., Golimowski, D.A., Illingworth, G.D., & Krist, J.E. 2008, *ApJ*, 682, 548

York, D.G. et al. 2000, *AJ*120, 1579

Zhao, B., Wang, M., Yang, J., Wang, H., Deng, L., Yan, J. & Chen, J. 1999, *AJ*, 118, 1347